frontiers | Research Topics

Environmentally-responsive biomaterials for major diseases treatment

Edited by
Donglin Xia, Jingwei Xie and Yao Luo

Published in
Frontiers in Bioengineering and Biotechnology

ISSN 1664-8714
ISBN 978-2-8325-6317-5
DOI 10.3389/978-2-8325-6317-5

About Frontiers

Frontiers is more than just an open access publisher of scholarly articles: it is a pioneering approach to the world of academia, radically improving the way scholarly research is managed. The grand vision of Frontiers is a world where all people have an equal opportunity to seek, share and generate knowledge. Frontiers provides immediate and permanent online open access to all its publications, but this alone is not enough to realize our grand goals.

Frontiers journal series

The Frontiers journal series is a multi-tier and interdisciplinary set of open-access, online journals, promising a paradigm shift from the current review, selection and dissemination processes in academic publishing. All Frontiers journals are driven by researchers for researchers; therefore, they constitute a service to the scholarly community. At the same time, the *Frontiers journal series* operates on a revolutionary invention, the tiered publishing system, initially addressing specific communities of scholars, and gradually climbing up to broader public understanding, thus serving the interests of the lay society, too.

Dedication to quality

Each Frontiers article is a landmark of the highest quality, thanks to genuinely collaborative interactions between authors and review editors, who include some of the world's best academicians. Research must be certified by peers before entering a stream of knowledge that may eventually reach the public - and shape society; therefore, Frontiers only applies the most rigorous and unbiased reviews. Frontiers revolutionizes research publishing by freely delivering the most outstanding research, evaluated with no bias from both the academic and social point of view. By applying the most advanced information technologies, Frontiers is catapulting scholarly publishing into a new generation.

What are Frontiers Research Topics?

Frontiers Research Topics are very popular trademarks of the *Frontiers journals series*: they are collections of at least ten articles, all centered on a particular subject. With their unique mix of varied contributions from Original Research to Review Articles, Frontiers Research Topics unify the most influential researchers, the latest key findings and historical advances in a hot research area.

Find out more on how to host your own Frontiers Research Topic or contribute to one as an author by contacting the Frontiers editorial office: frontiersin.org/about/contact

Environmentally-responsive biomaterials for major diseases treatment

Topic editors

Donglin Xia — Nantong University, China

Jingwei Xie — University of Nebraska Medical Center, United States

Yao Luo — Sichuan University, China

Citation

Xia, D., Xie, J., Luo, Y., eds. (2025). *Environmentally-responsive biomaterials for major diseases treatment*. Lausanne: Frontiers Media SA.

doi: 10.3389/978-2-8325-6317-5

Table of contents

frontiers | Frontiers in Bioengineering and Biotechnology

TYPE Editorial
PUBLISHED 25 April 2025
DOI 10.3389/fbioe.2025.1604616

OPEN ACCESS

EDITED AND REVIEWED BY
Candan Tamerler,
University of Kansas, United States

*CORRESPONDENCE
Donglin Xia,
xiadonglin@ntu.edu.cn
Yao Luo,
luoyao@scu.edu.cn

RECEIVED 02 April 2025
ACCEPTED 21 April 2025
PUBLISHED 25 April 2025

CITATION
Zhao Y, Xia D and Luo Y (2025) Editorial: Environmentally-responsive biomaterials for major diseases treatment.
Front. Bioeng. Biotechnol. 13:1604616.
doi: 10.3389/fbioe.2025.1604616

Editorial: Environmentally-responsive biomaterials for major diseases treatment

Yan Zhao[1], Donglin Xia[2]* and Yao Luo[3]*

[1]Institute of Biomedical Health Technology and Engineering, Shenzhen Bay Laboratory, Shenzhen, China, [2]School of Public Health of Nantong University, Nantong, China, [3]Department of Laboratory Medicine, Sichuan Medical Laboratory Clinical Medicine Research Center, West China Hospital, Sichuan University, Chengdu, China

KEYWORDS

biomedical materials, microenvironmental stimuli, disease treatment, injury repair, nanomedicine, targeted release, release mechanism

Editorial on the Research Topic
Environmentally-responsive biomaterials for major diseases treatment

1 Introduction

Environmentally-responsive biomaterials are a novel class of materials that undergo structural or functional changes by altering their internal atom arrangement in response to environmental stimuli. These stimuli include endogenous disease microenvironments, such as the acidic pH of tumor microenvironments or elevated enzymatic activity in inflamed tissues, external physical triggers, such as temperature, light, ultrasound, or magnetic fields, and the combinations of these stimuli (Mura et al., 2013; Chen et al., 2022; Zhu et al., 2023). A variety of environmentally-responsive biomaterials have been developed to date, including DNA nanostructures (Zhao et al., 2023; Li et al., 2024; Zhao et al., 2024c; Zhao et al., 2021; Liu et al., 2023; Ji et al., 2022), hydrogels (Ma et al., 2023; Zhao et al., 2024b; Guo et al., 2023), nanomicelles (Wang et al., 2024; Uthaman et al., 2024; Wang et al., 2023) and biomembranes-based materials (Su et al., 2022). Those environmentally-responsive biomaterials achieve the delivery and release of therapeutics with precise spatial and temporal control, minimizing off-target effects and maximizing treatment efficacy *in vitro* and *in vivo* (Xue et al., 2023; Cui et al., 2024; Wei et al., 2011; Xia et al., 2019).

For the treatment of clinical diseases, one of the primary advantages of environmentally-responsive biomaterials is their ability to provide targeted and on-demand therapeutic solutions. By leveraging the unique pathological microenvironments of diseases or physical stimuli, these materials enhance the selectivity and efficiency of treatments. Additionally, their adaptability reduces the need for external intervention, improving patient compliance and reducing systemic toxicity. Applications of environmentally-responsive biomaterials span across major disease treatments (Zhao L. et al., 2024; Guo et al., 2016; Duan et al., 2022; Xia et al., 2020), including cancer, diabetes, cardiovascular disorders. For example, pH-sensitive hydrogels

are used for localized drug delivery in cancer therapy (Lin et al., 2025), while thrombin-responsive DNA nanomachines aid in precise delivery and accurate dosing of tissue plasminogen activator release for thrombolytic therapy (Yin et al., 2024). Furthermore, advancements in this field are paving the way for tissue engineering (Zhang et al., 2018), regenerative medicine, and autoimmune diseases (Shodeinde et al., 2020), driving a paradigm shift in modern healthcare (Zhang et al., 2015). In summary, environmentally responsive biomaterials embody the intersection of material science and medicine, offering innovative and sustainable solutions to some of the most pressing challenges in disease treatment.

This Research Topic collected excellent works on the "Environmentally-responsive biomaterials for major diseases treatment," and a total of 9 articles from 38 authors were accepted. The contributions have deepened the understanding of this Research Topic from perspectives such as the development of environmentally-responsive biomaterials and the strategies for utilizing environmental signals in clinical treatment. This Research Topic can be broadly divided into the following three subfields.

2 External physical triggers

External stimuli, such as temperature, light, ultrasound, and magnetic fields, enable precise, controllable activation of biomaterials, allowing for non-invasive and on-demand therapeutic interventions. In our Research Topic, Zhang et al. developed an optogenetic-based mitochondrial aggregation system (Opto-MitoA) based on a CRY2clust/CIBN light-sensitive module. Through rapidly controlling mitochondrial aggregation in cells upon blue light illumination, this system could increase the energy-generating function of mitochondria and alleviate niclosamide-caused cell dysfunction. Chen et al. synthesized albumin-loaded Tanshinone IIA and near-infrared photothermal agent IR780 nanoparticles for managing chronic and infected wounds. The release of Tanshinone IIA was improved under laser irradiation, thus realizing enhanced wound healing. He et al. reviewed polydopamine-coated metal-organic frameworks (MOFs@PDA) multifunctional nanomaterial, highlighting their potential in cancer therapy. By leveraging strong photothermal responsiveness of polydopamine, MOFs@PDA enable controlled drug release triggered by near-infrared light, enhancing therapeutic precision and minimizing side effects in cancer treatment.

3 Endogenous disease microenvironments

Endogenous disease microenvironments, including acidic pH, hypoxia, and enzymatic activity, provide intrinsic biological triggers that enable biomaterials to achieve site-specific responses and targeted drug release. Bin et al. designed GSH-responsive nanomicelles that release glucose transporter 1 (GLUT1) inhibitor to block mononuclear phagocyte system (MPS) uptake, significantly improving tumor treatment. Chu et al. emphasized the critical role of rebuilding the myocardial microenvironment in mesenchymal stem cells (MSCs)-based myocardial regeneration. This review highlights the strategies for promoting angiogenesis to improve MSCs survival and function in the treatment of ischemic heart disease. Wu et al. developed a multiplexed microfluidic immunoassay chip based on nanozyme technology for detecting eight respiratory viruses, demonstrating its application in sensing endogenous microenvironments through virus-specific antigen detection. Zhang et al. reviewed reactive oxygen species (ROS)-responsive biomaterials for Myocardial ischemia-reperfusion injury (MIRI) treatment as the ROS microenvironment. They systematically summarized the fabrication strategies and therapeutic platforms of ROS-responsive biomaterials, paving the way for their clinical translation. Han et al. utilized nanodiamonds as carriers to deliver MicroRNA-7 into dopaminergic neurons for the treatment of Parkinson's disease. They used the nanodiamonds & MicroRNA-7 complex (N-7) to inhibit the expression of αsynuclein, reduce oxidative stress and restore dopamine levels effectively.

4 Multiple stimuli combinations

The combination of multiple stimuli integrates the advantages of both external and endogenous triggers, enhancing the specificity, efficiency, and adaptability of biomaterials in complex disease treatments. Xie and Xie reviewed the controlled drug release enabled by physical-, chemical-, biological- and multiple-stimuli-responsive hydrogels and their applications in treating brain disease. They propounded that a multidisciplinary approach that combines expertise from various fields is critical, will greatly enhance scientific research, and will ultimately lead to new treatment options for patients.

Author contributions

YZ: Investigation, Writing – original draft. DX: Conceptualization, Resources, Validation, Writing – review and editing. YL: Conceptualization, Resources, Validation, Writing – review and editing.

Funding

The author(s) declare that financial support was received for the research and/or publication of this article. This work is supported by the National Key R&D Program of China (2020YFA0908900), National Natural Science Foundation of China (32401179), Shenzhen Medical Research Fund (B2401001), Science and Technology Program of Sichuan Province (2024NSFSC1922).

Acknowledgments

I sincerely appreciate the guest editorial team and all the reviewers for their valuable contributions to the management of this Research Topic. At the same time, I deeply appreciate the authors for their exceptional contributions to this Research Topic.

Conflict of interest

The authors declare that the research was conducted in the absence of any commercial or financial relationships that could be construed as a potential conflict of interest.

Generative AI statement

The author(s) declare that no Generative AI was used in the creation of this manuscript.

Publisher's note

References

Chen, L., Liu, Y., Guo, W., and Liu, Z. (2022). Light responsive nucleic acid for biomedical application. *Exploration* 2 (5), 20210099. doi:10.1002/exp.20210099

Cui, M., Zhang, D., Zheng, X., Zhai, H., Xie, M., Fan, Q., et al. (2024). Intelligent modular DNA lysosome-targeting chimera nanodevice for precision tumor therapy. *J. Am. Chem. Soc.* 146 (43), 29609–29620. doi:10.1021/jacs.4c10010

Duan, Y., Shen, C., Zhang, Y., and Luo, Y. (2022). Advanced diagnostic and therapeutic strategies in nanotechnology for lung cancer. *Front. Oncol.* 12, 1031000. doi:10.3389/fonc.2022.1031000

Guo, D., Ji, X., Xie, H., Ma, J., Xu, C., Zhou, Y., et al. (2023). Targeted reprogramming of vitamin B3 metabolism as a nanotherapeutic strategy towards chemoresistant cancers. *Adv. Mater.* 35 (36), 2301257. doi:10.1002/adma.202301257

Guo, D. D., Li, Q., Tang, H. Y., Su, J., and Bi, H. S. (2016). Zinc oxide nanoparticles inhibit expression of manganese superoxide dismutase via amplification of oxidative stress, in murine photoreceptor cells. *Cell Prolif.* 49 (3), 386–394. doi:10.1111/cpr.12257

Ji, X., Li, Q., Song, H., and Fan, C. (2022). Protein-mimicking nanoparticles in biosystems. *Adv. Mater.* 34 (37), 2201562. doi:10.1002/adma.202201562

Li, L., Yin, J., Ma, W., Tang, L., Zou, J., Yang, L., et al. (2024). A DNA origami device spatially controls CD95 signalling to induce immune tolerance in rheumatoid arthritis. *Nat. Mater.* 23, 993–1001. doi:10.1038/s41563-024-01865-5

Lin, Y.-T., Meng, R., Zhang, S.-M., Zhou, H., Chen, H., Liang, J.-L., et al. (2025). Acid-responsive biocompatible hydrogel modulating tumor DNA self-repair collaborated with chemotherapy for boosting STING pathway-associated immunotherapy. *Nano Lett.* 25 (9), 3670–3680. doi:10.1021/acs.nanolett.5c00358

Liu, B., Qi, Z., and Chao, J. (2023). Framework nucleic acids directed assembly of Au nanostructures for biomedical applications. *Interdiscip. Med.* 1 (1), e20220009. doi:10.1002/inmd.20220009

Ma, J., Guo, D., Ji, X., Zhou, Y., Liu, C., Li, Q., et al. (2023). Composite hydrogel for spatiotemporal lipid intervention of tumor milieu. *Adv. Mater.* 35 (14), 2211579. doi:10.1002/adma.202211579

Mura, S., Nicolas, J., and Couvreur, P. (2013). Stimuli-responsive nanocarriers for drug delivery. *Nat. Mater.* 12 (11), 991–1003. doi:10.1038/nmat3776

Shodeinde, A. B., Murphy, A. C., Oldenkamp, H. F., Potdar, A. S., Ludolph, C. M., and Peppas, N. A. (2020). Recent advances in smart biomaterials for the detection and treatment of autoimmune diseases. *Adv. Funct. Mater.* 30 (37), 1909556. doi:10.1002/adfm.201909556

Su, Y., Yrastorza, J. T., Matis, M., Cusick, J., Zhao, S., Wang, G., et al. (2022). Biofilms: formation, research models, potential targets, and methods for prevention and treatment. *Adv. Sci.* 9 (29), 2203291. doi:10.1002/advs.202203291

Uthaman, S., Parvinroo, S., Mathew, A. P., Jia, X., Hernandez, B., Proctor, A., et al. (2024). Inhibiting the cGAS-STING pathway in ulcerative colitis with programmable micelles. *ACS Nano* 18 (19), 12117–12133. doi:10.1021/acsnano.3c11257

Wang, Y., Zhan, J., Huang, J., Wang, X., Chen, Z., Yang, Z., et al. (2023). Dynamic responsiveness of self-assembling peptide-based nano-drug systems. *Interdiscip. Med.* 1 (1), e20220005. doi:10.1002/inmd.20220005

Wang, Z., Wang, Q., Cao, H., Wang, Z., Wang, D., Liu, J., et al. (2024). Mitochondrial localized *in situ* self-assembly reprogramming tumor immune and metabolic microenvironment for enhanced cancer therapy. *Adv. Mater.* 36 (15), 2311043. doi:10.1002/adma.202311043

Wei, M., Chen, N., Li, J., Yin, M., Liang, L., He, Y., et al. (2011). Polyvalent immunostimulatory nanoagents with self-assembled CpG oligonucleotide-conjugated gold nanoparticles. *Angew. Chem. Int. Ed.* 51 (5), 1202–1206. doi:10.1002/anie.201105187

Xia, D., Hang, D., Li, Y., Jiang, W., Zhu, J., Ding, Y., et al. (2020). Au–Hemoglobin loaded platelet alleviating tumor hypoxia and enhancing the radiotherapy effect with low-dose X-ray. *ACS Nano* 14 (11), 15654–15668. doi:10.1021/acsnano.0c06541

Xia, D., Xu, P., Luo, X., Zhu, J., Gu, H., Huo, D., et al. (2019). Overcoming hypoxia by multistage nanoparticle delivery system to inhibit mitochondrial respiration for photodynamic therapy. *Adv. Funct. Mater.* 29 (13), 1807294. doi:10.1002/adfm.201807294

Xue, L., Thatte, A. S., Mai, D., Haley, R. M., Gong, N., Han, X., et al. (2023). Responsive biomaterials: optimizing control of cancer immunotherapy. *Nat. Rev. Mater.* 9 (2), 100–118. doi:10.1038/s41578-023-00617-2

Yin, J., Wang, S., Wang, J., Zhang, Y., Fan, C., Chao, J., et al. (2024). An intelligent DNA nanodevice for precision thrombolysis. *Nat. Mater.* 23, 854–862. doi:10.1038/s41563-024-01826-y

Zhang, K., Wang, S., Zhou, C., Cheng, L., Gao, X., Xie, X., et al. (2018). Advanced smart biomaterials and constructs for hard tissue engineering and regeneration. *Bone Res.* 6 (1), 31. doi:10.1038/s41413-018-0032-9

Zhang, Y., Wang, Z., Li, X., Wang, L., Yin, M., Wang, L., et al. (2015). Dietary iron oxide nanoparticles delay aging and ameliorate neurodegeneration in Drosophila. *Adv. Mater.* 28 (7), 1387–1393. doi:10.1002/adma.201503893

Zhao, L., Li, M., Shen, C., Luo, Y., Hou, X., Qi, Y., et al. (2024a). Nano-assisted radiotherapy strategies: new opportunities for treatment of non-small cell lung cancer. *Research* 7, 0429. doi:10.34133/research.0429

Zhao, S., Tian, R., Wu, J., Liu, S., Wang, Y., Wen, M., et al. (2021). A DNA origami-based aptamer nanoarray for potent and reversible anticoagulation in hemodialysis. *Nat. Commun.* 12 (1), 358. doi:10.1038/s41467-020-20638-7

Zhao, Y., Cao, S., Wang, Y., Li, F., Lin, L., Guo, L., et al. (2023). A temporally resolved DNA framework state machine in living cells. *Nat. Mach. Intell.* 5 (9), 980–990. doi:10.1038/s42256-023-00707-4

Zhao, Y., Du, J., Xu, Z., Wang, L., Ma, L., and Sun, L. (2024b). DNA adjuvant hydrogel-optimized enzymatic cascade reaction for tumor chemodynamic-immunotherapy. *Adv. Sci.* 11 (10), 2308229. doi:10.1002/advs.202308229

Zhao, Y., Hou, J., Guo, L., Zhu, S., Hou, X., Cao, S., et al. (2024c). DNA-engineered degradable invisibility cloaking for tumor-targeting nanoparticles. *J. Am. Chem. Soc.* 146 (36), 25253–25262. doi:10.1021/jacs.4c09479

Zhu, H., Yang, C., Yan, A., Qiang, W., Ruan, R., Ma, K., et al. (2023). Tumor-targeted nano-adjuvants to synergize photomediated immunotherapy enhanced antitumor immunity. *View* 4 (3), 20220067. doi:10.1002/viw.20220067

frontiers | Frontiers in Bioengineering and Biotechnology

TYPE Brief Research Report
PUBLISHED 16 May 2024
DOI 10.3389/fbioe.2024.1402831

OPEN ACCESS

EDITED BY
Chao Zhang,
Southern Medical University, China

REVIEWED BY
Jing Su,
Shandong Jiaotong University, China
Yu Li,
Naval Medical Center, China
Shu Xing,
Chinese Academy of Sciences (CAS), China

*CORRESPONDENCE
Ping Li,
li.ping@sz.tsinghua.edu.cn
Lan Ma,
malan@sz.tsinghua.edu.cn

RECEIVED 18 March 2024
ACCEPTED 15 April 2024
PUBLISHED 16 May 2024

CITATION
Wu F, Cai D, Shi X, Li P and Ma L (2024), Multiplexed detection of eight respiratory viruses based on nanozyme colorimetric microfluidic immunoassay.
Front. Bioeng. Biotechnol. 12:1402831.
doi: 10.3389/fbioe.2024.1402831

Multiplexed detection of eight respiratory viruses based on nanozyme colorimetric microfluidic immunoassay

Feng Wu[1,2], Defeng Cai[1,3], Xueying Shi[1], Ping Li[1]* and Lan Ma[1,4,5]*

[1]Institute of Biopharmaceutical and Health Engineering, Tsinghua Shenzhen International Graduate School, Tsinghua University, Shenzhen, China, [2]Shenzhen Institute for Drug Control, Shenzhen, China, [3]Department of Clinical Laboratory (Pathology) Centre, South China Hospital of Shenzhen University, Shenzhen, China, [4]State Key Laboratory of Chemical Oncogenomics, Tsinghua Shenzhen International Graduate School, Tsinghua University, Shenzhen, China, [5]Institute of Biomedical Health Technology and Engineering, Shenzhen Bay Laboratory, Shenzhen, China

Pandemics caused by respiratory viruses, such as the SARS-CoV-1/2, influenza virus, and respiratory syncytial virus, have resulted in serious consequences to humans and a large number of deaths. The detection of such respiratory viruses in the early stages of infection can help control diseases by preventing the spread of viruses. However, the diversity of respiratory virus species and subtypes, their rapid antigenic mutations, and the limited viral release during the early stages of infection pose challenges to their detection. This work reports a multiplexed microfluidic immunoassay chip for simultaneous detection of eight respiratory viruses with noticeable infection population, namely, influenza A virus, influenza B virus, respiratory syncytial virus, SARS-CoV-2, human bocavirus, human metapneumovirus, adenovirus, and human parainfluenza viruses. The nanomaterial of the nanozyme (Au@Pt nanoparticles) was optimized to improve labeling efficiency and enhance the detection sensitivity significantly. Nanozyme-binding antibodies were used to detect viral proteins with a limit of detection of 0.1 pg/mL with the naked eye and a microplate reader within 40 min. Furthermore, specific antibodies were screened against the conserved proteins of each virus in the immunoassay, and the clinical sample detection showed high specificity without cross reactivity among the eight pathogens. In addition, the microfluidic chip immunoassay showed high accuracy, as compared with the RT-PCR assay for clinical sample detection, with 97.2%/94.3% positive/negative coincidence rates. This proposed approach thus provides a convenient, rapid, and sensitive method for simultaneous detection of eight respiratory viruses, which is meaningful for the early diagnosis of viral infections. Significantly, it can be widely used to detect pathogens and biomarkers by replacing only the antigen-specific antibodies.

KEYWORDS

respiratory virus, nanozyme, microfluidics, immunoassay, multiplexed detection

Introduction

Acute respiratory tract diseases (ARDs) are often caused by viral infections and are one of the primary causes of morbidity and mortality related to communicable diseases worldwide (WHO, 2009; Diseases et al., 2020). One of the major features of an ARD is collaborative infection by multiple viruses (Renois et al., 2010; Pigny et al., 2021; Jiang et al., 2022), which poses challenges in diagnosis and treatment. The main respiratory viruses in such cases include the influenza virus, coronavirus, respiratory syncytial virus, human bocavirus, human metapneumovirus, adenovirus, human parainfluenza viruses, and rhinovirus, which impose a huge burden on the health system (Dhanasekaran et al., 2022; Haney et al., 2022). Therefore, it is of great significance to control the transmission of respiratory viruses, especially during the early stages of infection. Furthermore, diagnosis during the early stages of infection can help determine the basis of clinical treatment while reducing the development of severe cases. However, the diversity of respiratory virus species and their subtypes could result in insufficient diagnoses because of their common symptoms. At present, the frequently used detection methods for respiratory viruses include viral nucleic acid detection and viral antigen detection (Ren et al., 2023). Standard quantitative RT-PCR and multiplexed RT-PCR are widely used in diagnostic laboratories to detect viral nucleic acids with high sensitivity (Lee and Suarez, 2004; You et al., 2017; Corman et al., 2020; Goto et al., 2023). Next-generation sequencing (NGS) is a mean of the high-throughput readout (Yelagandula et al., 2021; Gaston David et al., 2022; Ramos et al., 2023), but these methods have limitations such as cumbersome procedures and poor timeliness for detection. Hence, there is urgent need for an ultrasensitive yet rapid detection technology for simultaneous diagnosis of multiple respiratory viruses.

Rapid and simple detection methods, such as the lateral flow immunoassay (LFIA), played a vital role during the COVID-19 pandemic (Castrejón-Jiménez et al., 2022; Filchakova et al., 2022). Noble metal catalytic nanoparticles (NPs) were widely used in the LFIA as they could regulate the local surface plasmon resonance effect though the morphology and deposition of platinum, which presents as dark blue or black, to improve the colorimetric sensitivity. These NPs showed high catalytic efficiency, extraordinary stability in complex environments, and facile production to emerge as promising materials for signal amplification in colorimetric immunoassays (Gao et al., 2017; Loynachan et al., 2017; Wrasman et al., 2018; Lin et al., 2021; Zhu et al., 2024). In this study, bioinformatics analysis and nanomaterial optimization were combined to systematically improve the sensitivity, specificity, and detection rate of viral diagnosis. Furthermore, the labeling of nanozymes was optimized to significantly enhance the sensitivity of detection of respiratory virus antigens. By combining the aforementioned efforts with a microfluidic chip design, rapid and sensitive detection of respiratory virus was achieved along with visual detection of the antigen with a limit of detection (LOD) of 0.1 pg/mL and high detection rate. This study provides a convenient multiplexed microfluidic immunoassay chip based on nanozymes for the detection of eight respiratory viruses, thus laying a foundation for the early diagnosis of other viruses and biomarkers.

Materials and methods

Reagents

Disodium hydrogenphosphate (Na_2HPO_4, ≥99.0%), sodium phosphate monobasic monohydrate ($NaH_2PO_4{\cdot}H_2O$, 98%–102.0%), sodium carbonate (Na_2CO_3, ≥99.0%), sodium bicarbonate ($NaHCO_3$, 99.7%–100.3%), 2-(N-morpholino) ethanesulfonic acid (MES), and Tween-20 were purchased from Sangon Biotech (Shanghai, China). Gold (III) chloride tetrahydrate ($HAuCL_4{\cdot}4H_2O$, Au>47.8%) was purchased from Beijing Huawei Ruike Chemical (Beijing, China). Hydrogen hexachloroplatinate (IV) hexahydrate ($H_2PtCL_6{\cdot}6H_2O$, 99%) was purchased from Energy Chemical (Shanghai, China). Polyvinylpyrrolidone (PVP, molecular weight: 10kDa) was purchased from Tokyo Chemical Industry. Streptavidin, sulfo-NHS-LC-biotin, 1-ethyl-3-[3-dimethylaminopropyl] carbodiimide hydrochloride (EDC), and N-hydroxysulfosuccinimide (sulfo-NHS) were purchased from Thermo Fisher Scientific (United States). Sodium citrate tribasic dihydrate (99%), L-ascorbic acid (AA, 99%), bovine serum albumin (BSA), and casein block buffer were purchased from Sigma-Aldrich. Polydimethylsiloxane (PDMS; Sylgard 184) was purchased from Dow Corning (United States); photoresist (SU-8 2050) was purchased from MicroChem Corp. (MA, United States); carboxyl-functionalized magnetic beads (MBs) with an average diameter of 10 μm were purchased from Suzhou Nanomicro Technology (China); one-step TMB substrate solution was purchased from Beijing Makewonderbio (Beijing, China). The respiratory virus proteins and antibodies (mAb IgG) were obtained from the Institute of Biopharmaceutical and Health Engineering, Tsinghua University. All aqueous solutions were prepared using deionized (DI) water with a resistivity of 18.2 MΩ·cm.

Anti-respiratory virus monoclonal antibodies

Monoclonal antibodies with high specificities against influenza A virus, influenza B virus, respiratory syncytial virus (RSV), SARS-CoV-2, human bocavirus (HBoV), human metapneumovirus (HMPV), adenovirus (AdV), and human parainfluenza viruses (HPIVs) were produced and identified, and their target proteins are shown in Table 1. The antibodies against the nucleocapsid proteins of the HPIVs cannot cross-react with other subtypes from among HPIV-1, HPIV-2, and HPIV-3, so specific antibodies were selected for each subtype and mixed to detect these three subtypes.

Synthesis of Au@Pt nanozyme

Platinum-decorated Au@Pt nanozyme (Au@Pt NPs) was synthesized as described in a previous study (Wu et al., 2022). In brief, 15-nm gold NPs were used as the seed and mixed with 190 mL of purified water, followed by the addition of 4 mL of PVP (20% w/v). This solution was mixed strongly for 2 min so that the polymer could coat and stabilize the AuNP seeds; then, 8 mL of L-ascorbic

TABLE 1 Monoclonal antibodies against respiratory viruses and their target proteins.

Monoclonal antibody	Respiratory virus	Targeted antigen protein
Anti-IVA-1, 2	Influenza A virus (IAV)	Nucleocapsid protein
Anti-IVB-1, 2	Influenza B virus (IBV)	Nucleocapsid protein
Anti-RSV-1, 2	Respiratory syncytial virus (RSV)	Nucleocapsid protein
Anti-SARS2-1, 2	SARS-CoV-2	Nucleocapsid protein
Anti-HBoV-1, 2	Human bocavirus (HBoV)	Major capsid protein VP1
Anti-HMPV-1, 2	Human metapneumovirus (HMPV)	Nucleocapsid protein
Anti-AdV-1, 2	Adenovirus (AdV)	Hexon protein
Anti-HPIV1-1, 2	Human parainfluenza virus 1 (HPIV1)	Nucleocapsid protein
Anti-HPIV2-1, 2	Human parainfluenza virus 2 (HPIV2)	Nucleocapsid protein
Anti-HPIV3-1, 2	Human parainfluenza virus 3 (HPIV3)	Nucleocapsid protein

acid (10% w/v) was added to the solution and mixed for 1 min. Next, approximately 1600 μL of chloroplatinic acid hydrate (0.5 M) was added to the mixture and mixed for 1 min; this solution was immediately heated to 65°C in an oil bath without stirring for 30 min until its color turned brown/black. The synthesized Au@Pt NPs were cooled to room temperature, purified by centrifugation (15 min, 14,000*g*), and resuspended in distilled water three times. Finally, Au@Pt NPs of size 75 nm were synthesized.

Preparation of nanozyme–antibody conjugates

In this study, antibodies were allowed to form coordination bonds with sulfur groups that were attached to the surfaces of the Au@Pt NPs. Briefly, 10 mg of DTT was dissolved per milliliter of water, and this solution was added to each labeling antibody at a concentration of 25 μL/mg. The mixtures were then incubated at 4°C for 30 min, following which the excess DTT was removed by ultrafiltration centrifugation using 20 mM sodium phosphate buffer. The modified L-mAbs should be used immediately in conjugation reactions. Next, 100 μL of 75 nm Au@Pt NPs (2.5 nM) was mixed with 400 μL of 20 mM sodium phosphate buffer, followed by addition of 54 μg of modified L-mAbs; this mixture was incubated for 2 h using gentle rotations at room temperature. The modified particles were subsequently blocked using 200 μL of the blocking solution (phosphate buffer containing 1 wt% casein block and 1 wt% glutathione) for 30 min with gentle rotations at room temperature. The excess reagents were removed through three washing steps by centrifugation (15 min, 14,000*g*) using 20 mM sodium phosphate buffer. Finally, the Au@Pt NPs-mAbs were resuspended in a storage buffer at a concentration of 500 p.m.

Antibody functionalization of MBs

Antibody-functionalized MBs were prepared in accordance with the streptavidin–biotin system, and streptavidin-conjugated MBs were prepared according to the EDC/NHS method. Briefly, 100 mg of carboxyl-functionalized MBs were separated using a magnet for 1 min and washed with MES buffer three times before being activated by 2 mM sulfo-NHS and 5 mM EDC for 30 min at 37°C with gentle rotations. The activated MBs were separated using a magnet, washed with MES buffer three times, and redispersed in 50 mM borate buffer to react with 1.5 mg streptavidin for 3 h at 37°C with gentle rotations. The residual active coupling sites or non-specific binding sites were blocked with a blocking solution for 30 min at 37°C, and the streptavidin-coated MBs were finally washed four times with 20 mM sodium phosphate buffer. Biotinylation of each coated antibody (C-mAb) was performed. Briefly, C-mAbs underwent dialysis against phosphate-buffered saline (PBS) and was diluted to a concentration of 2 mg/mL. Then, sulfo-NHS-LC-biotin was dissolved in DMSO at a concentration of 10 mM, and approximately 13.5 μL of the sulfo-NHS-LC-biotin solution was added to 1 mg of the C-mAbs solution and reacted for 24 h at 4°C. The unreacted biotinylation reagent and byproducts were removed by dialysis against PBS for 24 h at 4°C to purify the biotinylated antibodies. Then, the streptavidin-coated MBs and 0.3 mg of the biotinylated antibodies in PBS were incubated for 1 h at room temperature with gentle rotations. The antibody-coated MBs were separated using a magnet and washed four times using 20 mM sodium phosphate buffer. Finally, the MBs-streptavidin-mAbs were resuspended in phosphate buffer with 1 wt% BSA.

Preparation of multiplexed microfluidic immunoassay chips

The microfluidic chips were designed using AutoCAD 2019 and fabricated as described in a previous study (Wu et al., 2022). The structure of the multiplexed microfluidic immunoassay chip is shown in Figure 1A and consists of one sample Luer inlet port at the middle (white loop) surrounded by eight reaction Luer ports (yellow loop) and eight Luer outlet ports (red loop). There is a wash chamber (green loop) in each path between the reaction Luer port and outlet port. The inlet and outlet ports are connected to the chamber by channels of 1000 μm width, and a height of 100 μm was considered for the chamber. The structural overview of the microfluidic chip is given in Figure 1B.

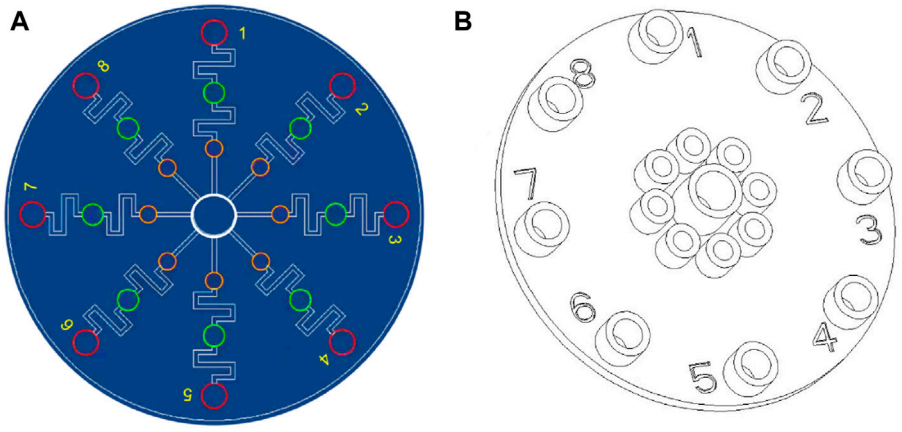

FIGURE 1
Schematic illustrations of the multiplexed microfluidic immunoassay chip: **(A)** AutoCAD layout of the microchannel structure; **(B)** top structural view of the microfluidic chip.

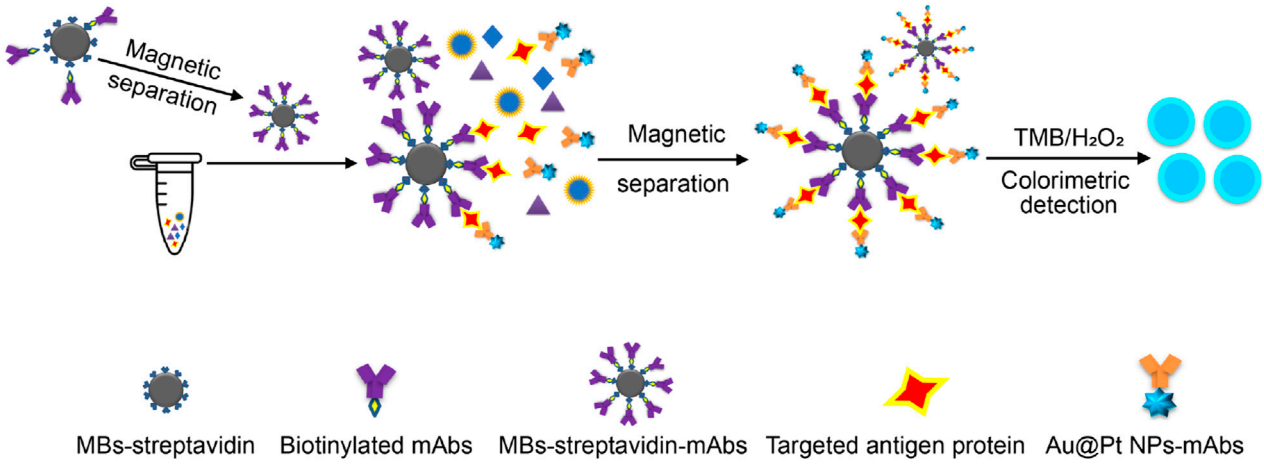

FIGURE 2
Schematic representation of the colorimetric formation of the sandwich immunoassay.

Analytical procedure

For the immunoassay preparation, each respiratory-virus-related nanozyme–antibody conjugate (Au@Pt NPs-mAbs) and antibody-functionalized-MBs (MBs-streptavidin-mAbs) were added to the corresponding reaction Luer ports of the microfluidic chip and freeze-dried overnight in vacuum. Upon removal from the freeze-dryer, the chips were stored in a sealed plastic bag filled with silica bead desiccant at room temperature. The two selected antibodies used in the formulation of the nanozyme–antibody conjugate (Au@Pt NPs-mAb) and antibody-functionalized-MBs (MBs-streptavidin-mAb) were designed to specifically recognize the same antigen protein of each virus. Figure 2 shows the formation of the sandwich immunoassay and its colorimetric formation.

The test procedure begins with placing the chip on the magnet, followed by addition of 400 μL of the standard protein solution or sample lysate into the sample Luer inlet port; then, the T-type silicone rubber plug is placed over the inlet and pressed till it touches the bottom. The samples are equally distributed to the eight reaction Luer ports, where the freeze-dried Au@Pt NPs-mAbs and MBs-streptavidin-mAbs recognize and bind with the antigen proteins in the samples to form a sandwich structure. After incubation for 30 min, T-type silicone rubber plugs are placed over each of the reaction Luer ports and pressed to sufficiently push the reaction mixture toward the wash chamber, where the MBs-complex is isolated from the reaction mixture by the magnet. Next, absorbent paper is placed in the eight Luer outlet ports, and approximately 600 μL of the wash buffer is injected from the sample Luer inlet port using a syringe to wash the MBs-complex, followed by removing the magnet and absorbent paper. Finally, 400 μL of the one-step TMB substrate solution is injected from the sample Luer inlet port using a syringe, and the results are detected after incubation for 1–10 min. Usually, the analytical procedure is completed within 40 min. The TMB substrate solution flushes the MBs-complex in the wash chamber into the Luer outlet port to react

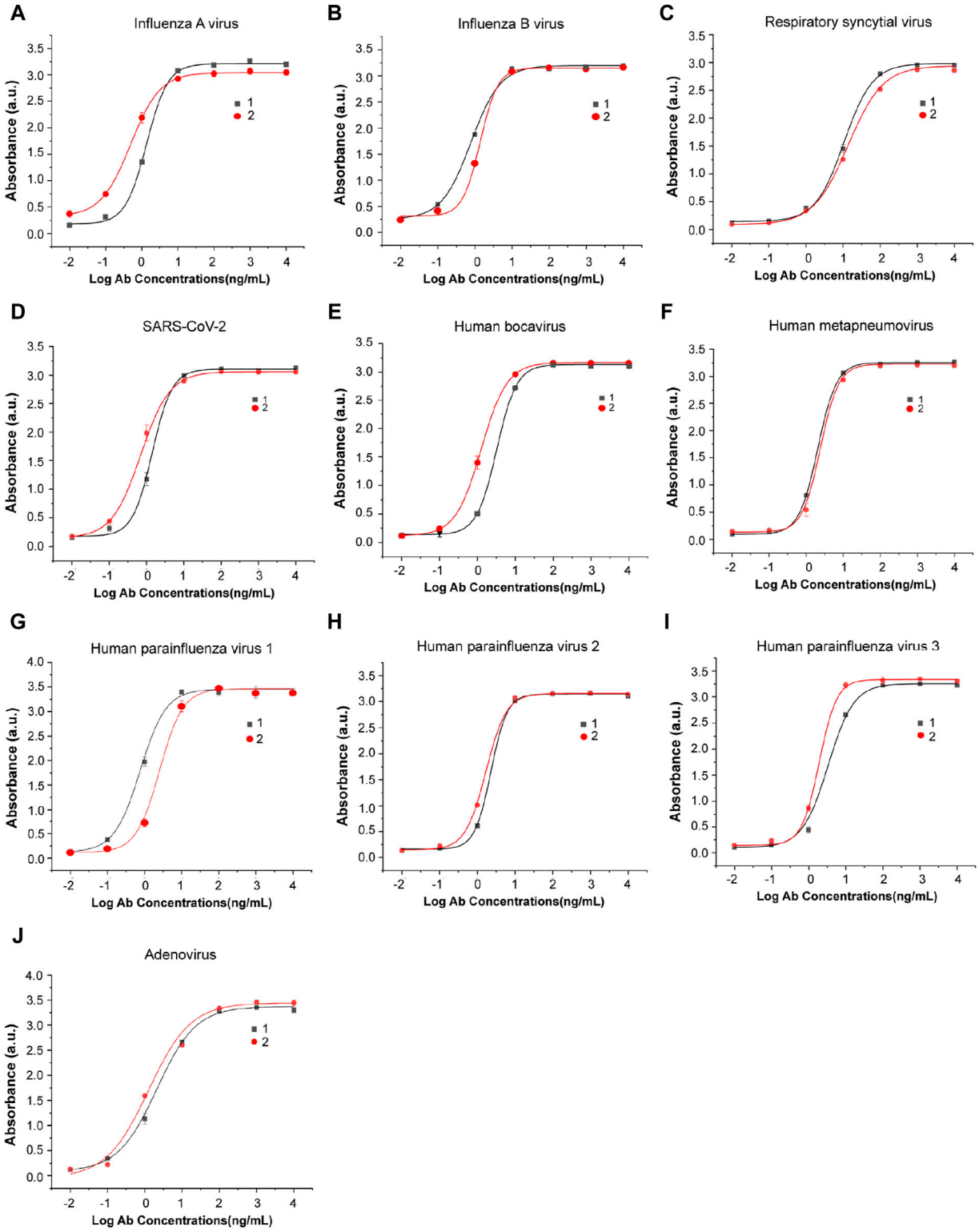

FIGURE 3
Antibody–antigen binding and titer identification of mAbs against eight types of respiratory viruses. Two specific antibodies were selected and detected by indirect ELISA for each virus: **(A)** influenza A virus, **(B)** influenza B virus, **(C)** respiratory syncytial virus, **(D)** SARS-CoV-2, **(E)** human bocavirus, **(F)** human metapneumovirus, **(G)** human parainfluenza virus 1, **(H)** human parainfluenza virus 2, **(I)** human parainfluenza virus 3, and **(J)** adenovirus. n = 3 biological replicates. The data are mean ± SEM.

10.3389/fbioe.2024.1402831

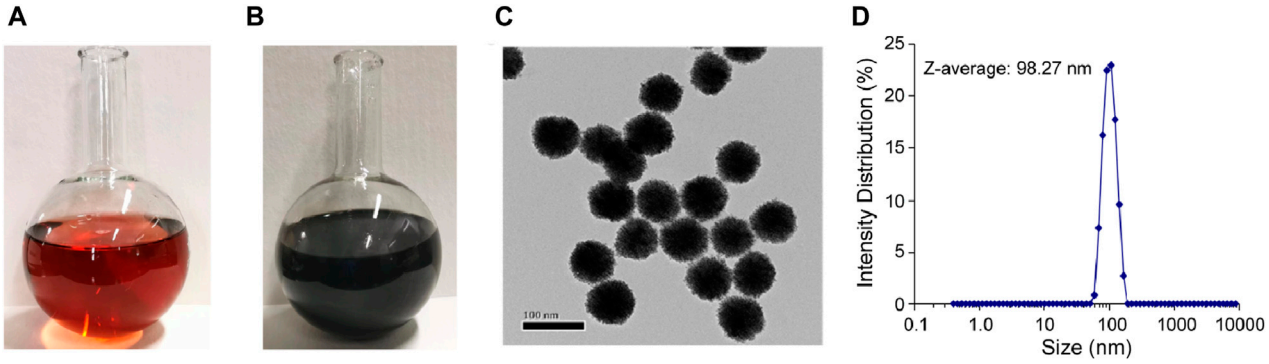

FIGURE 4
Properties of Au@Pt NPs. Images of Au@Pt NP reaction components **(A)** before and **(B)** after heat treatment. **(C)** TEM images of Au@Pt NPs. Scale bar, 100 nm. **(D)** Nanoparticle size detection by dynamic light scattering (DLS) experiments.

with the captured Au@Pt NPs and develop color. These developed colors can be conveniently examined and judged visually, or the mixture can be transferred to a microwell plate for absorbance detection at 630 nm using a microplate reader.

Results

Properties of antigen-specific monoclonal antibodies

The monoclonal antibodies used in this study were screened, expressed, and purified in the lab. Two antigen-specific antibodies with high affinity were selected for each virus. The binding capacities of these antibodies with their antigens were detected by indirect ELISA, and the results are shown in Figure 3. These antibodies were purified in a high titer and can recognize their antigens even at low concentrations, showing their sensitivity and potential for viral antigen detection.

Properties of Au@Pt NPs

The Au@Pt NPs were prepared with controlled sizes. The color of the platinum-decorated Au NPs changed from red (Figure 4A) to dark brown (Figure 4B) after heat treatment. Then, these Au@Pt NPs were investigated using transmission electron microscopy (TEM) for their structure and size (Figure 4C). The average size of Au@Pt NPs was further detected by dynamic light scattering (DLS) and was found to be approximately 98.27 nm (Figure 4D).

Properties of multiplexed microfluidic immunoassay chips

This multiplexed microfluidic immunoassay chip was designed for the simultaneous detection of eight respiratory viruses, namely, influenza A virus, influenza B virus, RSV, SARS-CoV-2, HBoV, HMPV, AdV, and HPIVs. The sensitivity of this chip was determined by testing recombinant protein standard samples at concentrations of 0.01–1000 pg/mL. The results of these standard samples could be inferred visually and also measured using a microplate reader at an absorbance of 630 nm. With the help of the nanozyme, the differential color intensity between the limit concentration and negative control was easily distinguishable via healthy color vision. As shown in Figure 5, the color intensity of the 0.1 pg/mL protein could be distinguished from the negative control visually. For detection with the microplate reader, the test limit concentration of each protein was as low as 0.1 pg/mL (Figure 6). These data indicate that the multiplexed microfluidic immunoassay chip can conveniently detect the eight viruses with high sensitivity.

Specificity of multiplexed microfluidic immunoassay chip

The specificity and cross reactivity of the multiplexed microfluidic immunoassay chip was analyzed by detecting the conserved nucleocapsid proteins of the influenza A virus (subtype H1N1), influenza B virus (subtype Yamagata strain), RSV (Long strain), SARS-CoV-2 (B.1.1.529 BA.1 and omicron strains), HMPV, HPIVs (subtypes 1, 2, 3, and 4), VP1 protein of HBoV, and HP protein of AdV. These proteins of each virus were mixed for detection; as shown in Figure 7, the multiplexed microfluidic immunoassay chip could detect each virus specifically without cross reactivity with the other seven viruses. Furthermore, all eight respiratory pathogens were detected successfully, demonstrating that the multiplexed microfluidic immunoassay chip could detect these viruses with high sensitivity and specificity.

Sample test

The studies involving human samples were reviewed and approved by the Bioethics Committee (BEC) of Tsinghua Shenzhen International Graduate School. In this study, human throat swab samples (n = 315) were collected from Shenzhen Children's Hospital and were diagnosed by real-time RT-PCR/PCR, whose results are shown in Table 2. These samples were

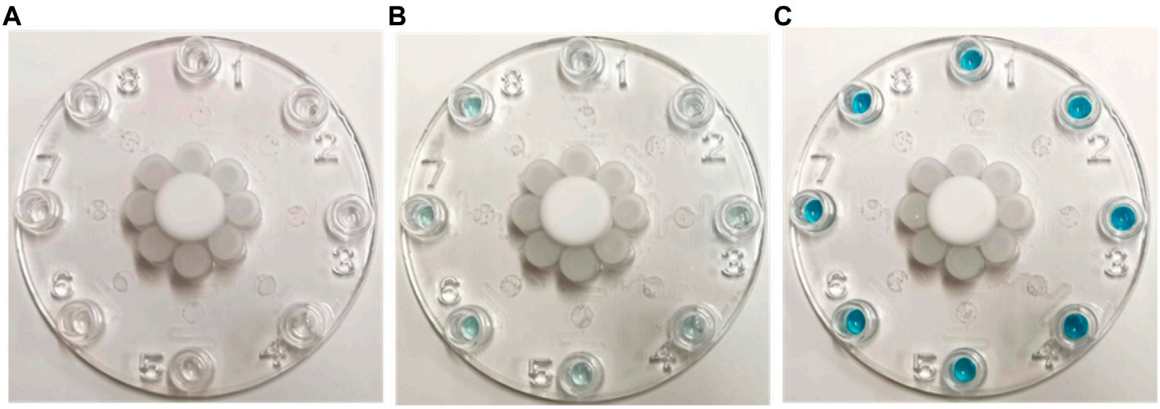

FIGURE 5
Images of multiplexed microfluidic immunoassay chip detection of different protein concentrations at **(A)** 0, **(B)** 0.1, and **(C)** 100 pg/mL. The positive results are shown in blue at the Luer outlet ports.

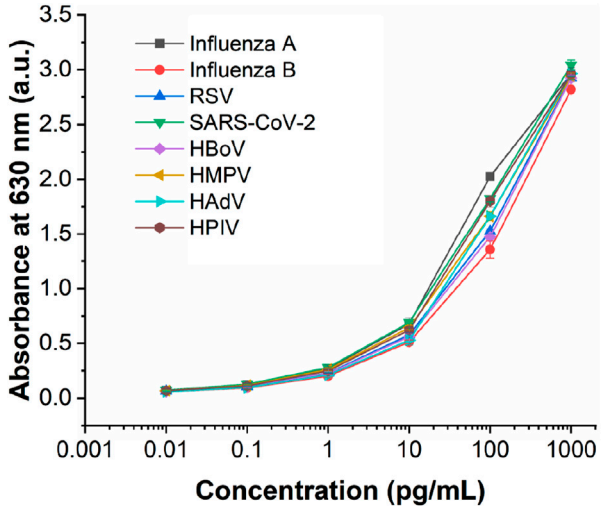

FIGURE 6
Analytical performance of the multiplexed microfluidic immunoassay chip for detecting the proteins of eight viruses, with absorbance intensities obtained at different protein concentrations ranging from 0.01 to 1000 pg/mL. n = 3 biological replicates. The data are mean ± SEM.

inactivated before testing with the multiplexed microfluidic immunoassay chip. Before detection, approximately 300 μL of the human throat swab sample and 300 μL of the lysis buffer (PBS containing 0.5% NP40, 0.2% Tween 20%, and 0.2% LNAC, pH 7.4) were mixed and incubated for 1 min, and the lysate was directly tested using the microfluidic chip immunoassay. As shown in Table 2, the multiplexed microfluidic immunoassay chip could efficiently recognize all eight respiratory viruses in the throat swab samples. Compared with the results of the real-time RT-PCR assay, the microfluidic chip immunoassay had accuracies of 100%, 96.5%, 100%, 100%, 96%, 96%, 96.5%, and 92% for the detection of influenza A virus, influenza B virus, RSV, SARS-CoV-2, HBoV, HMPV, AdV, and HPIVs, respectively. The positive coincidence rate between the multi respiratory virus microfluidic immunoassay and real-time RT-PCR results was 97.2%, negative coincidence rate was 94.3%, and total coincidence rate was 98.1%.

Discussion and conclusion

Given the diversity of viruses involved in acute respiratory tract infections and similarities between the clinical symptoms caused by different pathogens, it is difficult and insufficient to make judgments based on clinical manifestations and chest imaging (Lim et al., 2006). However, there are significant differences in the pathological course and treatment for different respiratory viruses. Therefore, it is of great significance to rapidly and accurately diagnose and identify pathogens to help determine their clinical treatments. Thus, numerous studies have been performed to develop multiplexed detection methods for diagnosing pathogens, especially in multiplexed infections cases (Chung et al., 2021; Banerjee et al., 2022). However, it is difficult for these assays based on nuclei acids to detect RNA or DNA viruses simultaneously, such as the DNA viruses like AdV and HBoV along with RNA viruses like the influenza viruses and HPIVs.

In the present study, nanozyme was combined with microfluidic technology to establish a simple and visual rapid detection technology for multiple respiratory viruses. The platinum-decorated Au nanozyme (Au@Pt NPs) that was previously designed and successfully used for SARS-CoV-2 detection was applied to improve the sensitivity of the multiplexed microfluidic immunoassay chip (Wu et al., 2022). The LOD could be decreased significantly to 0.1 pg/mL to enable visual detection, which was convenient for the early diagnosis of infections. This is important because infection by respiratory viruses show very low titer values at the early stages in some varieties, which may result in imprecise diagnoses. Significantly, the multiplexed microfluidic immunoassay chip could simultaneously determine eight pathogens through eight non-interfering microfluidic paths, rendering the diagnosis more accurate. The antibodies used in this study were against

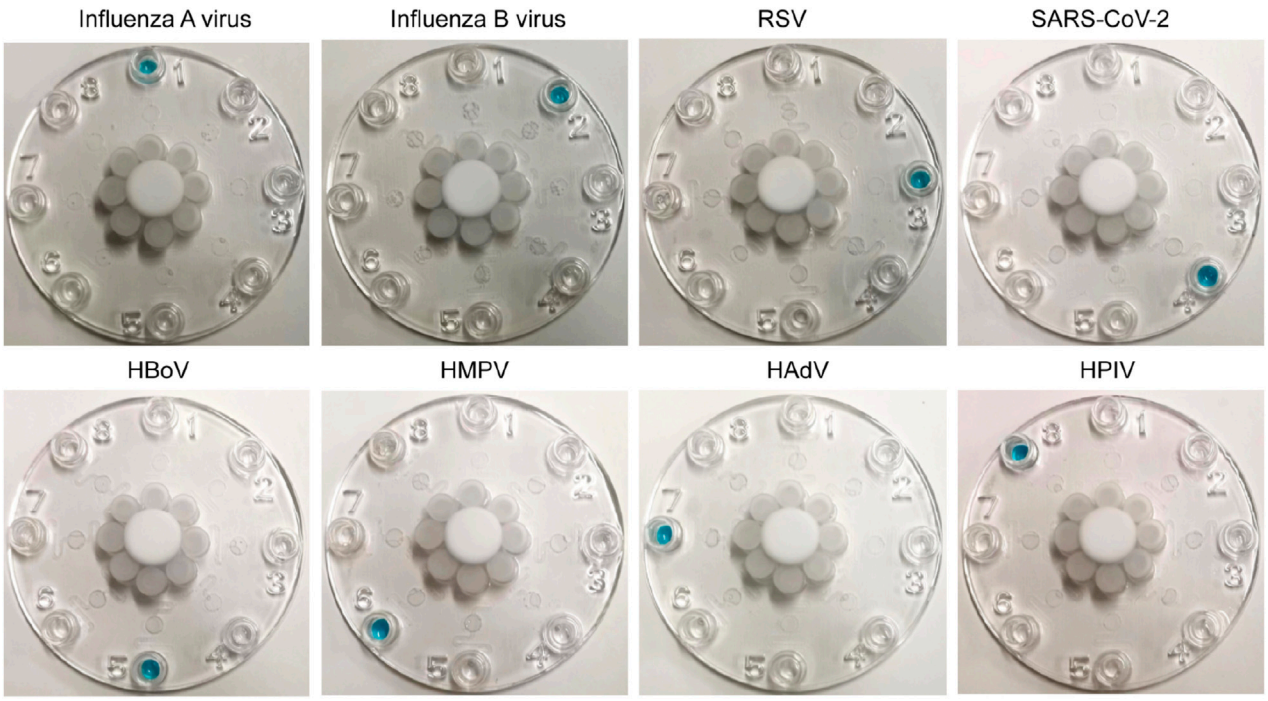

FIGURE 7
Cross reactions between the eight respiratory pathogens. Approximately 40 pg of protein from each virus in 400 μL of solution (100 pg/mL) was injected into the sample Luer inlet port at the middle, and the results were observed at the Luer outlet ports. The 1–8 Luer outlet ports of each chip show the detection results of influenza A virus (Luer 1), influenza B virus (Luer 2), respiratory syncytial virus (Luer 3), SARS-CoV-2 (Luer 4), human bocavirus (Luer 5), human metapneumovirus (Luer 6), human adenovirus (Luer 7), and human parainfluenza viruses (Luer 8). The positive results are shown in blue.

TABLE 2 Sample testing results from the multiplexed microfluidic immunoassay chip and real-time RT-PCR/PCR.

Respiratory virus	Number of samples	Microfluidic chip immunoassay (P/N)	Real-time RT-PCR/PCR (P/N)
Influenza A	30	30/0	30/0
Influenza B	30	29/1	30/0
RSV	30	30/0	30/0
SARS-CoV-2	20	20/0	20/0
HBoV	25	24/1	25/0
HMPV	25	24/1	25/0
AdV	30	29/1	30/0
HPIV	25	23/2	25/0
Negative sample	100	0/100	0/100

conserved proteins of the viruses to ensure detection of all subtypes of each virus and their mutants, such as the influenza viruses A and B, achieving sufficient diagnoses for multiple viruses. This detection was achieved within 40 min, which greatly improved the effectiveness and provided a new scheme for rapid and sensitive detection of respiratory viruses.

In summary, a multiplexed microfluidic rapid detection method based on nanozymes is proposed for diagnosing multiple respiratory viruses, and this method can be widely used to detect pathogens and biomarkers by replicating antigen-specific antibodies, which provide technical support for the development of point-of-care testing.

Data availability statement

The original contributions presented in the study are included in the article/supplementary material; further inquiries can be directed to the corresponding authors.

Ethics statement

The studies involving humans were approved by the Bioethics Committee (BEC) of Tsinghua Shenzhen International Graduate

School. The studies were conducted in accordance with the local legislations and institutional requirements. Written informed consent for participation in this study was provided by the participants' legal guardians/next of kin. No potentially identifiable images or data are presented in this study.

Author contributions

FW: writing–original draft and writing–review and editing. DC: writing–original draft. XS: writing–original draft. PL: writing–original draft and writing–review and editing. LM: writing–original draft and writing–review and editing.

Funding

The author(s) declare that financial support was received for the research, authorship, and/or publication of this article. This work was supported by the Shenzhen Science and Technology Research and Development Funds (No. JCYJ20200109143018683) and the State Key Laboratory of Chemical Oncogenomics of the Institute of Biomedical Health Technology and Engineering at Shenzhen Bay Laboratory.

Conflict of interest

The authors declare that the research was conducted in the absence of any commercial or financial relationships that could be construed as a potential conflict of interest.

Publisher's note

All claims expressed in this article are solely those of the authors and do not necessarily represent those of their affiliated organizations, or those of the publisher, the editors, and the reviewers. Any product that may be evaluated in this article, or claim that may be made by its manufacturer, is not guaranteed or endorsed by the publisher.

References

Banerjee, D., Hassan, F., Avadhanula, V., Piedra, P. A., Boom, J., Sahni, L. C., et al. (2022). Comparative analysis of three multiplex platforms for the detection of respiratory viral pathogens. *J. Clin. Virol.* 156, 105274. doi:10.1016/j.jcv.2022.105274

Castrejón-Jiménez, N. S., García-Pérez, B. E., Reyes-Rodríguez, N. E., Vega-Sánchez, V., Martínez-Juárez, V. M., and Hernández-González, J. C. (2022). Challenges in the detection of SARS-CoV-2: evolution of the lateral flow immunoassay as a valuable tool for viral diagnosis. *Biosensors* 12, 728. doi:10.3390/bios12090728

Chung, H. Y., Jian, M. J., Chang, C. K., Lin, J. C., Yeh, K. M., Chen, C. W., et al. (2021). Novel dual multiplex real-time RT-PCR assays for the rapid detection of SARS-CoV-2, influenza A/B, and respiratory syncytial virus using the BD MAX open system. *Emerg. Microbes Infect.* 10, 161–166. doi:10.1080/22221751.2021.1873073

Corman, V. M., Landt, O., Kaiser, M., Molenkamp, R., Meijer, A., Chu, D. K., et al. (2020). Detection of 2019 novel coronavirus (2019-nCoV) by real-time RT-PCR. *Eurosurveillance* 25, 2000045. doi:10.2807/1560-7917.Es.2020.25.3.2000045

Dhanasekaran, V., Sullivan, S., Edwards, K. M., Xie, R., Khvorov, A., Valkenburg, S. A., et al. (2022). Human seasonal influenza under COVID-19 and the potential consequences of influenza lineage elimination. *Nat. Commun.* 13, 1721. doi:10.1038/s41467-022-29402-5

Diseases, G. B. D., Injuries, C., Abbafati, C., Abbas, K. M., Abbasi, M., Abbasifard, M., et al. (2020). Global burden of 369 diseases and injuries in 204 countries and territories, 1990-2019: a systematic analysis for the Global Burden of Disease Study 2019. *Lancet* 396, 1204–1222. doi:10.1016/S0140-6736(20)30925-9

Filchakova, O., Dossym, D., Ilyas, A., Kuanysheva, T., Abdizhamil, A., and Bukasov, R. (2022). Review of COVID-19 testing and diagnostic methods. *Talanta* 244, 123409. doi:10.1016/j.talanta.2022.123409

Gao, Z., Ye, H., Tang, D., Tao, J., Habibi, S., Minerick, A., et al. (2017). Platinum-decorated gold nanoparticles with dual functionalities for ultrasensitive colorimetric *in vitro* diagnostics. *Nano Lett.* 17, 5572–5579. doi:10.1021/acs.nanolett.7b02385

Gaston David, C., Miller, H. B., Fissel, J. A., Jacobs, E., Gough, E., Wu, J., et al. (2022). Evaluation of metagenomic and targeted next-generation sequencing workflows for detection of respiratory pathogens from bronchoalveolar lavage fluid specimens. *J. Clin. Microbiol.* 60, e00526–e00522. doi:10.1128/jcm.00526-22

Goto, Y., Fukunari, K., Tada, S., Ichimura, S., Chiba, Y., and Suzuki, T. (2023). A multiplex real-time RT-PCR system to simultaneously diagnose 16 pathogens associated with swine respiratory disease. *J. Appl. Microbiol.* 134, lxad263. doi:10.1093/jambio/lxad263

Haney, J., Vijayakrishnan, S., Streetley, J., Dee, K., Goldfarb, D. M., Clarke, M., et al. (2022). Coinfection by influenza A virus and respiratory syncytial virus produces hybrid virus particles. *Nat. Microbiol.* 7, 1879–1890. doi:10.1038/s41564-022-01242-5

Jiang, X. W., Huang, T. S., Xie, L., Chen, S. Z., Wang, S. D., Huang, Z. W., et al. (2022). Development of a diagnostic assay by three-tube multiplex real-time PCR for simultaneous detection of nine microorganisms causing acute respiratory infections. *Sci. Rep.* 12, 13306. doi:10.1038/s41598-022-15543-6

Lee, C. W., and Suarez, D. L. (2004). Application of real-time RT-PCR for the quantitation and competitive replication study of H5 and H7 subtype avian influenza virus. *J. Virol. Methods* 119, 151–158. doi:10.1016/s0166-0934(04)00115-6

Lim, Y. W., Steinhoff, M., Girosi, F., Holtzman, D., Campbell, H., Boer, R., et al. (2006). Reducing the global burden of acute lower respiratory infections in children: the contribution of new diagnostics. *Nature* 444 (Suppl. 1), 9–18. doi:10.1038/nature05442

Lin, Q., Ji, X., Wu, F., and Ma, L. (2021). Conserved sequence analysis of influenza A virus ha segment and its application in rapid typing. *Diagnostics* 11, 1328. doi:10.3390/diagnostics11081328

Loynachan, C. N., Thomas, M. R., Gray, E. R., Richards, D. A., Kim, J., Miller, B. S., et al. (2017). Platinum nanocatalyst amplification: redefining the gold standard for lateral flow immunoassays with ultrabroad dynamic range. *ACS Nano* 12, 279–288. doi:10.1021/acsnano.7b06229

Pigny, F., Wagner, N., Rohr, M., Mamin, A., Cherpillod, P., Posfay-Barbe, K. M., et al. (2021). Viral co-infections among SARS-CoV-2-infected children and infected adult household contacts. *Eur. J. Pediatr.* 180, 1991–1995. doi:10.1007/s00431-021-03947-x

Ramos, N., Panzera, Y., Frabasile, S., Tomás, G., Calleros, L., Marandino, A., et al. (2023). A multiplex-NGS approach to identifying respiratory RNA viruses during the COVID-19 pandemic. *Archives Virology* 168, 87. doi:10.1007/s00705-023-05717-6

Ren, R., Cai, S., Fang, X., Wang, X., Zhang, Z., Damiani, M., et al. (2023). Multiplexed detection of viral antigen and RNA using nanopore sensing and encoded molecular probes. *Nat. Commun.* 14, 7362. doi:10.1038/s41467-023-43004-9

Renois, F., Talmud, D., Huguenin, A., Moutte, L., Strady, C., Cousson, J., et al. (2010). Rapid detection of respiratory tract viral infections and coinfections in patients with influenza-like illnesses by use of reverse transcription-PCR DNA microarray systems. *J. Clin. Microbiol.* 48, 3836–3842. doi:10.1128/JCM.00733-10

WHO (2009). *Infection-control measures for health care of patients with acute respiratory diseases in community settings: trainee's guide.*

Wrasman, C. J., Boubnov, A., Riscoe, A. R., Hoffman, A. S., Bare, S. R., and Cargnello, M. (2018). Synthesis of colloidal Pd/Au dilute alloy nanocrystals and their potential for selective catalytic oxidations. *J. Am. Chem. Soc.* 140, 12930–12939. doi:10.1021/jacs.8b07515

Wu, F., Mao, M., Cai, L., Lin, Q., Guan, X., Shi, X., et al. (2022). Platinum-decorated gold nanoparticle-based microfluidic chip immunoassay for ultrasensitive colorimetric detection of SARS-CoV-2 nucleocapsid protein. *ACS Biomaterials Sci. Eng.* 8, 3924–3932. doi:10.1021/acsbiomaterials.2c00600

Yelagandula, R., Bykov, A., Vogt, A., Heinen, R., Özkan, E., Strobl, M. M., et al. (2021). Multiplexed detection of SARS-CoV-2 and other respiratory infections in high throughput by SARSeq. *Nat. Commun.* 12, 3132. doi:10.1038/s41467-021-22664-5

You, H.-L., Chang, S. J., Yu, H. R., Li, C. C., Chen, C. H., and Liao, W. T. (2017). Simultaneous detection of respiratory syncytial virus and human metapneumovirus by one-step multiplex real-time RT-PCR in patients with respiratory symptoms. *BMC Pediatr.* 17, 89. doi:10.1186/s12887-017-0843-7

Zhu, J., Guo, G., Liu, J., Li, X., Yang, X., Liu, M., et al. (2024). One-pot synthesized Au@Pt nanostars-based lateral flow immunoassay for colorimetric and photothermal dual-mode detection of SARS-CoV-2 nucleocapsid antibody. *Anal. Chim. Acta* 1292, 342241. doi:10.1016/j.aca.2024.342241

frontiers | Frontiers in Bioengineering and Biotechnology

TYPE Mini Review
PUBLISHED 18 July 2024
DOI 10.3389/fbioe.2024.1450267

OPEN ACCESS

EDITED BY
Yao Luo,
Sichuan University, China

REVIEWED BY
Hongda Li,
Chongqing Medical University, China
Mei Li,
Sichuan University, China

*CORRESPONDENCE
Huangfan Xie,
xie1991@swmu.edu.cn

RECEIVED 17 June 2024
ACCEPTED 26 June 2024
PUBLISHED 18 July 2024

CITATION
Xie B and Xie H (2024), Application of stimuli-responsive hydrogel in brain disease treatment. *Front. Bioeng. Biotechnol.* 12:1450267. doi: 10.3389/fbioe.2024.1450267

Application of stimuli-responsive hydrogel in brain disease treatment

Bingqing Xie[1,2] and Huangfan Xie[1,2]*

[1]Laboratory of Neurological Diseases and Brain Function, The Affiliated Hospital, Southwest Medical University, Luzhou, Sichuan, China, [2]Institute of Epigenetics and Brain Science, Southwest Medical University, Luzhou, Sichuan, China

Treating brain diseases presents significant challenges due to neuronal degeneration, inflammation, and the intricate nature of the brain. Stimuli-responsive hydrogels, designed to closely resemble the brain's extracellular matrix, have emerged as promising candidates for controlled drug delivery and tissue engineering. These hydrogels have the unique ability to encapsulate therapeutic agents and release them in a controlled manner when triggered by environmental stimuli. This property makes them particularly suitable for delivering drugs precisely to targeted areas of the brain, while minimizing collateral damage to healthy tissue. Their preclinical success in treating various brain diseases in animal studies underscores their translational potential for human brain disease treatment. However, a deeper understanding of their long-term behavior, biodistribution, and biocompatibility within the brain remains crucial. Furthermore, exploring novel hydrogel systems and therapeutic combinations is paramount for advancing towards more effective treatments. This review summarizes the latest advancements in this field over the past 5 years, specifically highlighting preclinical progress with novel stimuli-responsive hydrogels for treating brain diseases.

KEYWORDS

stimuli-responsive, hydrogels, brain disease, drug delivery, tissue engineering

1 Introduction

Brain diseases are one of the primary neurological disorders with high incidence, including traumatic brain injury (TBI), Alzheimer's disease, Parkinson's disease, dementia, epilepsy, schizophrenia, stroke, depression, and glioblastoma (GBM) (Feigin et al., 2020). While their etiologies vary, they primarily involve progressive neuronal degeneration and inflammation. In most cases, the treatments to brain disease are limited to symptom reduction and palliative care. Curative therapies that can reverse the illness are lacking. Main challenges for brain disease treatment lie in the lack of structural support allowing repopulation of brain tissue from cell loss and the barriers for efficient drug delivery and release caused by blood-brain barriers (BBB) or other biological environment in brain tissues (Terstappen et al., 2021).

Stimuli-responsive hydrogels, characterized by their three-dimensional cross-linked polymer structure, possess unique properties that render them suitable for addressing various challenges in brain disease treatment. These hydrogels dynamically adapt their characteristics, including mechanical properties, swelling capacity, hydrophilicity, and permeability to bioactive molecules, in response to environmental stimuli such as temperature, pH, and biological agents (Mantha et al., 2019). Their water-absorbing

and swelling characteristics mimic the natural extracellular matrix (ECM), fostering an optimal environment for cellular growth and tissue engineering (Ma and Huang, 2020). Furthermore, they excel in encapsulating a range of therapeutic agents, including neuroprotective agents, chemotherapeutic drugs and even cells, and releasing them in a controlled manner, positioning them as exceptional candidates for drug delivery systems (Ghosh et al., 2024). Stimuli-responsive hydrogels have demonstrated encouraging potential in treating brain diseases over the past few decades (Peressotti et al., 2021; Grimaudo et al., 2022). However, further understanding of cell-biomaterial interaction and developing safer, more effective hydrogel systems are crucial for their translation into human therapy.

This review covers the last 5 years of fundamental research on stimuli-responsive hydrogels, discussing their characteristics, design, and preclinical applications in drug delivery and tissue engineering for brain disease treatment. It also highlights challenges and opportunities for future research in this field.

2 Characteristics of stimuli-responsive hydrogels

2.1 General characteristics of hydrogels

Based on polymer source, hydrogels are classified as natural, synthetic, or semi-synthetic. Natural hydrogels have biocompatibility and biodegradability but limited stability and mechanical strength (Alawami and Tannous, 2021; Janas-Naze and Zhang, 2022). Synthetic hydrogels provide mechanical strength but lack biological activity (Zhang and Huang, 2020). Semi-synthetic hydrogels combine the best of both, improving bioactivity and tunable properties (Dienes et al., 2021).

Hydrogel fabrication involves polymerization and crosslinking to create networks with varying mechanical and swelling properties (Grimaudo et al., 2022; Mashabela et al., 2022). Hydrogels can be administered intravenously, intracerebrally, intratumorally, or intranasally to treat brain diseases (Mashabela et al., 2022). Intravenous injection faces BBB penetration challenges, while intracerebral/intratumoral delivery demands hydrogels with high biocompatibility and safety. Intranasal administration offers direct access to the brain, bypassing the BBB, but is limited by nasal cavity size, mucociliary clearance, enzymatic degradation, and potential drug-induced irritation/neurotoxicity (Cassano et al., 2021).

2.2 Classification of stimuli-responsive of hydrogels

Stimuli-responsive hydrogels are categorized as physical, chemical, or biological-responsive, depending on their triggering factors. Here we summarize the characteristics of various stimuli-responsive hydrogels suitable for brain disease treatment.

2.2.1 Physical-responsive hydrogels

Physical-responsive hydrogels can be classified into thermo-, photo-, electro-, magnetic-, ultrasound-responsive types, each sensitive to temperature, light, electrical stimulation, magnetism and ultrasound respectively. Among these, thermo-, photo-, and electro-responsive hydrogels are the most widely used due to their practicality and effectiveness.

Thermo-responsive hydrogels shrink or expand with temperature changes, featuring hydrophobic (such as methyl, ethyl, and propyl) and hydrophilic groups (like amide and carboxyl) (Tang et al., 2021). Poloxamers (e.g., P407 and P188), also called Pluronics®, are commonly used for intranasal drug delivery due to their mucoadhesive and sol-gel transition properties (Ahmed et al., 2019; Abdeltawab et al., 2020). Hydrogels made from these poloxamers effectively deliver drugs like tetrandrine and rotigotine to the brain, but they lack mechanical strength and viscosity in physiological conditions (Wang et al., 2020; Zhang et al., 2020). To overcome this, they are often combined with other polymers like Carbopol, chitosan, and cellulose derivatives (Luo et al., 2023). Other agents, such as gellan and xanthan gums, are also used for brain drug delivery but may be costly (Rajput et al., 2018).

Photo-responsive hydrogels have photoreceptive moieties that can capture and convert light signal to chemical signals via photoreactions like isomerization, cleavage, and dimerization, thereby changing hydrogel's physical and chemical properties (Li et al., 2019). However, the primary use of ultraviolet-reactive groups in these systems restricts their biomedical applications.

Electro-responsive hydrogels, containing conducting materials, reversibly absorb and expel water upon electrical stimulation. Their hydration, flexibility, biocompatibility, and electrochemical properties make them suitable for brain implantation, enhancing neural signal transmission and ion transport (Khan et al., 2022). Integrating electroconductive materials into hydrogels reduces inflammation and material loss risks after brain implantation (Guo and Ma, 2018).

Magnetic-responsive hydrogels use magnetic particles, including γ-Fe_2O_3, Fe_3O_4 and $CoFe_2O_4$, to deliver drugs to specific sites in response to magnetic field (Zhang et al., 2023a). Currently, these hydrogels are limited to *in vitro* use due to toxicity and reproducibility concerns.

Ultrasound-responsive hydrogels, with imaging-compatible polymers or contrast agents, enhance ultrasound diagnostic accuracy. These hydrogels respond to ultrasound through three mechanisms: crosslinking disruption, hyperthermia, and acoustic streaming (Zhou et al., 2022). However, their use is currently limited to *in vitro* neural tissue engineering for structural guidance (Cheng et al., 2020).

Ion strength-responsive hydrogels alter in response to solution ion changes, resulting in protonation or deprotonation. Controlling ionic strength can regulate hydrogel reversibility for drug release. Deacylated gellan gum has been effectively utilized in the preparation process of this hydrogel (Chen et al., 2020).

2.2.2 Chemical-responsive hydrogels

Chemical-responsive hydrogels are classified into pH-, ROS-, hypoxia-responsive types, each sensitive to pH, reactive oxygen species (ROS), and hypoxia respectively.

pH-responsive hydrogels are composed of polymers with hydrophobic moieties that can swell in water depending on pH (Tulain et al., 2018). Recently, hydrogels based on Schiff base chemistry have received attention due to their quick formation via

TABLE 1 Summary of preclinical *in vivo* study evaluating the therapeutic efficacy of stimuli-responsive hydrogels in brain disease treatment.

Class of hydrogels	Main composition/ biomaterial	Crosslinker	Stimuli/ encapsulates	Disease	*In vivo* models	Route of administration	Outcome	References
Thermo-responsive	Poloxamer P407/P188, PEG 8000	—	Temperature/genipin, HP-β-CD	Depression	Male ICR mice, male SD rats	Intranasally	Elevated levels of 5-HT and norepinephrine within the hippocampus and striatum; enhanced antidepressant-like effects	Qi et al. (2021)
Thermo-responsive	Alginate, poloxamer P407/P188	Sodium chloride	Temperature/Icariin	Depression	Male ICR mice, male SD rats	Intranasally	Fast-acting antidepressant effect; effective repair of neuronal damage in the hippocampus	Xu et al. (2020)
Thermo-responsive	Carboxymethyl chitosan	—	Temperature/PAOPA-loaded oxidized starch NPs	Schizophrenia	Male SD rats	Intranasally	Alleviation of negative symptoms like behavioral abnormalities associated with schizophrenia	Majcher et al. (2021)
Thermo-responsive	Poloxamers P407/P188	—	Temperature/Tetrandrine and HP-β-CD	Microwave-induced brain injury	Male Wistar rats	Intranasally	Improved spatial memory and spontaneous exploratory behavior	Zhang et al. (2020)
Thermo-responsive	Pluronic F127, PLGA–PEG-PLGA	—	Temperature/Salinomycin	Glioblastoma	Female BALB/c nude mice	Intratumorally	Superior drug release profile; reduced tumor growth	Norouzi et al. (2021)
Thermo-responsive	CS-HEC-HA, GP	—	Temperature/hUC-MSCs	Traumatic brain injury	Male SD rats	Intracerebrally	Enhanced survival and retention of MSCs; increased neuron survival; improved learning and memory abilities	Yao et al. (2019)
Thermo-responsive	Chitosan, poloxamer P408	—	Temperature/Curcumin-loaded mesoporous silica NPs	Alzheimer's disease	Female Swiss albino mice	Intranasally	High permeation across nasal mucosa; reverting the cognitive deficit	Ribeiro et al. (2022)
Thermo-responsive	Pluronic F127, SCMC	—	Temperature/ Oxcarbazepine-loaded chitosan NPs	Epilepsy	Male SD rats	Intranasally	Increased anti-inflammation; decreased seizure score and prolonged survival	Abou-Taleb and El-Ganainy, (2023)
Enzyme-responsive	Para-sulfobenzoic acid	—	MMP-9/peptide SFNV	Traumatic brain injury	Female C57BL/6J mice	Intracerebrally	Providing ECM like environment with sulfate functionalities; supporting the survival of neurons	Adak et al. (2020)
Enzyme-responsive	Hyaluronic acid, chitosan, heparin sulfate	Adipic acid dihydrazide	MMP/SDF-1α- and bFGF-loaded polyelectrolyte complex NPs	Ischemic stroke	Male SD rats	Intracerebrally	Enhanced neurogenesis and angiogenesis; facilitated recovery of neurological behavior	Jian et al. (2018)

(Continued on following page)

10.3389/fbioe.2024.1450267

TABLE 1 (*Continued*) Summary of preclinical *in vivo* study evaluating the therapeutic efficacy of stimuli-responsive hydrogels in brain disease treatment.

Class of hydrogels	Main composition/ biomaterial	Crosslinker	Stimuli/ encapsulates	Disease	*In vivo* models	Route of administration	Outcome	References
Enzyme-responsive	Triglycerol monostearate	—	MMP/TMZ, O6-benzylamine	Glioma	Male BALB/c nude mice	Intratumorally	Enhanced effectiveness of TMZ in suppressing glioma growth; decreased recurrence rate of TMZ-resistant glioma following surgical intervention	Zhao et al. (2020)
Enzyme-responsive	PEG-b-PTyr-b-PAsp	—	Proteinase K/volasertib, ANG-CPP	Glioblastoma	Female BALB/c nude mice	Intravenously	Reduced toxicity; prolonged circulation time; better anti-tumor activity	Fan et al. (2021)
Enzyme-responsive	PEG-bis-AA	UV light	Hyaluronidase and esterase/ HA-DXM	Traumatic brain injury	Male SD rats	Intracerebrally	Sustained release of dexamethasone; higher neuronal cell survival; improved motor functional recovery	Jeong et al. (2021)
Photo-responsive	GelMA-imid	Blue light	Blue light/PDA@SDF-1α NPs, hASMCs	Traumatic brain injury	Male SD rats	Intracerebrally	Promoting the migration of hAMSCs to injury site; promoting the differentiation of hAMSCs into nerve cells	Zheng et al. (2021)
Electro-responsive	Chitosan, aniline pentamer, carboxylated Pluronic F127	Pluronic	Electricity/VEGF	Hippocampus ischemia	Adult male Wistar rats	Intracerebrally	Decreased infarction volume; improved hippocampal dependent learning and memory performance	Nourbakhsh et al. (2020)
ROS-responsive	HA-PBA; PVA	—	ROS/Desferoxamine mesylate	Traumatic brain injury	Male SD rats	Intracerebrally	Reducing iron overload; diminishing ROS level; promoting neuronal recovery after trauma	Qiu et al. (2024)
Hypoxia-responsive	Poly(phosphorylcholine)	Azobenzene	Hypoxia/doxorubicin hydrochloride	Glioblastoma	Nude female BALB/c mice	Intravenously	Prolonged blood circulation and favorable immune compatibility; effective penetration through the BBB; favorable tumor inhibition effect	Peng et al. (2021)
Dual-responsive	GelMA, PPS60	Blue Light	ROS, MMP/procyanidins	Traumatic brain injury	Male ICR mice	Intracerebrally	Inhibiting the oxidative stress response by depleting ROS	Huang et al. (2022)
Dual-responsive	HA-PBA, PVA	—	Glucose, ROS/NSC-EVs	Stroke	Type 2 diabetes mellitus mice	Intracerebrally	Excellent angiogenic effect; improved neurobehavioral recovery	Jiang et al. (2022)
Dual-responsive	Deacetylated gellan gum, poloxamer P407, sodium alginate	–	Temperature, ion/ timosaponin BII, HP-β-CD, chlorobutanol	Alzheimer's disease	C57BL/6J mice	Intranasally	Decreased levels of proinflammatory mediators; enhanced memory and language functions; reduced cognitive decline	Chen et al. (2020)

(Continued on following page)

10.3389/fbioe.2024.1450267

TABLE 1 (*Continued*) Summary of preclinical *in vivo* study evaluating the therapeutic efficacy of stimuli-responsive hydrogels in brain disease treatment.

Class of hydrogels	Main composition/ biomaterial	Crosslinker	Stimuli/ encapsulates	Disease	*In vivo* models	Route of administration	Outcome	References
Triple-responsive	Poloxamer P188/P407	—	Temperature, pH, ROS/Olz/RDPA NPs	Depression	Male Wistar rats	Intranasally	Efficient delivery of NPs to the brain; combined ROS depletion and inhibition of 5-HT dysfunction; alleviation of depression-like behaviors	Liu et al. (2023)
Dual-responsive	Poly (propylene sulfide)120	Triglycerol monostearate	ROS, MMP/curcumin	Traumatic brain injury	Male ICR mice	Intracerebrally	ROS depletion; reduced inflammation and brain edema; improved neural regeneration and behavior recovery	Qian et al. (2021)
Dual-responsive	Gelatin, carboxylic acid-terminated oligosulfamethazine	—	Temperature, pH/paclitaxel	Glioblastoma	BALB/c mice	Intratumorally	Sustained release of paclitaxel; inhibition of tumor growth	Kang et al. (2021)
Dual-responsive	Chitosan-g-poly(N-isopropylacrylamide)	Aldehyde-terminated difunctional polyurethane	Temperature, pH/SLP2 shRNA, (GO-CET)/CPT11	Glioblastoma	Female BALB/c nude mice	Intratumorally	60% tumor size reduction	Lu et al. (2020)

5-HT: 5-hydroxytryptamine; ANG-CPP: angiopep-2-docked chimeric polypeptide polymersome; BBB: blood-brain barrier; bFGF: basic fibroblast growth factor; CS-HEC-HA: chitosan, hydroxyethyl cellulose and hyaluronic acid; ECM: extracellular matrix; GelMA: gelatin methacrylate; GelMA-imid: imidazole groups-modified gelatin methacrylate; (GO-CET)/CPT11: cetuximab-conjugated graphene oxide; GP: β-glycerophosphate; HA-PBA: phenylboronic acid grafted hyaluronic acid; hAMSCs: human amniotic mesenchymal stromal cells; HP-β-CD: hydroxypropyl-β-cyclodextrin; HA-DXM: dexamethasone-conjugated hyaluronic acid; hUC-MSCs: human umbilical cord mesenchymal stem cells; MMP: matrix metalloproteinase; NPs: nanoparticles; NSC-EVs: neural stem cell-derived extracellular vesicles; Olz/RDPA: olanzapine/hexa-arginine-conjugated dextran coupled phenylboronic acid pinacol ester; PDA: polydopamine; PEG: polyethylene glycol; PEG-b-PTyr-b-PAsp: poly(ethylene glycol)-b-poly(L-tyrosine)-b-poly(Laspartic acid); PEG-bis-AA: poly (ethylene) glycol-bis-(acryloyloxy acetate); PLGA–PEG-PLGA: poly (dl-lactide-co-glycolide-b–ethylene glycol-b-dl-lactide-co-glycolide); PPS60: poly(propylene sulfide)60; PVA: polyvinyl alcohol; SCMC: sodium carboxymethyl cellulose; ROS: reactive oxygen species; SD: Sprague-Dawley; SDF-1α: stromal-cell-derived factor-1α; shRNA: short hairpin RNA; SLP2: stomatin-like protein 2; TMZ: temozolomide; UV: ultraviolet; VEGF: vascular endothelial growth factor.

10.3389/fbioe.2024.1450267

aldehyde-amine bonds and reversible pH-responsive properties (Zhang et al., 2023b).

ROS-responsive hydrogels interact with ROS using oxygen-sensitive groups, which alter the hydrogel network (Gao and Xiong, 2021). Boronic acid crosslinking is used to create various ROS-responsive hydrogels from polymers like sodium alginate, hyaluronic acid, cellulose, chitosan, gelatin, etc.

Hypoxia-responsive hydrogels can be synthesized through incorporation of hypoxia-sensitive moieties. These moieties, including 2-nitro imidazole, azobenzene derivatives, and nitro benzyl derivatives, enable the hydrogels to specifically release drugs within hypoxic environment (Peng et al., 2021).

2.2.3 Biological-responsive hydrogels

Biological-responsive hydrogels are classified into enzyme- and glucose-responsive types, each sensitive to enzymes or glucose.

Enzyme-responsive hydrogels incorporate biomolecules that can be cleaved by specific enzymes such as matrix metalloproteinases (MMPs), proteinase K, hyaluronidase and esterase, resulting in altered swelling properties of the gel (Sobczak, 2022). Hyaluronic acid hydrogels can be degraded by hyaluronidase and esterase, while in some cases, by adding MMP-cleavable (PLGL, GCDSGGRMSMPVSDGG) or inactive peptides (GCRDFGAIGQDGDRGG), hydrogels can be made responsive to MMPs (Jian et al., 2018; Adak et al., 2020).

Glucose-responsive hydrogels change their sol-gel behavior based on glucose levels, of which common types include concanavalin A, glucose oxidase, and phenylboronic acid (PBA) hydrogels (Morariu, 2023).

2.2.4 Multiple-stimuli-responsive hydrogels

To broaden the capabilities and uses of hydrogels, there's been a surge of interest in creating dual or even multiple-stimuli-responsive hydrogels. A straightforward method for creating these hydrogels is by incorporating multiple stimuli-responsive materials into existing composite hydrogel systems. Dual ROS/enzyme-, ROS/glucose-, pH/thermo-, ion strength/thermo-, and even triple ROS/pH/thermo-responsive hydrogels have been utilized in brain disease treatment (Table 1).

3 Design principle of stimuli-responsive hydrogels for brain disease treatment

Given the intricate composition of brain tissue, the restoration of functional connectivity between axons, neural circuits, and non-neuronal cells poses a significant challenge for stimuli-responsive hydrogels in treating brain diseases (Halim et al., 2021). These hydrogels must exhibit excellent biocompatibility and biodegradability to minimize immune activation during treatment (Lee et al., 2021; Zamproni et al., 2021). Additionally, the mechanical properties of the hydrogels must closely mimic the softness of brain tissue, typically ranging from 0.1 to 0.3 kPa, to favor neural growth, migration, and neurite extension (Xia et al., 2017; Yang et al., 2017). Substrate topography also plays a pivotal role, providing nano- or micro-structured environments that can guide cell growth and regulate neural cell differentiation (Seo et al., 2018; Wang et al., 2019). Moreover, porosity is a critical factor that influences nutrient diffusion, waste removal, and cell seeding, penetration, and growth within the hydrogel matrix (Bružauskaitė et al., 2016; Shi et al., 2022). Typically, pore sizes in the range of 95–150 μm are considered optimal for neural tissue culture (Shi et al., 2022). To support cell attachment and enhance cellular interactions, immobilization of substances such as poly-L-lysin, fibronectin, gelatin, laminin, collagen, and peptides (RGD, IKVAV, GRGDS, mi-GDPGYIGSR, and mi-GQASSIKVA) is often required (Balion et al., 2020; Long et al., 2020; El-Husseiny et al., 2022). Last, conductive materials show promise in electrical stimulation treatment and recording, but their safety and biocompatibility must be rigorously examined due to concerns regarding cytotoxicity and chronic inflammation (Khan et al., 2022).

Therapeutic agents, including small compounds, peptides, proteins, nucleic acids, cells, and extracellular vesicles, are the key component of stimuli-responsive hydrogels, playing a pivotal role in brain disease treatment by reducing ROS damage and inflammation, promoting neural regeneration, and inducing tumor cell death (Ghosh et al., 2024). To achieve precise and controlled targeted delivery of therapeutic agents, these hydrogels capitalize on the patient's physiological and pathological environments. Thermo-, ion strength-, and pH-responsive hydrogels exploit temperature variations, ion particles, and pH levels in nasal cavities or brain tissues to form *in situ* gels. Elevated ROS levels and enzyme expression in diseased brain tissues enable ROS- or enzyme-responsive hydrogels to release therapeutic agents with precision. In diabetics, high glucose triggers glucose-responsive hydrogels to release therapeutic agents. These hydrogels revolutionize brain disease treatment, providing controlled and targeted drug delivery.

Recently, hydrogels with self-assembly, self-healing, nanocomposite hybrid, and nano-size properties show promise for brain disease treatment (Jooken et al., 2023). Peptide-based self-assembling hydrogels exhibit high water content, tunable properties, and injectability, of which self-assembly process is governed by precise hydrophobic/hydrophilic interactions and hydrogen bond formation (Oliveira et al., 2022). Self-healing hydrogels overcome strength limitations, with reversible polymer chains enabling spontaneous repair and enhanced durability, in which chitosan and alginate are commonly used in their production (Zhu et al., 2023). Nanocomposite hydrogels hold superior physical, electrical, and biological properties, particularly for neural regeneration (Wang et al., 2022). Nano-sized hydrogels, or nanogels, are 20–200 nm in size, offering superior targeting and tissue access (Hajebi et al., 2019; Peng et al., 2021).

4 Preclinical progress in utilizing stimuli-responsive hydrogels for brain disease treatment

Brain diseases typically exhibit pathological features such as neural loss or death, vascular dysfunction, inflammation, oxidative stress, and increased expression of MMPs in affected tissues (El-Husseiny et al., 2022; Ghosh et al., 2024). These environmental cues can be exploited by hydrogels that respond to various stimuli, enabling targeted therapeutic delivery. Additionally, therapeutic agents like neuroprotective drugs, peptides, antioxidants, and growth factors can be released by hydrogels to alleviate these

pathological conditions. Exceptionally, hypoxia within GBM tissues can be targeted by hypoxia-responsive hydrogels loaded with antitumor drugs, ranging from small compounds to nucleic acids. Notably, nanocomposite hybrid hydrogels and nanogels demonstrate remarkable performance in drug delivery, effectively traversing BBB. Recent preclinical *in vivo* studies evaluating the therapeutic efficacy of stimuli-responsive hydrogels in brain disease treatment are listed in Table 1.

4.1 Bain injury

4.1.1 Traumatic brain injury

Encapsulating mesenchymal stromal cells (MSCs) or growth factors into hydrogels can enhance anti-inflammatory effects and promote neural regeneration. Yao et al. developed an injectable thermo-responsive hydrogel using chitosan, hydroxyethyl cellulose, hyaluronic acid, and beta-glycerophosphate (Yao et al., 2019). This hydrogel mimics brain tissue's rheological behavior, liquefying at <25°C and solidifying at body temperature. When loaded with human umbilical cord-derived MSCs (hUC-MSCs) and injected into TBI rat brains, it enhanced MSC survival and retention, resulting in elevated brain-derived neurotrophic factor, neuron survival, and improved learning and memory, outperforming that of MSC-alone treatment. Separately, Zheng et al. created a blue light crosslinked hydrogel with imidazole-modified gelatin methacrylate and polydopamine/stromal-cell derived factor-1 (PDA@SDF-1α) nanoparticles loaded with human amniotic MSCs (hAMSCs). This hydrogel promoted hAMSC migration to injury sites and neuronal differentiation, repairing cryogenic brain injury in rats (Zheng et al., 2021).

Utilizing enzymes in the injured brain tissues, Adak et al. designed MMP9-responsive peptide-based hydrogels (SFNV) for TBI treatment. These hydrogels released neuroprotective peptides (NAVSIQ) by MMP9-mediated cleavage of PLGL tetrapeptide linker, and promoted neurogenesis in hippocampal regions of cryogenic injury mice (Adak et al., 2020). In another case, Jeong et al. conjugated dexamethasone with hyaluronic acid in a poly (ethylene) glycol-bis-(acryloyloxy acetate) hydrogel (PEG-bis-AA), This formulation sustained dexamethasone release, reducing inflammatory cytokines and enhancing motor recovery in TBI rats 7 days post-injury (Jeong et al., 2021).

Iron overload worsens neurodegeneration by promoting ROS production (Tang et al., 2020). Qiu et al. incorporated desferoxamine mesylate, an iron chelator, into a boron ester-bonded hydrogel composed of 3-aminophenylboronic acid-grafted hyaluronic acid and polyvinyl alcohol (PVA). This hydrogel self-healed and responded to ROS due to the boron ester bond, alleviating iron overload and oxidative stress in brain-injured rats, improving motor, learning, and memory functions (Qiu et al., 2024). For better drug delivery and release, Qian et al. created an injectable dual ROS/enzyme-responsive hydrogel composed of poly (propylene sulfide)120 (PPS120) and curcumin within a triglycerol monostearate (TM) hydrogel. Injection into TBI mice brains caused MMPs to cleave the TM coat, PPS120 to react with ROS, and curcumin to scavenge ROS. This reduced reactive glia cells, inflammation, brain edema, and improved BBB integrity, enhancing nerve regeneration and behavioral recovery in TBI mice (Qian et al., 2021).

4.1.2 Stroke

Antioxidants and growth factors are embedded in hydrogels to promote neurogenesis and angiogenesis. In a case, a chitosan micellar hydrogel encapsulated hydrophilic minocycline and hydrophobic edaravone drugs for stroke treatment. Injection in rats promptly released the hydrophilic drug and sustains release of the hydrophobic drug, leading to significant behavioral recovery (~84%) due to sequential anti-inflammatory and neurogenesis effects (Lin et al., 2023). Another study reported the functional repair of the hippocampus post-ischemia using a pluronic-chitosan/aniline-pentamer hydrogel loaded with vascular endothelial growth factor (VEGF). This hydrogel mimics brain tissue conductivity (10^{-4} S/cm), enabling sustained VEGF release upon intracerebral administration. This approach significantly reduced infarct size by >70% and improved hippocampal-dependent learning and memory, outperforming VEGF delivery alone (Nourbakhsh et al., 2020). A third study used polyelectrolyte complex nanoparticles loaded with SDF-1α and basic fibroblast growth factor, modified with MMP-cleavable peptides, and combined with hyaluronic acid to form enzyme-responsive hydrogels. These hydrogels exhibited superior neurological recovery compared to free growth factors or bare hydrogels in an ischemic stroke model through intracerebral administration, enhancing neurogenesis and angiogenesis (Jian et al., 2018).

ROS and high blood glucose hamper stroke recovery. Jiang et al. designed a dual glucose/ROS-responsive hydrogel loaded with neural stem cell-derived extracellular vesicles (NSC-EVs) for diabetic stroke treatment (Jiang et al., 2022). The hydrogel, made from crosslinking PBA-modified hyaluronic acid with PVA, prolonged EV retention and activity in the brain. NSC-EVs released miRNAs vital for angiogenesis, reducing brain atrophy and enhancing neurobehavioral recovery in diabetic stroke mice.

4.2 Neurodegenerative diseases

The use of intranasal administration has demonstrated significantly improved drug delivery for the treatment of Alzheimer's disease. For instance, Curcumin-loaded mesoporous silica nanoparticles in chitosan and P407 hydrogel improved permeation of drugs and cognitive function in an Alzheimer's mouse model (Ribeiro et al., 2022). In another study, Chen et al. developed dual pH/thermo-responsive hydrogels with neuroprotective timosaponin BII for Alzheimer's disease (Chen et al., 2020). This hydrogel integrated ion-sensitive deacetylated gellan gum, thermo-sensitive Poloxamer 407, and sodium alginate, harnessing rapid sol-gel transition triggered by heat and Ca^{2+} in the nasal cavity. Studies on mice showed improved memory, language, reduced cognitive decline and neuroinflammation.

In recent 5 years, there has been a lack of preclinical animal studies for the treatment of Parkinson's disease.

4.3 Psychiatric disorders

4.3.1 Major depressive disorder

Intranasal administration of thermo-responsive gels can effectively deliver drugs to brain tissue. An antidepressant drug,

genipin, was combined with hydroxypropyl-β-cyclodextrin (HP-β-CD) and mixed with P407/P188/PEG8000 to create a thermo-responsive hydrogel for intranasal delivery. This hydrogel effectively and sustainably released genipin in mouse brains, improving antidepressant effects (Qi et al., 2021). In another case, icariin was encapsulated in alginate nanogels and integrated into a P407/P188 hydrogel for sustained release after intranasal administration, leading to rapid antidepressant effects in mice and rat models (Xu et al., 2020). Depression is linked to oxidative stress, making antioxidant therapy promising (Bhatt et al., 2020). Recently, a combination of nanoparticles and hydrogels demonstrated impressive drug delivery capabilities (Liu et al., 2023). In this system, amphiphilic polymers (DEX-g-PBAP) made of phenylboronic acid pinacol ester (PBAP) and dextran (DEX) with ROS-sensitive borate ester bonds were used to load antidepressant olanzapine (Olz) to form nanoparticles (Olz/DP NPs). Olz/DP NPs were then modified with amino borane to get Olz/DPA NPs, and further conjugated with hexa-arginine (R6) to create Olz/RDPA NPs. Olz/RDPA NPs were then encapsulated in a poloxamer (P407/P188) hydrogel. Upon intranasal administration in a rat model, the NPs were released from the hydrogel and transported to the brain via the nasal-brain pathway effectively. High ROS levels in the brain triggered NP breakdown, releasing Olz. Simultaneously, H_2 released from amino borane scavenged •OH, reversing oxidative stress in the brain and alleviating depressive-like behaviors.

4.3.2 Schizophrenia

PAOPA, a D2 allosteric modulator, significantly reduced schizophrenia-like symptoms in rats using hydrogels composed of oxidized starch nanoparticles and carboxymethyl chitosan. Its potency and bioavailability are emphasized by achieving relief with half the intraperitoneal dosage through intranasal delivery (Majcher et al., 2021).

4.3.3 Epilepsy

Chitosan nanoparticles were employed to enhance the delivery of the antiepileptic drug Oxcarbazepine in Pluronic F127 (also known as poloxamer P407) and sodium carboxymethyl cellulose hydrogel (Abou-Taleb and El-Ganainy, 2023). This formulation exhibited improved antiepileptic activity and anti-inflammatory effects upon intranasal administration.

4.4 Brain tumors

Direct intratumoral injection of stimuli-responsive hydrogels that leverage tumor microenvironment factors, such as low pH and high enzyme expression, is an efficient strategy to overcome the BBB impediment for drug delivery. Recently, injectable thermo-responsive hydrogels encapsulating salinomycin using copolymers Pluronic F127 and poly (dl-lactide-co-glycolide-b–ethylene glycol-b-dl-lactide-co-glycolide) (PLGA–PEG-PLGA) improved drug release and cytotoxicity, significantly reducing GBM tumor growth, surpassing the effect of free salinomycin alone (4-fold) (Norouzi et al., 2021). In another case, a dual pH/thermo-responsive hydrogel, made from carboxylic acid-terminated oligosulfamethazine and gelatin, transforms rapidly sol-to-gel in response to body temperature and low pH. This hydrogel can sustainably release paclitaxel intratumorally thanks to gelatin's MMP-cleavage site for antitumor effects in GBM mice (Kang et al., 2021). In a third study, TM-based MMP9-responsive hydrogels loaded with Temozolomide and O6-benzylamine prevented recurrence in post-operative glioma models (Zhao et al., 2020). Encapsulation of therapeutic nucleic acids is also a promising method for treating GBM. Recently, an injectable drug/gene delivery system using a thermosensitive chitosan-based polymer solution to entrap stomatin-like protein 2 (SLP2) shRNA and irinotecan (CPT-11)-loaded cetuximab (CET)-conjugated graphene oxide (GO-CET/CPT11) has been created (CPN@GO-CET/CPT11@shRNA). This formed a hydrogel depot for localized, sustained delivery of therapeutics. Efficient transfection of U87 cancer cells with SLP2 shRNA was achieved using this hydrogel, demonstrated *in vivo* using tumor-bearing mice. This hydrogel offers extended drug release and shRNA delivery advantages, broadening GBM treatment modalities (Lu et al., 2020).

Nanocomposite hybrids and nanosized gels, as emerging nanotechnologies, have demonstrated significant potential in enhancing intravenous drug delivery for the treatment of GBM. Plk1 upregulation in GBM can be suppressed by Plk1 inhibitor Volasertib. Loaded into angiopep-2-decorated chimeric polypeptide polymersome, Volasertib forms a nanogel with a size of approximately 76 nm from poly(ethylene glycol)-b-poly(L-tyrosine)-b-poly(Laspartic acid). This nanogel traversed BBB and GBM membranes via lipoprotein receptor-related protein 1 (LRP-1)-mediated transcytosis and endocytosis respectively, rapid releasing of Volasertib by proteinase K, suppressing GBM growth and enhancing survival in mice (Fan et al., 2021). In another case, hypoxia-degradable zwitterionic phosphorylcholine nanogel, ^{H}PMPC, penetrated the BBB by mimicking cell membrane structure after intravenous administration, releasing doxorubicin by azobenzene moiety degradation in tumor tissues of GBM mouse models (Peng et al., 2021).

5 Discussion

In this review, we examined the distinguishing features of a range of stimuli-responsive hydrogels, particularly those that respond to thermal, photonic, magnetic, electrical, and biological cues. Our emphasis lies in highlighting how these hydrogels can capitalize on the pathophysiological features of diseased brains by developing responsive biomaterials. Additionally, we outlined their varied applications and underlying therapeutic mechanisms, including neurogenesis promotion, anti-inflammatory, anti-apoptotic, anti-oxidative, and angiogenic effects, all contributing to the enhancement of therapeutic outcomes (summarized in Figure 1). These hydrogels offer numerous benefits, including precise targeting, controlled release, mechanical support, and biocompatibility, rendering them promising candidates for the treatment of brain diseases in the future.

These advanced systems, despite their potential, exhibit several limitations that necessitate careful consideration during their application based on the specific pathophysiological characteristics of the target disease. For instance, stimuli-

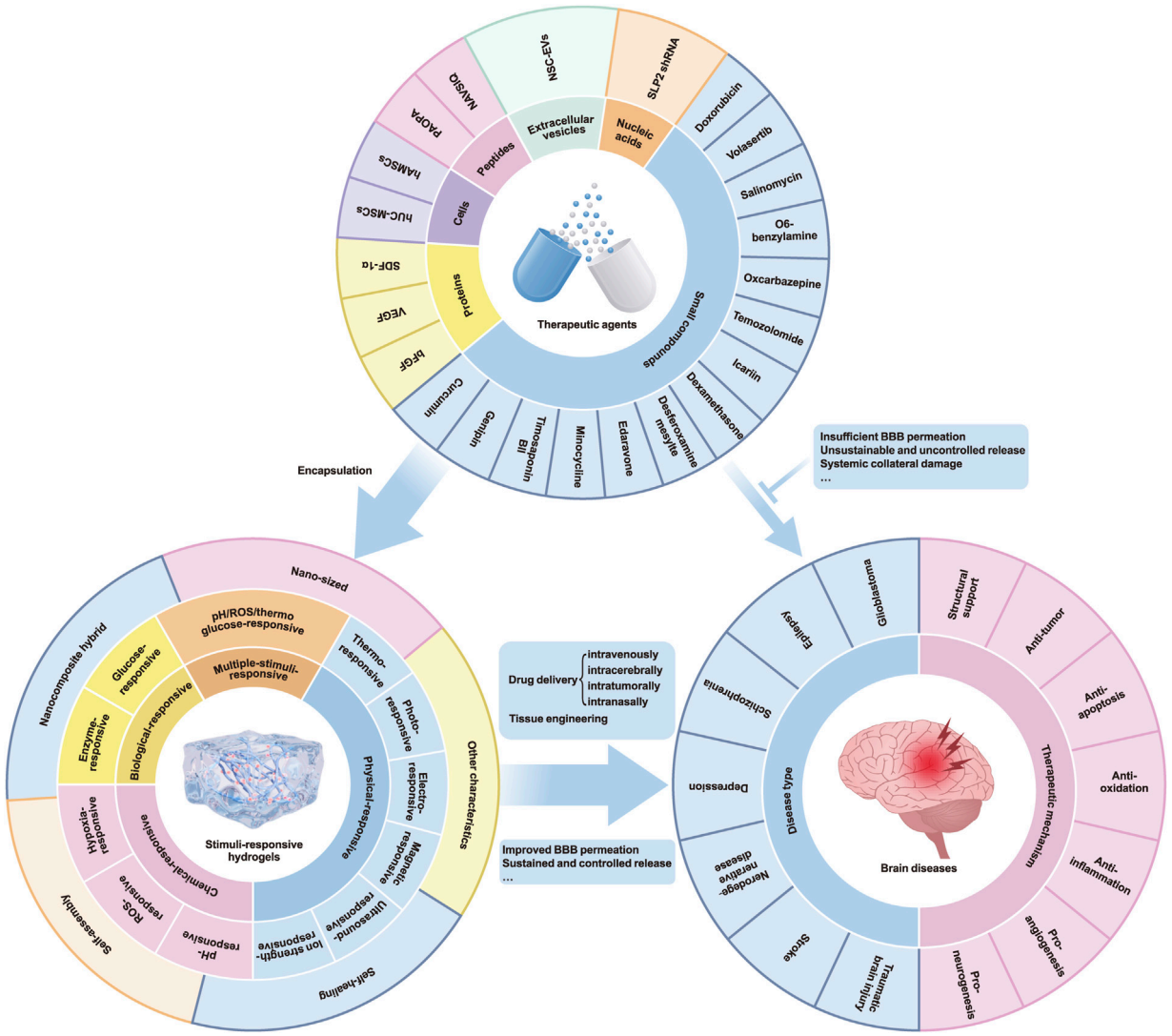

FIGURE 1
Schematic diagram of stimuli-responsive hydrogels for brain disease treatment in recent preclinical *in vivo* study. BBB: blood-brain barrier; bFGF: basic fibroblast growth factor; hAMSCs: human amniotic mesenchymal stromal cells; hUC-MSCs: human umbilical cord mesenchymal stem cells; NSC-EVs: neural stem cell-derived extracellular vesicles; ROS: reactive oxygen species; SDF-1α: stromal-cell-derived factor-1α; SLP2 shRNA: stomatin-like protein 2 short hairpin RNA; VEGF: vascular endothelial growth factor.

responsive systems relying on alterations in pH, ROS, or enzymes may exhibit suboptimal sensitivity to nuanced microenvironmental changes, potentially resulting in underperformance. Additionally, the *in vivo* microenvironment poses challenges, such as the formation of a protein corona around nanoparticles, which can significantly reduce or even eliminate the therapeutic efficacy of these systems. Other inherent limitations include thermal denaturation, UV-induced carcinogenesis, insufficient mechanical strength, and material toxicity. Furthermore, the hydrogels' propensity for high swelling can result in elevated local tissue pressure, which may compromise their mechanical integrity and exacerbate secondary brain injury. Therefore, a thorough understanding of these limitations and careful evaluation of their applicability in specific cases are essential for the optimal utilization of these systems in therapeutic applications.

The integration of nanotechnology, artificial intelligence, and three-dimensional printing into the development of hydrogels presents a compelling opportunity for the creation of innovative therapeutic strategies in brain diseases (Gao et al., 2023). Yet, a rigorous preclinical evaluation encompassing safety, efficacy, and stability is paramount before clinical translation. Key challenges include elucidating hydrogel-neural microenvironment interactions, minimizing immunogenicity, and optimizing targeted delivery. While animal models offer insights, they may not fully recapitulate human disease complexities. Therefore, bridging the gap between *in vitro*/*in vivo* models and human diseases remains a significant challenge (Shabani et al., 2023). Future research must prioritize enhancing hydrogel biocompatibility, especially by exploring natural materials that facilitate cellular recognition and integration. Identifying the optimal therapeutic window in various

brain diseases, considering disease progression, is crucial for maximizing therapeutic potential. Additionally, scalable manufacturing, regulatory adherence, and economic viability are essential for successful commercialization.

Collectively, future trends in stimuli-responsive hydrogel development emphasize: multifunctional biomaterials integrating therapy, imaging, tissue regeneration, stem cell support, immune modulation, and antibacterial properties; exploration of novel stimuli like inflammatory enzymes for enhanced targeting; optimization of biomaterials for biosafety, efficacy, and cost-effectiveness; addressing patient compliance, convenience, and cost issues; and advancing our pathological understanding of brain diseases to design effective therapies. Collaborations across disciplines are key to translating hydrogel technologies to clinical applications.

In conclusion, stimuli-responsive hydrogels hold significant potential for revolutionizing the treatment of brain diseases. A multidisciplinary approach that integrates expertise from various fields is crucial for advancing this research and ultimately bringing new therapeutic options to patients.

Author contributions

BX: Writing–original draft, Writing–review and editing. HX: Writing–original draft, Writing–review and editing.

Funding

The author(s) declare that financial support was received for the research, authorship, and/or publication of this article. The authors thank the financial support from the National Natural Science Foundation of China (32300675), Sichuan Science and Technology Program (2022YFS0615), Luzhou Science and Technology Program of China (2023SYF136, 2023JYJ019), Doctoral Research Initiation Fund of Affiliated Hospital of Southwest Medical University (22069, 22070).

Conflict of interest

The authors declare that the research was conducted in the absence of any commercial or financial relationships that could be construed as a potential conflict of interest.

Publisher's note

All claims expressed in this article are solely those of the authors and do not necessarily represent those of their affiliated organizations, or those of the publisher, the editors and the reviewers. Any product that may be evaluated in this article, or claim that may be made by its manufacturer, is not guaranteed or endorsed by the publisher.

References

Abdeltawab, H., Svirskis, D., and Sharma, M. (2020). Formulation strategies to modulate drug release from poloxamer based *in situ* gelling systems. *Expert Opin. Drug Deliv.* 17, 495–509. doi:10.1080/17425247.2020.1731469

Abou-Taleb, B. A., and EL-Ganainy, S. O. (2023). Thermoresponsive gel-loaded oxcarbazepine nanosystems for nose- to-brain delivery: enhanced antiepileptic activity in rats. *Pharm. Res.* 40, 1835–1852. doi:10.1007/s11095-023-03552-7

Adak, A., Das, G., Khan, J., Mukherjee, N., Gupta, V., Mallesh, R., et al. (2020). Extracellular matrix (ECM)-Mimicking neuroprotective injectable sulfo-functionalized peptide hydrogel for repairing brain injury. *ACS Biomater. Sci. Eng.* 6, 2287–2296. doi:10.1021/acsbiomaterials.9b01829

Ahmed, S., Gull, A., Aqil, M., Danish Ansari, M., and Sultana, Y. (2019). Poloxamer-407 thickened lipid colloidal system of agomelatine for brain targeting: characterization, brain pharmacokinetic study and behavioral study on Wistar rats. *Colloids Surf. B Biointerfaces* 181, 426–436. doi:10.1016/j.colsurfb.2019.05.016

Alawami, A. Z., and Tannous, Z. (2021). Late onset hypersensitivity reaction to hyaluronic acid dermal fillers manifesting as cutaneous and visceral angioedema. *J. Cosmet. Dermatol* 20, 1483–1485. doi:10.1111/jocd.13894

Balion, Z., Cėpla, V., Svirskiene, N., Svirskis, G., Druceikaitė, K., Inokaitis, H., et al. (2020). Cerebellar cells self-assemble into functional organoids on synthetic, chemically crosslinked ECM-mimicking peptide hydrogels. *Biomolecules* 10, 754. doi:10.3390/biom10050754

Bhatt, S., Nagappa, A. N., and Patil, C. R. (2020). Role of oxidative stress in depression. *Drug Discov. Today* 25, 1270–1276. doi:10.1016/j.drudis.2020.05.001

Bružauskaitė, I., Bironaitė, D., Bagdonas, E., and Bernotienė, E. (2016). Scaffolds and cells for tissue regeneration: different scaffold pore sizes-different cell effects. *Cytotechnology* 68, 355–369. doi:10.1007/s10616-015-9895-4

Cassano, R., Servidio, C., and Trombino, S. (2021). Biomaterials for drugs nose-brain transport: a new therapeutic approach for neurological diseases. *Mater. (Basel)* 14, 1802. doi:10.3390/ma14071802

Cheng, K. W., Alhasan, L., Rezk, A. R., AL-Abboodi, A., Doran, P. M., Yeo, L. Y., et al. (2020). Fast three-dimensional micropatterning of PC12 cells in rapidly crosslinked hydrogel scaffolds using ultrasonic standing waves. *Biofabrication* 12, 015013. doi:10.1088/1758-5090/ab4cca

Chen, W., Li, R., Zhu, S., Ma, J., Pang, L., Ma, B., et al. (2020). Nasal timosaponin BII dually sensitive *in situ* hydrogels for the prevention of Alzheimer's disease induced by lipopolysaccharides. *Int. J. Pharm.* 578, 119115. doi:10.1016/j.ijpharm.2020.119115

Dienes, J., Browne, S., Farjun, B., Amaral Passipieri, J., Mintz, E. L., Killian, G., et al. (2021). Semisynthetic hyaluronic acid-based hydrogel promotes recovery of the injured tibialis anterior skeletal muscle form and function. *ACS Biomater. Sci. Eng.* 7, 1587–1599. doi:10.1021/acsbiomaterials.0c01751

EL-Husseiny, H. M., Mady, E. A., Hamabe, L., Abugomaa, A., Shimada, K., Yoshida, T., et al. (2022). Smart/stimuli-responsive hydrogels: cutting-edge platforms for tissue engineering and other biomedical applications. *Mater Today Bio* 13, 100186. doi:10.1016/j.mtbio.2021.100186

Fan, Q., Liu, Y., Cui, G., Zhong, Z., and Deng, C. (2021). Brain delivery of Plk1 inhibitor via chimaeric polypeptide polymersomes for safe and superb treatment of orthotopic glioblastoma. *J. Control Release* 329, 1139–1149. doi:10.1016/j.jconrel.2020.10.043

Feigin, V. L., Vos, T., Nichols, E., Owolabi, M. O., Carroll, W. M., Dichgans, M., et al. (2020). The global burden of neurological disorders: translating evidence into policy. *Lancet Neurol.* 19, 255–265. doi:10.1016/s1474-4422(19)30411-9

Gao, F., and Xiong, Z. (2021). Reactive oxygen species responsive polymers for drug delivery systems. *Front. Chem.* 9, 649048. doi:10.3389/fchem.2021.649048

Gao, Q., Lee, J. S., Kim, B. S., and Gao, G. (2023). Three-dimensional printing of smart constructs using stimuli-responsive biomaterials: a future direction of precision medicine. *Int. J. Bioprint* 9, 638. doi:10.18063/ijb.v9i1.638

Ghosh, S., Ghosh, S., Sharma, H., Bhaskar, R., Han, S. S., and Sinha, J. K. (2024). Harnessing the power of biological macromolecules in hydrogels for controlled drug release in the central nervous system: a review. *Int. J. Biol. Macromol.* 254, 127708. doi:10.1016/j.ijbiomac.2023.127708

Grimaudo, M. A., Krishnakumar, G. S., Giusto, E., Furlani, F., Bassi, G., Rossi, A., et al. (2022). Bioactive injectable hydrogels for on demand molecule/cell delivery and for tissue regeneration in the central nervous system. *Acta Biomater.* 140, 88–101. doi:10.1016/j.actbio.2021.11.038

Guo, B., and Ma, P. X. (2018). Conducting polymers for tissue engineering. *Biomacromolecules* 19, 1764–1782. doi:10.1021/acs.biomac.8b00276

Hajebi, S., Rabiee, N., Bagherzadeh, M., Ahmadi, S., Rabiee, M., Roghani-Mamaqani, H., et al. (2019). Stimulus-responsive polymeric nanogels as smart drug delivery systems. *Acta Biomater.* 92, 1–18. doi:10.1016/j.actbio.2019.05.018

Halim, A., Qu, K. Y., Zhang, X. F., and Huang, N. P. (2021). Recent advances in the application of two-dimensional nanomaterials for neural tissue engineering and regeneration. *ACS Biomater. Sci. Eng.* 7, 3503–3529. doi:10.1021/acsbiomaterials.1c00490

Huang, X., Ye, Y., Zhang, J., Zhang, X., Ma, H., Zhang, Y., et al. (2022). Reactive oxygen species scavenging functional hydrogel delivers procyanidins for the treatment of traumatic brain injury in mice. *ACS Appl. Mater Interfaces* 14, 33756–33767. doi:10.1021/acsami.2c04930

Janas-Naze, A., and Zhang, W. (2022). Perioperative anaphylaxis to fibrin sealants in children with Noonan Syndrome: a retrospective study. *Ann. Allergy Asthma Immunol.* 129, 95–100. doi:10.1016/j.anai.2022.03.014

Jeong, D. U., Bae, S., Macks, C., Whitaker, J., Lynn, M., Webb, K., et al. (2021). Hydrogel-mediated local delivery of dexamethasone reduces neuroinflammation after traumatic brain injury. *Biomed. Mater.* 16, 035002. doi:10.1088/1748-605x/abc7f1

Jian, W. H., Wang, H. C., Kuan, C. H., Chen, M. H., Wu, H. C., Sun, J. S., et al. (2018). Glycosaminoglycan-based hybrid hydrogel encapsulated with polyelectrolyte complex nanoparticles for endogenous stem cell regulation in central nervous system regeneration. *Biomaterials* 174, 17–30. doi:10.1016/j.biomaterials.2018.05.009

Jiang, Y., Wang, R., Wang, C., Guo, Y., Xu, T., Zhang, Z., et al. (2022). Brain microenvironment responsive and pro-angiogenic extracellular vesicle-hydrogel for promoting neurobehavioral recovery in type 2 diabetic mice after stroke. *Adv. Healthc. Mater* 11, e2201150. doi:10.1002/adhm.202201150

Jooken, S., Deschaume, O., and Bartic, C. (2023). Nanocomposite hydrogels as functional extracellular matrices. *Gels* 9, 153. doi:10.3390/gels9020153

Kang, J. H., Turabee, M. H., Lee, D. S., Kwon, Y. J., and Ko, Y. T. (2021). Temperature and pH-responsive *in situ* hydrogels of gelatin derivatives to prevent the reoccurrence of brain tumor. *Biomed. Pharmacother.* 143, 112144. doi:10.1016/j.biopha.2021.112144

Khan, Z. M., Wilts, E., Vlaisavljevich, E., Long, T. E., and Verbridge, S. S. (2022). Electroresponsive hydrogels for therapeutic applications in the brain. *Macromol. Biosci.* 22, e2100355. doi:10.1002/mabi.202100355

Lee, W. H., Cha, G. D., and Kim, D. H. (2021). Flexible and biodegradable electronic implants for diagnosis and treatment of brain diseases. *Curr. Opin. Biotechnol.* 72, 13–21. doi:10.1016/j.copbio.2021.07.027

Li, L., Scheiger, J. M., and Levkin, P. A. (2019). Design and applications of photoresponsive hydrogels. *Adv. Mater* 31, e1807333. doi:10.1002/adma.201807333

Lin, S.-H., Huang, A. P.-H., and Hsu, S.-H. (2023). Injectable, micellar chitosan self-healing hydrogel for asynchronous dual-drug delivery to treat stroke rats. *Adv. Funct. Mater.* 33, 2303853. doi:10.1002/adfm.202303853

Liu, L., Liu, M., Xiu, J., Zhang, B., Hu, H., Qiao, M., et al. (2023). Stimuli-responsive nanoparticles delivered by a nasal-brain pathway alleviate depression-like behavior through extensively scavenging ROS. *Acta Biomater.* 171, 451–465. doi:10.1016/j.actbio.2023.09.038

Long, Y., Yan, L., Dai, H., Yang, D., Wu, X., Dong, X., et al. (2020). Enhanced proliferation and differentiation of neural stem cells by peptide-containing temperature-sensitive hydrogel scaffold. *Mater Sci. Eng. C Mater Biol. Appl.* 116, 111258. doi:10.1016/j.msec.2020.111258

Lu, Y. J., Lan, Y. H., Chuang, C. C., Lu, W. T., Chan, L. Y., Hsu, P. W., et al. (2020). Injectable thermo-sensitive chitosan hydrogel containing CPT-11-loaded EGFR-targeted graphene oxide and SLP2 shRNA for localized drug/gene delivery in glioblastoma therapy. *Int. J. Mol. Sci.* 21, 7111. doi:10.3390/ijms21197111

Luo, J., Zhao, X., Guo, B., and Han, Y. (2023). Preparation, thermal response mechanisms and biomedical applications of thermosensitive hydrogels for drug delivery. *Expert Opin. Drug Deliv.* 20, 641–672. doi:10.1080/17425247.2023.2217377

Ma, J., and Huang, C. (2020). Composition and mechanism of three-dimensional hydrogel system in regulating stem cell fate. *Tissue Eng. Part B Rev.* 26, 498–518. doi:10.1089/ten.teb.2020.0021

Majcher, M. J., Babar, A., Lofts, A., Leung, A., Li, X., Abu-Hijleh, F., et al. (2021). *In situ*-gelling starch nanoparticle (SNP)/O-carboxymethyl chitosan (CMCh) nanoparticle network hydrogels for the intranasal delivery of an antipsychotic peptide. *J. Control Release* 330, 738–752. doi:10.1016/j.jconrel.2020.12.050

Mantha, S., Pillai, S., Khayambashi, P., Upadhyay, A., Zhang, Y., Tao, O., et al. (2019). Smart hydrogels in tissue engineering and regenerative medicine. *Mater. (Basel)* 12, 3323. doi:10.3390/ma12203323

Mashabela, L. T., Maboa, M. M., Miya, N. F., Ajayi, T. O., Chasara, R. S., Milne, M., et al. (2022). A comprehensive review of cross-linked gels as vehicles for drug delivery to treat central nervous system disorders. *Gels* 8, 563. doi:10.3390/gels8090563

Morariu, S. (2023). Advances in the design of phenylboronic acid-based glucose-sensitive hydrogels. *Polym. (Basel)* 15, 582. doi:10.3390/polym15030582

Norouzi, M., Firouzi, J., Sodeifi, N., Ebrahimi, M., and Miller, D. W. (2021). Salinomycin-loaded injectable thermosensitive hydrogels for glioblastoma therapy. *Int. J. Pharm.* 598, 120316. doi:10.1016/j.ijpharm.2021.120316

Nourbakhsh, M., Zarrintaj, P., Jafari, S. H., Hosseini, S. M., Aliakbari, S., Pourbadie, H. G., et al. (2020). Fabricating an electroactive injectable hydrogel based on pluronic-chitosan/aniline-pentamer containing angiogenic factor for functional repair of the hippocampus ischemia rat model. *Mater Sci. Eng. C Mater Biol. Appl.* 117, 111328. doi:10.1016/j.msec.2020.111328

Oliveira, C. B. P., Gomes, V., Ferreira, P. M. T., Martins, J. A., and Jervis, P. J. (2022). Peptide-based supramolecular hydrogels as drug delivery agents: recent advances. *Gels* 8, 706. doi:10.3390/gels8110706

Peng, S., Ouyang, B., Xin, Y., Zhao, W., Shen, S., Zhan, M., et al. (2021). Hypoxia-degradable and long-circulating zwitterionic phosphorylcholine-based nanogel for enhanced tumor drug delivery. *Acta Pharm. Sin. B* 11, 560–571. doi:10.1016/j.apsb.2020.08.012

Peressotti, S., Koehl, G. E., Goding, J. A., and Green, R. A. (2021). Self-assembling hydrogel structures for neural tissue repair. *ACS Biomater. Sci. Eng.* 7, 4136–4163. doi:10.1021/acsbiomaterials.1c00030

Qi, X.-J., Xu, D., Tian, M.-L., Zhou, J.-F., Wang, Q.-S., and Cui, Y.-L. (2021). Thermosensitive hydrogel designed for improving the antidepressant activities of genipin via intranasal delivery. *Mater. Des.* 206, 109816. doi:10.1016/j.matdes.2021.109816

Qian, F., Han, Y., Han, Z., Zhang, D., Zhang, L., Zhao, G., et al. (2021). *In situ* implantable, post-trauma microenvironment-responsive, ROS Depletion Hydrogels for the treatment of Traumatic brain injury. *Biomaterials* 270, 120675. doi:10.1016/j.biomaterials.2021.120675

Qiu, Y., Zeng, Y., Zhang, C., Lv, X., Ling, Y., Si, Y., et al. (2024). A ROS-responsive loaded desferoxamine (DFO) hydrogel system for traumatic brain injury therapy. *Biomed. Mater* 19, 025016. doi:10.1088/1748-605x/ad1dfd

Rajput, A., Bariya, A., Allam, A., Othman, S., and Butani, S. B. (2018). *In situ* nanostructured hydrogel of resveratrol for brain targeting: *in vitro-in vivo* characterization. *Drug Deliv. Transl. Res.* 8, 1460–1470. doi:10.1007/s13346-018-0540-6

Ribeiro, T. D. C., SáBIO, R. M., Luiz, M. T., DE Souza, L. C., Fonseca-Santos, B., Cides Da Silva, L. C., et al. (2022). Curcumin-loaded mesoporous silica nanoparticles dispersed in thermo-responsive hydrogel as potential alzheimer disease therapy. *Pharmaceutics* 14, 1976. doi:10.3390/pharmaceutics14091976

Seo, J., Kim, J., Joo, S., Choi, J. Y., Kang, K., Cho, W. K., et al. (2018). Nanotopography-promoted formation of axon collateral branches of hippocampal neurons. *Small* 14, e1801763. doi:10.1002/smll.201801763

Shabani, L., Abbasi, M., Azarnew, Z., Amani, A. M., and Vaez, A. (2023). Neuro-nanotechnology: diagnostic and therapeutic nano-based strategies in applied neuroscience. *Biomed. Eng. Online* 22, 1. doi:10.1186/s12938-022-01062-y

Shi, M., Xu, Q., Ding, L., Xia, Y., Zhang, C., Lai, H., et al. (2022). Cell infiltrative inner connected porous hydrogel improves neural stem cell migration and differentiation for functional repair of spinal cord injury. *ACS Biomater. Sci. Eng.* 8, 5307–5318. doi:10.1021/acsbiomaterials.2c01127

Sobczak, M. (2022). Enzyme-responsive hydrogels as potential drug delivery systems-state of knowledge and future prospects. *Int. J. Mol. Sci.* 23, 4421. doi:10.3390/ijms23084421

Tang, L., Wang, L., Yang, X., Feng, Y., Li, Y., and Feng, W. (2021). Poly(N-isopropylacrylamide)-based smart hydrogels: design, properties and applications. *Prog. Mater. Sci.* 115, 100702. doi:10.1016/j.pmatsci.2020.100702

Tang, S., Gao, P., Chen, H., Zhou, X., Ou, Y., and He, Y. (2020). The role of iron, its metabolism and ferroptosis in traumatic brain injury. *Front. Cell Neurosci.* 14, 590789. doi:10.3389/fncel.2020.590789

Terstappen, G. C., Meyer, A. H., Bell, R. D., and Zhang, W. (2021). Strategies for delivering therapeutics across the blood-brain barrier. *Nat. Rev. Drug Discov.* 20, 362–383. doi:10.1038/s41573-021-00139-y

Tulain, U. R., Ahmad, M., Rashid, A., Malik, M. Z., and Iqbal, F. M. (2018). Fabrication of pH-responsive hydrogel and its *in vitro* and *in vivo* evaluation. *Adv. Polym. Technol.* 37, 290–304. doi:10.1002/adv.21668

Wang, F., Yang, Z., Liu, M., Tao, Y., Li, Z., Wu, Z., et al. (2020). Facile nose-to-brain delivery of rotigotine-loaded polymer micelles thermosensitive hydrogels: *in vitro* characterization and *in vivo* behavior study. *Int. J. Pharm.* 577, 119046. doi:10.1016/j.ijpharm.2020.119046

Wang, L., Wu, Y., Hu, T., Ma, P. X., and Guo, B. (2019). Aligned conductive core-shell biomimetic scaffolds based on nanofiber yarns/hydrogel for enhanced 3D neurite outgrowth alignment and elongation. *Acta Biomater.* 96, 175–187. doi:10.1016/j.actbio.2019.06.035

Wang, X., Ye, L., He, W., Teng, C., Sun, S., Lu, H., et al. (2022). *In situ* targeting nanoparticles-hydrogel hybrid system for combined chemo-immunotherapy of glioma. *J. Control. Release* 345, 786–797. doi:10.1016/j.jconrel.2022.03.050

Xia, T., Liu, W., and Yang, L. (2017). A review of gradient stiffness hydrogels used in tissue engineering and regenerative medicine. *J. Biomed. Mater Res. A* 105, 1799–1812. doi:10.1002/jbm.a.36034

Xu, D., Lu, Y.-R., Kou, N., Hu, M.-J., Wang, Q.-S., and Cui, Y.-L. (2020). Intranasal delivery of icariin via a nanogel-thermoresponsive hydrogel compound system to improve its antidepressant-like activity. *Int. J. Pharm.* 586, 119550. doi:10.1016/j.ijpharm.2020.119550

Yang, Y., Wang, K., Gu, X., and Leong, K. W. (2017). Biophysical regulation of cell behavior-cross talk between substrate stiffness and nanotopography. *Eng. (Beijing)* 3, 36–54. doi:10.1016/j.eng.2017.01.014

Yao, M., Chen, Y., Zhang, J., Gao, F., Ma, S., and Guan, F. (2019). Chitosan-based thermosensitive composite hydrogel enhances the therapeutic efficacy of human umbilical cord MSC in TBI rat model. *Mater. Today Chem.* 14, 100192. doi:10.1016/j.mtchem.2019.08.011

Zamproni, L. N., Mundim, M., and Porcionatto, M. A. (2021). Neurorepair and regeneration of the brain: a decade of bioscaffolds and engineered microtissue. *Front. Cell Dev. Biol.* 9, 649891. doi:10.3389/fcell.2021.649891

Zhang, J., Wang, Y., Shu, X., Deng, H., Wu, F., and He, J. (2023a). Magnetic chitosan hydrogel induces neuronal differentiation of neural stem cells by activating RAS-dependent signal cascade. *Carbohydr. Polym.* 314, 120918. doi:10.1016/j.carbpol.2023.120918

Zhang, L., Pang, L., Zhu, S., Ma, J., Li, R., Liu, Y., et al. (2020). Intranasal tetrandrine temperature-sensitive *in situ* hydrogels for the treatment of microwave-induced brain injury. *Int. J. Pharm.* 583, 119384. doi:10.1016/j.ijpharm.2020.119384

Zhang, W., Liu, W., Long, L., He, S., Wang, Z., Liu, Y., et al. (2023b). Responsive multifunctional hydrogels emulating the chronic wounds healing cascade for skin repair. *J. Control Release* 354, 821–834. doi:10.1016/j.jconrel.2023.01.049

Zhang, Y., and Huang, Y. (2020). Rational design of smart hydrogels for biomedical applications. *Front. Chem.* 8, 615665. doi:10.3389/fchem.2020.615665

Zhao, Z., Shen, J., Zhang, L., Wang, L., Xu, H., Han, Y., et al. (2020). Injectable postoperative enzyme-responsive hydrogels for reversing temozolomide resistance and reducing local recurrence after glioma operation. *Biomater. Sci.* 8, 5306–5316. doi:10.1039/d0bm00338g

Zheng, Y., Wu, G., Chen, L., Zhang, Y., Luo, Y., Zheng, Y., et al. (2021). Neuro-regenerative imidazole-functionalized GelMA hydrogel loaded with hAMSC and SDF-1α promote stem cell differentiation and repair focal brain injury. *Bioact. Mater.* 6, 627–637. doi:10.1016/j.bioactmat.2020.08.026

Zhou, Y., Liu, G., and Guo, S. (2022). Advances in ultrasound-responsive hydrogels for biomedical applications. *J. Mater. Chem. B* 10, 3947–3958. doi:10.1039/d2tb00541g

Zhu, W., Zhang, J., Wei, Z., Zhang, B., and Weng, X. (2023). Advances and progress in self-healing hydrogel and its application in regenerative medicine. *Mater. (Basel)* 16, 1215. doi:10.3390/ma16031215

frontiers | Frontiers in Bioengineering and Biotechnology

TYPE Review
PUBLISHED 02 September 2024
DOI 10.3389/fbioe.2024.1469393

OPEN ACCESS

EDITED BY
Donglin Xia,
Nantong University, China

REVIEWED BY
Yuda Zhu,
The Affiliated Hospital of Southwest Medical University, China
Jinyang Li,
Southwest Jiaotong University, China

*CORRESPONDENCE
Tao Wang,
terrywang1126@scu.edu.cn

†These authors have contributed equally to this work

RECEIVED 23 July 2024
ACCEPTED 21 August 2024
PUBLISHED 02 September 2024

CITATION
Zhang Y, Jiang M and Wang T (2024) Reactive oxygen species (ROS)-responsive biomaterials for treating myocardial ischemia-reperfusion injury.
Front. Bioeng. Biotechnol. 12:1469393.
doi: 10.3389/fbioe.2024.1469393

Reactive oxygen species (ROS)-responsive biomaterials for treating myocardial ischemia-reperfusion injury

Ying Zhang[1,2†], Mantang Jiang[1†] and Tao Wang[1,2*]

[1]Natural and Biomimetic Medicine Research Center, Tissue-Orientated Property of Chinese Medicine Key Laboratory of Sichuan Province, West China Hospital, Sichuan University, Chengdu, China, [2]Institute of Integrated Traditional Chinese and Western Medicine, West China Hospital, Sichuan University, Chengdu, China

Myocardial ischemia-reperfusion injury (MIRI) is a critical issue that arises when restoring blood flow after an ischemic event in the heart. Excessive reactive oxygen species (ROS) production during this process exacerbates cellular damage and impairs cardiac function. Recent therapeutic strategies have focused on leveraging the ROS microenvironment to design targeted drug delivery systems. ROS-responsive biomaterials have emerged as promising candidates, offering enhanced therapeutic efficacy with reduced systemic adverse effects. This review examines the mechanisms of ROS overproduction during myocardial ischemia-reperfusion and summarizes significant advancements in ROS-responsive biomaterials for MIRI treatment. We discuss various chemical strategies to impart ROS sensitivity to these materials, emphasizing ROS-induced solubility switches and degradation mechanisms. Additionally, we highlight various ROS-responsive therapeutic platforms, such as nanoparticles and hydrogels, and their unique advantages in drug delivery for MIRI. Preclinical studies demonstrating the efficacy of these materials in mitigating MIRI in animal models are reviewed, alongside their mechanisms of action and potential clinical implications. We also address the challenges and future prospects of translating these state of the art biomaterial-based therapeutics into clinical practice to improve MIRI management and cardiac outcomes. This review will provide valuable insights for researchers and clinicians working on novel therapeutic strategies for MIRI intervention.

KEYWORDS

myocardial ischemia-reperfusion injury, ROS-responsive biomaterials, nanoparticals, hydrogels, biomimetic biomaterials

1 Introduction

Myocardial infarction (MI) remains the leading cause of morbidity and mortality worldwide, underscoring the urgent need for innovative therapeutic strategies (Reed et al., 2017; Laforgia et al., 2022). MI is characterized by the occlusion of coronary arteries, resulting in a deprivation of oxygen and nutrients to the damaged myocardium. Re-establishing blood flow through reperfusion, typically via percutaneous coronary intervention or thrombolysis, is critical for saving the ischemic myocardium (Thygesen et al., 2007; Saito et al., 2023). However, this process induces a series of harmful effects, including oxidative stress caused by a surge in reactive oxygen species (ROS), calcium overload, and a strong inflammatory response, leading to further

myocardial damage, known as myocardial ischemia-reperfusion injury (MIRI) (Yellon and Hausenloy, 2007; Algoet et al., 2023; Liu Y. et al., 2023).

ROS, including superoxide anion ($O_2^{\bullet-}$), hydroxyl radical ($^{\bullet}OH$), and hydrogen peroxide (H_2O_2), are natural byproducts of cellular metabolism, primarily generated in mitochondria during oxidative phosphorylation (Sies et al., 2022). Under normal physiological conditions, ROS are tightly regulated by endogenous antioxidant systems, maintaining redox homeostasis. However, during myocardial I/R, the abrupt reintroduction of oxygen during reperfusion disrupt the balance between ROS production and scavenging, resulting in an uncontrolled burst of ROS from various sources, including the mitochondria, xanthine oxidase, NADPH oxidases, and uncoupled nitric oxide synthase (NOS). This excessive ROS generation triggers a cascade of deleterious events, including lipid peroxidation, protein oxidation, DNA damage, inflammation, and various forms of programmed cell death (e.g., apoptosis, pyroptosis, ferroptosis), ultimately exacerbating myocardial injury and dysfunction (Cadenas, 2018; Dubois-Deruy et al., 2020).

Over the past few decades, significant progress has been made in developing anti-MIRI drugs (Ibanez et al., 2015; Zhou et al., 2021), however, systemic drug administration faces challenges such as poor targeting, limited efficacy, and potential toxic side effects. Recent advancements in nanotechnology and biomaterials have paved the way for creating targeted therapeutic strategies that deliver drugs specifically to ischemia-reperfusion injured myocardium (Luo et al., 2023). The unique ischemia-reperfusion microenvironment (IME), characterized by acidosis, elevated ROS levels, and massive inflammatory cell infiltration, has become a critical target for developing controlled-release strategies for anti-MIRI drugs (Hausenloy and Yellon, 2013; Li and Gao, 2023).

Among the various strategies targeting the IME, ROS-responsive nanomaterials are currently the most advanced and promising. These materials are engineered to specifically detect abnormal ROS levels at the site of injury and to trigger the controlled release of therapeutic agents or modulation of cellular signaling pathways, thereby improving tissue inflammation (Chung et al., 2015; Lee et al., 2018; Xia et al., 2023), impaired angiogenesis (Chen et al., 2021; Zheng et al., 2022a), or fibrosis (Surendran et al., 2020; Gaytan et al., 2023; Zhang J. et al., 2024). Strategies for fabricating ROS-responsive biomaterials encompass a diverse array of approaches, primarily based on ROS-induced solubility switches and degradation mechanisms (Lee S. H. et al., 2013; Xu et al., 2016b). Solubility switching strategies exploit the reversible transformation of the amphiphilic nature of materials towards ROS, thereby achieving controlled release of the encapsulated therapeutic agent. In contrast, the ROS-induced degradation strategy involves incorporating ROS-labile linkages within the polymer backbone, designed to cleave upon exposure to ROS, leading to material degradation and subsequent release of the therapeutic agent. Biomaterials that utilize ROS-induced solubility switching or degradation elements, including polymeric nanoparticles, injectable hydrogels, and biomimetic nanoparticles, loaded with anti-MIRI drugs possessing antioxidant, anti-inflammatory, pro-survival, or pro-angiogenic properties, have become promising targeted therapeutic strategies for MIRI in the past decade (Bae et al., 2016; Ziegler et al., 2019; Li et al., 2020; Li et al., 2021; Hao T. et al., 2022; Hou et al., 2022; Huang et al., 2022; Lan et al., 2022; Li et al., 2022; Weng et al., 2022; Zhang X. et al., 2022). These ROS-responsive nanomedicines have demonstrated their precise targeting and controlled drug release capabilities and achieved enhanced therapeutic effects in MIRI animal models, providing strong support for their future clinical applications.

In this review, we aim to provide a comprehensive overview of the progress in ROS-responsive biomaterials for treating MIRI over the past decade (Figure 1). We summarize the mechanisms underlying ROS overproduction during myocardial I/R, strategies for fabricating ROS-responsive biomaterials, and the current ROS-responsive therapeutic platforms for MIRI intervention. We also discuss the challenges and future prospects of translating these technologies into clinical practice, aiming to improve cardiovascular health and patient outcomes.

2 ROS overproduction during myocardial I/R

The excessive generation of ROS is a pivotal factor in MIRI. This ROS storm triggers a cascade of deleterious events, including mitochondrial dysfunction and lipid peroxidation, leading to cardiomyocyte necrosis and various forms of programmed cell death such as apoptosis, pyroptosis, and ferroptosis (Cadenas, 2018; Gong et al., 2024). Several recent reviews have well elucidated the mechanisms of ROS generation following myocardial I/R and its complex role in MIRI (Cadenas, 2018; Bugger and Pfeil, 2020). Here, we focus on providing a summary of current knowledge about the source and mechanism of ROS overproduction after myocardial I/R from the perspective of different cell types in damaged myocardium, including cardiomyocytes and non-cardiomyocytes (e.g., inflammatory cells, endothelial cells, and platelets). (Figure 2).

2.1 ROS generation in cardiomyocytes

2.1.1 Mitochondrial electron transport chain (ETC)

Mitochondria are the primary sources of ROS production in damaged cardiomyocytes during myocardial I/R (Bugger and Pfeil, 2020). The ETC complexes, particularly complexes I and III, are key sites where electron leakage occurs, leading to the formation of superoxide anion ($O_2^{\bullet-}$). During ischemia, the activity of complex I is inhibited due to oxygen depletion, causing electron accumulation. Upon reperfusion, these electrons react with the reintroduced oxygen, generating a significant amount of $O_2^{\bullet-}$ through reverse electron transport (RET) (Paradies et al., 2004; Chen et al., 2008; Vinogradov and Grivennikova, 2016). This process is exacerbated by the accumulation of succinate during ischemia, which is rapidly oxidized upon reperfusion, driving RET and enhancing ROS production (Chouchani et al., 2014). Complex II also contributes to ROS generation, though to a lesser extent than complexes I and III (Chouchani et al., 2014; Chouchani et al., 2016). Additionally, Fe^{2+} released by the ruptured mitochondria reacts with intracellular H_2O_2, triggering the Fenton reaction and generating the highly strong oxidant •OH (Gordan et al., 2018).

2.1.2 NADPH oxidase (NOX)

NADPH oxidases are another critical source of ROS in both cardiomyocytes and non-cardiomyocytes (Kahles and Brandes,

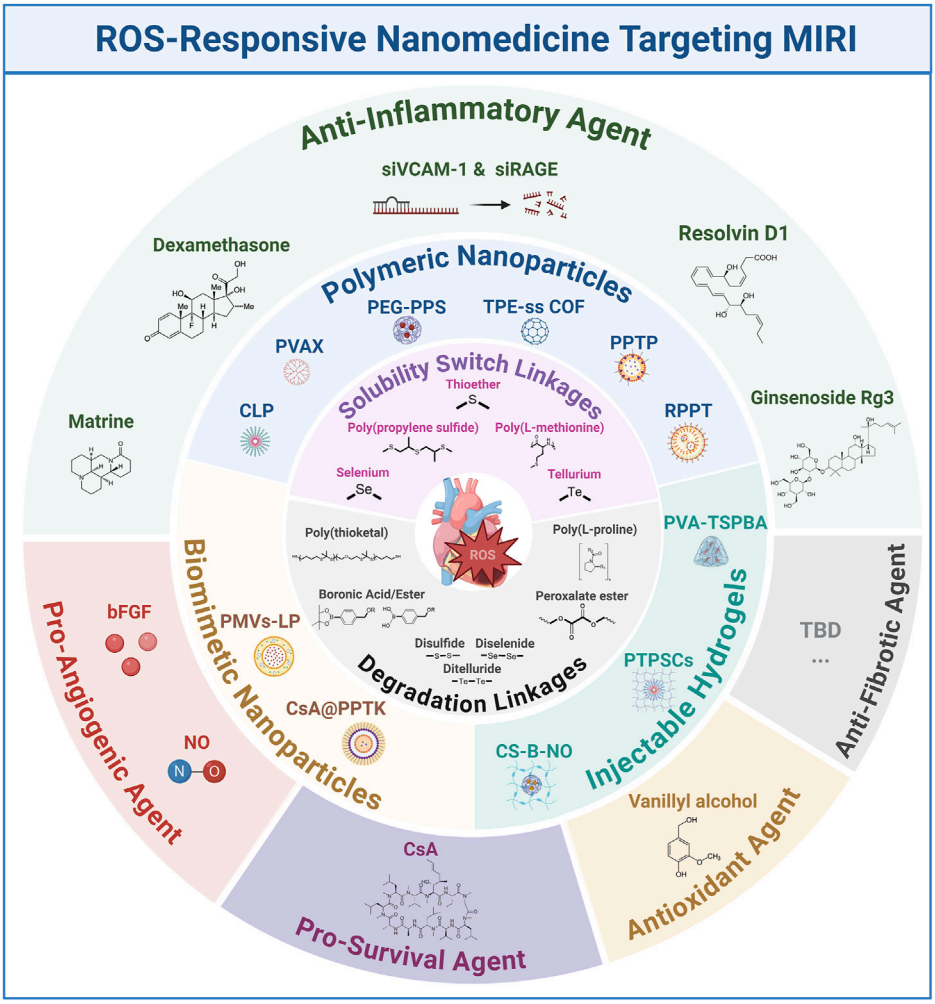

FIGURE 1
Schematic representation of ROS-responsive nanomedicines targeting MIRI. bFGF: basic fibroblast growth factor; COF: covalent organic framework; CLP: an amphiphilic copolymer was designed and synthesized by sequentially conjugating luminol and PEG with Ce6; CS-B-NO: chitosan modified by boronate-protected diazeniumdiolate; LP: liposome; NO: nitric oxide; PPTP: PGE_2-PEG modified tellurium-crosslinked polyethyleneimine; PEG: poly (ethylene glycol); PPS: poly (propylene sulfide); PMVs: platelet mem brane vesicles; PVA: poly (vinyl alcohol); PTPSCs: PLGA-TK-PEG-SS31; TBD: to be determined; TPE: Tetraphenylethene; TSPBA: N1-(4-boronobenzyl)-N3-(4-boronophenyl)-N1,N1,N3,N3-tetramethylpropane-1,3-diaminium.

2013). NOX enzymes, particularly NOX2 and NOX4, are upregulated in response to I/R injury (Braunersreuther et al., 2013). These enzymes transfer electrons from NADPH to oxygen, producing $O_2^{\bullet-}$. NOX-derived ROS are implicated in various pathophysiological processes, including endothelial dysfunction and inflammation (Paravicini and Touyz, 2008). Inhibition of NOX activity has been shown to reduce myocardial infarct size and ROS levels (Thirunavukkarasu et al., 2012; Braunersreuther et al., 2013), underscoring its significance in I/R injury.

2.1.3 Xanthine oxidase (XO)

Xanthine oxidase is a key enzyme in purine metabolism that generates ROS as a byproduct in cardiomyocytes (Boueiz et al., 2008). During ischemia, xanthine dehydrogenase is converted to XO, which then produces $O_2^{\bullet-}$ and H_2O_2 during reperfusion. XO-derived ROS contribute significantly to oxidative stress and tissue damage in MIRI (Madesh and Hajnoczky, 2001; Hool, 2009). The use of XO inhibitors, such as allopurinol, has demonstrated cardioprotective effects by reducing ROS production and subsequent cellular injury (Grimaldi-Bensouda et al., 2015).

2.2 ROS generation in endothelial cells (ECs)

ECs are pivotal in the pathophysiology of MIRI and other cardiovascular diseases, largely due to their role as major sources of ROS (Yang et al., 2016; Chen et al., 2019; Haybar et al., 2019). Among the key mechanisms regulated by ECs is the synthesis of nitric oxide (NO), a vasodilator with protective cardiovascular effects, mediated by endothelial nitric oxide synthase (eNOS) (Mount et al., 2007). Under physiological conditions, eNOS efficiently produces NO, which not only promotes vascular relaxation but also exerts antioxidant effects. However, during

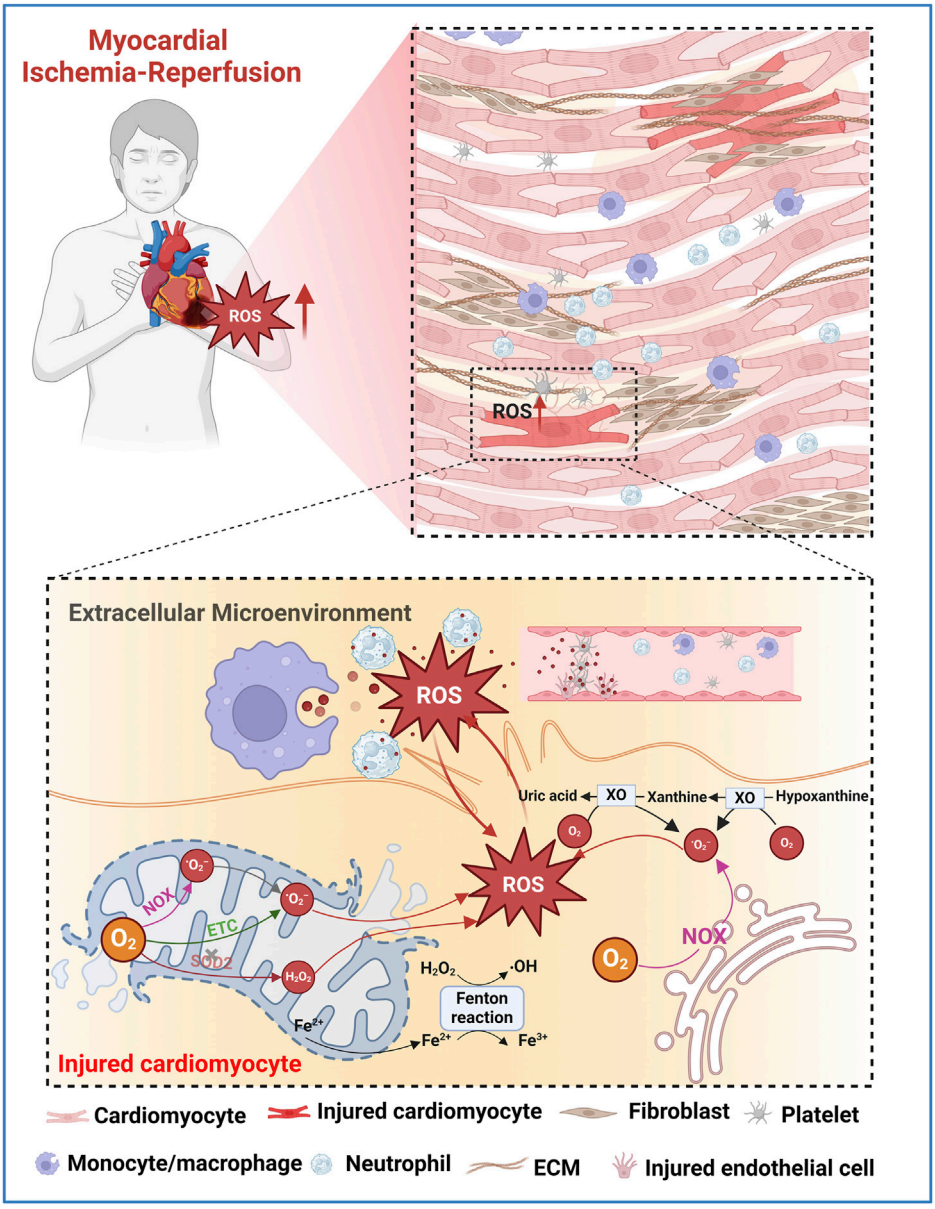

FIGURE 2
Schematic illustration of potential ROS sources in injured myocardium during MIRI. $O_2^{\bullet-}$ are primarily produced in the mitochondrial ETC. Fe^{2+} released by the ruptured mitochondria generates ●OH via Fenton reaction. Mitochondrial NOX also generates $O_2^{\bullet-}$. Damaged antioxidant systems, such as SOD2, fail to adequately remove $O_2^{\bullet-}$ or H_2O_2 leading to the accumulation of ROS. In the extramitochondrial space, NOX and XO play major roles in ROS production during I/R. Excessive ROS causes oxidative damage to lipids, proteins, and nucleic acids, leading to cell death and exacerbating I/R injury. The increased oxidative stress in the extracellular microenvironment of the injured myocardium is mainly attributed to the contents released after the rupture of the plasma membrane of damaged cardiomyocytes, as well as the ROS released by neutrophils, macrophages, endothelial cells, and activated platelets.

oxidative stress, the cofactor tetrahydrobiopterin (BH4), essential for eNOS function, undergoes oxidation, leading to the uncoupling of eNOS. This uncoupling diverts eNOS activity from NO production to the generation of $O_2^{\bullet-}$, thereby increasing ROS levels and exacerbating endothelial dysfunction (Dumitrescu et al., 2007; Alkaitis and Crabtree, 2012). Strategies to recouple eNOS, such as supplementation with BH4 or its precursors, have shown promise in reducing ROS production and ameliorating cardiac damage (Antoniades et al., 2006). Despite the antioxidant role of NO under normal conditions, its interaction with $O_2^{\bullet-}$ can result in the formation of peroxynitrite ($ONOO^-$), a harmful oxidant (Radi, 2013). The presence of $ONOO^-$ further intensifies oxidative stress, contributing to greater myocardial damage during IR injury (Liu et al., 2005; Yu et al., 2018).

2.3 ROS generation in inflammatory cells

Inflammatory cells, such as neutrophils and macrophages, are recruited to the site of injury during reperfusion. These cells produce

TABLE 1 ROS-responsive elements.

ROS-responsive mechanism	ROS-responsive elements		Chemical structure and oxidation	Sensitivity	References
Solubility Switch	Sulfur-Based linkages	Thioether	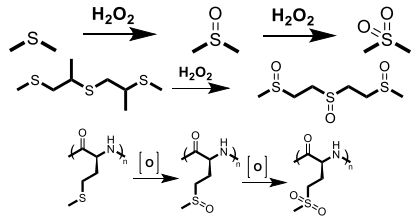	H_2O_2: 3.3 vol%	Gruhlke and Slusarenko (2012), Xu et al. (2016a), Wang et al. (2022), Yue et al. (2023), Yang et al. (2024)
		Poly (propylene sulfide)		H_2O_2 : 100 μM	
		Poly (L-methionine)		H_2O_2 : 1 mM	
	Selenium-linkages		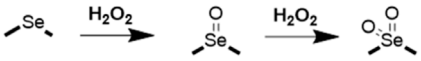	H_2O_2 : 0.1% v/v	Ma et al. (2010), Tan et al. (2012), Xu et al. (2013)
	Tellurium- linkages		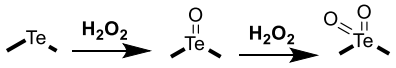	H_2O_2 : 100 μM	Cao et al. (2015), Wang et al. (2015)
Degradation	Phenylboronic Acid and Ester		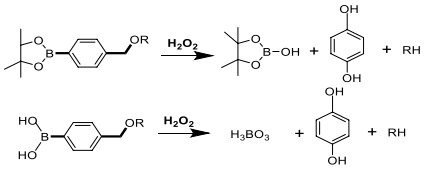	H_2O_2 : 50 μM	Sun et al. (2013), Stubelius et al. (2019), Han and Domaille (2022)
	Poly (thioketal)		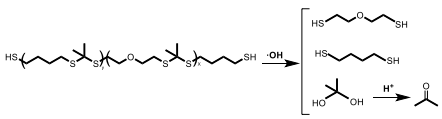	H_2O_2 : 0.2% v/v	Liu and Thayumanavan (2020), Wang et al. (2020), Xie et al. (2022), Yao et al. (2022b), Shen et al. (2024)
	Peroxalate ester		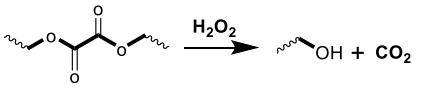	H_2O_2: >50 nM	Romanyuk et al. (2017)
	Poly (L-proline)		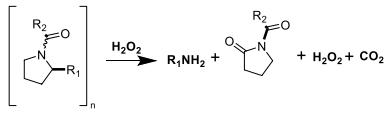	H_2O_2 : 5 mM	Yu et al. (2011), Lee et al. (2014), Gupta et al. (2015)
	Disulfide, diselenide, and ditelluride bond		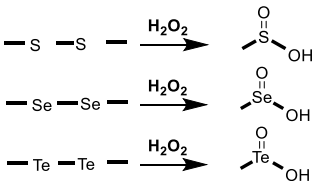	H_2O_2: <20 μM	Hou et al. (2022), Lan et al. (2022), Cao et al. (2024), Kang et al. (2024)

large amounts of ROS via their NADPH oxidase systems in response to inflammatory stimuli (Chakraborti et al., 2000). Neutrophil-derived ROS contribute to tissue damage by exacerbating oxidative stress and promoting further recruitment of inflammatory cells (Jordan et al., 1999). The interaction between inflammatory cells and damaged endothelium also creates a vicious cycle of ROS production and cellular injury (Knock, 2019).

2.4 ROS generation in activated platelets

Platelets also contribute to ROS production after myocardial I/R. During I/R, platelets become activated and release ROS through their mitochondrial pathways and NADPH oxidase systems (Begonja et al., 2005). Platelet-derived ROS also plays a significant role in amplifying the inflammatory response and promoting thrombus formation, which can further obstruct blood flow and exacerbate myocardial injury (Takaya et al., 2005; Xu et al., 2006). Targeting platelet activation has shown potential in reducing the extent of myocardial damage and improving reperfusion outcomes (Schanze et al., 2023).

Collectively, the overproduction of ROS during myocardial I/R injury arises from various cellular sources, including cardiomyocytes, endothelial cells, inflammatory cells, and platelets. Functional impairment or activity changes of mitochondrial ETC, NADPH oxidase, XO and uncoupled eNOS during I/R are the core regulatory mechanisms leading to excessive ROS generation in different cell types in the injured myocardium. Understanding these sources and their mechanisms provides critical insights into the pathophysiology of MIRI. Future efforts to design

ROS-responsive biomaterials should focus on targeting the specific features of excessive ROS production in the myocardial IME, with an emphasis on developing innovative biomaterials with precise cell type-specific and subcellular organelle-targeting (e.g, mitochondria) properties.

3 Strategies for ROS-responsive biomaterials fabrication

The emergence and widespread application of ROS-responsive biomaterials have greatly changed the limitations of current anti-MIRI drug interventions. These advanced materials are designed to engage proactively with the pathophysiological oxidative milieu, offering a targeted and controlled release of therapeutic agents. This section delves into the mainstream strategies for the fabrication of ROS-responsive biomaterials, focusing on ROS-induced solubility switching and degradation mechanisms (Table 1).

3.1 ROS-induced solubility switch

The principal strategy for fabricating ROS-responsive biomaterials involves the incorporation of functional groups that undergo significant solubility changes in response to ROS. Under oxidative conditions, these groups typically transform from hydrophobic to hydrophilic states, enhancing water solubility and facilitating the release of encapsulated drugs.

3.1.1 Sulfur-containing polymers

Sulfur-containing polymers are among the earliest developed ROS-responsive systems (Yue et al., 2023). Due to sulfur's diverse oxidation states, ranging from −2 to +6, these materials can undergo significant changes upon exposure to ROS. When oxidized, sulfide-containing polymers form sulfoxides or sulfones, increasing their hydrophilicity. This change leads to polymer swelling, disassembly, and eventual drug release (Gruhlke and Slusarenko, 2012). Poly (propylene sulfide) (PPS) is the most fundamental used sulfur-containing ROS-responsive functional group. PPS-based nanoparticles, stable in water, degrade rapidly upon exposure to H_2O_2 but not to superoxide, releasing encapsulated drugs effectively (Shofolawe-Bakare et al., 2022; Bezold et al., 2023). Thioether is another well-studied ROS-responsive linker that undergoes a hydrophobic to hydrophilic transition upon oxidation, which makes thioether-containing polymers widely used in the precise delivery and release of drugs in response to oxidative microenvironment-related diseases (Wang et al., 2022). Additionally, poly (L-methionine), an amino acid-based polymer, exhibits ROS-responsive behavior through the oxidation of its sulfur-containing methionine residues to sulfoxides and sulfones. This oxidation alters the polymer's hydrophobicity, leading to structural changes and the release of therapeutic agents (Xu et al., 2016a; Yang et al., 2024). Given the inherent advantages of this amino acid-based polymer, such as biocompatibility and biodegradability, it may become a key material in the design of next-generation therapeutics for the treatment of ROS-related diseases, such as cancer and chronic liver disease (Yoo et al., 2017; Hao Y. M. et al., 2022).

3.1.2 Selenium-containing polymers

Selenium-based materials exhibit a more pronounced response to ROS compared to sulfur-based ones due to selenium's lower electronegativity and larger atomic radius (Xu et al., 2013). These materials can undergo a solubility switch due to the oxidation of selenium moieties to selenoxides or selenones upon exposure to low concentrations of H_2O_2 (0.01% v/v) (Ma et al., 2010), leading to the release of encapsulated therapeutic agents. The development of selenium-containing block copolymers, such as PEG-PUSe-PEG, has shown promise in drug delivery applications where the hydrophobic polyurethane block containing selenides can self-assemble into micelles that disassemble upon ROS exposure (Tan et al., 2012). In addition, the biological significance of selenium, particularly its role in enhancing the catalytic activity of glutathione peroxidase (GPx), makes it an ideal candidate for the design of ROS-responsive materials (Kieliszek and Blazejak, 2013).

3.1.3 Tellurium-containing polymers

Tellurium, positioned below selenium in the periodic table, offers even higher sensitivity to ROS due to its chemical properties, making tellurium-containing polymers ultra-responsive and suitable for applications in pathological microenvironment with relative low levels of ROS (Cao et al., 2015; Wang et al., 2015). Similar to selenium-based delivery systems, tellurium-containing biomaterials exhibit pronounced solubility changes under oxidative conditions (Wang et al., 2015), ensuring timely and controlled drug release. Their potential in therapeutic applications, particularly in inflammation and tumor progression sites (Lu et al., 2017; Dominguez-Alvarez et al., 2022), is being explored, although research in this area remains limited.

3.2 ROS-induced degradation

Another critical strategy involves the design of biomaterials that degrade upon exposure to ROS through the cleavage of specific chemical bonds within the polymer backbone, thereby releasing the therapeutic agents in a controlled manner. This degradation mechanism is pivotal for the functionality of ROS-responsive biomaterials in targeted drug delivery and tissue engineering applications.

3.2.1 Phenylboronic acid and ester-containing polymers

Phenylboronic acid and its ester derivatives are exceptionally sensitive to ROS, undergoing rapid oxidative degradation due to the cleavage of the boron-carbon bond (Han and Domaille, 2022). Under oxidizing conditions, the linkage between boronic acids/esters and the material or drug molecules of interest becomes oxidized with the insertion of oxygen (Stubelius et al., 2019). Notably, the reaction kinetics are significantly influenced by the nucleophilicity of the boron center, with nucleophilic boronic esters reacting more quickly than their corresponding acids (Sun et al., 2013). Moreover, recent studies have shown that boronic esters with ether bonds exhibit excellent degradation kinetics at biologically relevant concentrations of H_2O_2, around 50 μM (Jourden et al.,

2011). This sensitivity makes boronic ester-containing polymers some of the most ROS-responsive materials available, particularly suitable for applications requiring high sensitivity to ROS and precise control over the release of therapeutic agents.

Interestingly, most of currently reported anti-MIRI hydrogel drug delivery systems that employ ROS-responsive degradation mechanisms incorporate boronic acid or boronic ester as their core ROS-responsive functional groups (detailed in Section 4) (Li et al., 2021; Hao T. et al., 2022; Zhang X. et al., 2022). This preference is likely due to their proven effectiveness in maintaining hydrogel stability while allowing for precisely controlled degradation and drug release in response to oxidative stress.

3.2.2 Poly (thioketal) (TK) polymers

Similar to boronic esters, thioketal linkages are destabilized in the presence of $O_2^{\bullet-}$and H_2O_2, leading to the oxidation into ketones and organic thiols or disulfides (Liu and Thayumanavan, 2020). This degradation mechanism has been widely used to develop ROS-responsive materials containing thioketals for targeted drug release therapy in diseases characterized by high ROS microenvironments, such as enteritis (Shen et al., 2024), wound repair (Martin et al., 2014), and ischemic heart disease (Xie et al., 2022; Yao Y. et al., 2022).

3.2.3 Peroxalate ester-containing polymers

Peroxalate esters are another class of ROS-responsive polymers that degrade in the presence of relative low H_2O_2 (>50 nM), producing carbon dioxide and other byproducts, with the potential to generate chemiluminescence (Romanyuk et al., 2017; Hao Y. M. et al., 2022). This characteristic makes them particularly valuable in applications that benefit from real-time monitoring of ROS levels, as the chemiluminescence can serve as an optical signal for the presence of oxidative stress.

In the context of MIRI, peroxalate ester-containing polymers have shown potential in both diagnostic and therapeutic roles. The generated luminescent signals can help in the detection of ROS bursts during reperfusion, while the degradation of the polymer allows for the controlled release of therapeutic agents precisely when ROS levels are elevated (Lee D. et al., 2013). Recent advancements in the design of peroxalate ester-based hydrogels have also demonstrated their capability to act as both ROS scavengers and drug delivery platforms, thereby providing a dual function in mitigating oxidative damage and delivering cardioprotective drugs (Bae et al., 2016).

3.2.4 Poly (L-proline)-containing polymers

Poly (L-proline) is another naturally occurring amino acid-based polymer that has shown particularly sensitive to ROS due to the presence of pyrrolidine rings (Tian et al., 2021). Under oxidative stress, the proline residue undergoes oxidation, leading to the cleavage of the polymer backbone (Amici et al., 1989). This degradation results in the release of entrapped drugs or therapeutic agents, making poly (L-proline) a useful material in drug delivery systems, particularly for applications where controlled degradation is essential (Dai et al., 2023). Poly (L-proline) has been widely used in the fabrication of scaffolds for tissue engineering applications where the degradation rate can be matched to the tissue regeneration process (Yu et al., 2011; Lee et al., 2014). The ROS-responsiveness of these scaffolds can be further enhanced by incorporating additional ROS-sensitive elements such as boronic esters or thioketal groups.

3.2.5 Disulfide, diselenide, and ditelluride bond-bontaining polymers

Compared with the integration of individual chalcogen elements (sulfur, selenium, tellurium) to impart solubility transition properties to nanomaterials, recent studies have increasingly favored the use of disulfide, diselenide, and ditelluride bonds as ROS-responsive degradation elements (Yuan et al., 2021; Hou et al., 2022; Lan et al., 2022; Weng et al., 2022; Qiu et al., 2024). These bonds spontaneously cleave under oxidative conditions, leading to the degradation of nanomaterials and enabling controlled drug release.

Disulfide bond (-S-S-) is widely used due to their stability under normal conditions and their ability to break in the presence of ROS, such as H_2O_2 (as low as 20 μM), making them ideal for delivery systems for tumors and diseases related to ischemia-reperfusion injury (Kang et al., 2024; Qiu et al., 2024). Diselenide bond (-Se-Se-), with lower bond dissociation energy than disulfides, responds more quickly to ROS and have been explored in neurodegenerative diseases and MIRI (Yuan et al., 2021; Weng et al., 2022). Although less studied, the ditellurium bond (-Te-Te-) is the most sensitive to ROS and can respond rapidly, and has recently been increasingly studied for its application in nanomaterial design to alleviate diseases such as MIRI where excessive ROS production is present (Hou et al., 2022; Lan et al., 2022).

4 ROS-responsive therapeutic platforms for MIRI intervention

In recent decades, ROS-responsive functional groups have been extensively integrated into various biomaterials, such as polymer nanoparticles, hydrogels, patches, and biomimetic materials (Zhang et al., 2015; Xu et al., 2016a; Chakraborty et al., 2023). These advancements enable targeted and controlled drug release at sites with elevated ROS levels. Given the excessive ROS production in damaged myocardium following ischemia-reperfusion injury (Cadenas, 2018), recent developments in nanomedicine have increasingly utilized these ROS-responsive elements to achieve precise, targeted delivery of cardioprotective drugs with anti-inflammatory (Li et al., 2020; Hou et al., 2022; Huang et al., 2022; Lan et al., 2022; Weng et al., 2022), antioxidant (Bae et al., 2016), pro-survival (Li et al., 2022; Zhang X. et al., 2022), or pro-angiogenic properties (Li et al., 2021; Hao T. et al., 2022). By responding to ROS stimuli, these drugs can be released specifically at the site of myocardial injury, enhancing therapeutic efficacy while minimizing side effects.

Although several recent reviews have comprehensively explored the landscape of ROS-related nanoplatforms for alleviating MIRI, their main focus is on ROS-scavenging nanozymes and nanomaterials loaded with antioxidant drugs (Zhang Z. et al., 2022; Li et al., 2023). In contrast, here we focus on the application of various ROS-responsive biomaterials in alleviating MIRI in the past decade. Additionally, we systematically summarize the preferred ROS-responsive functional groups used in these

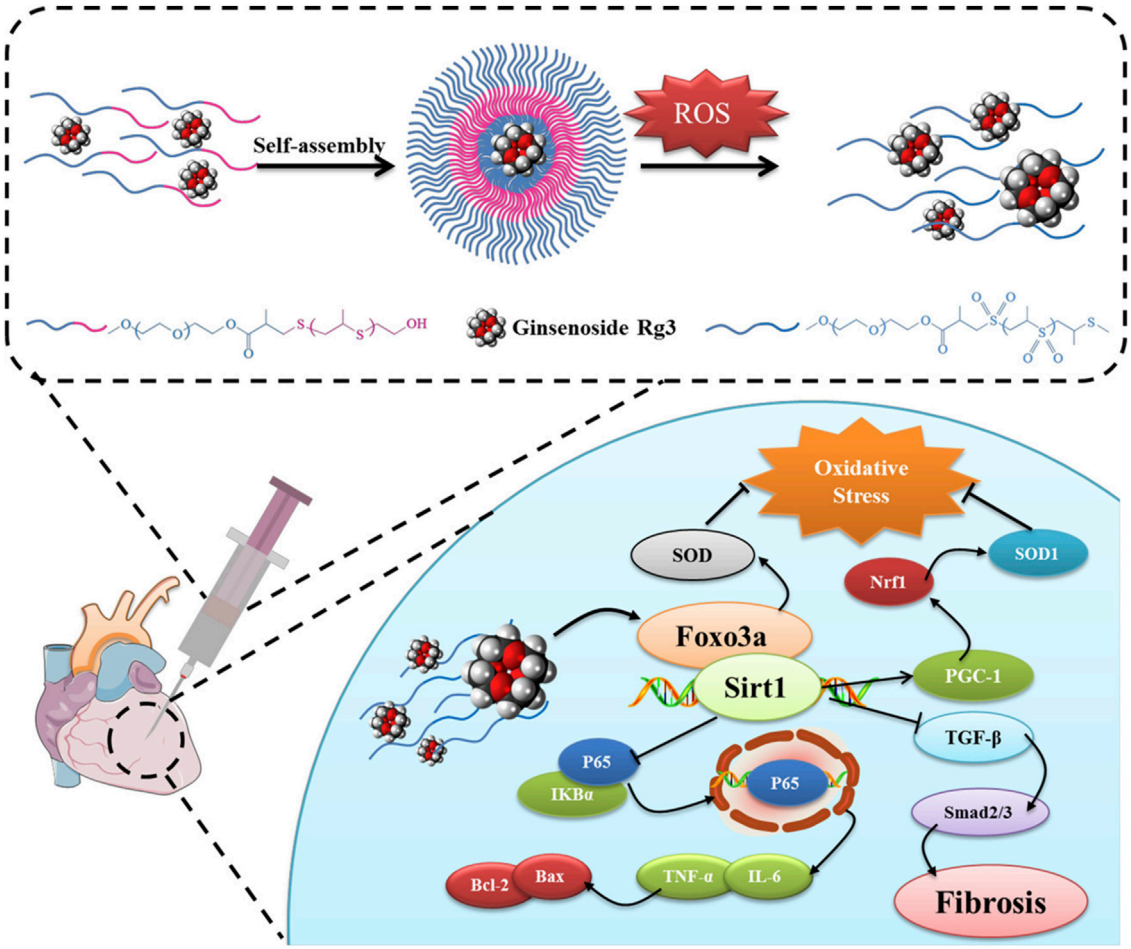

FIGURE 3
ROS-responsive polymeric nanoparticles were created through the self-assembly of diblock copolymers of poly (ethylene glycol) (PEG) and poly (propylene sulfide) (PPS) and used to encapsulate and deliver Rg3 to sites of MIRI. Upon intramyocardial injection, the Rg3-loaded PEG-b-PPS nanoparticles responded to ROS, releasing Rg3, which then mitigated MIRI by interacting with FoxO3a, exerting anti-oxidative, anti-inflammatory, and anti-fibrotic effects. Reproduced with permission (Li et al., 2020). Copyright 2019, Elsevier.

biomaterials and highlight the cardioprotective properties of the encapsulated drugs.

4.1 Polymeric nanoparticles

Biocompatible and versatile polymers such as poly (lactide-co-glycolide) (PLGA), poly (ethylene glycol) (PEG), and polyethylenimine (PEI) are commonly used to create multifunctional drug-loaded nanoparticles (Sah et al., 2013). To achieve ROS-responsive drug release, these nanoparticles often incorporate ROS-sensitive functional groups as linkers either between polymeric backbone chains or between the polymer and the drug molecule. Upon exposure to elevated ROS levels, these linkers undergo degradation or solubility changes, triggering the controlled release of the encapsulated drugs (Xu et al., 2016b). Currently, sulfide and tellurium moieties are particularly prevalent as ROS-responsive components in polymeric nanoparticles designed to selectively respond to the oxidative stress in the injured myocardium.

4.1.1 Sulfide-based linkages

Li and colleagues have developed a ROS-responsive polymeric nanoparticle synthesized from diblock copolymers of PEG and PPS for the delivery of ginsenoside Rg3, a natural product with potent antioxidant properties, to mitigate MIRI (Li et al., 2020). Upon encountering ROS, the sulfide linkages within the PPS undergoes oxidative conversion from a hydrophobe to a hydrophile, releasing Rg3 specifically at the site of injury. In a rat model of MIRI, the intramyocardial injection of these nanoparticles demonstrated improved cardiac function and reduced infarct size (Figure 3). The therapeutic action of Rg3 was found to be mediated through activating FoxO3a, a protein involved in oxidative stress regulation (Link, 2019).

Distinct from sulfide-based ROS-responsive solubility transitions, Huang et al. developed a biodegradable, redox-responsive covalent organic framework (COF) nanocarrier integrating tetraphenylethene (TPE) and disulfide moieties (ss) for prolonged MIRI therapy (Huang et al., 2022). The TPE-ss COF system demonstrated exceptional redox-responsiveness, degrading efficiently in the presence of H_2O_2 and facilitating the

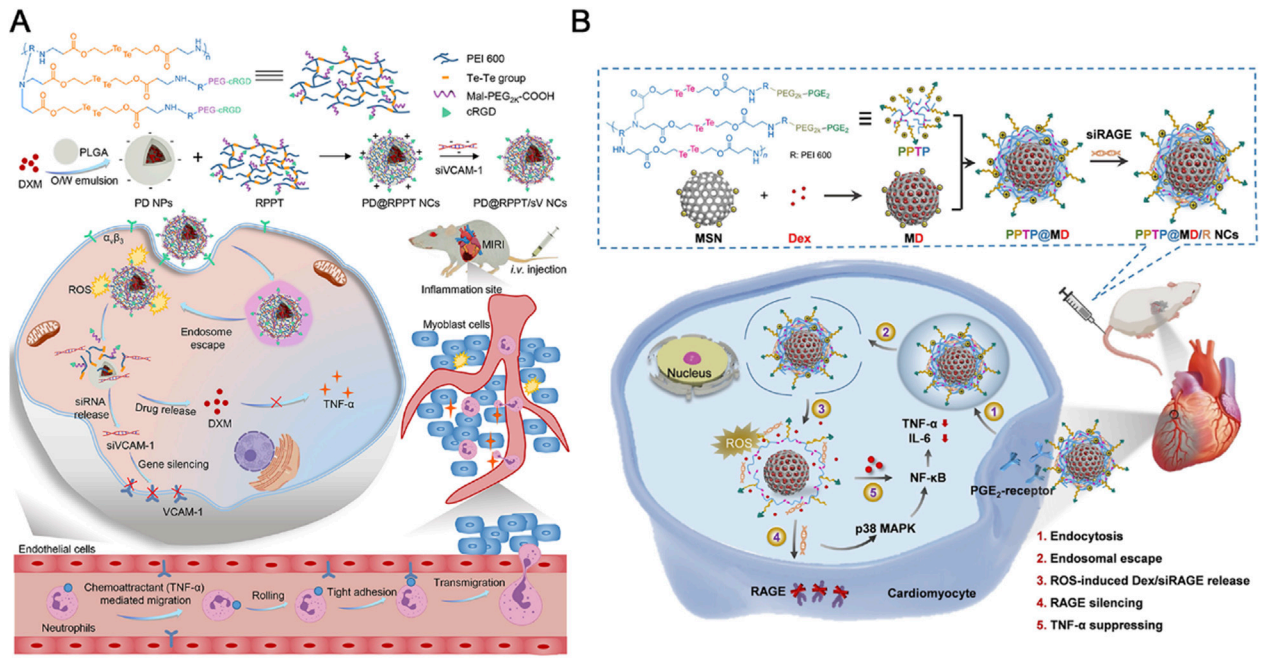

FIGURE 4
(A) The endothelial cell-targeting, ROS-ultrasensitive NCs for co-delivery of siVCAM-1 and DXM aim to treat MIRI inflammation. The ROS-cleavable RPPT, containing ditellurium, was designed to enclose DXM-loaded PLGA NPs and siVCAM-1. After i. v. injection into rats with MIRI, RPPT@siVCAM-1 NCs efficiently targeted inflamed endothelial cells by binding to over-expressed αvβ3 receptors. In the ROS-rich cytoplasm, RPPT degraded, releasing siVCAM-1, enhancing VCAM-1 silencing. This reduced neutrophil recruitment to the injured myocardium, significantly improving anti-inflammatory efficacy and myocardial function recovery. Reproduced with permission (Hou et al., 2022). Copyright 2022, Elsevier. **(B)** Cardiomyocyte-targeted nanotherapeutics for ROS-sensitive co-delivery of siRAGE and Dex were developed. Dex-loaded MSNs, coated with PPTP (a ditellurium-containing polycation), complexed with siRAGE and gated the MSNs to prevent Dex pre-leakage. After systemic injection into myocardial IR-injured rats, the nanotherapeutics entered inflamed cardiomyocytes via PGE2 recognition of over-expressed EP receptors. Intracellular ROS degraded PPTP, releasing siRAGE and Dex to silence RAGE and manage myocardial inflammation. Reproduced with permission (Lan et al., 2022). Copyright 2022, Tsinghua University Press.

controlled release of therapeutic agent matrine, a natural quinolizidine alkaloid that protects cells from ischemia-reperfusion injury by attenuating c-Jun N-terminal kinase (JNK) signaling. In rat models, intravenous administration of TPE-ss COF@Matrine markedly reduced myocardial infarction area, enhanced cardiac function, and alleviated myocardial fibrosis and cardiomyocyte apoptosis. Additionally, the nanocarrier exhibited prolonged retention in cardiac tissue, enabling sustained drug delivery.

4.1.2 Ditellurium linkages

Tellurium's superior responsiveness to ROS makes it a valuable component in polymeric nanoparticle design, facilitating the controlled delivery of encapsulated drugs by regulating material's solubility changes under oxidative conditions (Cao et al., 2015). For instance, Hou and colleagues have engineered an endothelial cell-targeting and ROS-ultrasensitive nanocomplex system for the co-delivery of dexamethasone (DXM) and VCAM-1 siRNA (siVCAM-1) to treat MIRI (Hou et al., 2022). The nanocomplexes, termed RPPT, were synthesized by crosslinking PEI with ditellurium and subsequently modified with PEG and the endothelial cell-targeting peptide cRGD (Figure 4A). Upon systemic administration in a rat model of MIRI, the cRGD-modified nanocomplexes efficiently targeted and entered the inflamed endothelial cells located in the injured myocardium. There, RPPT was sensitively degraded by overproduced ROS, triggering the release of intracellular siVCAM-1 and DXM, thereby effectively abolishing the expression of the neutrophil recruiter VCAM-1 and inhibiting the production of proinflammatory factors such as TNF-α. The combined action of DXM and siVCAM-1 cooperatively inhibited both migration and adhesion of neutrophils, effectively mitigating the inflammatory response and reducing MIRI.

Interestingly, the same research team used a similar design strategy to create an anti-inflammatory nanocomplex that specifically targets inflamed cardiomyocytes to combat MIRI (Lan et al., 2022). This ROS-responsive nanocomplex was synthesized by conjugating PEGylated prostaglandin E2 (PGE_2-PEG) with ditellurium-crosslinked polyethyleneimine (PEI), which was then coated with DXM and loaded with receptor for advanced glycation end-products (RAGE) siRNA (siRAGE) onto mesoporous silica nanoparticles (MSNs) (Figure 4B). The resulting nanocomplex exhibited high stability in serum, preventing premature degradation of siRNA and enabling efficient ROS-responsive release of siRAGE, achieving a 72% RAGE silencing efficiency, along with the delivery of DXM within inflamed cardiomyocytes. When administered intravenously to MIRI rats, this nanocomplex significantly reduced myocardial inflammation, leading to substantial improvements in myocardial function and reduced fibrosis.

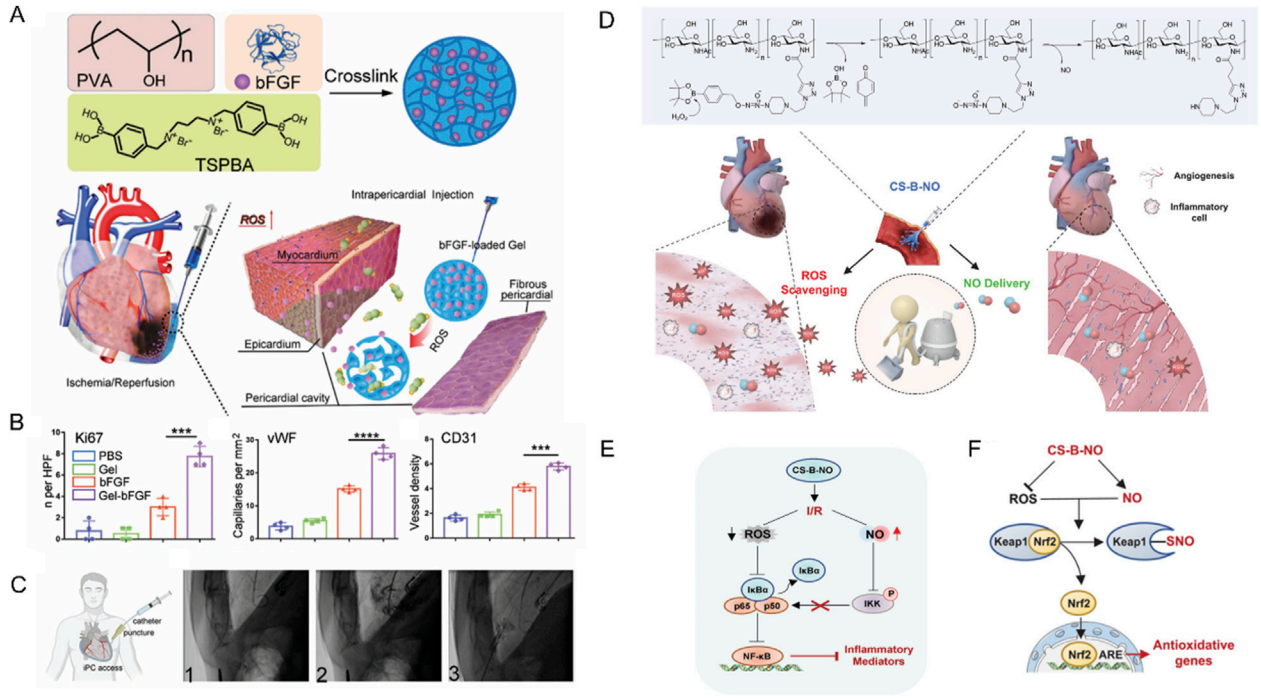

FIGURE 5
(A) Schematic illustration of Gel-bFGF fabrication and overall strategy. **(B)** Quantitative data corresponding to ki67, vWF CD 31 staining showed that Gel-bFGF injection promoted angiomyogenesis. **(C)** A schematic illustrating minimally invasive iPC access in human patients alongside fluoroscopy images from a patient who underwent a LARIAT procedure. Reproduced with permission (Li et al., 2021). Copyright 2021, Wiley. **(D)** Schematic illustration of the treatment of I/R heart injury by CS-B-NO. **(E)** Schematic illustration summarizing the mechanism of CS-B-NO hydrogel on inhibiting the NF-κB signaling pathway after I/R injury. **(F)** Schematic illustration summarizing the mechanism of CS-B-NO hydrogel on activation of the Nrf2 pathway agains oxidative stress via enhancing Keap1 S-nitrosylation. Reproduced with permission (Hao T. et al., 2022). Copyright 2022, Wiley.

4.1.3 Others

In addition to the commonly used chalcogen compounds mentioned above, peroxalate ester linkages with H_2O_2 sensitivity and scavenging capabilities have been utilized to develop ROS-responsive nanoparticles for treating MIRI (Bae et al., 2016). Specifically, Bae and colleagues designed H_2O_2-responsive antioxidant polymer nanoparticles, known as PVAX, by incorporating peroxalate ester linkages with the naturally occurring antioxidant compound vanillyl alcohol (VA) in their backbone. These nanoparticles were synthesized using an emulsion/solvent evaporation method. The PVAX polymer rapidly degraded at sites of ROS overproduction, demonstrating superior therapeutic effects by reducing myocardial infarction size and apoptosis through its potent antioxidant properties.

Moreover, with the breakthrough development of fluorescent nanoprobes in the field of precise disease diagnosis, there have been continuous studies in recent years to design environmentally responsive fluorescent nanoprobes to respond to specific stimuli (such as ROS) to achieve simultaneous high-contrast imaging and targeted treatment of lesion areas (Shen et al., 2021; Xu et al., 2022; Liu J. et al., 2023; Sun et al., 2023). For example, in the study of Ziegler et al., a self-assembled fluorescent nanoprobe was developed for imaging and therapy of MIRI. This nanoprobe is composed of an amphiphilic copolymer that incorporates a hydrophilic chain of PEG and hydrophobic components of luminol-conjugated chlorin e6 (Ce6) (Ziegler et al., 2019). The unique design allows the nanoprobe to self-assemble into nanoparticles that can specifically target areas of injured myocardium due to the local increase in ROS. The nanoprobe demonstrated high specificity for the ischemic/reperfused myocardium with fluorescence signals up to 24 h post reperfusion in a mouse model of myocardial I/R. Moreover, this study further discusses the broader implications of using ROS-responsive nanoprobe for targeted drug delivery in other ROS-associated conditions such as stroke, renal infarction, and inflammatory diseases. This dual functionality-imaging and therapy-makes fluorescent nanoprobes an attractive platform for the development of theranostics, which combine diagnostics with therapy.

4.2 Injectable hydrogels

Hydrogels are high molecular weight polymer materials with a three-dimensional cross-linked network structure, known for their exceptional water absorption and swelling properties, making them excellent drug delivery carriers (Hamidi et al., 2008). Injectable hydrogels, in particular, have emerged as a versatile platform in nanomedicine, offering several advantages in drug delivery and tissue engineering (Bae et al., 2013). They can facilitate local treatment through minimally invasive administration, reducing systemic side effects and improving patient compliance. These hydrogels can be engineered to respond to specific microenvironmental triggers, such as pH, temperature, and oxidative stress, allowing for precise control of drug release and enhancing therapeutic efficacy (Abdollahiyan et al., 2020).

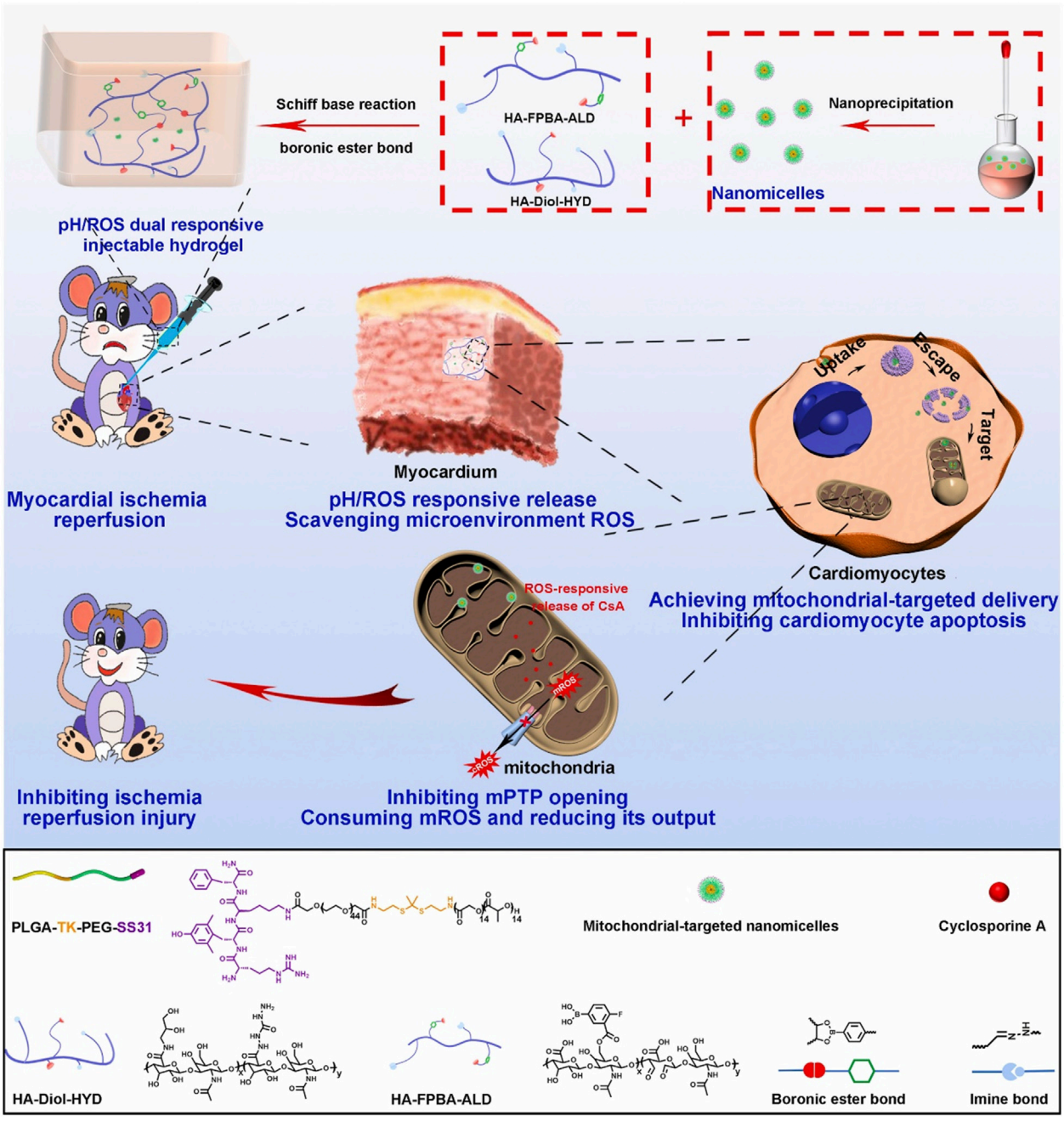

FIGURE 6
Schematic illustrating the preparation of ROS-responsive, mitochondria-targeted nanomicelles encapsulating CsA, and the construction of a pH/ROS dually responsive CsA nanomicelle-loaded injectable hydrogel using Schiff base reactions and boronic ester bonding crosslinks. In a rat model of myocardial ischemia-reperfusion injury, this hydrogel ensures precise delivery of nanodrugs to mitochondria in response to low pH and high ROS, reducing oxidative stress at microenvironmental, cellular, and subcellular levels, and restoring mitochondrial and myocardial functions. Reproduced with permission (Zhang X. et al., 2022). Copyright 2022, Elsevier.

By taking advantage of the high concentration of ROS in the damaged myocardium after I/R, in recent years, there have been continuous studies on the development of ROS-responsive hydrogels to achieve precise targeting and sustained release of drugs by intramyocardial or intrapericardial injection in the damaged area (Li et al., 2021; Hao T. et al., 2022; Zhang X. et al., 2022). These hydrogel designs all use similar ROS-responsive degradation elements, namely boronic acid/ester functional groups. The preference for boronic acid/ester as ROS-responsive elements in hydrogel design may stem from their stability under normal physiological conditions but superior reactivity to elevated ROS levels and ability to undergo rapid degradation to facilitate the precise release of encapsulated therapeutic agents in the injured myocardium.

For example, Li and colleagues have engineered a ROS-responsive hydrogel loaded with basic fibroblast growth factor

(bFGF) for myocardial repair following I/R injury (Li et al., 2021). This innovative hydrogel was synthesized from poly (vinyl alcohol) (PVA) cross-linked with a ROS-sensitive benzoboric acid derivative, enabling the delivery of bFGF directly to the heart's surface upon injection into the pericardial cavity (iPC) (Figure 5A). This design takes advantage of the elevated ROS levels in the damaged myocardium to trigger "on-demand" release of bFGF, thereby facilitating angiogenesis and enhancing cardiac function in a rat model of I/R injury (Figure 5B). Most importantly, these researchers also proved the feasibility of minimally invasive iPC access in a human patient during a standard LARIAT procedure, highlighting the potential for clinical translation (Figure 5C).

Similarly, Hao and colleagues utilized boronic ester as ROS-responsive element to fabricate an innovative, injectable dual-function hydrogel, CS-B-NO, designed to counteract MIRI by addressing the ROS/NO disequilibrium (Hao T. et al., 2022). This hydrogel, synthesized from chitosan modified with boronate-protected diazeniumdiolate, stands out for its ability to release NO in response to ROS stimulation, thereby modulating the ROS/NO imbalance post-I/R injury (Figure 5D). The CS-B-NO hydrogel exhibited significant therapeutic effects in attenuating cardiac injury and adverse cardiac remodeling in a mouse model of MIRI. The underlying mechanism involved the activation of the antioxidant defense system and protection against oxidative stress induced by I/R injury through the adaptive regulation of the Nrf2-Keap1 pathway, leading to a reduction in inflammation by inhibiting the activation of NF-κB signaling (Bellezza et al., 2018).

In addition, Zhang and colleagues have devised a hierarchical targeting pH and ROS dual-responsive hydrogel system that aimed to restore mitochondrial function and alleviate oxidative stress (Zhang X. et al., 2022). Notably, this system utilized both thioketal and boronic ester linkages known for their ROS-responsive degradation properties. Initially, mitochondrial-targeting polymeric micelles (PTPSC) were constructed, which self-assemble from thioketal-crosslinked PLGA and PEG (PLGA-TK-PEG) modified with the mitochondrial-targeting Szeto-Schiller (SS31) peptide. Subsequently, these PTPSC micelles were encapsulated within a pH/ROS dual-responsive injectable hydrogel crosslinked by reversible imine and boronic ester bonds, and loaded with cyclosporine A (CsA), a well-established drug known to inhibit the opening of the mitochondrial permeability transition pore (mPTP). In response to the low pH and high ROS in cardiac tissue during reperfusion, the imine and boronate bonds in the hydrogels were broken and the CsA-loaded PTPSCs were controllably released from the hydrogel matrix into damaged cardiomyocytes (Figure 6). The elevated intracellular ROS further induced the cleavage of the thioketal linker and targeted the release of CsA into the mitochondria via SS31 peptide, thereby blocking the opening of the mPTP and inhibiting mitochondria-mediated cardiomyocyte apoptosis, while attenuating the output of mitochondrial ROS to reduce cytoplasmic ROS levels. In rat models, this novel smart hydrogel system demonstrated remarkable therapeutic efficacy by restoring mitochondrial and cardiac functions, underscoring its potent ROS scavenging capabilities and innovative contribution to cardiac repair. The integration of these state of the art biomaterials and mechanisms underscores a promising approach for targeted therapy, especially in mitigating oxidative stress-related pathologies where mitochondrial dysfunction plays a pivotal role.

4.3 Biomimetic biomaterials

Given the remarkable biocompatibility, low immunogenicity, and low toxicity of biomimetic nanomaterials that incorporate cells, cellular components (such as membranes, lipoproteins, etc.), and extracellular vesicles (EVs), biomimetic nanomaterials have emerged as a prominent strategy in nanomedicine development (Yaman et al., 2020). In the treatment of ischemic heart disease, this biomimetic approach enables nanomaterials to disguise themselves as endogenous substances and target damaged myocardial areas, thereby minimizing toxicity and enhancing biocompatibility (Laiva et al., 2015; Kang and Kwon, 2022). A recent systematic review comprehensively summarized the research progress on biomimetic nanomaterials based on different cell types of biomembranes and EVs for ischemic heart disease therapy (Yu et al., 2024). Notably, in recent years, research has focused on integrating various microenvironmental responsive elements into these biomimetic nanodelivery platforms to improve their drug loading targeting and controlled release capabilities (Rios et al., 2015; Wu et al., 2016; Kobayashi et al., 2018; Liu et al., 2019). In studies on alleviating MIRI, to date, only two study has used ROS-responsive polymeric materials to load anti-inflammatory and pro-suvival drugs and integrated them into platelet membrane chimeric nanodelivery system to achieve targeted drug delivery in damaged myocardium (Li et al., 2022; Weng et al., 2022).

Specifically, Weng and colleagues developed this innovative platelet-bionic ROS-responsive delivery platform, PLP-RvD1, utilizing platelet membrane chimerism modified liposomes to achieve targeted delivery to myocardial macrophages at the injury site and mediate ROS-responsive release of the anti-inflammatory drug Resolvin D1 via diselenide bonds (Figure 7A) (Weng et al., 2022). In a mouse MIRI model, the intravenous injection of PLP-RvD1 resulted in the enrichment of RvD1 in the injured myocardium, promoting macrophage efferocytosis of apoptotic cardiomyocytes, production of specialized proresolving mediators (SPMs), and angiogenesis during injury repair process, effectively improving ventricular remodeling and protecting cardiac function. Furthermore, biosafety assessment of this delivery system demonstrated that PLP-RvD1 did not induce acute inflammatory responses, exhibited no potential immune reactions, and lacked organ toxicity, suggesting its suitability for potential clinical applications.

Similarly, Li and colleagues employed a biomimetic strategy to develop a platelet membrane-cloaked nanoparticle, CsA@PPTK (Figure 7B). This nanoparticle is constructed using poly (thioketal) (PTK), a material rich in thioketal bonds that are sensitive to various types of ROS. The ROS sensitivity allows the nanoparticle to release its encapsulated anti-apoptotic drug, CsA, specifically at the site of injury where ROS levels are elevated (Li et al., 2022). Upon intravenous injection, CsA@PPTK effectively accumulated in the infarcted myocardium of MIRI mice, where it scavenged ROS and modulated the inflammatory response. This modulation was achieved by increasing the generation of regulatory T cells (Tregs) and enhancing the M2/M1 macrophage ratio. As a result, this targeted delivery and responsive release strategy significantly reduced cardiomyocyte apoptosis, decreased infarct size, and mitigated fibrosis, leading to improved cardiac function and left ventricular remodeling. Furthermore, biosafety assessments

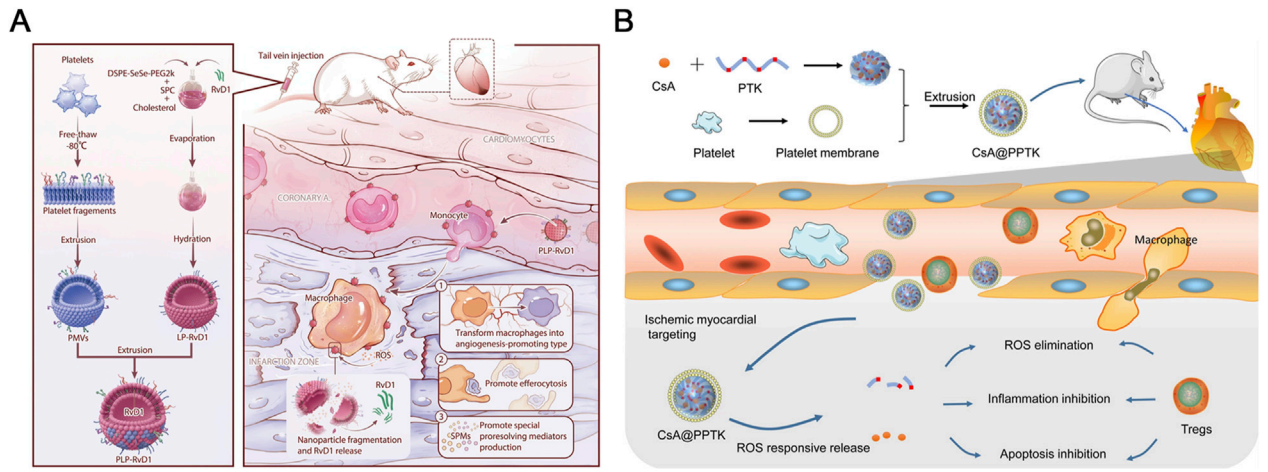

FIGURE 7
(A) A delivery platform called PLP-RvD1, which is responsive to ROS and mimics platelets, was designed. It is created by combining ROS-responsive liposomes loaded with RvD1 and platelet membranes. This platform retains the platelets' ability to interact with monocytes, allowing it to reach cardiac injury sites by hitching a ride with chemotactic circulating monocytes following intravenous injection. The high levels of ROS at the injury site break down the platform, releasing RvD1 quickly. The released RvD1 then facilitates the clearance of dead cardiomyocytes, the production of SPMs, and angiogenesis, which helps improve ventricular remodeling and maintain cardiac function in mice with myocardial I/R injury. Reproduced with permission (Weng et al., 2022). Copyright 2022, BioMed Central. **(B)** CsA@PPTK effectively accumulated in the ischemic myocardium of MI/RI mice, where it significantly reduced ROS and promoted the generation of Tregs while increasing the ratio of M2 to M1 macrophages. Additionally, CsA@PPTK notably decreased cardiomyocyte apoptosis, reduced infarct size and fibrosis in the ischemic myocardium, and lowered MMP-9 protein expression while increasing CX43 protein expression in the affected tissue. These effects led to a substantial reduction in left ventricular remodeling and a marked improvement in heart function in MI/RI mice. Copyright 2022, BioMed Central.

revealed that CsA@PPTK did not induce acute inflammation, immune reactions, or organ toxicity, highlighting its potential as a promising candidate for clinical applications in treating MIRI.

In addition to the above-mentioned ROS-responsive therapeutic platforms specifically designed for MIRI, recent studies have also extensively explored ROS-responsive nanomaterials with nearly identical design principles, including the same ROS-responsive elements and material types, for the treatment of myocardial infarction (MI). These nanomaterials are often loaded with drugs that possess anti-inflammatory, antioxidant, pro-angiogenic, and anti-fibrotic properties (Yao M. Y. et al., 2022; Zheng et al., 2022b; Ji et al., 2023; Sun et al., 2024; Zhang J. H. et al., 2024). Given the close similarities in the pathological processes underlying MI and MIRI, it is highly probable that the nanomedicines developed for MI could also yield significant therapeutic benefits in the treatment of MIRI. Notably, while ROS-responsive nanomaterials carrying anti-fibrotic agents have been effectively utilized in MI therapy (Ji et al., 2023; Sun et al., 2024), they have not yet been applied in the context of MIRI treatment. The future development of anti-MIRI nanomedicine may need to adopt a more holistic approach. This would involve integrating a spectrum of cardioprotective drugs with multiple therapeutic properties, aimed at providing comprehensive protection of cardiac structure and function throughout the disease progression, from acute injury to chronic remodeling.

5 Prospects and conclusion

ROS overproduction during I/R play a crucial role in myocardial injury, presenting both a challenge and an opportunity for innovative treatment strategies. ROS-responsive biomaterials have emerged as a promising approach to addressing I/R injury in the heart as well as other organs such as liver, kidney and brain. Despite their potential, several challenges must be overcome to translate these biomaterials from the laboratory to clinical practice. 1) One significant challenge is the integration of multifunctionality in current ROS-responsive biomaterials to address both diagnostic and therapeutic needs. The ability to combine therapy with real-time imaging could significantly improve monitoring and treatment precision for MIRI. Furthermore, integrating multiple therapeutic modalities such as antioxidant, anti-inflammatory, pro-angiogenic, and anti-fibrotic therapies may produce synergistic effects, thereby enhancing myocardial recovery and function. 2) Another critical challenge is the complexity of the myocardial I/R microenvironment, characterized by fluctuating ROS levels and diverse pathological features that vary depending on the extent of myocardial injury in each patient. This variability directly impacts the efficacy of nanomaterials. To overcome this, it is crucial to enhance our understanding of ROS biology, focusing on the spatiotemporal changes of ROS in the myocardium after I/R. Future designs should also integrate multi-stimulus-responsive capabilities that can react to additional I/R markers such as pH and inflammation. This strategy will facilitate the creation of smart-responsive systems that can dynamically adapt to these microenvironmental changes, thereby enhancing targeting precision and therapeutic efficacy. 3) With the exception of *in situ* injected biomaterials, such as hydrogels, current therapeutic polymeric or biomimetic nanoparticles injected intravenously are difficult to effectively target to the heart and are often cleared by the liver or kidneys. Therefore, the design of these materials should also incorporate strategies that enhance their affinity and retention within the damaged myocardium, possibly through the use of

heart-specific peptides or antibodies. 4) Addressing the biosafety and systemic toxicity of these advanced materials is paramount. Although nanomedicine can enhance drug bioavailability and prolong circulation times, the long-term effects require thorough investigation. Understanding the pharmacokinetics, biodegradation, and metabolic profiles of these materials is essential to ensuring their safe clinical application. Preclinical studies and clinical trials should explore the efficacy of these nanomaterials in larger animal models to better evaluate their clinical potential. A focus on rigorous preclinical testing and streamlined regulatory processes will also be essential to facilitate the transition from bench to bedside. 5) Finally, the scalability of production is another hurdle that must be overcome. As these biomaterials move towards clinical application, the need for efficient manufacturing processes that maintain material integrity and functionality at scale becomes evident. This is crucial for meeting the demands of clinical practice while ensuring cost-effectiveness.

In conclusion, significant advances in ROS-responsive biomaterials, including polymeric nanoparticles, hydrogels, and biomimetic nanomaterials, offer a promising approach to treating ischemia-reperfusion injuries by enabling targeted therapeutic delivery. These biomaterials can reduce myocardial damage more effectively than current therapeutics, but challenges remain in patient variability, targeting specificity, biocompatibility, long-term safety and efficacy, and manufacturing scalability. Continued research focusing on these areas is crucial. By addressing these challenges, ROS-responsive biomaterials could revolutionize the management of ischemic conditions across multiple organ systems, significantly improving patient outcomes and paving the way for personalized medical interventions.

Author contributions

YZ: Visualization, Writing–original draft, Writing–review and editing, Investigation. MJ: Investigation, Visualization, Writing–original draft. TW: Conceptualization, Funding acquisition, Investigation, Supervision, Visualization, Writing–original draft, Writing–review and editing.

Funding

The author(s) declare that financial support was received for the research, authorship, and/or publication of this article. This work was funded by grant 82000266 form the National Natural Science Foundation of China (to TW).

Conflict of interest

The authors declare that the research was conducted in the absence of any commercial or financial relationships that could be construed as a potential conflict of interest.

Publisher's note

References

Abdollahiyan, P., Baradaran, B., De La Guardia, M., Oroojalian, F., and Mokhtarzadeh, A. (2020). Cutting-edge progress and challenges in stimuli responsive hydrogel microenvironment for success in tissue engineering today. *J. Control Release* 328, 514–531. doi:10.1016/j.jconrel.2020.09.030

Algoet, M., Janssens, S., Himmelreich, U., Gsell, W., Pusovnik, M., Van Den Eynde, J., et al. (2023). Myocardial ischemia-reperfusion injury and the influence of inflammation. *Trends Cardiovasc Med.* 33, 357–366. doi:10.1016/j.tcm.2022.02.005

Alkaitis, M. S., and Crabtree, M. J. (2012). Recoupling the cardiac nitric oxide synthases: tetrahydrobiopterin synthesis and recycling. *Curr. Heart Fail Rep.* 9, 200–210. doi:10.1007/s11897-012-0097-5

Amici, A., Levine, R. L., Tsai, L., and Stadtman, E. R. (1989). Conversion of amino acid residues in proteins and amino acid homopolymers to carbonyl derivatives by metal-catalyzed oxidation reactions. *J. Biol. Chem.* 264, 3341–3346. doi:10.1016/s0021-9258(18)94071-8

Antoniades, C., Shirodaria, C., Warrick, N., Cai, S., De Bono, J., Lee, J., et al. (2006). 5-methyltetrahydrofolate rapidly improves endothelial function and decreases superoxide production in human vessels: effects on vascular tetrahydrobiopterin availability and endothelial nitric oxide synthase coupling. *Circulation* 114, 1193–1201. doi:10.1161/circulationaha.106.612325

Bae, K. H., Wang, L. S., and Kurisawa, M. (2013). Injectable biodegradable hydrogels: progress and challenges. *J. Mater Chem. B* 1, 5371–5388. doi:10.1039/c3tb20940g

Bae, S., Park, M., Kang, C., Dilmen, S., Kang, T. H., Kang, D. G., et al. (2016). Hydrogen peroxide-responsive nanoparticle reduces myocardial ischemia/reperfusion injury. *J. Am. Heart Assoc.* 5, e003697. doi:10.1161/jaha.116.003697

Begonja, A. J., Gambaryan, S., Geiger, J., Aktas, B., Pozgajova, M., Nieswandt, B., et al. (2005). Platelet NAD(P)H-oxidase–generated ROS production regulates αIIbβ3-integrin activation independent of the NO/cGMP pathway. *Blood* 106, 2757–2760. doi:10.1182/blood-2005-03-1047

Bellezza, I., Giambanco, I., Minelli, A., and Donato, R. (2018). Nrf2-Keap1 signaling in oxidative and reductive stress. *Biochim. Biophys. Acta Mol. Cell Res.* 1865, 721–733. doi:10.1016/j.bbamcr.2018.02.010

Bezold, M. G., Hanna, A. R., Dollinger, B. R., Patil, P., Yu, F., Duvall, C. L., et al. (2023). Hybrid shear-thinning hydrogel integrating hyaluronic acid with ROS-responsive nanoparticles. *Adv. Funct. Mater* 33, 2213368. doi:10.1002/adfm.202213368

Boueiz, A., Damarla, M., and Hassoun, P. M. (2008). Xanthine oxidoreductase in respiratory and cardiovascular disorders. *Am. J. Physiol. Lung Cell Mol. Physiol.* 294, L830–L840. doi:10.1152/ajplung.00007.2008

Braunersreuther, V., Montecucco, F., Asrih, M., Pelli, G., Galan, K., Frias, M., et al. (2013). Role of NADPH oxidase isoforms NOX1, NOX2 and NOX4 in myocardial ischemia/reperfusion injury. *J. Mol. Cell Cardiol.* 64, 99–107. doi:10.1016/j.yjmcc.2013.09.007

Bugger, H., and Pfeil, K. (2020). Mitochondrial ROS in myocardial ischemia reperfusion and remodeling. *Biochim. Biophys. Acta Mol. Basis Dis.* 1866, 165768. doi:10.1016/j.bbadis.2020.165768

Cadenas, S. (2018). ROS and redox signaling in myocardial ischemia-reperfusion injury and cardioprotection. *Free Radic. Biol. Med.* 117, 76–89. doi:10.1016/j.freeradbiomed.2018.01.024

Cao, B. J., Zhang, H. Y., Sun, M. Z., Xu, C. L., Kuang, H., and Xu, L. G. (2024). Chiral MoSe2 nanoparticles for ultrasensitive monitoring of reactive oxygen species *in vivo*. *Adv. Mater.* 36, e2208037. doi:10.1002/adma.202208037

Cao, W., Gu, Y., Li, T., and Xu, H. (2015). Ultra-sensitive ROS-responsive tellurium-containing polymers. *Chem. Commun. (Camb)* 51, 7069–7071. doi:10.1039/c5cc01779c

Chakraborti, T., Mandal, A., Mandal, M., Das, S., and Chakraborti, S. (2000). Complement activation in heart diseases. *Cell Signal* 12, 607–617. doi:10.1016/s0898-6568(00)00111-x

Chakraborty, A., Alexander, S., Luo, W., Al-Salam, N., Van Oirschot, M., Ranganath, S. H., et al. (2023). Engineering multifunctional adhesive hydrogel patches for biomedical applications. *Interdiscip. Med.* 1. doi:10.1002/inmd.20230008

Chen, G. H., Yang, Y. J., Tang, R. J., and Huang, C. R. (2019). Activation of mir-145/P70s6k1/enos pathway in microvascular endothelial cells by tongxinluo alleviates myocardial ischemia/reperfusion injury-role of exosomal linc-ror from cardiomyocytes. *J. Am. Coll. Cardiol.* 73, 46. doi:10.1016/s0735-1097(19)30655-2

Chen, Q., Moghaddas, S., Hoppel, C. L., and Lesnefsky, E. J. (2008). Ischemic defects in the electron transport chain increase the production of reactive oxygen species from isolated rat heart mitochondria. *Am. J. Physiol. Cell Physiol.* 294, C460–C466. doi:10.1152/ajpcell.00211.2007

Chen, Z., Duan, J., Diao, Y., Chen, Y., Liang, X., Li, H., et al. (2021). ROS-responsive capsules engineered from EGCG-Zinc networks improve therapeutic angiogenesis in mouse limb ischemia. *Bioact. Mater* 6, 1–11. doi:10.1016/j.bioactmat.2020.07.013

Chouchani, E. T., Pell, V. R., Gaude, E., Aksentijevic, D., Sundier, S. Y., Robb, E. L., et al. (2014). Ischaemic accumulation of succinate controls reperfusion injury through mitochondrial ROS. *Nature* 515, 431–435. doi:10.1038/nature13909

Chouchani, E. T., Pell, V. R., James, A. M., Work, L. M., Saeb-Parsy, K., Frezza, C., et al. (2016). A unifying mechanism for mitochondrial superoxide production during ischemia-reperfusion injury. *Cell Metab.* 23, 254–263. doi:10.1016/j.cmet.2015.12.009

Chung, M. F., Chia, W. T., Wan, W. L., Lin, Y. J., and Sung, H. W. (2015). Controlled release of an anti-inflammatory drug using an ultrasensitive ROS-responsive gas-generating carrier for localized inflammation inhibition. *J. Am. Chem. Soc.* 137, 12462–12465. doi:10.1021/jacs.5b08057

Dai, Y. L., Li, Y. Q., Hu, X., Jiang, N., Liu, W. Z., Meng, Y., et al. (2023). Nonstructural protein NS17 of grass carp reovirus Honghu strain promotes virus infection by mediating cell-cell fusion and apoptosis. *Virus Res.* 334, 199150. doi:10.1016/j.virusres.2023.199150

Dominguez-Alvarez, E., Racz, B., Marc, M. A., Nasim, M. J., Szemeredi, N., Viktorova, J., et al. (2022). Selenium and tellurium in the development of novel small molecules and nanoparticles as cancer multidrug resistance reversal agents. *Drug Resist Updat* 63, 100844. doi:10.1016/j.drup.2022.100844

Dubois-Deruy, E., Peugnet, V., Turkieh, A., and Pinet, F. (2020). Oxidative stress in cardiovascular diseases. *Antioxidants (Basel)* 9, 864. doi:10.3390/antiox9090864

Dumitrescu, C., Biondi, R., Xia, Y., Cardounel, A. J., Druhan, L. J., Ambrosio, G., et al. (2007). Myocardial ischemia results in tetrahydrobiopterin (BH4) oxidation with impaired endothelial function ameliorated by BH4. *Proc. Natl. Acad. Sci. U. S. A.* 104, 15081–15086. doi:10.1073/pnas.0702986104

Gaytan, S. L., Beaven, E., Gadad, S. S., and Nurunnabi, M. (2023). Progress and prospect of nanotechnology for cardiac fibrosis treatment. *Interdiscip. Med.* 1, e20230018. doi:10.1002/inmd.20230018

Gong, G., Wan, W., Zhang, X., Chen, X., and Yin, J. (2024). Management of ROS and regulatory cell death in myocardial ischemia-reperfusion injury. *Mol. Biotechnol*. doi:10.1007/s12033-024-01173-y

Gordan, R., Wongjaikam, S., Gwathmey, J. K., Chattipakorn, N., Chattipakorn, S. C., and Xie, L. H. (2018). Involvement of cytosolic and mitochondrial iron in iron overload cardiomyopathy: an update. *Heart Fail. Rev.* 23, 801–816. doi:10.1007/s10741-018-9700-5

Grimaldi-Bensouda, L., Alperovitch, A., Aubrun, E., Danchin, N., Rossignol, M., Abenhaim, L., et al. (2015). Impact of allopurinol on risk of myocardial infarction. *Ann. Rheum. Dis.* 74, 836–842. doi:10.1136/annrheumdis-2012-202972

Gruhlke, M. C., and Slusarenko, A. J. (2012). The biology of reactive sulfur species (RSS). *Plant Physiol. Biochem.* 59, 98–107. doi:10.1016/j.plaphy.2012.03.016

Gupta, M. K., Lee, S. H., Crowder, S. W., Wang, X., Hofmeister, L. H., Nelson, C. E., et al. (2015). Oligoproline-derived nanocarrier for dual stimuli-responsive gene delivery. *J. Mater Chem. B* 3, 7271–7280. doi:10.1039/c5tb00988j

Hamidi, M., Azadi, A., and Rafiei, P. (2008). Hydrogel nanoparticles in drug delivery. *Adv. Drug Deliv. Rev.* 60, 1638–1649. doi:10.1016/j.addr.2008.08.002

Han, G. S., and Domaille, D. W. (2022). Connecting the dynamics and reactivity of arylboronic acids to emergent and stimuli-responsive material properties. *J. Mater Chem. B* 10, 6263–6278. doi:10.1039/d2tb00968d

Hao, T., Qian, M., Zhang, Y., Liu, Q., Midgley, A. C., Liu, Y., et al. (2022a). An injectable dual-function hydrogel protects against myocardial ischemia/reperfusion injury by modulating ROS/NO disequilibrium. *Adv. Sci. (Weinh)* 9, e2105408. doi:10.1002/advs.202105408

Hao, Y. M., Song, K. C., Tan, X. C., Ren, L., Guo, X. P., Zhou, C. C., et al. (2022b). Reactive oxygen species-responsive polypeptide drug delivery system targeted activated hepatic stellate cells to ameliorate liver fibrosis. *Acs Nano* 16, 20739–20757. doi:10.1021/acsnano.2c07796

Hausenloy, D. J., and Yellon, D. M. (2013). Myocardial ischemia-reperfusion injury: a neglected therapeutic target. *J. Clin. Invest.* 123, 92–100. doi:10.1172/jci62874

Haybar, H., Shahrabi, S., Rezaeeyan, H., Shirzad, R., and Saki, N. (2019). Endothelial cells: from dysfunction mechanism to pharmacological effect in cardiovascular disease. *Cardiovasc. Toxicol.* 19, 13–22. doi:10.1007/s12012-018-9493-8

Hool, L. C. (2009). The L-type Ca(2+) channel as a potential mediator of pathology during alterations in cellular redox state. *Heart Lung Circ.* 18, 3–10. doi:10.1016/j.hlc.2008.11.004

Hou, M., Wu, X., Zhao, Z., Deng, Q., Chen, Y., and Yin, L. (2022). Endothelial cell-targeting, ROS-ultrasensitive drug/siRNA co-delivery nanocomplexes mitigate early-stage neutrophil recruitment for the anti-inflammatory treatment of myocardial ischemia reperfusion injury. *Acta Biomater.* 143, 344–355. doi:10.1016/j.actbio.2022.02.018

Huang, C., Zhou, S., Chen, C., Wang, X., Ding, R., Xu, Y., et al. (2022). Biodegradable redox-responsive AIEgen-based-covalent organic framework nanocarriers for long-term treatment of myocardial ischemia/reperfusion injury. *Small* 18, e2205062. doi:10.1002/smll.202205062

Ibanez, B., Heusch, G., Ovize, M., and Van De Werf, F. (2015). Evolving therapies for myocardial ischemia/reperfusion injury. *J. Am. Coll. Cardiol.* 65, 1454–1471. doi:10.1016/j.jacc.2015.02.032

Ji, X. Q., Meng, Y. B., Wang, Q. Y., Tong, T., Liu, Z., Lin, J. Q., et al. (2023). Cysteine-based redox-responsive nanoparticles for fibroblast-targeted drug delivery in the treatment of myocardial infarction. *Acs Nano* 17, 5421–5434. doi:10.1021/acsnano.2c10042

Jordan, J. E., Zhao, Z. Q., and Vinten-Johansen, J. (1999). The role of neutrophils in myocardial ischemia-reperfusion injury. *Cardiovasc Res.* 43, 860–878. doi:10.1016/s0008-6363(99)00187-x

Jourden, J. L., Daniel, K. B., and Cohen, S. M. (2011). Investigation of self-immolative linkers in the design of hydrogen peroxide activated metalloprotein inhibitors. *Chem. Commun. (Camb)* 47, 7968–7970. doi:10.1039/c1cc12526e

Kahles, T., and Brandes, R. P. (2013). Which NADPH oxidase isoform is relevant for ischemic stroke? The case for nox 2. *Antioxid. Redox Signal* 18, 1400–1417. doi:10.1089/ars.2012.4721

Kang, I. S., and Kwon, K. (2022). Potential application of biomimetic exosomes in cardiovascular disease: focused on ischemic heart disease. *BMB Rep.* 55, 30–38. doi:10.5483/bmbrep.2022.55.1.161

Kang, L. T., Han, X. L., Chang, X., Su, Z. P., Fu, F. H., Shan, Y., et al. (2024). Redox-sensitive self-assembling polymer micelles based on oleanolic modified hydroxyethyl starch: synthesis, characterisation, and oleanolic release. *Int. J. Biol. Macromol.* 266, 131211. doi:10.1016/j.ijbiomac.2024.131211

Kieliszek, M., and Blazejak, S. (2013). Selenium: significance, and outlook for supplementation. *Nutrition* 29, 713–718. doi:10.1016/j.nut.2012.11.012

Knock, G. A. (2019). NADPH oxidase in the vasculature: expression, regulation and signalling pathways; role in normal cardiovascular physiology and its dysregulation in hypertension. *Free Radic. Biol. Med.* 145, 385–427. doi:10.1016/j.freeradbiomed.2019.09.029

Kobayashi, K., Oh, S. H., Yoon, C., and Gracias, D. H. (2018). Multitemperature responsive self-folding soft biomimetic structures. *Macromol. Rapid Commun.* 39. doi:10.1002/marc.201700692

Laforgia, P. L., Auguadro, C., Bronzato, S., and Durante, A. (2022). The reduction of mortality in acute myocardial infarction: from bed rest to future directions. *Int. J. Prev. Med.* 13, 56. doi:10.4103/ijpvm.ijpvm_122_20

Laiva, A. L., Venugopal, J. R., Navaneethan, B., Karuppuswamy, P., and Ramakrishna, S. (2015). Biomimetic approaches for cell implantation to the restoration of infarcted myocardium. *Nanomedicine (Lond)* 10, 2907–2930. doi:10.2217/nnm.15.124

Lan, M., Hou, M., Yan, J., Deng, Q., Zhao, Z., Lv, S., et al. (2022). Cardiomyocyte-targeted anti-inflammatory nanotherapeutics against myocardial ischemia reperfusion (IR) injury. *Nano Res.* 15, 9125–9134. doi:10.1007/s12274-022-4553-6

Lee, D., Bae, S., Hong, D., Lim, H., Yoon, J. H., Hwang, O., et al. (2013a). H2O2-responsive molecularly engineered polymer nanoparticles as ischemia/reperfusion-targeted nanotherapeutic agents. *Sci. Rep.* 3, 2233. doi:10.1038/srep02233

Lee, S., Stubelius, A., Hamelmann, N., Tran, V., and Almutairi, A. (2018). Inflammation-responsive drug-conjugated dextran nanoparticles enhance anti-inflammatory drug efficacy. *ACS Appl. Mater Interfaces* 10, 40378–40387. doi:10.1021/acsami.8b08254

Lee, S. H., Boire, T. C., Lee, J. B., Gupta, M. K., Zachman, A. L., Rath, R., et al. (2014). ROS-cleavable proline oligomer crosslinking of polycaprolactone for pro-angiogenic host response. *J. Mater Chem. B* 2, 7109–7113. doi:10.1039/c4tb01094a

Lee, S. H., Gupta, M. K., Bang, J. B., Bae, H., and Sung, H. J. (2013b). Current progress in Reactive Oxygen Species (ROS)-Responsive materials for biomedical applications. *Adv. Healthc. Mater* 2, 908–915. doi:10.1002/adhm.201200423

Li, D., and Gao, S. (2023). The interplay between T lymphocytes and macrophages in myocardial ischemia/reperfusion injury. *Mol. Cell Biochem.* 479, 1925–1936. doi:10.1007/s11010-023-04822-z

Li, F., Liu, D., Liu, M., Ji, Q., Zhang, B., Mei, Q., et al. (2022). Tregs biomimetic nanoparticle to reprogram inflammatory and redox microenvironment in infarct tissue to treat myocardial ischemia reperfusion injury in mice. *J. Nanobiotechnology* 20, 251. doi:10.1186/s12951-022-01445-2

Li, L., Wang, Y., Guo, R., Li, S., Ni, J., Gao, S., et al. (2020). Ginsenoside Rg3-loaded, reactive oxygen species-responsive polymeric nanoparticles for alleviating myocardial ischemia-reperfusion injury. *J. Control Release* 317, 259–272. doi:10.1016/j.jconrel.2019.11.032

Li, X., Ou, W., Xie, M., Yang, J., Li, Q., and Li, T. (2023). Nanomedicine-based therapeutics for myocardial ischemic/reperfusion injury. *Adv. Healthc. Mater.* 12, e2300161. doi:10.1002/adhm.202300161

Li, Z., Zhu, D., Hui, Q., Bi, J., Yu, B., Huang, Z., et al. (2021). Injection of ROS-responsive hydrogel loaded with basic fibroblast growth factor into the pericardial cavity for heart repair. *Adv. Funct. Mater.* 31, 2004377. doi:10.1002/adfm.202004377

Link, W. (2019). Introduction to FOXO biology. *Methods Mol. Biol.* 1890, 1–9. doi:10.1007/978-1-4939-8900-3_1

Liu, B., and Thayumanavan, S. (2020). Mechanistic investigation on oxidative degradation of ROS-responsive thioacetal/thioketal moieties and their implications. *Cell Rep. Phys. Sci.* 1, 100271. doi:10.1016/j.xcrp.2020.100271

Liu, G., Zhao, X., Zhang, Y., Xu, J., Xu, J., Li, Y., et al. (2019). Engineering biomimetic platesomes for pH-responsive drug delivery and enhanced antitumor activity. *Adv. Mater.* 31, e1900795. doi:10.1002/adma.201900795

Liu, J., He, Z., Zhong, Y., Zhu, L., Yan, M., Mou, N., et al. (2023a). Reactive oxygen species-responsive sequentially targeted AIE fluorescent probe for precisely identifying the atherosclerotic plaques. *ACS Appl. Mater Interfaces* 15, 47381–47393. doi:10.1021/acsami.3c09573

Liu, Y., Li, L., Wang, Z., Zhang, J., and Zhou, Z. (2023b). Myocardial ischemia-reperfusion injury; Molecular mechanisms and prevention. *Microvasc. Res.* 149, 104565. doi:10.1016/j.mvr.2023.104565

Liu, Y. H., Carretero, O. A., Cingolani, O. H., Liao, T. D., Sun, Y., Xu, J., et al. (2005). Role of inducible nitric oxide synthase in cardiac function and remodeling in mice with heart failure due to myocardial infarction. *Am. J. Physiology-Heart Circulatory Physiology* 289, H2616–H2623. doi:10.1152/ajpheart.00546.2005

Lu, X., Mestres, G., Singh, V. P., Effati, P., Poon, J. F., Engman, L., et al. (2017). Selenium- and tellurium-based antioxidants for modulating inflammation and effects on osteoblastic activity. *Antioxidants (Basel)* 6, 13. doi:10.3390/antiox6010013

Luo, Q., Sun, W., Li, Z., Sun, J., Xiao, Y., Zhang, J., et al. (2023). Biomaterials-mediated targeted therapeutics of myocardial ischemia-reperfusion injury. *Biomaterials* 303, 122368. doi:10.1016/j.biomaterials.2023.122368

Ma, N., Li, Y., Xu, H., Wang, Z., and Zhang, X. (2010). Dual redox responsive assemblies formed from diselenide block copolymers. *J. Am. Chem. Soc.* 132, 442–443. doi:10.1021/ja908124g

Madesh, M., and Hajnoczky, G. (2001). VDAC-dependent permeabilization of the outer mitochondrial membrane by superoxide induces rapid and massive cytochrome c release. *J. Cell Biol.* 155, 1003–1015. doi:10.1083/jcb.200105057

Martin, J. R., Gupta, M. K., Page, J. M., Yu, F., Davidson, J. M., Guelcher, S. A., et al. (2014). A porous tissue engineering scaffold selectively degraded by cell-generated reactive oxygen species. *Biomaterials* 35, 3766–3776. doi:10.1016/j.biomaterials.2014.01.026

Mount, P. F., Kemp, B. E., and Power, D. A. (2007). Regulation of endothelial and myocardial NO synthesis by multi-site eNOS phosphorylation. *J. Mol. Cell Cardiol.* 42, 271–279. doi:10.1016/j.yjmcc.2006.05.023

Paradies, G., Petrosillo, G., Pistolese, M., Di Venosa, N., Federici, A., and Ruggiero, F. M. (2004). Decrease in mitochondrial complex I activity in ischemic/reperfused rat heart: involvement of reactive oxygen species and cardiolipin. *Circ. Res.* 94, 53–59. doi:10.1161/01.res.0000109416.56608.64

Paravicini, T. M., and Touyz, R. M. (2008). NADPH oxidases, reactive oxygen species, and hypertension: clinical implications and therapeutic possibilities. *Diabetes Care* 31 (Suppl. 2), S170–S180. doi:10.2337/dc08-s247

Qiu, Y. W., Yu, C. J., Yue, Z. W., Ren, Y. C., Wang, W. T., Yu, Q. Y., et al. (2024). Chronological-programmed black phosphorus hydrogel for responsive modulation of the pathological microenvironment in myocardial infarction. *Acs Appl. Mater. and Interfaces* 16, 17323–17338. doi:10.1021/acsami.4c01956

Radi, R. (2013). Peroxynitrite, a stealthy biological oxidant. *J. Biol. Chem.* 288, 26464–26472. doi:10.1074/jbc.r113.472936

Reed, G. W., Rossi, J. E., and Cannon, C. P. (2017). Acute myocardial infarction. *Lancet* 389, 197–210. doi:10.1016/s0140-6736(16)30677-8

Rios, C., Longo, J., Zahouani, S., Garnier, T., Vogt, C., Reisch, A., et al. (2015). A new biomimetic route to engineer enzymatically active mechano-responsive materials. *Chem. Commun. (Camb)* 51, 5622–5625. doi:10.1039/c5cc00329f

Romanyuk, A. V., Grozdova, I. D., Ezhov, A. A., and Melik-Nubarov, N. S. (2017). Peroxyoxalate chemiluminescent reaction as a tool for elimination of tumour cells under oxidative stress. *Sci. Rep.* 7, 3410. doi:10.1038/s41598-017-03527-w

Sah, H., Thoma, L. A., Desu, H. R., Sah, E., and Wood, G. C. (2013). Concepts and practices used to develop functional PLGA-based nanoparticulate systems. *Int. J. Nanomedicine* 8, 747–765. doi:10.2147/ijn.s40579

Saito, Y., Oyama, K., Tsujita, K., Yasuda, S., and Kobayashi, Y. (2023). Treatment strategies of acute myocardial infarction: updates on revascularization, pharmacological therapy, and beyond. *J. Cardiol.* 81, 168–178. doi:10.1016/j.jjcc.2022.07.003

Schanze, N., Hamad, M. A., Nuhrenberg, T. G., Bode, C., and Duerschmied, D. (2023). Platelets in myocardial ischemia/reperfusion injury. *Hamostaseologie* 43, 110–121. doi:10.1055/a-1739-9351

Shen, C., Gao, M., Chen, H., Zhan, Y., Lan, Q., Li, Z., et al. (2021). Reactive oxygen species (ROS)-responsive nanoprobe for bioimaging and targeting therapy of osteoarthritis. *J. Nanobiotechnology* 19, 395. doi:10.1186/s12951-021-01136-4

Shen, J., Jiao, W., Yuan, B., Xie, H., Chen, Z., Wei, M., et al. (2024). Oral curcumin-thioketal-inulin conjugate micelles against radiation-induced enteritis. *Antioxidants (Basel)* 13, 417. doi:10.3390/antiox13040417

Shofolawe-Bakare, O. T., De Mel, J. U., Mishra, S. K., Hossain, M., Hamadani, C. M., Pride, M. C., et al. (2022). ROS-responsive glycopolymeric nanoparticles for enhanced drug delivery to macrophages. *Macromol. Biosci.* 22, e2200281. doi:10.1002/mabi.202200281

Sies, H., Belousov, V. V., Chandel, N. S., Davies, M. J., Jones, D. P., Mann, G. E., et al. (2022). Defining roles of specific reactive oxygen species (ROS) in cell biology and physiology. *Nat. Rev. Mol. Cell Biol.* 23, 499–515. doi:10.1038/s41580-022-00456-z

Stubelius, A., Lee, S., and Almutairi, A. (2019). The chemistry of boronic acids in nanomaterials for drug delivery. *Acc. Chem. Res.* 52, 3108–3119. doi:10.1021/acs.accounts.9b00292

Sun, K., Xu, R., Xue, B., Liu, P., Bai, J., Tian, Y., et al. (2023). ROS-responsive ADPH nanoparticles for image-guided surgery. *Front. Chem.* 11, 1121957. doi:10.3389/fchem.2023.1121957

Sun, X., Xu, S. Y., Flower, S. E., Fossey, J. S., Qian, X., and James, T. D. (2013). "Integrated" and "insulated" boronate-based fluorescent probes for the detection of hydrogen peroxide. *Chem. Commun. (Camb)* 49, 8311–8313. doi:10.1039/c3cc43265c

Sun, Y. G., Zhang, X. P., Nie, X. F., Yang, R., Zhao, X. R., Cui, C. Y., et al. (2024). Dough-kneading-inspired design of an adhesive cardiac patch to attenuate cardiac fibrosis and improve cardiac function via regulating glycometabolism. *Adv. Healthc. Mater.* 13, e2303685. doi:10.1002/adhm.202303685

Surendran, S. P., Thomas, R. G., Moon, M. J., Park, R., Lee, J. H., and Jeong, Y. Y. (2020). A bilirubin-conjugated chitosan nanotheranostics system as a platform for reactive oxygen species stimuli-responsive hepatic fibrosis therapy. *Acta Biomater.* 116, 356–367. doi:10.1016/j.actbio.2020.09.014

Takaya, N., Katoh, Y., Iwabuchi, K., Hayashi, I., Konishi, H., Itoh, S., et al. (2005). Platelets activated by collagen through the immunoreceptor tyrosine-based activation motif in the Fc receptor gamma-chain play a pivotal role in the development of myocardial ischemia-reperfusion injury. *J. Mol. Cell Cardiol.* 39, 856–864. doi:10.1016/j.yjmcc.2005.07.006

Tan, X., Yu, Y., Liu, K., Xu, H., Liu, D., Wang, Z., et al. (2012). Single-molecule force spectroscopy of selenium-containing amphiphilic block copolymer: toward disassembling the polymer micelles. *Langmuir* 28, 9601–9605. doi:10.1021/la301703t

Thirunavukkarasu, M., Adluri, R. S., Juhasz, B., Samuel, S. M., Zhan, L., Kaur, A., et al. (2012). Novel role of NADPH oxidase in ischemic myocardium: a study with Nox2 knockout mice. *Funct. Integr. Genomics* 12, 501–514. doi:10.1007/s10142-011-0256-x

Thygesen, K., Alpert, J. S., White, H. D., Jaffe, A. S., Apple, F. S., Galvani, M., et al. (2007). Universal definition of myocardial infarction. *Circulation* 116, 2634–2653. doi:10.1161/circulationaha.107.187397

Tian, Z. Y., Wang, S., and Lu, H. (2021). Hydroxyproline-derived biomimetic and biodegradable polymers. *Curr. Opin. Solid State and Mater. Sci.* 25, 100902. doi:10.1016/j.cossms.2021.100902

Vinogradov, A. D., and Grivennikova, V. G. (2016). Oxidation of NADH and ROS production by respiratory complex I. *Biochim. Biophys. Acta* 1857, 863–871. doi:10.1016/j.bbabio.2015.11.004

Wang, D., Wang, S., Xia, Y., Liu, S., Jia, R., Xu, G., et al. (2020). Preparation of ROS-responsive core crosslinked polycarbonate micelles with thioketal linkage. *Colloids Surf. B Biointerfaces* 195, 111276. doi:10.1016/j.colsurfb.2020.111276

Wang, G., Huang, P., Wang, L., Chen, X., Zhou, Y., Huang, W., et al. (2022). ROS-responsive thioether-containing hyperbranched polymer micelles for light-triggered drug release. *SmartMat* 3, 522–531. doi:10.1002/smm2.1092

Wang, L., Fan, F., Cao, W., and Xu, H. (2015). Ultrasensitive ROS-responsive coassemblies of tellurium-containing molecules and phospholipids. *ACS Appl. Mater Interfaces* 7, 16054–16060. doi:10.1021/acsami.5b04419

Weng, X., Tan, H., Huang, Z., Chen, J., Zhang, N., Wang, Q., et al. (2022). Targeted delivery and ROS-responsive release of Resolvin D1 by platelet chimeric liposome ameliorates myocardial ischemia-reperfusion injury. *J. Nanobiotechnology* 20, 454. doi:10.1186/s12951-022-01652-x

Wu, M., Cao, Z., Zhao, Y., Zeng, R., Tu, M., and Zhao, J. (2016). Novel self-assembled pH-responsive biomimetic nanocarriers for drug delivery. *Mater Sci. Eng. C Mater Biol. Appl.* 64, 346–353. doi:10.1016/j.msec.2016.03.099

Xia, Y., Chen, R., Ke, Y., Han, Q., Ma, Z., and Shi, Q. (2023). ROS-responsive phenylboronic ester-based nanovesicles as multifunctional drug delivery systems for the treatment of inflammatory and thrombotic complications. *Biomater. Sci.* 11, 7805–7816. doi:10.1039/d3bm01427d

Xie, J., Yao, Y., Wang, S., Fan, L., Ding, J., Gao, Y., et al. (2022). Alleviating oxidative injury of myocardial infarction by a fibrous polyurethane patch with condensed ROS-scavenging backbone units. *Adv. Healthc. Mater* 11, e2101855. doi:10.1002/adhm.202101855

Xu, H., Cao, W., and Zhang, X. (2013). Selenium-containing polymers: promising biomaterials for controlled release and enzyme mimics. *Acc. Chem. Res.* 46, 1647–1658. doi:10.1021/ar4000339

Xu, Q., He, C., Ren, K., Xiao, C., and Chen, X. (2016a). Thermosensitive polypeptide hydrogels as a platform for ROS-triggered cargo release with innate cytoprotective ability under oxidative stress. *Adv. Healthc. Mater* 5, 1979–1990. doi:10.1002/adhm.201600292

Xu, Q., He, C., Xiao, C., and Chen, X. (2016b). Reactive oxygen species (ROS) responsive polymers for biomedical applications. *Macromol. Biosci.* 16, 635–646. doi:10.1002/mabi.201500440

Xu, X., Li, Q., and Zhang, J. (2022). Reactive oxygen species-responsive and self-illuminating nanoparticles for inflammation and tumor imaging. *Methods Mol. Biol.* 2525, 21–34. doi:10.1007/978-1-0716-2473-9_3

Xu, Y., Huo, Y., Toufektsian, M. C., Ramos, S. I., Ma, Y., Tejani, A. D., et al. (2006). Activated platelets contribute importantly to myocardial reperfusion injury. *Am. J. Physiol. Heart Circ. Physiol.* 290, H692–H699. doi:10.1152/ajpheart.00634.2005

Yaman, S., Chintapula, U., Rodriguez, E., Ramachandramoorthy, H., and Nguyen, K. T. (2020). Cell-mediated and cell membrane-coated nanoparticles for drug delivery and cancer therapy. *Cancer Drug Resist* 3, 879–911. doi:10.20517/cdr.2020.55

Yang, J. W., Dong, X. Z., Wei, W. Y., Liu, K., Wu, X. P., and Dai, H. L. (2024). An injectable hydrogel dressing for controlled release of hydrogen sulfide pleiotropically mediates the wound microenvironment. *J. Mater. Chem. B* 12, 5377–5390. doi:10.1039/d4tb00411f

Yang, Q., He, G. W., Underwood, M. J., and Yu, C. M. (2016). Cellular and molecular mechanisms of endothelial ischemia/reperfusion injury: perspectives and implications for postischemic myocardial protection. *Am. J. Transl. Res.* 8, 765–777.

Yao, M. Y., Lu, Y. F., Shi, L., Huang, Y., Zhang, Q., Tan, J. L., et al. (2022a). A ROS-responsive, self-immolative and self-reporting hydrogen sulfide donor with multiple biological activities for the treatment of myocardial infarction. *Bioact. Mater.* 9, 168–182. doi:10.1016/j.bioactmat.2021.07.011

Yao, Y., Li, A., Wang, S., Lu, Y., Xie, J., Zhang, H., et al. (2022b). Multifunctional elastomer cardiac patches for preventing left ventricle remodeling after myocardial infarction *in vivo*. *Biomaterials* 282, 121382. doi:10.1016/j.biomaterials.2022.121382

Yellon, D. M., and Hausenloy, D. J. (2007). Myocardial reperfusion injury. *N. Engl. J. Med.* 357, 1121–1135. doi:10.1056/nejmra071667

Yoo, J., Rejinold, N. S., Lee, D., Jon, S., and Kim, Y. C. (2017). Protease-activatable cell-penetrating peptide possessing ROS-triggered phase transition for enhanced cancer therapy. *J. Control. Release* 264, 89–101. doi:10.1016/j.jconrel.2017.08.026

Yu, S. S., Koblin, R. L., Zachman, A. L., Perrien, D. S., Hofmeister, L. H., Giorgio, T. D., et al. (2011). Physiologically relevant oxidative degradation of oligo(proline) cross-linked polymeric scaffolds. *Biomacromolecules* 12, 4357–4366. doi:10.1021/bm201328k

Yu, T., Xu, Q., Chen, X., Deng, X., Chen, N., Kou, M. T., et al. (2024). Biomimetic nanomaterials in myocardial infarction treatment: harnessing bionic strategies for advanced therapeutics. *Mater Today Bio* 25, 100957. doi:10.1016/j.mtbio.2024.100957

Yu, X., Ge, L., Niu, L., Lian, X., Ma, H. C., and Pang, L. (2018). The dual role of inducible nitric oxide synthase in myocardial ischemia/reperfusion injury: friend or foe? *Oxidative Med. Cell. Longev.* 2018, 8364848. doi:10.1155/2018/8364848

Yuan, X. Y., Jia, Z., Li, J., Liu, Y. N., Huang, Y. Q., Gong, Y. C., et al. (2021). A diselenide bond-containing ROS-responsive ruthenium nanoplatform delivers nerve growth factor for Alzheimer's disease management by repairing and promoting neuron regeneration. *J. Mater. Chem. B* 9, 7835–7847. doi:10.1039/d1tb01290h

Yue, T. J., Ren, W. M., and Lu, X. B. (2023). Copolymerization involving sulfur-containing monomers. *Chem. Rev.* 123, 14038–14083. doi:10.1021/acs.chemrev.3c00437

Zhang, D., Wei, Y., Chen, K., Zhang, X., Xu, X., Shi, Q., et al. (2015). Biocompatible reactive oxygen species (ROS)-responsive nanoparticles as superior drug delivery vehicles. *Adv. Healthc. Mater* 4, 69–76. doi:10.1002/adhm.201400299

Zhang, J., Su, L., Liu, Z., Tang, J., Zhang, L., Li, Z., et al. (2024a). A responsive hydrogel modulates innate immune cascade fibrosis to promote ocular surface reconstruction after chemical injury. *J. Control Release* 365, 1124–1138. doi:10.1016/j.jconrel.2023.12.025

Zhang, J. H., Sun, D., Guo, Y. S., Tong, J. R., Liu, Q. Y., Gao, R., et al. (2024b). Targeted delivery of black phosphorus nanosheets by ROS responsive complex hydrogel based on angiogenesis and antioxidant promotes myocardial infarction repair. *J. Nanobiotechnology* 22, 433. doi:10.1186/s12951-024-02685-0

Zhang, X., Sun, Y., Yang, R., Liu, B., Liu, Y., Yang, J., et al. (2022a). An injectable mitochondria-targeted nanodrug loaded-hydrogel for restoring mitochondrial function and hierarchically attenuating oxidative stress to reduce myocardial ischemia-reperfusion injury. *Biomaterials* 287, 121656. doi:10.1016/j.biomaterials.2022.121656

Zhang, Z., Dalan, R., Hu, Z., Wang, J. W., Chew, N. W., Poh, K. K., et al. (2022b). Reactive oxygen species scavenging nanomedicine for the treatment of ischemic heart disease. *Adv. Mater* 34, e2202169. doi:10.1002/adma.202202169

Zheng, Z., Lei, C., Liu, H., Jiang, M., Zhou, Z., Zhao, Y., et al. (2022a). A ROS-responsive liposomal composite hydrogel integrating improved mitochondrial function and pro-angiogenesis for efficient treatment of myocardial infarction. *Adv. Healthc. Mater* 11, e2200990. doi:10.1002/adhm.202200990

Zheng, Z., Lei, C., Liu, H. B., Jiang, M. C., Zhou, Z. T., Zhao, Y. Q., et al. (2022b). A ROS-responsive liposomal composite hydrogel integrating improved mitochondrial function and pro-angiogenesis for efficient treatment of myocardial infarction. *Adv. Healthc. Mater.* 11, e2200990. doi:10.1002/adhm.202200990

Zhou, M., Yu, Y., Luo, X., Wang, J., Lan, X., Liu, P., et al. (2021). Myocardial ischemia-reperfusion injury: therapeutics from a mitochondria-centric perspective. *Cardiology* 146, 781–792. doi:10.1159/000518879

Ziegler, M., Xu, X., Yap, M. L., Hu, H., Zhang, J., and Peter, K. (2019). A self-assembled fluorescent nanoprobe for imaging and therapy of cardiac ischemia/reperfusion injury. *Adv. Ther.* 2, 1800133. doi:10.1002/adtp.201800133

frontiers | Frontiers in Bioengineering and Biotechnology

TYPE Review
PUBLISHED 20 September 2024
DOI 10.3389/fbioe.2024.1468833

OPEN ACCESS

EDITED BY
Donglin Xia,
Nantong University, China

REVIEWED BY
Wenyi Zheng,
Karolinska Institutet (KI), Sweden
Biao Wang,
BeiGene, China

*CORRESPONDENCE
Ying Xiao,
yingxiao@wchscu.cn

†These authors have contributed equally to this work

RECEIVED 22 July 2024
ACCEPTED 09 September 2024
PUBLISHED 20 September 2024

CITATION
Chu Q, Jiang X and Xiao Y (2024) Rebuilding the myocardial microenvironment to enhance mesenchymal stem cells-mediated regeneration in ischemic heart disease. *Front. Bioeng. Biotechnol.* 12:1468833. doi: 10.3389/fbioe.2024.1468833

Rebuilding the myocardial microenvironment to enhance mesenchymal stem cells-mediated regeneration in ischemic heart disease

Qing Chu[1†], Xin Jiang[2,3†] and Ying Xiao[1,4*]

[1]Regenerative Medicine Research Center, Sichuan University West China Hospital, Chengdu, Sichuan, China, [2]Department of Laboratory Medicine, Sichuan University West China Hospital, Chengdu, Sichuan, China, [3]Innovation Institute for Integration of Medicine and Engineering, Sichuan University West China Hospital, Chengdu, Sichuan, China, [4]Department of Postgraduate, Sichuan University West China Hospital, Chengdu, Sichuan, China

Mesenchymal stem cells (MSCs) are naturally-derived regenerative materials that exhibit significant potential in regenerative medicine. Previous studies have demonstrated that MSCs-based therapy can improve heart function in ischemia-injured hearts, offering an exciting therapeutic intervention for myocardial ischemic infarction, a leading cause of worldwide mortality and disability. However, the efficacy of MSCs-based therapies is significantly disturbed by the myocardial microenvironment, which undergoes substantial changes following ischemic injury. After the ischemic injury, blood vessels become obstructed and damaged, and cardiomyocytes experience ischemic conditions. This activates the hypoxia-induced factor 1 (HIF-1) pathway, leading to the rapid production of several cytokines and chemokines, including vascular endothelial growth factor (VEGF) and stromal-derived factor 1 (SDF-1), which are crucial for angiogenesis, cell migration, and tissue repair, but it is not sustainable. MSCs respond to these cytokines and chemokines by homing to the injured site and participating in myocardial regeneration. However, the deteriorated microenvironment in the injured myocardium poses challenges for cell survival, interacting with MSCs, and constraining their homing, retention, and migration capabilities, thereby limiting their regenerative potential. This review discusses how the deteriorated microenvironment negatively affects the ability of MSCs to promote myocardial regeneration. Recent studies have shown that optimizing the microenvironment through the promotion of angiogenesis can significantly enhance the efficacy of MSCs in treating myocardial infarction. This approach harnesses the full therapeutic potential of MSCs-based therapies for ischemic heart disease.

KEYWORDS

mesenchymal stem cells, microenvironment, agiogenesis, myocardial regeneration, ischemic heart disease

1 Introduction

Ischemic heart disease (IHD), caused by stenosis or blockage of the coronary arteries resulting in a lack of blood supply to the myocardium, remains one of the leading causes of death worldwide (Bradley and Berry, 2022; Pastena et al., 2024). Following myocardial ischemia, there is an extensive loss of cardiomyocytes, which are then replaced by excessive collagen deposition. This leads to impaired heart contraction and relaxation, eventually resulting in heart failure (Stone et al., 2023). Current clinical treatments, such as vasodilation, diuresis, and inotropic therapies, can temporarily relieve ischemic symptoms but do not regenerate new cardiomyocytes for functional recovery (Ahmadi et al., 2016; Boden et al., 2023; Niccoli et al., 2021). Given the limited self-renewal capacity of cardiomyocytes, cell-based strategies to replenish lost cardiomyocytes or promote endogenous repair offer a new option for patients (Hsiao et al., 2013; Madonna, 2022).

Mesenchymal stem cells (MSCs) are naturally derived regenerative materials with the capacity for self-renewal and multi-lineage differentiation, and they are widely distributed across various tissues (Castilla-Casadiego et al., 2020; Chang et al., 2021; Cherian et al., 2020). MSCs-based therapies have shown promising potential in promoting myocardial recovery from ischemic injury (Ward et al., 2018). However, the mechanistic understanding of MSCs in myocardial regeneration remains controversial (Najar et al., 2021). Although a growing body of preclinical and clinical studies has observed improvements in heart function, more cautious analyses have revealed that the quantity of cardiomyocytes differentiated from MSCs is far below the sufficiency needed to support significant myocardial recovery from MSCs treatment (Ward et al., 2018; Eschenhagen et al., 2017).

One of the most significant challenges is the low efficiency of MSCs homing to the infarcted heart, with cells often redistributing to other organs, including the lung, liver, and spleen (Chan et al., 2022; Penna et al., 2008). Additionally, a rapid loss of transplanted MSCs occurs within the first 48 h after transplantation via intravenous, intracoronary, or intramyocardial injection (Malik et al., 2020; Chin et al., 2024). Although there are techniques to enhance MSCs retention at the injured myocardium, such as cell patches, these MSCs primarily exert their effects through paracrine mechanisms, improving the microenvironment by promoting angiogenesis, reducing fibrosis, and modulating inflammation (Shi et al., 2021; Wu and Zhao, 2012; Yan et al., 2022; Zhang et al., 2016a). These findings suggest a critical issue: the ischemia-injured myocardium is unsuitable for MSCs homing, retention, and differentiation into cardiomyocytes, thereby limiting their potential for myogenesis.

The myocardial microenvironment is composed of various physiological, chemical, and biological factors primarily generated by non-cardiomyocyte cells, including immune cells, stromal cells, and vascular cells (Tang et al., 2020). Following ischemic injury, these cells undergo substantial changes, leading to a dynamic shift in the microenvironment (Li et al., 2021). Immune cells such as macrophages, neutrophils, and lymphocytes are rapidly activated in response to ischemic insult, migrating to the injured myocardium to eliminate debris from dead cells (Sun et al., 2021). The vasculature is damaged due to the ischemia-induced loss of vascular cells, including endothelial cells, pericytes, and smooth muscle cells (Lupu et al., 2020). Angiogenesis is then initiated, relying on viable endothelial cells from collateral vessels, contributing to the reconstruction of vasculature and partially alleviating hypoxia (Xiao et al., 2020). Stromal cells, mainly fibroblasts, are activated and transformed into myofibroblasts, producing abundant collagen and facilitating collagen crosslinking, leading to cardiac fibrosis (Li et al., 2014). These changes significantly impact the biological activities and functions of MSCs in myocardial regeneration (Khalil and McCain, 2021).

In this review, we summarized the current understanding of MSCs involved in myocardial regeneration and the relationship between changes in the myocardial microenvironment and the biological activities of MSCs during ischemic injury progression, providing a novel insight into the critical role of rebuilding the microenvironment in promoting the efficacy of MSCs in myocardial regeneration.

2 MSCs applied in IHDs therapy

MSCs are multipotent stem cells characterized by self-renewal, robust proliferative capacity, and multilineage differentiation potential. MSCs predominantly express positive markers such as CD29, CD90, CD105, and CD44, while showing negative expression of hematopoietic and vascular markers like CD45, CD34, CD19, CD11b, and CD14 (Dominici et al., 2006). MSCs can differentiate into various mesoderm lineages and cell types, including osteoblasts, adipocytes (Casado-Diaz et al., 2016), skeletal muscle myocytes/myotubes (Park et al., 2016), and cardiomyocytes (Makino et al., 1999) under growth factor-rich selective media. MSCs can be derived from a wide range of sources, including bone marrow, adipose tissue, umbilical cord, placenta, and dental pulp (Prakash et al., 2023). Bone marrow-derived MSCs (BM-MSCs) were the first identified and isolated from bone marrow (Friedenstein et al., 1970; Friedenstein et al., 1966) and have emerged as one of the leading candidates for clinical translational applications. Due to the invasive nature of harvesting BM-MSCs and their poor cell viability, alternative sources of MSCs have been explored. Among these, umbilical cord mesenchymal stem cells (UC-MSCs) are considered one of the most ideal sources for transplantation therapy due to their ease of collection, wide availability, and low immunogenicity (Sriramulu et al., 2018). Additionally, adipose-derived mesenchymal stem cells (AD-MSCs) exhibit stronger immunomodulatory properties compared to other MSCs and have also been extensively studied (Czerwiec et al., 2023). While MSCs from different sources have varying characteristics in terms of collection, proliferation, differentiation, and functional regulation (Hoogduijn et al., 2014), their capacity for myocardial regeneration is recognized for its encouraging potential in the therapeutic effect of IHD. Since the early 2000s, when landmark studies reported that bone marrow cells could potentially replace damaged myocardium in the adult heart (Orlic et al., 2001), MSCs have been studied for the treatment of IHD for over 20 years, yielding promising preclinical results and mixed clinical outcomes.

2.1 Preclinical studies

Since Orlic et al. reported the potential of bone marrow cells to replace damaged adult myocardium in 2001, a finding that was later

TABLE 1 Summary of the ongoing clinical trials for IHD.

Trial ID	Trial title	Cell source	Condition	Phase	Routine
NCT06147986	Evaluate the Efficacy and Safety of Allogeneic Umbilical Cord Mesenchymal Stem Cells as an Add-On Treatment for Acute ST-elevation Myocardial Infarction (STEMI) Patients	Allogeneic umbilical cord mesenchymal stem cells	ST-elevation Myocardial Infarction	III	Intracoronary and Intravenous
NCT05935423	Umbilical Cord Mesenchymal Stem Cell Improve Cardiac Function on ST-elevation Myocardial Infarction (STEMI) Patients	Umbilical Cord Mesenchymal Stem Cell	ST Elevation Myocardial Infarction	III	Intracoronary
NCT05043610	MSCs for Prevention of MI-induced HF	Umbilical Cord Mesenchymal Stem Cell	Myocardial Infarction, Acute	III	Intracoronary
NCT04776239	Allogeneic Mesenchymal Human Stem Cell Infusion Therapy for Endothelial DySfunctiOn in Diabetic Subjects With Symptomatic Ischemic Heart Disease. (ACESO-IHD)	Umbilical Cord Mesenchymal Stem Cell	Ischemic Heart Disease; Diabetes Mellitus	I/II	Intravenous

challenged, MSCs-based therapies for myocardial regeneration have been extensively studied. These studies have utilized differentiated or undifferentiated MSCs from allogeneic, autologous, and even xenogeneic sources, employing various delivery approaches (Huang et al., 2010; Jansen Of Lorkeers et al., 2015; Luger et al., 2017; Tomita et al., 1999). Meta-analyses have reported an overall 12% increase in left ventricular ejection fraction (LVEF) in rodent studies following MSCs administration compared to untreated groups. Additionally, a 7% increase in LVEF was observed in large species such as pigs, with only 7 out of 16 studies showing favorable results for MSCs. Correspondingly, an 8% reduction in infarct size was observed in half of the preclinical studies in rodents, and a 6.4% reduction in pig hearts was noted in the seven studies that reported favorable results for MSCs administration (Kanelidis et al., 2017).

2.2 Clinical trials

Most clinical trials of cell therapy for IHD have concentrated on BM-, with AD- and UC-MSCs also being studied in recent years (Ward et al., 2018). These trials have demonstrated favorable safety and tolerability. The treatment of acute myocardial infarction (AMI) typically involves the intracoronary injection of MSCs following percutaneous coronary intervention (PCI), with intravenous injection being used in some cases. A meta-analysis of 13 clinical trials in AMI reported a highly significant 3.78% increase in LVEF for the MSCs-treated group compared to the control group (Attar et al., 2021). MSCs have also been investigated for the treatment of chronic ischemia and ischemic cardiomyopathy. The primary route of treatment for chronic myocardial infarction (MI) is intramyocardial, rather than intracoronary or intravenous (Wang et al., 2015a). A meta-analysis demonstrated the efficacy of MSCs, highlighting the overall safety and efficacy of autologous BM-MSCs in chronic MI treatment (Kanelidis et al., 2017). A randomized controlled trial by Zhang et al. assessed the efficacy of MSCs transplantation in patients with chronic MI, reporting significant improvements in LVEF and reduced infarct size (Wang et al., 2015b). These findings supported the long-term outcomes of MSCs therapy, observing improved survival rates, reduced rehospitalization, and enhanced quality of life among treated patients (Afzal et al., 2015). Nowadays, there are 2 related MSC products approved for the treatment of peripheral vascular disease. One is Stempeucel for atherosclerotic and non-atherosclerotic critical limb ischemia, developed by Stempeutics; and the other is Vescell (ACP-01), under development by Hemostemix, for the treatment of IHD. Several clinical trials are currently underway for the treatment of IHD using UC-MSCs (Table 1).

2.3 Mechanisms of MSCs in promoting myocardial regeneration

2.3.1 Differentiation, paracrine effects and immunomodulation of MSCs

Numerous studies have demonstrated the ability of MSCs to differentiate into cardiomyocytes, endothelial cells, and smooth muscle cells. Notably, evidence of MSCs differentiating into functional cardiomyocytes, including the acquisition of contractile properties and the expression of cardiomyocyte marker genes *in vitro*, has been observed after treatment with 5-azacytidine, a hypomethylating agent (Tomita et al., 1999). Due to safety concerns, further studies have shifted from the use of 5-azacytidine to alternative agents, such as insulin and dexamethasone, to induce MSCs differentiation into cardiomyocytes (Shim et al., 2004). Transplantation of these MSCs-derived cardiomyocytes into ischemic-injured hearts has been shown to contribute to myocardial functional recovery (Iso et al., 2007). Of note, undesirable integration of these transplanted cells with the resident cardiomyocytes, and the occurrence of arrhythmia post-transplantation primarily hinders the application of MSCs in the treatment of IHD (Yagyu et al., 2019). Moreover, several studies have reported when MSCs were directly transplanted into the myocardium, they rarely differentiated into cardiomyocytes, possibly ascribed to lacking of appropriate signals and microenvironment (Eschenhagen et al., 2017; Leiker et al., 2008). Results from animal and patients have demonstrated that MSCs can improve cardiac function, although this improvement is likely not due solely to the replacement of injured contractile cardiomyocytes. With the advancement of research technology, more evidence shows that MSCs promote the improvement of cardiac function not through the differentiation into cardiomyocytes but through paracrine effects and immunomodulation (Gallina et al., 2015).

Paracrine effects are currently widely studied for understanding MSCs-induced myocardial regeneration (Li et al., 2023). MSCs primarily secrete various growth factors and cytokines, such as vascular endothelial growth factor (VEGF), fibroblast growth

factor (FGF), and insulin-like growth factor-1 (IGF-1) (Gallina et al., 2015). These factors promote angiogenesis in ischemic regions, improving blood supply to the myocardial tissue and providing necessary nutrients and oxygen for cardiomyocyte regeneration (Yin et al., 2023). Additionally, MSCs produce anti-fibrotic factors that reduce scar tissue formation by inhibiting fibroblast-to-myofibroblast transition and reducing collagen fiber deposition (Takahashi et al., 2006). Moreover, MSCs secrete immunomodulatory factors that inhibit T-cell activation, thereby reducing the production of pro-inflammatory cytokines that might further damage cardiomyocytes (Gomez-Ferrer et al., 2021).

MSCs can activate intrinsic immune responses. Direct injection of adult stem cells can trigger an acute inflammatory response characterized by $CCR2^{+}$ and $CX3CR1^{+}$ macrophage accumulation, which alters fibroblast activity, reduces fibrosis, and enhances the mechanical properties of the injured heart (Vagnozzi et al., 2020). Furthermore, MSCs interact directly with immune cells, such as macrophages, T-cells, and natural killer (NK) cells. They can polarize macrophages towards an M2 phenotype, associated with anti-inflammatory and pro-repair activities. This shift promotes the clearance of cellular debris and supports angiogenesis while inhibiting the release of harmful pro-inflammatory cytokines (Ben-Mordechai et al., 2013). Similarly, MSCs can suppress T-cell proliferation and activation, reducing the risk of allograft rejection and alloreactivity in transplantation settings (Martinez et al., 2017).

2.3.2 The processes of MSCs participation in myocardial regeneration

The underlying processes of MSCs in myocardial regeneration involve their homing to the injured myocardium and retention there for subsequent functions. These processes require precise regulation of multiple signals and structural support.

2.3.2.1 Homing

MSCs homing refers to the biological activities that enable MSCs to move towards the injured site, which is the first and foremost step for their participation in myocardial regeneration (Szydlak, 2019). The direction of MSCs migration is determined by several cytokines, chemokines, and pro-inflammatory factors. These signals, produced in response to ischemic injury, act as navigators for MSCs homing and are termed tissue injury signals. Stromal cell-derived factor-1 (SDF-1), also known as CXCL12, is one of the most important tissue injury signals for MSCs homing (Zhang et al., 2016a). After ischemic injury, SDF-1 proteins are rapidly upregulated in the injured myocardium and released into the circulation (Rota, 2010). SDF-1 proteins bind to the receptor CXCR4 on MSCs, activating intracellular signal transduction via the mitogen-activated protein kinase (MAPK) pathways to phosphorylate cytoskeletal proteins like vimentin for cell migration (Chen et al., 2020; Tang et al., 2011). Consequently, MSCs are mobilized from their resident niche into the circulation and then move towards the injured myocardium (Tang et al., 2011). Other tissue injury signals, including pro-inflammatory factors (interleukins [ILs] and tumor-necrosis factor-α [TNF-α]) and growth factors (VEGF, PDGF and TGF-β), also play a role in MSCs homing (Szydlak, 2019). The process of MSCs homing generally occurs in the early phase after ischemic injury, accompanied by the upregulation of tissue injury signals at the injured site (Kang and Zheng, 2013).

The conduit for tissue injury signal transduction is primarily the vasculature-dependent circulation system. This conduit is essential for the movement of circulating stem cells and their arrival at the injury site (Kang and Zheng, 2013). When MSCs reach the injured site, regional chemokines and cytokines in high concentrations bind to receptors on the MSCs, mediating their rolling along endothelial cells. Thereafter, adhesive molecules like vascular cell adhesion molecule-1 (VCAM-1) on the surface of endothelial cells bind to integrins on the membranes of MSCs, inducing MSCs adhesion and subsequent transmigration through the endothelial layer, thus completing MSCs homing (Segers et al., 2006; Nitzsche et al., 2017).

Direct injection of MSCs into the injured myocardium bypasses the homing process, and forces MSCs to remain there. This technique is widely used in MSC-based therapy for IHDs but is an invasive procedure that brings additional risks to patients (Kanelidis et al., 2017). Moreover, intramyocardial injection of MSCs can create isolated cell islands with poor connections to native cardiomyocytes, potentially causing arrhythmias in the future (Yagyu et al., 2019).

2.3.2.2 Retention

After homing to the injured myocardium, MSCs must survive and be colonized there for long-term retention. Essential oxygen and nutrients are necessary for the survival of MSCs, and both are mainly provided by vasculature. Some research has demonstrated that MSCs can tolerate lower oxygen levels (5%) via the activation of the HIF-1 signaling pathway, with their paracrine function to promote angiogenesis being enhanced under hypoxic conditions compared to normal conditions with 21% oxygen (Sun et al., 2020a). However, in the context of MSCs transplantation in IHDs, deprivation of oxygen and nutrients by damaged vasculature usually creates a deteriorated microenvironment, leading to massive MSCs apoptosis post-transplantation (Chen et al., 2018). Poor retention of transplanted MSCs is a significant drawback that limits the clinical application of MSCs-based therapy for IHDs (Kanki et al., 2011).

The colonization of MSCs after homing to the injured myocardium is also regulated by mechanical stress provided by the extracellular matrix (ECM) (Raimondi et al., 2013). MSCs are sensitive to changes in mechanical stress via ion channels on the cell surface, including Piezo1, which activates the intracellular Hippo pathway effector YAP/TAZ to regulate cell morphology, proliferation, and differentiation. A previous study revealed that a 3D soft and elastic hydrogel could effectively enhance cell growth, proliferation, and osteogenic differentiation of MSCs (Di et al., 2023). Additionally, the differentiation of embryonic stem cells (ESCs) into cardiomyocytes favored 3D cultures with less mechanical stress than 2D cultures (Ou et al., 2011). However, an increase in mechanical stress due to excessive collagen deposition after ischemic injury may hinder the colonization, proliferation, and differentiation of transplanted MSCs (Li et al., 2014).

2.3.2.3 Promotion of myocardial regeneration

After MSCs homing and retention in the injured myocardium, they can perform functions such as secretion and differentiation for myocardial regeneration.

The role of MSCs in myocardial regeneration is debated, particularly whether they can differentiate into cardiomyocytes to replace lost cardiomyocytes after ischemic injury, as we also noted

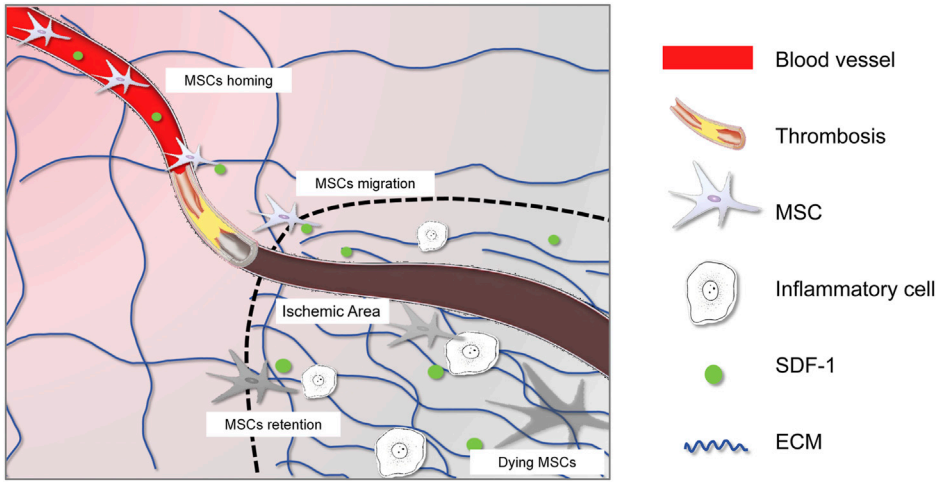

FIGURE 1
Interplay between MSCs and the altered microenvironment after ischemic injury. The graphic symbols were listed in the right panel.

above. One crucial requirement for MSCs differentiation is the induction of specific signals (Eschenhagen et al., 2017). During heart development, several factors, including BMPs, WNTs, and FGFs, and the sequential activation of transcription factors like MIXL1, Nkx2.5, and GATA4, are involved in the differentiation from MSCs into cardiomyocytes (Buijtendijk et al., 2020). The first report in 1999 indicated the induction of adult MSCs differentiation into cardiomyocyte-like cells with sarcomere for spontaneous contraction by adding 5-azacytidine into the cultures (Makino et al., 1999; Tomita et al., 1999). Further studies have developed various methods by combining different chemicals to improve the efficiency of MSCs differentiation into cardiomyocytes, and these induced cardiomyocytes have been applied for cell transplantation in IHDs for myocardial regeneration (Shim et al., 2004). However, little studies have observed that MSCs differentiate into cardiomyocytes *in vivo* (Leiker et al., 2008), likely due to the lack of appropriate signals in the microenvironment.

3 Interplay between MSCs and the altered microenvironment after ischemic injury

The myocardial microenvironment is a complex system composed of various non-cardiomyocytes, including immune cells, vascular cells, and fibroblasts, as well as the non-cellular extracellular matrix. It plays a critical role in modulating the behavior of MSCs and influencing their ability to effectively participate in tissue repair and regeneration (Franchi et al., 2020).

3.1 Pathological changes after myocardial ischemia

The dramatic pathological changes following myocardial ischemia include the massive loss of cardiomyocytes, destruction of microvessels, and recruitment and activation of immune cells (Figure 1). Current knowledge indicates that the regenerative capacity of cardiomyocytes is extremely weak, leading to fibrotic repair to maintain the heart's integrity. Various fibrotic mediators and cytokines released by macrophages, lymphocytes, and other cells create a fibrotic microenvironment in the ischemic area, stimulating the transformation of fibroblasts into myofibroblasts (Xiao et al., 2023). These myofibroblasts produce large amounts of extracellular matrix proteins, leading to collagen deposition and cardiac fibrosis, which induces adverse remodeling that can gradually progress to heart failure (Prabhu and Frangogiannis, 2016).

3.2 Change of vasculature and the deteriorated microenvironment

Appropriate vasculature is crucial for the survival and normal function of cardiac cells, as it provides essential oxygen, nutrients, growth factors, and cytokines (Brutsaert, 2003). Ischemic injury, arising from the obstruction of blood vessels, can lead to further structural damage in these vessels (Xiao et al., 2021a). Endothelial cells, in particular, are highly susceptible to ischemic insults and may experience impaired integrity and increased permeability. This disruption of the endothelial barrier facilitates the leakage of fluid and macromolecules into the surrounding tissue, exacerbating the ischemic injury (Chu et al., 2023). Additionally, ischemic insults can damage the basement membrane, resulting in the loss of its structural support and regulatory functions. Furthermore, smooth muscle cells in the vessel wall may undergo apoptosis or dysfunction, compromising the structural integrity of blood vessels and contributing to the progression of vascular remodeling and dysfunction (Heitzer et al., 2001). In response to ischemia-induced hypoxia, angiogenesis is initiated, sprouting from existing endothelial cells and expanding towards the injured site to recover blood supply (Nofi et al., 2018). However, angiogenesis is often not sustained, and vascular remodeling further impairs the ability of blood vessels to withstand hemodynamic stress (Xiao et al., 2021a).

The ischemic injury leading to vascular changes directly affect the survival and migration of MSCs. As blood vessels are the primary route for MSCs to obtain oxygen, nutrients, and growth factors, vascular obstruction or damage disrupts the microenvironment, compromising their survival and normal functions (Kang and Zheng, 2013). On the other hand, endothelial cells losing their integrity and increasing vascular permeability might facilitate the migration of MSCs from blood vessels to the injured site (Chu et al., 2023). Additionally, in response to ischemia-induced hypoxia, MSCs might activate their paracrine effects on immunomodulation and suppress inflammatory responses (Xiao et al., 2021b). Some studies showed that hypoxia might shift the differentiation preference of MSCs towards vascular repair-related cell types, including endothelial cells and smooth muscle cells (Tian et al., 2022).

Following ischemic injury, the heart undergoes a series of intricate immune responses involving the activation and infiltration of various immune cells. These include both innate immune cells, such as neutrophils and macrophages, and adaptive immune cells, including T and B cells (Nahrendorf et al., 2007; Frangogiannis, 2014). These immune cells accumulate at the site of cardiac injury and release a multitude of inflammatory mediators and cytokines, such as interleukins (IL-1, IL-6, IL-17), tumor necrosis factor-alpha (TNF-α), chemokines (CXCL1, CCL2), and reactive oxygen species (ROS), which further promote the inflammatory response and tissue repair (Swirski and Nahrendorf, 2013). The immune response typically peaks within 4–7 days following ischemic injury and subsequently reduces to a stable state over time (Xiao et al., 2021a).

MSCs respond to cytokines and chemokines released from the injured myocardium, rapidly mobilizing and migrating towards the site of injury under the guidance of these factors (Kang and Zheng, 2013). Once in the injured myocardium, MSCs interact with various immune cells. Macrophages play a pivotal role in the inflammatory response following ischemic heart injury, with the ability to polarize into M1 (pro-inflammatory) or M2 (anti-inflammatory) phenotypes, each exerting distinct effects on MSCs (Ben-Mordechai et al., 2013). M1 macrophages release pro-inflammatory cytokines that can compromise MSCs survival and function, while M2 macrophages foster a more conducive environment for MSCs-mediated tissue repair. Reciprocally, MSCs can influence macrophage polarization, favoring the M2 phenotype, which aids in reducing inflammation and promoting healing (Neupane et al., 2023). Additionally, MSCs can mitigate the inflammatory response by suppressing T cell proliferation and activation (Behm et al., 2024), as well as inhibiting NK cell activation and cytotoxicity, thereby protecting heart tissue from immune-mediated damage. The interplay between MSCs and immune cells is dynamic, with MSCs promoting a more balanced immune response that supports tissue repair (Najar et al., 2010).

On the other hand, the ECM forms the native cellular support network and has a strong interplay with its residing cells. Following myocardial ischemic injury, the ECM undergoes significant remodeling, particularly in its composition (Chu et al., 2021). Activated cardiac fibroblasts proliferate and increase the synthesis of collagenous proteins, primarily types I and III collagen, which are then deposited in the ECM. This excessive deposition of collagenous proteins leads to fibrosis, altering the structural integrity of the myocardium (Xiao et al., 2023). In addition to collagen, non-collagenous components of the ECM, such as glycosaminoglycans, proteoglycans, elastin, and laminin, may also undergo changes in their content and distribution, further contributing to ECM remodeling (Bonnans et al., 2014).

This remodeling process creates a new microenvironment that supports MSCs migration and affects their biological behavior. Firstly, the remodeled ECM provides a structural framework and essential cues for MSCs migration. Specific signals and adhesion molecules, including growth factors, cytokines, and chemokines embedded within the remodeled ECM, could guide MSCs to the injured area, acting as chemoattractants for efficient homing and tissue repair processes (Zhu et al., 2006). Additionally, the mechanical stress altered by the remodeled ECM might change MSCs biological functions, including their paracrine effects to attenuate myofibroblast transition-induced fibrosis (Galie and Stegemann, 2014) and promote angiogenesis (Piao et al., 2005). Furthermore, MSCs could acquire contraction ability when exposed to mechanical stretch, contributing to functional recovery after ischemic injury (Choi et al., 2017; Girao-Silva et al., 2014; Izadpanah et al., 2022). However, excessive collagen deposition leads to fibrotic scar formation, resulting in a deteriorated microenvironment for MSCs characterized by stiff ECM, intensive mechanical stress, and reduced blood vessels (Li et al., 2021). Therefore, this situation should be avoided when utilizing MSCs treatment for IHDs.

4 Rebuilding of myocardial microenvironment for MSCs promotion of myocardial regeneration

As discussed earlier, the efficacy of MSCs-based therapies largely depends on the quality of the recipient myocardial microenvironment. Enhancing the myocardial microenvironment is pivotal for maximizing the regenerative capacity of MSCs. By addressing the underlying deficiencies in the myocardial microenvironment and creating a more favorable setting for MSCs engraftment, the regenerative potential of MSCs can be fully realized, opening new therapeutic avenues for myocardial regeneration.

The essential role of vasculature in facilitating MSCs homing to injured tissue is well-documented (Shi et al., 2021). In IHDs, the destruction of blood vessels disrupts the signaling between the injured myocardium and MSCs and impedes MSCs migration to the injury site, ultimately hindering tissue regeneration. Numerous studies have demonstrated that promoting angiogenesis beforehand benefits the survival of transplanted MSCs (Shi et al., 2021; Chin et al., 2021). Recovering vasculature in the injured myocardium enhances the survival prospects of grafted MSCs, making angiogenesis a promising therapeutic approach (Figure 2).

4.1 Regulation of angiogenesis in the ischemic myocardium

The HIF-1 signaling pathway is a central regulator of angiogenesis, orchestrating the expression of multiple pro-angiogenic factors and metabolic adaptations essential for vessel formation (Semenza, 2014). HIF-1 is a heterodimeric transcription factor with two subunits: HIF-1α and HIF-1β (ARNT). HIF-1α, the

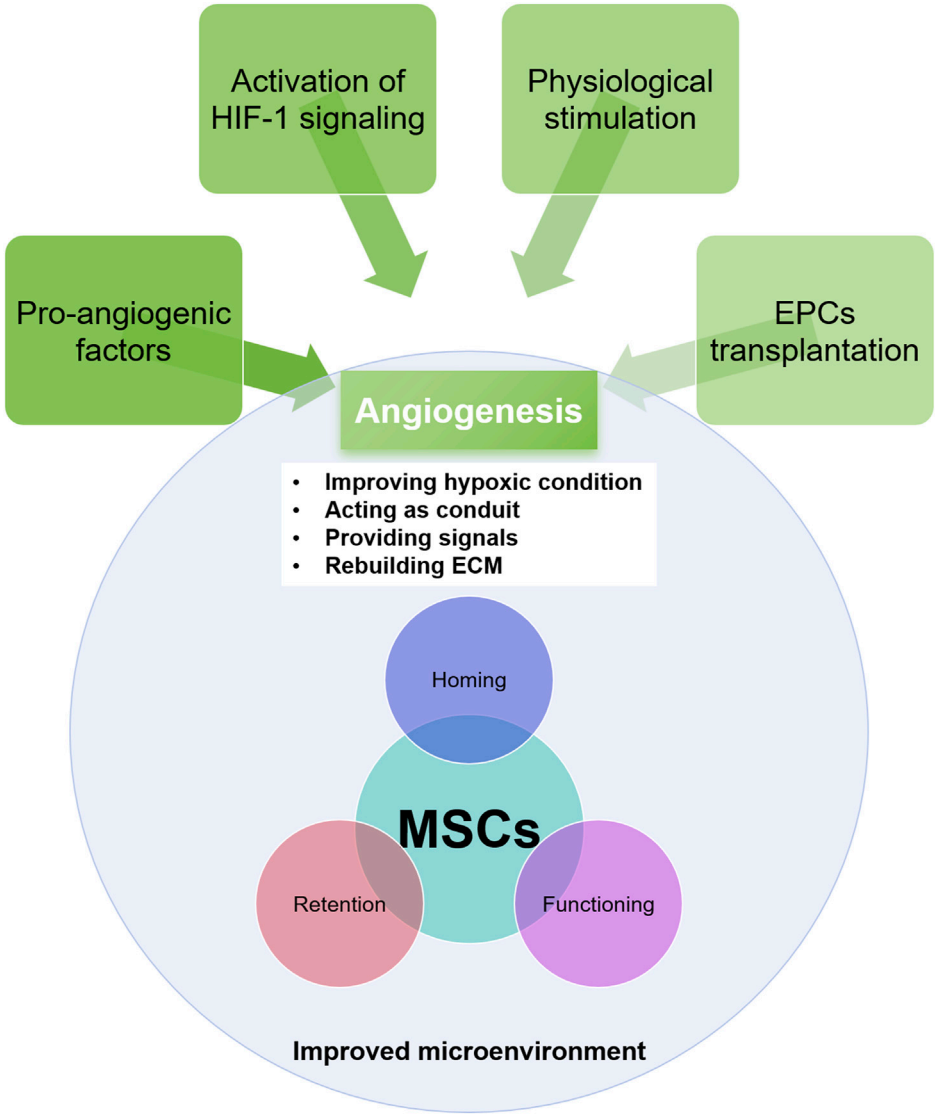

FIGURE 2
The approaches for angiogenesis and its role in rebuilding the microenvironment and in improving MSCs efficacy.

oxygen-sensitive subunit, is tightly regulated by cellular oxygen levels. Under hypoxic conditions, HIF-1α escapes hydroxylation and proteasomal degradation, translocates to the nucleus, and dimerizes with HIF-1β to form an active transcription complex (Wang et al., 1995). This complex binds to hypoxia-responsive elements (HREs) in target gene promoters, inducing their expression. One crucial target of HIF-1 in angiogenesis is VEGF, which promotes endothelial cell proliferation, migration, and tube formation (Liu et al., 2018; Cheng et al., 2016). HIF-1 directly upregulates VEGF expression, initiating and enhancing the angiogenic response and revascularization to improve tissue perfusion (Liu et al., 2018; Li et al., 2012).

However, the angiogenic response following myocardial ischemic injury is often impaired (Zhang et al., 2016b). While angiogenesis is rapidly activated in response to ischemic injury, peaking at day 4 and declining after 1 week, HIF-1α consistently accumulates in the ischemic myocardium (Xiao et al., 2020; Xiao et al., 2021a). The primary issue may be impaired activation of HIF-1 regulation of angiogenic factors, leading to an imbalance between angiogenic factors and their inhibitors. This imbalance hinders new blood vessel formation and limits tissue revascularization, ultimately affecting MSCs-mediated tissue repair. Additionally, the inflammatory response following myocardial ischemia releases pro-inflammatory cytokines that inhibit angiogenesis and promote fibrosis (Gomez-Ferrer et al., 2021).

4.2 Rebuilding of the microenvironment and enhancement of MSCs efficacy

Several mechanisms underlie the beneficial effects of angiogenesis on the ischemic myocardial microenvironment and MSCs function (Shi et al., 2021). Firstly, new blood vessel formation increases oxygen and nutrient delivery to the injured tissue and

removes waste products, creating a more conducive environment for MSCs survival and proliferation (Sun et al., 2020b). Secondly, angiogenesis stimulates the release of growth factors and cytokines beneficial for MSCs function. For instance, VEGF and FGF, potent angiogenic factors, also promote MSCs proliferation, migration, and differentiation (King et al., 2021). The restoration of functional vasculature in the ischemic myocardium provides a route for MSCs to migrate to the injury site and plays a key role in ECM reconstruction and inflammatory response modulation (Gomez-Ferrer et al., 2021; Sun et al., 2020b). Vasculature-derived ECM supports MSCs adhesion and migration, essential for efficient recruitment to damaged tissue (King et al., 2021). Angiogenesis also modulates the inflammatory response by promoting anti-inflammatory cell infiltration and reducing pro-inflammatory cytokine levels, creating a less hostile microenvironment for MSCs, allowing for better cell survival and function (Chin et al., 2021).

Promoting angiogenesis in ischemic heart disease can be achieved through activating angiogenic factors (Lupu et al., 2020). Direct intravenous injection, intramyocardial injection, or gene therapy with VEGF and FGF can significantly increase capillary density (Henning, 2016). Overexpression of HIF-1α via adenoviral or lentiviral vectors stimulates angiogenic factor expression (Huang et al., 2014). A recent study showed that while HIF-1α proteins consistently accumulate in the infarct zone, angiogenic factor expression is impaired, possibly due to dysfunction in selective HIF-1 signaling regulation. Supplementing the trace element copper can retune this dysregulation and reactivate HIF-1 target angiogenic factor expression without excessively increasing HIF-1α accumulation (Xiao et al., 2023; Zhang et al., 2016b).

Other techniques, including physical stimuli like low-intensity pulsed ultrasound (LIPUS) and electrical stimulation, have also been explored as non-invasive means to enhance VEGF expression and promote capillary formation (Amaral et al., 2001; Li et al., 2022). Electrical stimulation stimulates the release of angiogenic growth factors from endogenous cells and promotes neovascularization (Zhao et al., 2021). Both techniques have shown positive effects on angiogenesis and cardiac function in preclinical studies.

Another approach involves cell-based therapies, particularly using endothelial progenitor cells (EPCs). EPCs exhibit inherent angiogenic properties and secrete a diverse range of growth factors promoting blood vessel formation. When injected into the ischemic myocardium, EPCs can differentiate into vascular endothelial cells, directly participating in new blood vessel formation (Ghem et al., 2017; Zhang et al., 2008). Combining MSCs and EPCs for ischemic heart disease treatment represents an innovative and promising therapeutic approach. MSCs, known for their immunomodulatory effects, reduce inflammation and promote tissue repair, while EPCs specifically target endothelial cells regeneration. This combination harnesses the regenerative and angiogenic potential of these stem cells to promote cardiac tissue repair and restore blood flow to ischemic regions of the heart.

5 Conclusion and perspective

In conclusion, MSCs have emerged as a promising therapeutic option for IHDs due to their paracrine properties, which promote angiogenesis, modulate inflammatory responses, and inhibit the fibrotic process. However, the efficacy of MSCs-based therapies is significantly disturbed by the myocardial microenvironment, which undergoes dramatic changes following ischemic injury. Rebuilding the myocardial microenvironment, particularly by promoting angiogenesis, is a pivotal strategy to enhance the regenerative capacity of MSCs. Angiogenesis improves tissue perfusion and creates a more conducive environment for MSCs survival and function. Strategies to promote angiogenesis, such as activating the HIF-1 signaling pathway, supplementing copper, and combining EPCs and MSCs-based therapies, have shown promising results in preclinical studies. Future research should focus on elucidating the mechanisms underlying MSCs promotion of myocardial regeneration, developing novel techniques to rejuvenate the ischemic microenvironment, and conducting rigorous clinical trials to validate the efficacy and safety of these therapeutic approaches. With continued advancements in stem cell biology and regenerative medicine, MSCs-based therapies hold great potential for treating IHD, ultimately improving patient outcomes and quality of life.

Author contributions

QC: Writing–original draft. XJ: Writing–original draft. YX: Writing–original draft, Writing–review and editing.

Funding

The author(s) declare that financial support was received for the research, authorship, and/or publication of this article. This work was supported by China Postdoctoral Science Foundation (2023M732445 to JX) and Sichuan University West China Hospital.

Acknowledgments

The authors acknowledge the Chat Generative Pre-trained Transformer (ChatGPT, version GPT3.5 developed by OpenAI) in checking grammar and sentence structure of the manuscript.

Conflict of interest

The authors declare that the research was conducted in the absence of any commercial or financial relationships that could be construed as a potential conflict of interest.

Publisher's note

References

Afzal, M. R., Samanta, A., Shah, Z. I., Jeevanantham, V., Abdel-Latif, A., Zuba-Surma, E. K., et al. (2015). Adult bone marrow cell therapy for ischemic heart disease: evidence and insights from randomized controlled trials. *Circ. Res.* 117 (6), 558–575. doi:10.1161/circresaha.114.304792

Ahmadi, A., Stone, G. W., Leipsic, J., Shaw, L. J., Villines, T. C., Kern, M. J., et al. (2016). Prognostic determinants of coronary atherosclerosis in stable ischemic heart disease: anatomy, physiology, or morphology? *Circ. Res.* 119 (2), 317–329. doi:10.1161/circresaha.116.308952

Amaral, S. L., Linderman, J. R., Morse, M. M., and Greene, A. S. (2001). Angiogenesis induced by electrical stimulation is mediated by angiotensin II and VEGF. *Microcirculation* 8 (1), 57–67. doi:10.1080/mic.8.1.57.67

Attar, A., Bahmanzadegan Jahromi, F., Kavousi, S., Monabati, A., and Kazemi, A. (2021). Mesenchymal stem cell transplantation after acute myocardial infarction: a meta-analysis of clinical trials. *Stem Cell Res. Ther.* 12 (1), 600. doi:10.1186/s13287-021-02667-1

Behm, C., Milek, O., Rausch-Fan, X., Moritz, A., and Andrukhov, O. (2024). Paracrine- and cell-contact-mediated immunomodulatory effects of human periodontal ligament-derived mesenchymal stromal cells on CD4(+) T lymphocytes. *Stem Cell Res. Ther.* 15 (1), 154. doi:10.1186/s13287-024-03759-4

Ben-Mordechai, T., Holbova, R., Landa-Rouben, N., Harel-Adar, T., Feinberg, M. S., Abd Elrahman, I., et al. (2013). Macrophage subpopulations are essential for infarct repair with and without stem cell therapy. *J. Am. Coll. Cardiol.* 62 (20), 1890–1901. doi:10.1016/j.jacc.2013.07.057

Boden, W. E., Marzilli, M., Crea, F., Mancini, G. B. J., Weintraub, W. S., Taqueti, V. R., et al. (2023). Evolving management paradigm for stable ischemic heart disease patients: JACC review topic of the week. *J. Am. Coll. Cardiol.* 81 (5), 505–514. doi:10.1016/j.jacc.2022.08.814

Bonnans, C., Chou, J., and Werb, Z. (2014). Remodelling the extracellular matrix in development and disease. *Nat. Rev. Mol. Cell Biol.* 15 (12), 786–801. doi:10.1038/nrm3904

Bradley, C., and Berry, C. (2022). Definition and epidemiology of coronary microvascular disease. *J. Nucl. Cardiol.* 29 (4), 1763–1775. doi:10.1007/s12350-022-02974-x

Brutsaert, D. L. (2003). Cardiac endothelial-myocardial signaling: its role in cardiac growth, contractile performance, and rhythmicity. *Physiol. Rev.* 83 (1), 59–115. doi:10.1152/physrev.00017.2002

Buijtendijk, M. F. J., Barnett, P., and van den Hoff, M. J. B. (2020). Development of the human heart. *Am. J. Med. Genet. C Semin. Med. Genet.* 184 (1), 7–22. doi:10.1002/ajmg.c.31778

Casado-Diaz, A., Anter, J., Dorado, G., and Quesada-Gomez, J. M. (2016). Effects of quercetin, a natural phenolic compound, in the differentiation of human mesenchymal stem cells (MSC) into adipocytes and osteoblasts. *J. Nutr. Biochem.* 32, 151–162. doi:10.1016/j.jnutbio.2016.03.005

Castilla-Casadiego, D. A., Reyes-Ramos, A. M., Domenech, M., and Almodovar, J. (2020). Effects of physical, chemical, and biological stimulus on h-MSC expansion and their functional characteristics. *Ann. Biomed. Eng.* 48 (2), 519–535. doi:10.1007/s10439-019-02400-3

Chan, A. M. L., Sampasivam, Y., and Lokanathan, Y. (2022). Biodistribution of mesenchymal stem cells (MSCs) in animal models and implied role of exosomes following systemic delivery of MSCs: a systematic review. *Am. J. Transl. Res.* 14 (4), 2147–2161.

Chang, D., Fan, T., Gao, S., Jin, Y., Zhang, M., and Ono, M. (2021). Application of mesenchymal stem cell sheet to treatment of ischemic heart disease. *Stem Cell Res. Ther.* 12 (1), 384. doi:10.1186/s13287-021-02451-1

Chen, M., Li, R., Yin, W., Wang, T., and Kang, Y. J. (2020). Copper promotes migration of adipose-derived stem cells by enhancing vimentin-Ser39 phosphorylation. *Exp. Cell Res.* 388 (2), 111859. doi:10.1016/j.yexcr.2020.111859

Chen, T., Zhu, H., Wang, Y., Zhao, P., Chen, J., Sun, J., et al. (2018). Apoptosis of bone marrow mesenchymal stromal/stem cells via the MAPK and endoplasmic reticulum stress signaling pathways. *Am. J. Transl. Res.* 10 (8), 2555–2566.

Cheng, C., Li, P., Wang, Y. G., Bi, M. H., and Wu, P. S. (2016). Study on the expression of VEGF and HIF-1α in infarct area of rats with AMI. *Eur. Rev. Med. Pharmacol. Sci.* 20 (1), 115–119.

Cherian, D. S., Bhuvan, T., Meagher, L., and Heng, T. S. P. (2020). Biological considerations in scaling up therapeutic cell manufacturing. *Front. Pharmacol.* 11, 654. doi:10.3389/fphar.2020.00654

Chin, S. P., Marzuki, M., Tai, L., Mohamed Shahrehan, N. A., Ricky, C., Fanty, A., et al. (2024). Dynamic tracking of human umbilical cord mesenchymal stem cells (hUC-MSCs) following intravenous administration in mice model. *Regen. Ther.* 25, 273–283. doi:10.1016/j.reth.2024.01.003

Chin, S. P., Maskon, O., Tan, C. S., Anderson, J. E., Wong, C. Y., Hassan, H. H. C., et al. (2021). Synergistic effects of intracoronary infusion of autologous bone marrow-derived mesenchymal stem cells and revascularization procedure on improvement of cardiac function in patients with severe ischemic cardiomyopathy. *Stem Cell Investig.* 8, 2. doi:10.21037/sci-2020-026

Choi, M. Y., Kim, J. T., Lee, W. J., Lee, Y., Park, K. M., Yang, Y. I., et al. (2017). Engineered extracellular microenvironment with a tunable mechanical property for controlling cell behavior and cardiomyogenic fate of cardiac stem cells. *Acta Biomater.* 50, 234–248. doi:10.1016/j.actbio.2017.01.002

Chu, Q., Song, X., Xiao, Y., and Kang, Y. J. (2023). Alteration of endothelial permeability ensures cardiomyocyte survival from ischemic insult in the subendocardium of the heart. *Exp. Biol. Med. (Maywood)* 248 (16), 1364–1372. doi:10.1177/15353702231194344

Chu, Q., Xiao, Y., Song, X., and Kang, Y. J. (2021). Extracellular matrix remodeling is associated with the survival of cardiomyocytes in the subendocardial region of the ischemic myocardium. *Exp. Biol. Med. (Maywood)* 246 (24), 2579–2588. doi:10.1177/15353702211042020

Czerwiec, K., Zawrzykraj, M., Deptula, M., Skoniecka, A., Tyminska, A., Zielinski, J., et al. (2023). Adipose-derived mesenchymal stromal cells in basic research and clinical applications. *Int. J. Mol. Sci.* 24 (4), 3888. doi:10.3390/ijms24043888

Di, X., Gao, X., Peng, L., Ai, J., Jin, X., Qi, S., et al. (2023). Cellular mechanotransduction in health and diseases: from molecular mechanism to therapeutic targets. *Signal Transduct. Target Ther.* 8 (1), 282. doi:10.1038/s41392-023-01501-9

Dominici, M., Le Blanc, K., Mueller, I., Slaper-Cortenbach, I., Marini, F., Krause, D., et al. (2006). Minimal criteria for defining multipotent mesenchymal stromal cells. The International Society for Cellular Therapy position statement. *Cytotherapy* 8 (4), 315–317. doi:10.1080/14653240600855905

Eschenhagen, T., Bolli, R., Braun, T., Field, L. J., Fleischmann, B. K., Frisen, J., et al. (2017). Cardiomyocyte regeneration: a consensus statement. *Circulation* 136 (7), 680–686. doi:10.1161/circulationaha.117.029343

Franchi, F., Ramaswamy, V., Olthoff, M., Peterson, K. M., Paulmurugan, R., and Rodriguez-Porcel, M. (2020). The myocardial microenvironment modulates the biology of transplanted mesenchymal stem cells. *Mol. Imaging Biol.* 22 (4), 948–957. doi:10.1007/s11307-019-01470-y

Frangogiannis, N. G. (2014). The inflammatory response in myocardial injury, repair, and remodelling. *Nat. Rev. Cardiol.* 11 (5), 255–265. doi:10.1038/nrcardio.2014.28

Friedenstein, A. J., Chailakhjan, R. K., and Lalykina, K. S. (1970). The development of fibroblast colonies in monolayer cultures of Guinea-pig bone marrow and spleen cells. *Cell Tissue Kinet.* 3 (4), 393–403. doi:10.1111/j.1365-2184.1970.tb00347.x

Friedenstein, A. J., Piatetzky, S., and Petrakova, K. V. (1966). Osteogenesis in transplants of bone marrow cells. *J. Embryol. Exp. Morphol.* 16 (3), 381–390.

Galie, P. A., and Stegemann, J. P. (2014). Injection of mesenchymal stromal cells into a mechanically stimulated *in vitro* model of cardiac fibrosis has paracrine effects on resident fibroblasts. *Cytotherapy* 16 (7), 906–914. doi:10.1016/j.jcyt.2014.01.416

Gallina, C., Turinetto, V., and Giachino, C. (2015). A new paradigm in cardiac regeneration: the mesenchymal stem cell secretome. *Stem Cells Int.* 2015, 1–10. doi:10.1155/2015/765846

Ghem, C., Dias, L. D., Sant'Anna, R. T., Kalil, R. A. K., Markoski, M., and Nardi, N. B. (2017). Combined analysis of endothelial, hematopoietic, and mesenchymal stem cell compartments shows simultaneous but independent effects of age and heart disease. *Stem Cells Int.* 2017, 5237634. doi:10.1155/2017/5237634

Girao-Silva, T., Bassaneze, V., Campos, L. C., Barauna, V. G., Dallan, L. A., Krieger, J. E., et al. (2014). Short-term mechanical stretch fails to differentiate human adipose-derived stem cells into cardiovascular cell phenotypes. *Biomed. Eng. Online* 13, 54. doi:10.1186/1475-925x-13-54

Gomez-Ferrer, M., Villanueva-Badenas, E., Sanchez-Sanchez, R., Sanchez-Lopez, C. M., Baquero, M. C., Sepulveda, P., et al. (2021). HIF-1α and pro-inflammatory signaling improves the immunomodulatory activity of MSC-derived extracellular vesicles. *Int. J. Mol. Sci.* 22 (7), 3416. doi:10.3390/ijms22073416

Heitzer, T., Schlinzig, T., Krohn, K., Meinertz, T., and Munzel, T. (2001). Endothelial dysfunction, oxidative stress, and risk of cardiovascular events in patients with coronary artery disease. *Circulation* 104 (22), 2673–2678. doi:10.1161/hc4601.099485

Henning, R. J. (2016). Therapeutic angiogenesis: angiogenic growth factors for ischemic heart disease. *Future Cardiol.* 12 (5), 585–599. doi:10.2217/fca-2016-0006

Hoogduijn, M. J., Betjes, M. G., and Baan, C. C. (2014). Mesenchymal stromal cells for organ transplantation: different sources and unique characteristics? *Curr. Opin. Organ Transpl.* 19 (1), 41–46. doi:10.1097/mot.0000000000000036

Hsiao, L. C., Carr, C., Chang, K. C., Lin, S. Z., and Clarke, K. (2013). Stem cell-based therapy for ischemic heart disease. *Cell Transpl.* 22 (4), 663–675. doi:10.3727/096368912x655109

Huang, B., Qian, J., Ma, J., Huang, Z., Shen, Y., Chen, X., et al. (2014). Myocardial transfection of hypoxia-inducible factor-1α and co-transplantation of mesenchymal stem cells enhance cardiac repair in rats with experimental myocardial infarction. *Stem Cell Res. Ther.* 5 (1), 22. doi:10.1186/scrt410

Huang, X. P., Sun, Z., Miyagi, Y., McDonald Kinkaid, H., Zhang, L., Weisel, R. D., et al. (2010). Differentiation of allogeneic mesenchymal stem cells induces immunogenicity and limits their long-term benefits for myocardial repair. *Circulation* 122 (23), 2419–2429. doi:10.1161/circulationaha.110.955971

Iso, Y., Spees, J. L., Serrano, C., Bakondi, B., Pochampally, R., Song, Y. H., et al. (2007). Multipotent human stromal cells improve cardiac function after myocardial infarction in mice without long-term engraftment. *Biochem. Biophys. Res. Commun.* 354 (3), 700–706. doi:10.1016/j.bbrc.2007.01.045

Izadpanah, P., Golchin, A., Firuzyar, T., Najafi, M., Jangjou, A., and Hashemi, S. (2022). The effect of shear stress on cardiac differentiation of mesenchymal stem cells. *Mol. Biol. Rep.* 49 (4), 3167–3175. doi:10.1007/s11033-022-07149-y

Jansen Of Lorkeers, S. J., Eding, J. E., Vesterinen, H. M., van der Spoel, T. I., Sena, E. S., Duckers, H. J., et al. (2015). Similar effect of autologous and allogeneic cell therapy for ischemic heart disease: systematic review and meta-analysis of large animal studies. *Circ. Res.* 116 (1), 80–86. doi:10.1161/circresaha.116.304872

Kanelidis, A. J., Premer, C., Lopez, J., Balkan, W., and Hare, J. M. (2017). Route of delivery modulates the efficacy of mesenchymal stem cell therapy for myocardial infarction: a meta-analysis of preclinical studies and clinical trials. *Circ. Res.* 120 (7), 1139–1150. doi:10.1161/circresaha.116.309819

Kang, Y. J., and Zheng, L. (2013). Rejuvenation: an integrated approach to regenerative medicine. *Regen. Med. Res.* 1 (1), 7. doi:10.1186/2050-490x-1-7

Kanki, S., Segers, V. F., Wu, W., Kakkar, R., Gannon, J., Sys, S. U., et al. (2011). Stromal cell-derived factor-1 retention and cardioprotection for ischemic myocardium. *Circ. Heart Fail* 4 (4), 509–518. doi:10.1161/circheartfailure.110.960302

Khalil, N. N., and McCain, M. L. (2021). Engineering the cellular microenvironment of post-infarct myocardium on a chip. *Front. Cardiovasc Med.* 8, 709871. doi:10.3389/fcvm.2021.709871

King, O., Sunyovszki, I., and Terracciano, C. M. (2021). Vascularisation of pluripotent stem cell-derived myocardium: biomechanical insights for physiological relevance in cardiac tissue engineering. *Pflugers Arch.* 473 (7), 1117–1136. doi:10.1007/s00424-021-02557-8

Leiker, M., Suzuki, G., Iyer, V. S., Canty, J. M., and Lee, T. (2008). Assessment of a nuclear affinity labeling method for tracking implanted mesenchymal stem cells. *Cell Transpl.* 17 (8), 911–922. doi:10.3727/096368908786576444

Li, A. H., Liu, P. P., Villarreal, F. J., and Garcia, R. A. (2014). Dynamic changes in myocardial matrix and relevance to disease: translational perspectives. *Circ. Res.* 114 (5), 916–927. doi:10.1161/circresaha.114.302819

Li, J., Guo, W., Yu, F., Liu, L., Wang, X., Li, L., et al. (2022). Low-intensity pulsed ultrasound promotes angiogenesis via the AKT pathway and DNA methylation in human umbilical vein endothelial cells. *Ultrasonics* 118, 106561. doi:10.1016/j.ultras.2021.106561

Li, Q., Li, B., Ye, T., Xu, W., Yin, H., Deng, Z., et al. (2023). Requirements for human mesenchymal stem cell-derived small extracellular vesicles. *Interdiscip. Med.* 1 (1), e20220015. doi:10.1002/inmd.20220015

Li, S., Xie, H., Li, S., and Kang, Y. J. (2012). Copper stimulates growth of human umbilical vein endothelial cells in a vascular endothelial growth factor-independent pathway. *Exp. Biol. Med. (Maywood)* 237 (1), 77–82. doi:10.1258/ebm.2011.011267

Li, X., Zhang, Y., Ren, X., Wang, Y., Chen, D., Li, Q., et al. (2021). Ischemic microenvironment-responsive therapeutics for cardiovascular diseases. *Adv. Mater* 33 (52), e2105348. doi:10.1002/adma.202105348

Liu, X., Zhang, W., Wu, Z., Yang, Y., and Kang, Y. J. (2018). Copper levels affect targeting of hypoxia-inducible factor 1α to the promoters of hypoxia-regulated genes. *J. Biol. Chem.* 293 (38), 14669–14677. doi:10.1074/jbc.ra118.001764

Luger, D., Lipinski, M. J., Westman, P. C., Glover, D. K., Dimastromatteo, J., Frias, J. C., et al. (2017). Intravenously delivered mesenchymal stem cells: systemic anti-inflammatory effects improve left ventricular dysfunction in acute myocardial infarction and ischemic cardiomyopathy. *Circ. Res.* 120 (10), 1598–1613. doi:10.1161/circresaha.117.310599

Lupu, I. E., De Val, S., and Smart, N. (2020). Coronary vessel formation in development and disease: mechanisms and insights for therapy. *Nat. Rev. Cardiol.* 17 (12), 790–806. doi:10.1038/s41569-020-0400-1

Madonna, R. (2022). Exploring enhanced cell-based therapy for ischemic heart disease and heart failure. *J. Clin. Med.* 11 (13), 3837. doi:10.3390/jcm11133837

Makino, S., Fukuda, K., Miyoshi, S., Konishi, F., Kodama, H., Pan, J., et al. (1999). Cardiomyocytes can be generated from marrow stromal cells *in vitro*. *J. Clin. Invest* 103 (5), 697–705. doi:10.1172/jci5298

Malik, R., Darche, F. A., Rivinius, R., Seckinger, A., Krause, U., Koenen, M., et al. (2020). Quantitative efficacy and fate of mesenchymal stromal cells targeted to cardiac sites by radiofrequency catheter ablation. *Cell Transpl.* 29, 096368972091423. doi:10.1177/0963689720914236

Martinez, V. G., Ontoria-Oviedo, I., Ricardo, C. P., Harding, S. E., Sacedon, R., Varas, A., et al. (2017). Overexpression of hypoxia-inducible factor 1 alpha improves immunomodulation by dental mesenchymal stem cells. *Stem Cell Res. Ther.* 8 (1), 208. doi:10.1186/s13287-017-0659-2

Nahrendorf, M., Swirski, F. K., Aikawa, E., Stangenberg, L., Wurdinger, T., Figueiredo, J. L., et al. (2007). The healing myocardium sequentially mobilizes two monocyte subsets with divergent and complementary functions. *J. Exp. Med.* 204 (12), 3037–3047. doi:10.1084/jem.20070885

Najar, M., Melki, R., Khalife, F., Lagneaux, L., Bouhtit, F., Moussa, A. D., et al. (2021). Therapeutic mesenchymal stem/stromal cells: value, challenges and optimization. *Front. Cell Dev. Biol.* 9, 716853. doi:10.3389/fcell.2021.716853

Najar, M., Raicevic, G., Boufker, H. I., Fayyad Kazan, H., De Bruyn, C., Meuleman, N., et al. (2010). Mesenchymal stromal cells use PGE2 to modulate activation and proliferation of lymphocyte subsets: combined comparison of adipose tissue, Wharton's Jelly and bone marrow sources. *Cell Immunol.* 264 (2), 171–179. doi:10.1016/j.cellimm.2010.06.006

Neupane, Y. R., Handral, H. K., Alkaff, S. A., Chng, W. H., Venkatesan, G., Huang, C., et al. (2023). Cell-derived nanovesicles from mesenchymal stem cells as extracellular vesicle-mimetics in wound healing. *Acta Pharm. Sin. B* 13 (5), 1887–1902. doi:10.1016/j.apsb.2022.10.022

Niccoli, G., Morrone, D., De Rosa, S., Montone, R. A., Polimeni, A., Aimo, A., et al. (2021). The central role of invasive functional coronary assessment for patients with ischemic heart disease. *Int. J. Cardiol.* 331, 17–25. doi:10.1016/j.ijcard.2021.01.055

Nitzsche, F., Muller, C., Lukomska, B., Jolkkonen, J., Deten, A., and Boltze, J. (2017). Concise review: MSC adhesion cascade-insights into homing and transendothelial migration. *Stem Cells* 35 (6), 1446–1460. doi:10.1002/stem.2614

Nofi, C., Bogatyryov, Y., and Dedkov, E. I. (2018). Preservation of functional microvascular bed is vital for long-term survival of cardiac myocytes within large transmural post-myocardial infarction scar. *J. Histochem Cytochem* 66 (2), 99–120. doi:10.1369/0022155417741640

Orlic, D., Kajstura, J., Chimenti, S., Jakoniuk, I., Anderson, S. M., Li, B., et al. (2001). Bone marrow cells regenerate infarcted myocardium. *Nature* 410 (6829), 701–705. doi:10.1038/35070587

Ou, D. B., He, Y., Chen, R., Teng, J. W., Wang, H. T., Zeng, D., et al. (2011). Three-dimensional co-culture facilitates the differentiation of embryonic stem cells into mature cardiomyocytes. *J. Cell Biochem.* 112 (12), 3555–3562. doi:10.1002/jcb.23283

Park, S., Choi, Y., Jung, N., Yu, Y., Ryu, K. H., Kim, H. S., et al. (2016). Myogenic differentiation potential of human tonsil-derived mesenchymal stem cells and their potential for use to promote skeletal muscle regeneration. *Int. J. Mol. Med.* 37 (5), 1209–1220. doi:10.3892/ijmm.2016.2536

Pastena, P., Frye, J. T., Ho, C., Goldschmidt, M. E., and Kalogeropoulos, A. P. (2024). Ischemic cardiomyopathy: epidemiology, pathophysiology, outcomes, and therapeutic options. *Heart Fail Rev.* 29 (1), 287–299. doi:10.1007/s10741-023-10377-4

Penna, C., Raimondo, S., Ronchi, G., Rastaldo, R., Mancardi, D., Cappello, S., et al. (2008). Early homing of adult mesenchymal stem cells in normal and infarcted isolated beating hearts. *J. Cell Mol. Med.* 12 (2), 507–521. doi:10.1111/j.1582-4934.2007.00121.x

Piao, H., Youn, T. J., Kwon, J. S., Kim, Y. H., Bae, J. W., Bora, S., et al. (2005). Effects of bone marrow derived mesenchymal stem cells transplantation in acutely infarcting myocardium. *Eur. J. Heart Fail* 7 (5), 730–738. doi:10.1016/j.ejheart.2004.09.019

Prabhu, S. D., and Frangogiannis, N. G. (2016). The biological basis for cardiac repair after myocardial infarction: from inflammation to fibrosis. *Circ. Res.* 119 (1), 91–112. doi:10.1161/circresaha.116.303577

Prakash, N., Kim, J., Jeon, J., Kim, S., Arai, Y., Bello, A. B., et al. (2023). Progress and emerging techniques for biomaterial-based derivation of mesenchymal stem cells (MSCs) from pluripotent stem cells (PSCs). *Biomater. Res.* 27 (1), 31. doi:10.1186/s40824-023-00371-0

Raimondi, M. T., Eaton, S. M., Lagana, M., Aprile, V., Nava, M. M., Cerullo, G., et al. (2013). Three-dimensional structural niches engineered via two-photon laser polymerization promote stem cell homing. *Acta Biomater.* 9 (1), 4579–4584. doi:10.1016/j.actbio.2012.08.022

Rota, M. (2010). SDF-1 axis and myocardial repair. *Am. J. Physiol. Heart Circ. Physiol.* 299 (5), H1307–H1308. doi:10.1152/ajpheart.00876.2010

Segers, V. F., Van Riet, I., Andries, L. J., Lemmens, K., Demolder, M. J., De Becker, A. J., et al. (2006). Mesenchymal stem cell adhesion to cardiac microvascular endothelium: activators and mechanisms. *Am. J. Physiol. Heart Circ. Physiol.* 290 (4), H1370–H1377. doi:10.1152/ajpheart.00523.2005

Semenza, G. L. (2014). Hypoxia-inducible factor 1 and cardiovascular disease. *Annu. Rev. Physiol.* 76, 39–56. doi:10.1146/annurev-physiol-021113-170322

Shi, W., Xin, Q., Yuan, R., Yuan, Y., Cong, W., and Chen, K. (2021). Neovascularization: the main mechanism of MSCs in ischemic heart disease therapy. *Front. Cardiovasc Med.* 8, 633300. doi:10.3389/fcvm.2021.633300

Shim, W. S., Jiang, S., Wong, P., Tan, J., Chua, Y. L., Tan, Y. S., et al. (2004). *Ex vivo* differentiation of human adult bone marrow stem cells into cardiomyocyte-like cells. *Biochem. Biophys. Res. Commun.* 324 (2), 481–488. doi:10.1016/j.bbrc.2004.09.087

Sriramulu, S., Banerjee, A., Di Liddo, R., Jothimani, G., Gopinath, M., Murugesan, R., et al. (2018). Concise review on clinical applications of conditioned medium derived from human umbilical cord-mesenchymal stem cells (UC-MSCs). *Int. J. Hematol. Oncol. Stem Cell Res.* 12 (3), 230–234.

Stone, P. H., Libby, P., and Boden, W. E. (2023). Fundamental pathobiology of coronary atherosclerosis and clinical implications for chronic ischemic heart disease management-the plaque hypothesis: a narrative review. *JAMA Cardiol.* 8 (2), 192–201. doi:10.1001/jamacardio.2022.3926

Sun, J., Shen, H., Shao, L., Teng, X., Chen, Y., Liu, X., et al. (2020a). HIF-1α overexpression in mesenchymal stem cell-derived exosomes mediates cardioprotection in myocardial infarction by enhanced angiogenesis. *Stem Cell Res. Ther.* 11 (1), 373. doi:10.1186/s13287-020-01881-7

Sun, K., Li, Y. Y., and Jin, J. (2021). A double-edged sword of immuno-microenvironment in cardiac homeostasis and injury repair. *Signal Transduct. Target Ther.* 6 (1), 79. doi:10.1038/s41392-020-00455-6

Sun, X., Wu, J., Qiang, B., Romagnuolo, R., Gagliardi, M., Keller, G., et al. (2020b). Transplanted microvessels improve pluripotent stem cell-derived cardiomyocyte engraftment and cardiac function after infarction in rats. *Sci. Transl. Med.* 12 (562), eaax2992. doi:10.1126/scitranslmed.aax2992

Swirski, F. K., and Nahrendorf, M. (2013). Leukocyte behavior in atherosclerosis, myocardial infarction, and heart failure. *Science* 339 (6116), 161–166. doi:10.1126/science.1230719

Szydlak, R. (2019). Mesenchymal stem cells' homing and cardiac tissue repair. *Acta Biochim. Pol.* 66 (4), 483–489. doi:10.18388/abp.2019_2890

Takahashi, M., Li, T. S., Suzuki, R., Kobayashi, T., Ito, H., Ikeda, Y., et al. (2006). Cytokines produced by bone marrow cells can contribute to functional improvement of the infarcted heart by protecting cardiomyocytes from ischemic injury. *Am. J. Physiol. Heart Circ. Physiol.* 291 (2), H886–H893. doi:10.1152/ajpheart.00142.2006

Tang, J. M., Wang, J. N., Zhang, L., Zheng, F., Yang, J. Y., Kong, X., et al. (2011). VEGF/SDF-1 promotes cardiac stem cell mobilization and myocardial repair in the infarcted heart. *Cardiovasc Res.* 91 (3), 402–411. doi:10.1093/cvr/cvr053

Tang, X., Li, P. H., and Chen, H. Z. (2020). Cardiomyocyte senescence and cellular communications within myocardial microenvironments. *Front. Endocrinol. (Lausanne)* 11, 280. doi:10.3389/fendo.2020.00280

Tian, X. Q., Qian, X. S., Wang, H., and Yang, Y. J. (2022). Adiponectin improves the therapeutic efficacy of mesenchymal stem cells by enhancing their engraftment and survival in the peri-infarct myocardium through the AMPK pathway. *Am. J. Transl. Res.* 14 (1), 534–553.

Tomita, S., Li, R. K., Weisel, R. D., Mickle, D. A., Kim, E. J., Sakai, T., et al. (1999). Autologous transplantation of bone marrow cells improves damaged heart function. *Circulation* 100 (19 Suppl. l), II247–56. doi:10.1161/01.cir.100.suppl_2.ii-247

Vagnozzi, R. J., Maillet, M., Sargent, M. A., Khalil, H., Johansen, A. K. Z., Schwanekamp, J. A., et al. (2020). An acute immune response underlies the benefit of cardiac stem cell therapy. *Nature* 577 (7790), 405–409. doi:10.1038/s41586-019-1802-2

Wang, G. L., Jiang, B. H., Rue, E. A., and Semenza, G. L. (1995). Hypoxia-inducible factor 1 is a basic-helix-loop-helix-PAS heterodimer regulated by cellular O2 tension. *Proc. Natl. Acad. Sci. U. S. A.* 92 (12), 5510–5514. doi:10.1073/pnas.92.12.5510

Wang, H., Wang, Z., Jiang, H., Ma, D., Zhou, W., Zhang, G., et al. (2015b). Effect of autologous bone marrow cell transplantation combined with off-pump coronary artery bypass grafting on cardiac function in patients with chronic myocardial infarction. *Cardiology* 130 (1), 27–33. doi:10.1159/000369381

Wang, X., Zhang, J., Zhang, F., Li, J., Li, Y., Tan, Z., et al. (2015a). The clinical status of stem cell therapy for ischemic cardiomyopathy. *Stem Cells Int.* 2015, 1–13. doi:10.1155/2015/135023

Ward, M. R., Abadeh, A., and Connelly, K. A. (2018). Concise review: rational use of mesenchymal stem cells in the treatment of ischemic heart disease. *Stem Cells Transl. Med.* 7 (7), 543–550. doi:10.1002/sctm.17-0210

Wu, Y., and Zhao, R. C. (2012). The role of chemokines in mesenchymal stem cell homing to myocardium. *Stem Cell Rev. Rep.* 8 (1), 243–250. doi:10.1007/s12015-011-9293-z

Xiao, X., Xu, M., Yu, H., Wang, L., Li, X., Rak, J., et al. (2021b). Mesenchymal stem cell-derived small extracellular vesicles mitigate oxidative stress-induced senescence in endothelial cells via regulation of miR-146a/Src. *Signal Transduct. Target Ther.* 6 (1), 354. doi:10.1038/s41392-021-00765-3

Xiao, Y., Feng, Q., Huang, L., Meng, X., Han, P., Zhang, W., et al. (2023). Copper promotes cardiac functional recovery via suppressing the transformation of fibroblasts to myofibroblasts in ischemia-infarcted monkey hearts. *J. Nutr. Biochem.* 111, 109180. doi:10.1016/j.jnutbio.2022.109180

Xiao, Y., Song, X., Wang, T., Meng, X., Feng, Q., Li, K., et al. (2021a). Copper preserves vasculature structure and function by protecting endothelial cells from apoptosis in ischemic myocardium. *J. Cardiovasc Transl. Res.* 14 (6), 1146–1155. doi:10.1007/s12265-021-10128-6

Xiao, Y., Wang, T., Song, X., Yang, D., Chu, Q., and Kang, Y. J. (2020). Copper promotion of myocardial regeneration. *Exp. Biol. Med. (Maywood)* 245 (10), 911–921. doi:10.1177/1535370220911604

Yagyu, T., Yasuda, S., Nagaya, N., Doi, K., Nakatani, T., Satomi, K., et al. (2019). Long-term results of intracardiac mesenchymal stem cell transplantation in patients with cardiomyopathy. *Circ. J.* 83 (7), 1590–1599. doi:10.1253/circj.cj-18-1179

Yan, W., Chen, Y., Guo, Y., Xia, Y., Li, C., Du, Y., et al. (2022). Irisin promotes cardiac homing of intravenously delivered MSCs and protects against ischemic heart injury. *Adv. Sci. (Weinh)* 9 (7), e2103697. doi:10.1002/advs.202103697

Yin, X., Lin, L., Fang, F., Zhang, B., and Shen, C. (2023). Mechanisms and optimization strategies of paracrine exosomes from mesenchymal stem cells in ischemic heart disease. *Stem Cells Int.* 2023, 6500831–6500920. doi:10.1155/2023/6500831

Zhang, S. J., Song, X. Y., He, M., and Yu, S. B. (2016a). Effect of TGF-β1/SDF-1/CXCR4 signal on BM-MSCs homing in rat heart of ischemia/perfusion injury. *Eur. Rev. Med. Pharmacol. Sci.* 20 (5), 899–905.

Zhang, W., Zhao, X., Xiao, Y., Chen, J., Han, P., Zhang, J., et al. (2016b). The association of depressed angiogenic factors with reduced capillary density in the Rhesus monkey model of myocardial ischemia. *Metallomics* 8 (7), 654–662. doi:10.1039/c5mt00332f

Zhang, X., Wei, M., Zhu, W., and Han, B. (2008). Combined transplantation of endothelial progenitor cells and mesenchymal stem cells into a rat model of isoproterenol-induced myocardial injury. *Arch. Cardiovasc Dis.* 101 (5), 333–342. doi:10.1016/j.acvd.2008.05.002

Zhao, Y., Wang, P., Chen, Z., Li, M., Zhang, D., Yang, L., et al. (2021). Research progress of electrical stimulation in ischemic heart disease. *Front. Cardiovasc Med.* 8, 761877. doi:10.3389/fcvm.2021.761877

Zhu, H., Mitsuhashi, N., Klein, A., Barsky, L. W., Weinberg, K., Barr, M. L., et al. (2006). The role of the hyaluronan receptor CD44 in mesenchymal stem cell migration in the extracellular matrix. *Stem Cells* 24 (4), 928–935. doi:10.1634/stemcells.2005-0186

frontiers | Frontiers in Bioengineering and Biotechnology

TYPE Original Research
PUBLISHED 23 October 2024
DOI 10.3389/fbioe.2024.1487660

OPEN ACCESS

EDITED BY
Yao Luo,
Sichuan University, China

REVIEWED BY
Mahboubeh Nabavinia,
The Research Institute at Nationwide Children's Hospital, United States
Chao Chen,
The First Affiliated Hospital of Xi'an Jiaotong University, China
Gaolian Xu,
Fudan University, China

*CORRESPONDENCE
Kaikai Wang,
kirk2008@126.com
Chaoqun Ma,
mcq_1964@sina.com

†These authors have contributed equally to this work

RECEIVED 28 August 2024
ACCEPTED 14 October 2024
PUBLISHED 23 October 2024

CITATION
Chen H, Li Y, Chen D, Fang Y, Gong X, Wang K and Ma C (2024) Photothermally enhanced antibacterial wound healing using albumin-loaded tanshinone IIA and IR780 nanoparticles. *Front. Bioeng. Biotechnol.* 12:1487660. doi: 10.3389/fbioe.2024.1487660

Photothermally enhanced antibacterial wound healing using albumin-loaded tanshinone IIA and IR780 nanoparticles

Haidong Chen[1†], Yimei Li[1†], Dexuan Chen[2], Yong Fang[1], Xuchu Gong[1], Kaikai Wang[1,3]* and Chaoqun Ma[2]*

[1]Department of General Surgery, Nantong Hospital Affiliated to Nanjing University of Chinese Medicine, Nantong, China, [2]Department of General Surgery, Jiangsu Province Hospital of Chinese Medicine, Affiliated Hospital of Nanjing University of Chinese Medicine, Nanjing, China, [3]School of Pharmacy, Nantong University, Nantong, China

Chronic and infected wounds, particularly those caused by bacterial infections, present significant challenges in medical treatment. This study aimed to develop a novel nanoparticle formulation to enhance wound healing by combining antimicrobial and photothermal therapy using albumin as a carrier for Tanshinone IIA and the near-infrared photothermal agent IR780. The nanoparticles were synthesized to exploit the antimicrobial effects of Tanshinone IIA and the photothermal properties of IR780 when exposed to near-infrared laser irradiation. Characterization of the nanoparticles was performed using Transmission Electron Microscopy (TEM) and spectroscopic analysis to confirm their successful synthesis. *In vitro* antibacterial activity was evaluated using cultures of methicillin-resistant *Staphylococcus aureus* (MRSA), and *in vivo* efficacy was tested in a mouse model of MRSA-infected wounds. Wound healing progression was assessed over 16 days, with statistical analysis performed using two-way ANOVA followed by Tukey's post-hoc test. The nanoparticles demonstrated significant photothermal properties, enhancing bacterial eradication and promoting the controlled release of Tanshinone IIA. *In vitro* studies showed superior antibacterial activity, especially under photothermal activation, leading to a substantial reduction in bacterial viability in MRSA cultures. In vivo, nanoparticle treatment combined with near-infrared laser irradiation significantly improved wound closure rates compared to controls and treatments without photothermal activation. By the 16th day post-treatment, significant improvements in wound healing were observed, highlighting the potential of the combined photothermal and pharmacological approach. These findings suggest that albumin-loaded nanoparticles containing Tanshinone IIA and IR780, activated by near-infrared light, could offer an effective therapeutic strategy for managing chronic and infected wounds, promoting both infection control and tissue repair.

KEYWORDS

tanshinone IIA, albumin nanoparticles, wound healing, photothermal therapy, antibacterial

1 Introduction

Skin is the largest organ in the human body. It not only protects the body from external microbes, chemicals, and physical stimuli, but also plays critical roles in regulating body temperature, maintaining moisture balance, and sensing the external environment (Nestle et al., 2009; Proksch et al., 2008; Wang et al., 2024). However, skin injuries can be caused by various factors such as trauma, burns, and surgery. These injuries disrupt the integrity of the skin, leading to imbalances in internal and external environments and potential risks of infection (Zhou et al., 2023). Once the skin is injured, the body immediately initiates a series of complex biological responses to address the damage and promote the healing and repair process. This process involves the coordinated action of multiple cell types, signaling molecules, and biological processes (Mahdavian Delavary et al., 2011; Sorg et al., 2017). Initially, the inflammatory response phase triggers vasodilation, increased vascular permeability, and the infiltration of inflammatory cells, aiming to clear dead tissue, pathogens, and cellular debris (Xiao et al., 2023). Subsequently, the new tissue formation stage involves the migration and proliferation of fibroblasts and the synthesis of collagen, thus filling the wound and forming preliminary repair tissue. Finally, the tissue remodeling stage involves further remodeling and regeneration of the repair tissue, as well as the regeneration of blood vessels and nerves, to achieve complete wound healing and functional restoration (Takeo et al., 2015).

Managing skin injuries is not just about simple wound treatment; it requires a comprehensive consideration of the biological processes of wound healing and taking appropriate measures to promote the healing process. This might include cleaning the wound, local antibacterial treatment, appropriate dressing selection, nutritional support, and surgical intervention when necessary (Sun et al., 2014). Effective management can speed up wound healing and reduce the occurrence of infections and complications. After skin damage, its ability to resist bacteria significantly decreases; exposure to a moist environment provides suitable conditions for bacterial growth, potentially leading to infectious wounds. A large number of bacteria in an infectious wound will recruit inflammatory cells, such as macrophages and neutrophils, to the injury site (Eming et al., 2007; Naik et al., 2017). In the early stages of skin repair, macrophages tend to frequently differentiate into M1-type macrophages, leading to the appearance of acute inflammation. Acute inflammation is the body's protective response to the injured site (Shi et al., 2022). In the microenvironment, inflammatory cells control wound infections by phagocytosing bacteria, thereby promoting wound healing. However, persistent bacterial infections can lead to prolonged chronic inflammation and delay the transition of the wound healing process to the next proliferation stage, further delaying normal wound healing and turning it into a chronic wound (Chiller et al., 2001; Zegadlo et al., 2023).

Traditional wound dressings (gauze, bandages, etc.) only have simple functions such as quick hemostasis and absorption of exudates. Their singular functionality during the wound healing process can lead to secondary wound infections and the recurrence of inflammation (Cullen and Gefen, 2023). Therefore, there is a need to develop a multifunctional nanomedicine to comprehensively treat the problem of chronic wounds that are difficult to heal (Wolf et al., 2009). This type of multifunctional nanomedicine needs to have strong antibacterial capabilities, anti-inflammatory properties, and the ability to regulate the local immune environment.

Photothermal therapy (PTT) has attracted attention due to its novel mechanism, which differs from traditional therapies (Su et al., 2019; Duan et al., 2023). Traditional antibiotics, such as penicillin and its related beta-lactams, are the most widely used antibiotics that kill bacteria by inhibiting bacterial cell wall synthesis through binding to penicillin-binding proteins (Chen et al., 2020). In contrast, PTT directly targets photothermal agents such as gold, molybdenum disulfide, near-infrared organic small molecules, and graphene nanomaterials, which have high photothermal conversion efficiency under near-infrared laser (Yu et al., 2019). Nanomaterials under near-infrared convert light energy into heat energy, causing irreversible damage to bacteria. Compared to traditional therapies, PTT is an ideal antimicrobial treatment method because it causes less trauma, has a shorter treatment duration, strong penetration ability, and fewer side effects (Chen et al., 2020).

Salvia miltiorrhiza, also known as Danshen, is a traditional Chinese herb made from the dried roots and rhizomes of the plant (Jiang et al., 2019). It has been found to alleviate pain, promote blood circulation, and eliminate blood stasis. Modern pharmacological research has shown that Danshen can dilate coronary arteries, prevent myocardial ischemia and myocardial infarction, improve microcirculation, and reduce myocardial oxygen consumption (Lin and Hsieh, 2010). Numerous experimental and clinical studies have reported benefits to the heart during pathological processes such as myocardial ischemia, myocardial infarction, and reperfusion injury (Zhou et al., 2005). Tanshinone IIA is a representative lipid-soluble component of Danshen, and other tanshinones and the hydrophilic component (Danshen) also play important roles in the pharmacological activities of Danshen in treating various diseases (Zhang et al., 2020; Zhang et al., 2012). Terpenoids are easily reduced to dihydro derivatives, then oxidized and readily transformed. Quinone compounds play a role in transferring electrons in the metabolic products of organisms, exhibiting various biological activities by promoting or interfering with various biochemical reactions in the body. They serve as coenzymes in biological reactions to promote some biochemical processes or disrupt their action, thus displaying various pharmacological effects such as anti-atherosclerosis, anti-myocardial ischemia, anti-arrhythmic, repairing vascular endothelial cells, improving coronary blood flow, anti-myocardial hypertrophy, and anti-tumor effects (Guo et al., 2020). Research has found that Tanshinone IIA plays an important role in the activation, development, and normal function of immune cells. Tanshinone IIA has been shown to exhibit significant antibacterial activity against both Gram-positive and Gram-negative bacteria. Studies have demonstrated that Tanshinone IIA can disrupt bacterial cell membranes, inhibit biofilm formation, and reduce bacterial adhesion (Li and Zhou, 2018; Wang et al., 2023). Tanshinone IIA participates in both innate and acquired immune responses, promoting the various stages of the inflammatory pathway (Gong et al., 2020).

To date, a variety of biomaterials have been used for rapid wound healing, including electrospun nanofibers, porous foams, biocompatible membranes, nanopreparations, and functional

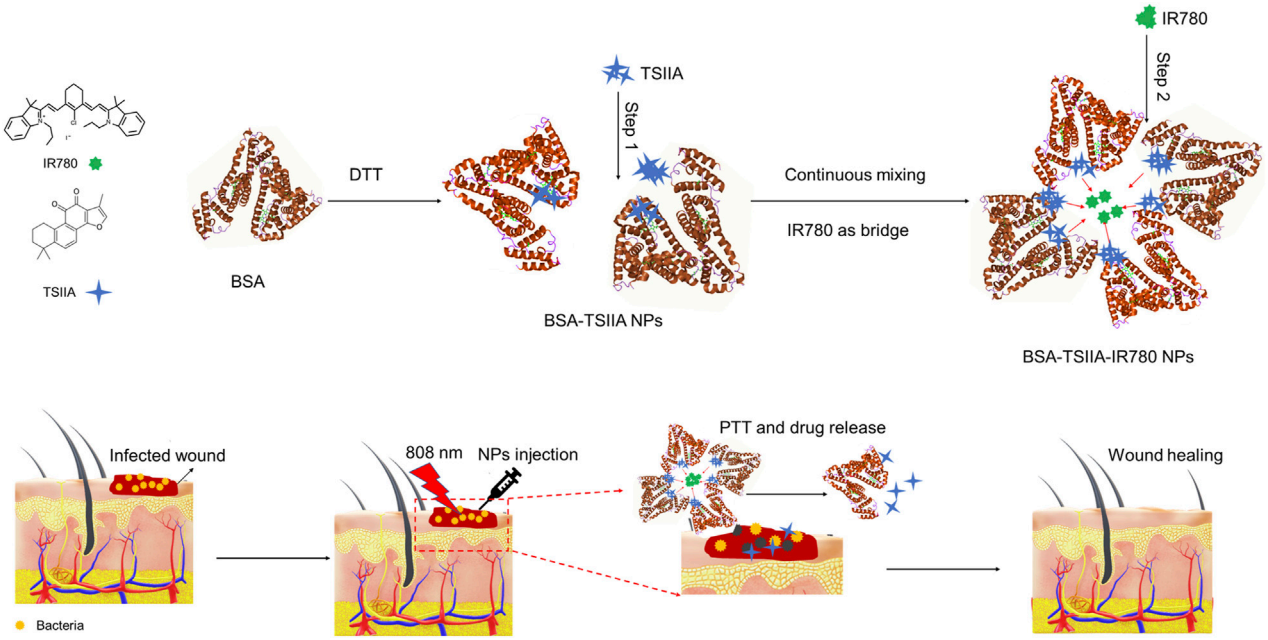

FIGURE 1
Schematic diagram of the preparation of albumin nanoparticles loaded with Tanshinone IIA and IR780 using the "molecular switch" method and their combined photothermal treatment effect on wound healing caused by bacterial infection. This combination of photothermal therapy and drug release accelerates tissue repair and regeneration, leading to improved wound closure and recovery.

hydrogels (Zhang et al., 2023; Naderi et al., 2018). Among these, nanopreparations are the most widely used, especially those using albumin as a carrier (da Silva et al., 2018). Albumin nanoparticles can serve as an effective vehicle for drugs, encapsulating them inside or on the surface to increase drug stability, solubility, and bioavailability (Elzoghby et al., 2012). This type of carrier can achieve controlled drug release by adjusting the size, surface properties, and drug release rates of the nanoparticles, thereby enhancing the therapeutic effects of the drugs.

In this study, albumin-loaded Tanshinone IIA and the near-infrared small molecule IR780 nanoparticles were prepared using the "molecular switch" method via a two-step process (Gong et al., 2012). First, the disulfide bonds within the albumin molecule were opened by dithiothreitol (DTT), exposing the hydrophobic regions of albumin. In the second step, the composite nanoparticles were further obtained through the electrostatic adsorption and hydrophobic interactions of IR780 (Figure 1). In the wound healing model, we infected mouse wounds with methicillin-resistant *Staphylococcus aureus* (MRSA) to obtain a clinically relevant model of difficult-to-heal wounds and fully evaluated the combined therapeutic effects of albumin-loaded Tanshinone IIA and IR780 nanoparticles.

2 Materials and methods

2.1 Materials

IR780 (95%) and Tanshinone IIA (98%) were sourced from Shanghai Macklin Biochemical Co., Ltd., while Bovine Serum Albumin (98%) was acquired from Shanghai Aladdin Reagent Co., Ltd. Dithiothreitol (DTT) was provided by Nanjing Wanqing Chemical Glassware Instrument Co. Ltd. (China). The cell counting kit-8 (CCK-8) was obtained from Dojindo Laboratories (Japan). Unless specified otherwise, all additional reagents were purchased from Nanjing Wanqing Chemical Glassware Instrument Co. Ltd. and were used without further modification.

2.2 Preparation and characterization of nanoparticles

Using the "molecular switch" method, Tanshinone IIA (TSIIA) and IR780 (BSA-TSIIA-IR780 NPs) dual-loaded albumin nanoparticles were prepared by a two-step method. Initially, 100 mg of Bovine Serum Albumin (BSA) was completely dissolved in 50 mL of phosphate-buffered saline (PBS). Subsequently, 100 μL of dithiothreitol (DTT) solution (10 mg/mL) was added to the BSA solution at 45°C. During the reaction, DTT effectively opened the hydrophobic spaces within BSA. Then, while continuously stirring, 2 mL of ethanol solution containing Tanshinone IIA (10 mg/mL) was gradually added to the BSA solution, resulting in the formation of BSA-TSIIA nanoparticles (BSA-TSIIA NPs).

In the second step, 1 mL of ethanol solution containing IR780 (2 mg/mL) was added to the aforementioned solution. The interaction of intermolecular electrostatic forces and hydrophobic interactions facilitated the formation of BSA-TSIIA-IR780 nanoparticles. Subsequently, the nanoparticle solution was ultrafiltered three times to remove free IR780, TSIIA, and ethanol. The final concentrated solution was about 3 mL, suitable for subsequent experiments.

The content of IR780 in the BSA-TSIIA-IR780 nanoparticles was analyzed using a spectrophotometric method. Briefly, the BSA-TSIIA-IR780 nanoparticles were degraded by acetonitrile (volume ratio 1:1). Afterwards, the resulting mixture was diluted 25-fold in chloroform and sonicated for 10 min to ensure complete extraction of IR780. The concentration of IR780 was determined by measuring the absorbance at 785 nm using a UV-vis-NIR spectrophotometer (UV-2450, Shimadzu, Japan) and calculating it from the standard curve of IR780 in chloroform. The content of TSIIA was calculated using high-performance liquid chromatography (HPLC) with reference to the standard curve. TSIIA detection was conducted at a wavelength of 270 nm, using a reverse phase C18 column (5 μm, 4.6 mm × 250 mm, Agilent, United States) at 25°C. The flow rate was maintained at 1.0 mL/min. The elution solvents were phase A (methanol) and phase B (water), with a ratio of 85% A to 15% B (Meng et al., 2015). The BSA concentration was determined using the Coomassie Brilliant Blue method.

The particle size of the BSA-TSIIA-IR780 nanoparticles was determined by Dynamic Light Scattering (DLS) using a Zeta Plus (Brookhaven Instruments Corporation, United States). Before and after irradiation with an 808 nm laser (power density of 1w/cm^2, for 5 min), the nanoparticles were negatively stained with phosphotungstic acid, and their morphology was assessed using a Transmission Electron Microscope (TEM, Hitachi H-600, Japan).

2.3 *In Vitro* heating curve

BSA-TSIIA-IR780 nanoparticles were diluted to 0.05 mg/mL (concentration of IR780) and exposed to an 808 nm near-infrared laser at a power density of 1.0 W/cm^2 for a continuous duration of 3 min. A thermometer was used to measure the temperature every 30 s. BSA-IR780 nanoparticles, free IR780, and PBS were used as controls.

2.4 Drug release study

To study the release curve of TSIIA from nanoparticles, 1 mL of BSA-TSIIA-IR780 nanoparticles and BSA-TSIIA nanoparticles were separately placed into dialysis bags (molecular weight cutoff of 3.5 kDa) and immersed in 15 mL of release medium (PBS containing 1% Tween 80, pH 7.4). The release behavior of BSA-TSIIA-IR780 nanoparticles was investigated with and without irradiation by an 808 nm laser (power of 1w/cm^2 for 5 min). Samples (release solution) were collected at predetermined time points (0–72 h) and the same volume of release medium was replenished. The content of TSIIA was measured by HPLC (as previously described), and the drug release curve was obtained based on the standard curve.

2.5 *In Vitro* antibacterial experiment

The model bacterium used in the antibacterial experiment was methicillin-resistant *S. aureus* (MRSA, ATCC 43300). MRSA cells were cultured in lysogeny broth (LB) medium at 37°C under aerobic conditions until they reached mid-exponential growth phase (Liu et al., 2022). To assess the *in vitro* antibacterial activity of various concentrations of BSA-TSIIA-IR780 nanoparticles, a suspension of MRSA (100 μL, 1 × 10^5 CFU/mL) was added to a 96-well plate, along with a range of concentrations of BSA-TSIIA-IR780 nanoparticles (100 μL; 0.5, 1.0, 2.0, and 5 μg/mL IR780; 5.0, 10.0, 20.0, and 50.0 μg/mL TSIIA), BSA-TSIIA nanoparticles (5.0, 10.0, 20.0, and 50.0 μg/mL TSIIA), and BSA-IR780 nanoparticles (100 μL; 0.5, 1.0, 2.0, and 5 μg/mL IR780). LB solution was used as a control. In the photothermal treatment group, the 96-well plate was irradiated with a near-infrared laser (808 nm, 1.0 W/cm^2) for 5 min. After incubation for 120 min at 37°C, CCK-8 solution (10 μL/well) was added to the 96-well plate. After incubating for 30 min in the dark at room temperature, the plate was placed in an enzyme-linked immunosorbent assay reader to measure the absorbance at 450 nm, which reflects the number of live bacteria in each well. Each group included five replicate wells. Cell viability was expressed as the mean absorbance ±standard deviation (SD) of the five wells per group. The experiment was repeated three times (Xu et al., 2021).

2.6 Establishment of mouse wound model and pharmacological study

All animal experiments were conducted in compliance with the Animal Care and Use Committee of Nantong University. For the wound healing model, this experiment used 5 week-old male ICR mice. Prior to wound creation, the mice were given an intraperitoneal injection of an anesthetic mixture (ketamine/xylazine), and then the hair on their dorsal surface was shaved. A skin wound measuring 1 × 1 cm^2 was created on the dorsal surface of the mice using a 28-gauge needle. Five minutes after creating the wound, each scratch area was inoculated with 40 μL of a suspension containing 1 × 10^8 CFU/mL MRSA, dispersed in PBS. Twenty-4 h after the wounds were infected with the MRSA suspension, the mice were randomly assigned to different treatment groups (each group, n = 4) as follows: control group (100 μL PBS), BSA-TSIIA NPs (100 μL, 200 μg/mL TSIIA), BSA-TSIIA-IR780 NPs without laser (100 μL, 200 μg/mL TSIIA and 20 μg/mL IR780), BSA-IR780 NPs (100 μL, 20 μg/mL IR780) plus laser, and BSA-TSIIA-IR780 NPs (100 μL, 200 μg/mL TSIIA and 20 μg/mL IR780) plus laser. A near-infrared laser (808 nm, 1.0 W/cm^2) was used to irradiate the treatment area for 5 min, 24 h after nanoparticle application to the mice. Wound size was measured using a digital caliper and photographed on days 0, 2, 4, 8, and 16. Wound healing rate was calculated using the following equation:

$$\text{Relative wound area (\%)} = W_{\triangle} / W_0 \times 100\%$$

Where $W_{\triangle}$ is the wound area on a specific day, and W_0 is the wound area on day 0.

2.7 Statistical analysis

Comparison between two groups was performed using Student's t-test. Comparisons among more than two groups were conducted using two-way Analysis of Variance (ANOVA), followed by Tukey post-hoc analysis to compare the means of two groups. *$p < 0.05$,

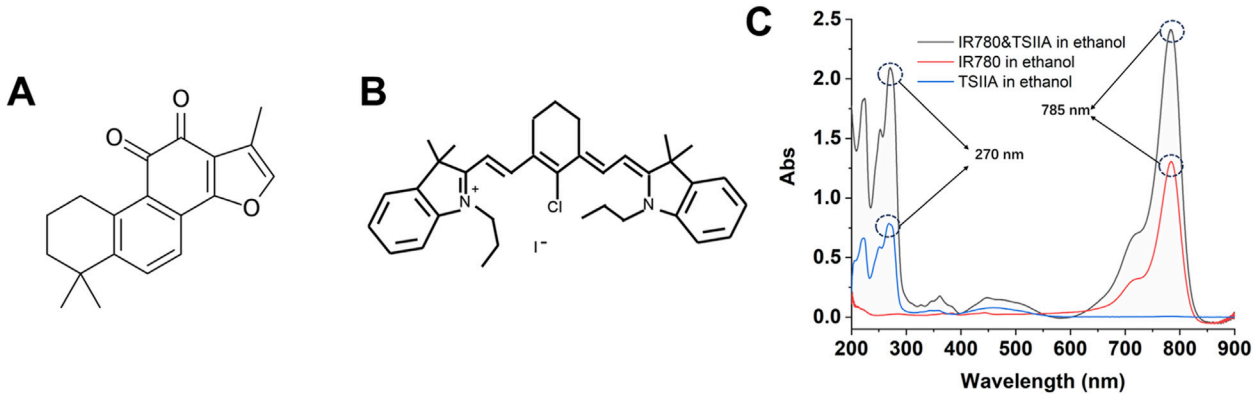

FIGURE 2
Chemical structures of Tanshinone IIA **(A)** and IR780 **(B)** and their UV characteristic absorption spectra **(C)**.

$^{**}p < 0.01$, $^{\#}p < 0.05$, $^{\#\#}p < 0.01$, data are presented as mean ± standard deviation.

3 Results and discussion

3.1 Nanoparticle preparation and characterization

This experiment employed two model molecules, including the hydrophobic Tanshinone IIA and the near-infrared small molecule IR780. As shown in Figure 2A, Tanshinone IIA belongs to the diterpene class of compounds, featuring a typical diterpene ketone skeleton that includes multiple rings and functional groups. The molecule of Tanshinone IIA contains a ketone group, which is one of the key functional groups contributing to its activity. Tanshinone IIA also features a complex side-chain structure, which may influence its pharmacological activity and bioavailability (Jiang et al., 2019; Huang et al., 2022). The structure of the compound accounts for its multiple biological activities, including anti-inflammatory, antioxidant, antitumor, and antimicrobial properties. IR780 (Figure 2B) is a cyanine dye compound with near-infrared light absorption properties, commonly used in photothermal therapy and biological imaging. The indocyanine group in IR780 molecules is one of the main reasons for its absorption capability in the near-infrared region. Additionally, the presence of an amino group endows IR780 with a certain positive charge, offering unique advantages during the nanoparticle assembly process (Zhang et al., 2014). Figure 2C shows the ultraviolet characteristic absorption peak of Tanshinone IIA at 270 nm, while IR780 has a characteristic absorption peak at 785 nm, with no interference between them, which can be utilized to separate them in quantitative experiments using the differences in ultraviolet characteristic absorption.

According to the literature and experimental procedures, we used UV-vis-NIR spectroscopy to determine IR780, and high-performance liquid chromatography (HPLC) for Tanshinone IIA. As shown in Supplementary Figure S1A, there is a very good linear relationship within a certain concentration range (0.0625–2.0 μg/mL) in organic solvents ($R^2 = 1$). From Supplementary Figure S1B, it can be observed that Tanshinone IIA is well separated in the HPLC, with the elution time at 5.5 min and a regular peak shape without significant tailing, which can serve as a quantitative method for Tanshinone IIA.

DTT (dithiothreitol) used in nanoparticle preparation reduces the disulfide bonds in albumin, forming free thiol groups and opening hydrophobic regions. Tanshinone IIA is then added to form initial nanoparticles. IR780, as a hydrophobic charged small molecule, further promotes the assembly of albumin nanoparticles, resulting in drug-loaded nanoparticles with an average diameter of about 185 nm (Figure 3A). Under laser irradiation, IR780 degrades, leading to the “disassembly” of the nanoparticles, which enables the release of Tanshinone IIA. From Figure 3B, it can also be seen that the nanoparticle distribution is broad, with smaller nanoparticles (42 nm) and larger nanoparticles (285 nm), indicating significant changes in the nanoparticles under laser irradiation. The process of IR780 acting as a photosensitizer to generate heat under laser exposure can be explained by the photothermal conversion mechanism. In the presence of a photosensitizer, the laser energy is absorbed and excites the electrons of the photosensitizer to an excited state, forming excited-state photosensitizer molecules. These excited-state molecules, possessing higher energy, release some energy during non-radiative decay, a process known as internal conversion. The released energy is then absorbed by the internal vibrations and rotations of the molecules, causing an increase in internal temperature. This leads to the degradation of the nanoparticles from within, reflected in changes in size and in transmission electron microscopy images (Figures 3C, D). In Figure 3C transmission electron microscopy image, we observed that the albumin nanoparticles were generally uniform and spherical in structure, contributing to their stability in solution. The nanoparticles demonstrated excellent stability in phosphate-buffered saline (PBS) over a period of 7 days, with minimal aggregation or changes in particle size (Narayanan and El-Sayed, 2005). However, after laser irradiation, this regular structure was disrupted, resulting in the appearance of irregular and larger particles. It was demonstrated that after laser irradiation, the structure of the albumin nanoparticles was altered, making the drug more easily released, thereby achieving enhanced therapeutic effects.

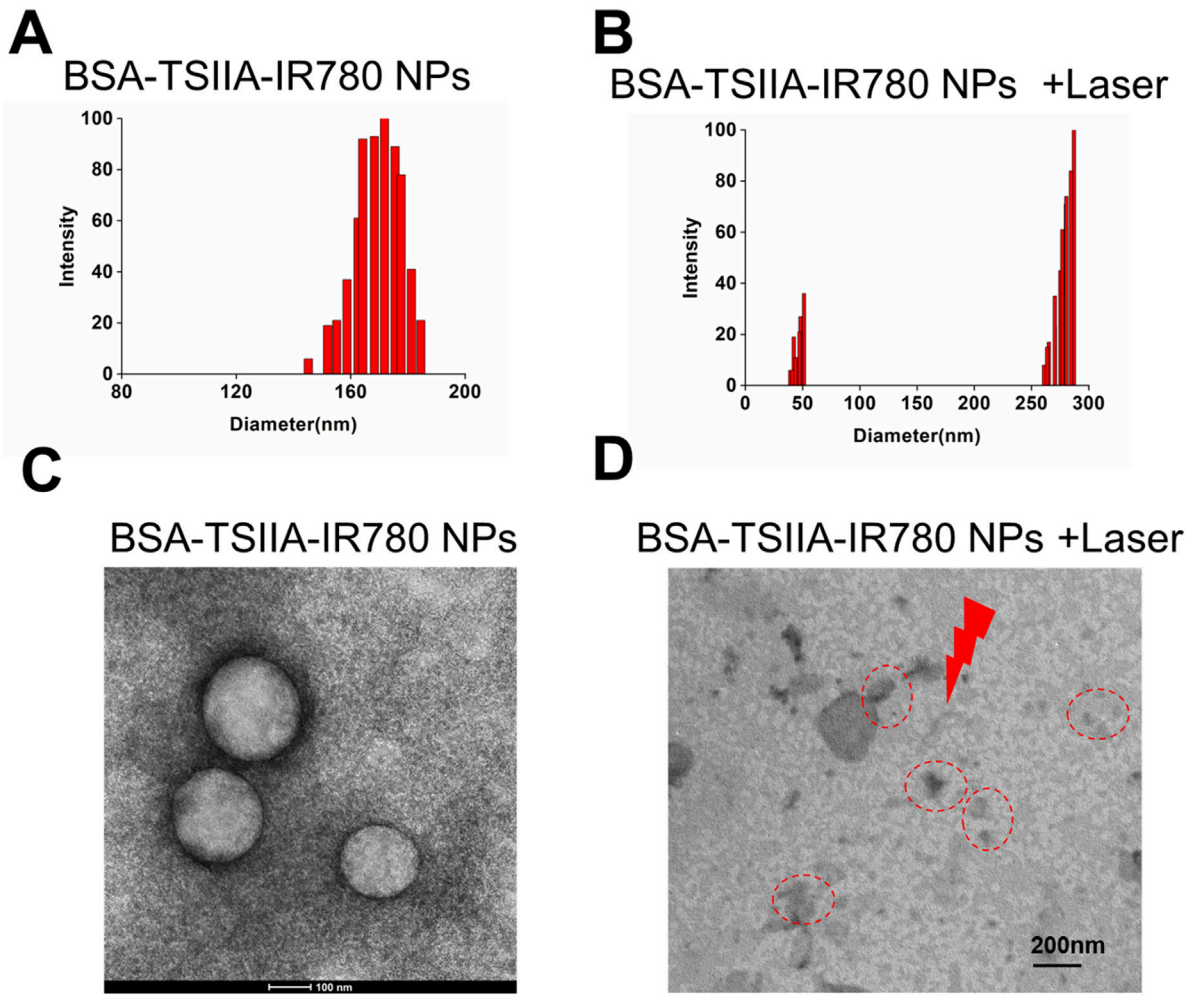

FIGURE 3
Preparation and characterization of albumin-loaded Tanshinone IIA and IR780 nanoparticles. **(A)**. Particle size and distribution of BSA-TSIIA-IR780 NPs; **(B)**. Particle size distribution of BSA-TSIIA-IR780 NPs after laser irradiation; **(C)**. TEM image of BSA-TSIIA-IR780 NPs; **(D)**. TEM image of BSA-TSIIA-IR780 NPs after laser irradiation.

3.2 Photothermal properties of the nanoparticles

In addition to leveraging the anti-inflammatory, antioxidant, antitumor, and antimicrobial biological activities of Tanshinone IIA itself, this project primarily utilizes IR780 as a near-infrared molecule for its heat-producing characteristics. Through photothermal action, it aims to kill bacteria, thus accelerating the wound healing process. Photothermal therapy uses the heat effect produced after a photosensitizer absorbs light to destroy the structure and function of bacterial cells, achieving an antibacterial purpose. Bacteria are sensitive to high temperatures; localized heat effects can cause disruption of bacterial cell membranes, denaturation of proteins, and DNA damage (Xu et al., 2019). Furthermore, high temperatures can also impact bacterial growth and metabolic processes, thereby effectively killing bacteria. Therefore, we evaluated the heat production characteristics of BSA-TSIIA-IR780 NPs in solution (Figure 4). Under conditions of 50 μg/mL IR780 concentration, within 30 s of laser irradiation, the temperature of the BSA-TSIIA-IR780 NPs solution increased from 24°C to 37°C, reached 46.8°C at 60 s, and a maximum of 58.9°C, indicating that under laser irradiation, the photosensitizer IR780 can rapidly heat up and thus kill bacteria to achieve therapeutic purposes.

3.3 *In Vitro* release of nanoparticles

Albumin-loaded nanoparticles containing Tanshinone IIA and IR780 exhibit the capability of enhancing drug release under laser irradiation. Effective release of the drug from the formulation is a prerequisite for its action, and stimulus-responsive release nanopreparations possess the function of "on-demand" and "microenvironment-responsive" release. Therefore, we compared the release behaviors of albumin-loaded Tanshinone IIA nanoparticles and albumin-loaded Tanshinone IIA with IR780 nanoparticles, and verified the laser-responsive release characteristics of the latter (Figure 5). As shown in the figure, compared to the composite nanoparticles, albumin-loaded Tanshinone IIA nanoparticles released Tanshinone IIA faster within 24 h (28.1% vs. 20.9% at the 24th hour), and the

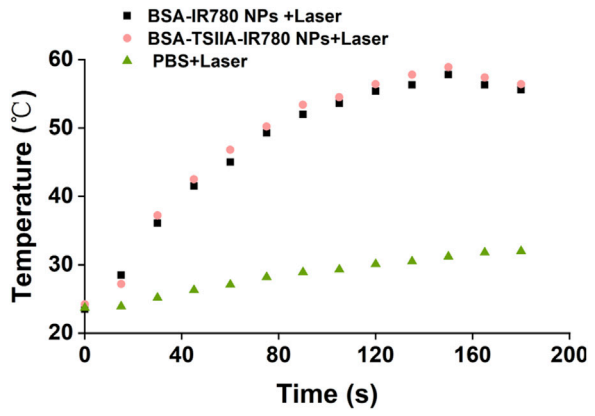

FIGURE 4
The heating characteristics of BSA-TSIIA-IR780 nanoparticles (0.05 mg/mL IR780), with BSA-IR780 nanoparticles, free IR780, and PBS serving as controls.

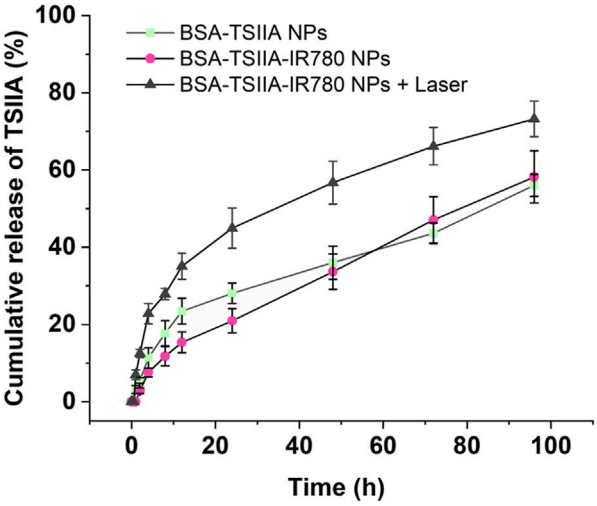

FIGURE 5
The release study of Tanshinone IIA from nanoparticles with or without laser irradiation. Release medium: PBS containing 1% Tween 80, pH 7.4.

trend was similar at the 12th hour (23.7% vs. 15.4%). This may be due to the addition of the small molecule IR780 in the composite nanoparticles, which as a cationic hydrophobic molecule, provides additional forces (such as electrostatic adsorption and hydrophobic interactions) during nanoparticle formation, making it more difficult for Tanshinone IIA to be released from the composite nanoparticles. However, after 48 h, there was no significant difference in the release from the two types of nanopreparations, indicating that the state of nanoparticles in the release medium became consistent after 48 h, as did the behavior of drug release. Under laser irradiation, albumin-loaded nanoparticles containing Tanshinone IIA and IR780 showed a significant increase in release, starting from the first hour after irradiation (12.5% at the second h vs. 2.8%; 35.1% at the 12th hour vs. 15.4%; 56.7% at the 48th hour vs. 33.7%). These results demonstrate that albumin-loaded nanoparticles containing Tanshinone IIA and IR780 have excellent laser-responsive release functionality. This experimental section utilizes albumin to deliver two molecules, IR780 and Tanshinone IIA, leveraging both the heat-producing effect of IR780 under laser irradiation and the antimicrobial and anti-inflammatory pharmacological effects of Tanshinone IIA to treat challenging-to-heal wounds. In the early stages of skin damage, due to potential bacterial infections, there is a need to completely eradicate bacteria and other pathogens, thus photothermal action can meet this requirement; simultaneously, the composite nanoparticles release more Tanshinone IIA under laser irradiation, which has excellent antimicrobial and anti-inflammatory pharmacological effects, allowing better penetration into the skin wound, exerting its effects and regulating the immune microenvironment at the wound site to promote rapid healing and recovery (Huang et al., 2022; Xu et al., 2019).

3.4 *In Vitro* antibacterial experiment

The *in vitro* antibacterial experiment utilized the CCK-8 assay for measurement. Firstly, we validated the antibacterial properties of Tanshinone IIA. As shown in Figure 6A, both albumin-loaded Tanshinone IIA and free Tanshinone IIA exhibited certain antibacterial effects at high concentrations. At a concentration of 50 μg/mL, the inhibition rate was around 20%, and at 100 μg/mL, the inhibition rate reached 35%–40%. Although there were some antibacterial effects, they were not ideal, hence the addition of photothermal therapy was necessary to further enhance bactericidal activity. From Figure 6B, we observed that the bactericidal capability of the nanoparticles was greatly enhanced with the addition of laser treatment. The laser irradiation group showed significant antibacterial ability even at a Tanshinone IIA concentration of 20 μg/mL (inhibition rate of 40%), and at 100 μg/mL, the inhibition rate reached 93%, indicating that the photothermal effect significantly enhances the antibacterial capability of the nanopreparations. As shown in Figures 3D, 5, the albumin nanoparticles under laser irradiation can more effectively release Tanshinone IIA, which plays an important role in utilizing the antibacterial effects of Tanshinone IIA itself. This is also the main reason why the nanoparticles can achieve a synergistic antibacterial effect under laser irradiation. Upon near-infrared laser irradiation, the IR780 generates localized heat, increasing the temperature of the bacterial environment. The heat generated causes damage to the bacterial cell membrane by increasing membrane fluidity and permeability, ultimately leading to cell lysis. The loss of membrane integrity compromises the bacteria's ability to maintain homeostasis, which is critical for survival (Xu et al., 2023). This experiment demonstrates that the antibacterial performance of albumin-loaded nanoparticles containing Tanshinone IIA and IR780 primarily relies on the heat generation capability of the near-infrared small molecules, while Tanshinone IIA mainly plays a role in anti-inflammatory responses, scavenging free radicals, and regulating immune therapeutic effects in treatment. The nanoparticles enhance bacterial clearance through the synergistic action of Tanshinone IIA's antimicrobial properties and the photothermal effect of IR780. Under near-infrared laser irradiation, IR780 generates localized heat that leads to bacterial cell membrane disruption and protein denaturation, while Tanshinone IIA further inhibits bacterial growth (Xu et al., 2023).

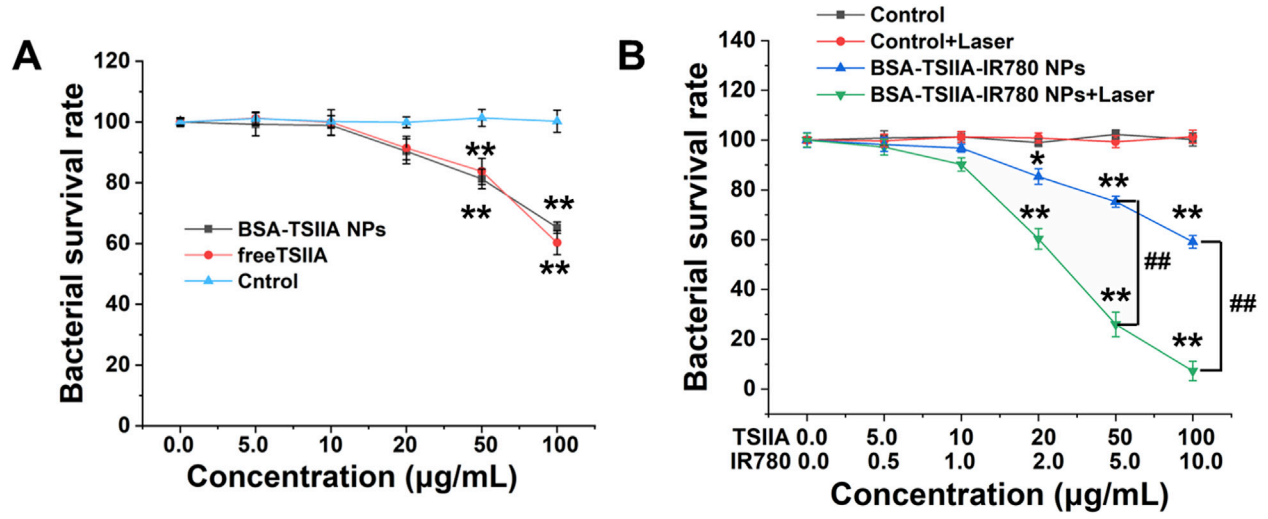

FIGURE 6
In vitro antibacterial characteristics of albumin-loaded Tanshinone IIA and IR780 nanoparticles. **(A)**. Bacterial survival rates at different concentrations of albumin-loaded Tanshinone IIA and free Tanshinone IIA; **(B)**. Bacterial survival rates of albumin-loaded Tanshinone IIA and IR780 nanoparticles with and without laser irradiation. $^{*}p < 0.05$, $^{**}p < 0.01$ (vs. control), $^{\#}p < 0.05$, $^{\#\#}p < 0.01$ (vs. indicated groups).

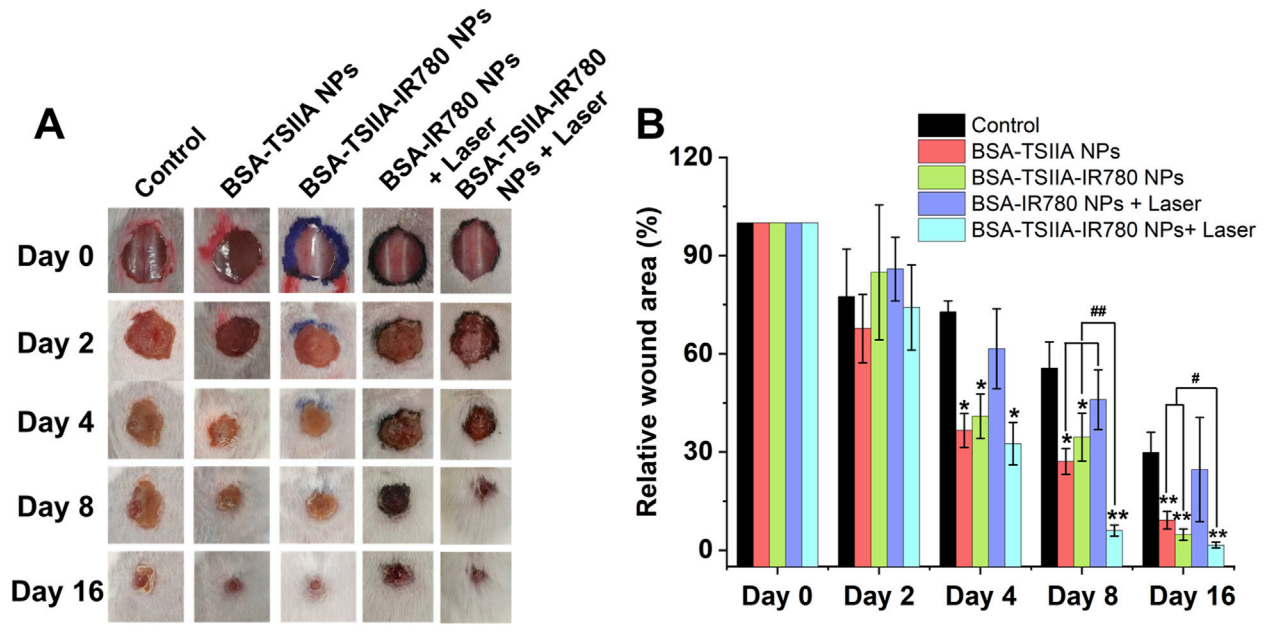

FIGURE 7
Therapeutic effects of albumin-loaded Tanshinone IIA and IR780 nanoparticles in a mouse wound healing model infected with MRSA bacteria. **(A)**. Representative images of the wound healing process under different treatment regimens; **(B)**. Relative wound areas for each group at different time points. $^{*}p < 0.05$, $^{**}p < 0.01$ (vs. control), $^{\#}p < 0.05$, $^{\#\#}p < 0.01$ (vs. indicated groups).

3.5 *In Vivo* wound healing experiment in mice

We validated the combined effects of nanoparticle-based photothermal therapy and the antibacterial properties of Tanshinone IIA on enhancing wound healing in a mouse wound healing model. The MRSA infected mouse wound model is characterized by its difficulty in healing (Figure 7A Control group), and by the 16th day after establishing the wound model, the relative wound area was 29.9%, confirming the successful establishment of this model. Our treatment group, with albumin-loaded Tanshinone IIA nanoparticles, showed a significantly better therapeutic effect, with a relative wound area of 9.2% on the 16th day, demonstrating the nanoparticles'

excellent capability to promote wound healing and the important role of Tanshinone IIA in wound healing (Figure 7B). In the group treated with albumin-loaded Tanshinone IIA and IR780 nanoparticles, we obtained similar results to the Tanshinone IIA nanoparticle group, with a relative wound area of 4.8% on the 16th day, and statistical results showed no significant difference from the Tanshinone IIA nanoparticle group. In the laser irradiation group, we found that the albumin IR780 nanoparticles without Tanshinone IIA performed no differently from the Control group, proving that photothermal therapy alone under this study's conditions does not significantly enhance wound healing in mice, with a relative wound area of only 24.7% on the 16th day. However, the final treatment group, albumin-loaded Tanshinone IIA and IR780 nanoparticles combined with laser treatment, leveraging the dual advantages of photothermal sterilization and enhanced release of Tanshinone IIA, exhibited significant antibacterial performance and greatly enhanced the healing of difficult wounds (16th day, relative wound area of only 1.5%). Beyond bacterial clearance, Tanshinone IIA is known for its anti-inflammatory properties. It helps regulate the inflammatory response by reducing the infiltration of inflammatory cells and downregulating pro-inflammatory cytokines, which prevents chronic inflammation and promotes the transition to the proliferation phase of wound healing. This anti-inflammatory effect accelerates tissue repair by reducing tissue damage caused by excessive inflammation (Guo et al., 2020). The results prove that our designed composite nanoparticles have an excellent ability to promote wound healing.

4 Conclusion

We have reported a nanoparticle system composed of albumin loaded with Tanshinone IIA, a monomeric active molecule derived from traditional Chinese medicine, and IR780, a near-infrared small molecule capable of producing photothermal effects. These nanoparticles were prepared using molecular self-assembly and applied to bacterial-infected wound healing. Albumin-loaded Tanshinone IIA and IR780 nanoparticles demonstrated good photothermal properties, biocompatibility, and excellent antibacterial activity under near-infrared irradiation, suggesting potential clinical applications in wound dressings. Various characterization methods, including electron microscopy, particle size distribution, and UV spectroscopy, confirmed the successful creation of these functionalized nanoparticles. Compared to the absence of laser irradiation, the albumin-loaded Tanshinone IIA and IR780 nanoparticles enhanced the release of Tanshinone IIA under near-infrared light, indicating that this nanoparticle combination possesses near-infrared light-activated drug release properties. The photothermal effect, along with the antibacterial, anti-inflammatory, and free radical scavenging activities of Tanshinone IIA, which also modulate the immune microenvironment of the wound, enhanced the antibacterial behavior both *in vitro* and *in vivo*. Overall, these results suggest that protein-loaded Tanshinone IIA and IR780 nanoparticles under laser irradiation may be an ideal therapeutic approach for enhancing the healing of bacterial-infected wounds.

Tanshinone IIA is an effective traditional Chinese medicine extract with multiple biological activities. Advancing its clinical application is a responsibility for every researcher and clinician; however, its poor water solubility requires the use of organic solvents for dissolution, which can lead to potential toxic side effects. Albumin has multiple binding sites for hydrophobic drugs, naturally making it a carrier for hydrophobic drug delivery. Albumin nanoparticle formulations have also gained widespread clinical use, such as commercially available albumin-bound paclitaxel nanoparticles and albumin-bound rapamycin nanoparticles (Fu et al., 2022). Therefore, developing an albumin-based nanoparticle formulation holds significant clinical value. This part of the study started from effective components of traditional Chinese medicine, combined with the advantages of nanoparticle formulations, and applied the relatively novel photothermal therapy to develop albumin-loaded Tanshinone IIA composite nanoparticles, which were comprehensively evaluated and preliminarily validated *in vivo*. In addition to its antimicrobial and anti-inflammatory actions, Tanshinone IIA has been shown to promote angiogenesis. By stimulating endothelial cell proliferation and migration, Tanshinone IIA contributes to the formation of new blood vessels, enhancing oxygen and nutrient supply to the wound site, which is critical for tissue regeneration and accelerated wound healing (Guo et al., 2020). However, further improvements are needed for this project, such as explaining the mechanisms by which Tanshinone IIA promotes wound healing and how photothermal therapy synergistically enhances the pharmacological actions of Tanshinone IIA. These aspects will be further explored in our subsequent work. While the results are promising, translating this nanoparticle system into clinical practice poses several challenges. These include scaling up production, ensuring consistent drug release profiles, and conducting rigorous clinical trials to verify safety and efficacy in human patients. Overcoming these challenges will be essential for the potential clinical application of this system in treating chronic and infected wounds.

Data availability statement

The original contributions presented in the study are included in the article/Supplementary Material, further inquiries can be directed to the corresponding authors.

Ethics statement

The animal study was approved by the Animal Care and Use Committee of Nantong University. The study was conducted in accordance with the local legislation and institutional requirements.

Author contributions

HC: Conceptualization, Data curation, Formal Analysis, Funding acquisition, Investigation, Methodology, Validation,

Writing–original draft. YL: Data curation, Formal Analysis, Investigation, Methodology, Project administration, Writing–review and editing. DC: Methodology, Supervision, Validation, Writing–review and editing. YF: Investigation, Supervision, Writing–review and editing. XG: Investigation, Supervision, Writing–review and editing. KW: Conceptualization, Methodology, Resources, Supervision, Writing–original draft, Writing–review and editing. CM: Conceptualization, Funding acquisition, Resources, Supervision, Writing–review and editing.

Funding

The author(s) declare that financial support was received for the research, authorship, and/or publication of this article. This work was supported by the Natural Science Foundation of Nanjing University of Chinese Medicine (No. XZR2021084) and the Seventh Batch of the National Famous Old TCM Teacher Training Program (National TCM People's Education Letter [2022]76).

Conflict of interest

The authors declare that the research was conducted in the absence of any commercial or financial relationships that could be construed as a potential conflict of interest.

Publisher's note

All claims expressed in this article are solely those of the authors and do not necessarily represent those of their affiliated organizations, or those of the publisher, the editors and the reviewers. Any product that may be evaluated in this article, or claim that may be made by its manufacturer, is not guaranteed or endorsed by the publisher.

Supplementary material

The Supplementary Material for this article can be found online at: https://www.frontiersin.org/articles/10.3389/fbioe.2024.1487660/full#supplementary-material

References

Chen, Y., Gao, Y., Liu, L., Mo, A., and Peng, Q. (2020). Nanomaterials-based photothermal therapy and its potentials in antibacterial treatment. *J. Control Release* 328, 251–262. doi:10.1016/j.jconrel.2020.08.055

Chiller, K., Selkin, B. A., and Murakawa, G. J. (2001). Skin microflora and bacterial infections of the skin. *J. Investig. Dermatol Symp. Proc.* 6 (3), 170–174. doi:10.1046/j.0022-202x.2001.00043.x

Cullen, B., and Gefen, A. (2023). The biological and physiological impact of the performance of wound dressings. *Int. Wound J.* 20 (4), 1292–1303. doi:10.1111/iwj.13960

da Silva, N. I. O., Salvador, E. A., Rodrigues Franco, I., de Souza, G. A. P., de Souza Morais, S. M., Prado Rocha, R., et al. (2018). Bovine serum albumin nanoparticles induce histopathological changes and inflammatory cell recruitment in the skin of treated mice. *Biomed. Pharmacother.* 107, 1311–1317. doi:10.1016/j.biopha.2018.08.106

Duan, S., Hu, Y., Zhao, Y., Tang, K., Zhang, Z., Liu, Z., et al. (2023). Nanomaterials for photothermal cancer therapy. *RSC Adv.* 13 (21), 14443–14460. doi:10.1039/d3ra02620e

Elzoghby, A. O., Samy, W. M., and Elgindy, N. A. (2012). Albumin-based nanoparticles as potential controlled release drug delivery systems. *J. Control Release* 157 (2), 168–182. doi:10.1016/j.jconrel.2011.07.031

Eming, S. A., Krieg, T., and Davidson, J. M. (2007). Inflammation in wound repair: molecular and cellular mechanisms. *J. Invest Dermatol* 127 (3), 514–525. doi:10.1038/sj.jid.5700701

Fu, Z., Wang, X., Lu, X., Yang, Y., Zhao, L., Zhou, L., et al. (2022). Mannose-decorated ginsenoside Rb1 albumin nanoparticles for targeted anti-inflammatory therapy. *Front. Bioeng. Biotechnol.* 10, 962380. doi:10.3389/fbioe.2022.962380

Gong, G., Xu, Y., Zhou, Y., Meng, Z., Ren, G., Zhao, Y., et al. (2012). Molecular switch for the assembly of lipophilic drug incorporated plasma protein nanoparticles and *in vivo* image. *Biomacromolecules* 13 (1), 23–28. doi:10.1021/bm201401s

Gong, Y., Liu, Y. C., Ding, X. L., Fu, Y., Cui, L. J., and Yan, Y. P. (2020). Tanshinone IIA ameliorates CNS autoimmunity by promoting the differentiation of regulatory T cells. *Neurotherapeutics* 17 (2), 690–703. doi:10.1007/s13311-019-00789-2

Guo, R., Li, L., Su, J., Li, S., Duncan, S. E., Liu, Z., et al. (2020). Pharmacological activity and mechanism of tanshinone IIA in related diseases. *Drug Des. Devel Ther.* 14, 4735–4748. doi:10.2147/dddt.s266911

Huang, X., Deng, H., Shen, Q. K., and Quan, Z. S. (2022). Tanshinone IIA: Pharmacology, total synthesis, and progress in structure-modifications. *Curr. Med. Chem.* 29 (11), 1959–1989. doi:10.2174/0929867328666211108110025

Jiang, Z., Gao, W., and Huang, L. (2019). Tanshinones, critical pharmacological components in salvia miltiorrhiza. *Front. Pharmacol.* 10, 202. doi:10.3389/fphar.2019.00202

Li, Y., and Zhou, Y. (2018). The therapeutic effect of tanshinone IIA on Propionibacterium acnes-induced inflammation *in vitro*. *Dermatol Ther.* 31 (6), e12716. doi:10.1111/dth.12716

Lin, T. H., and Hsieh, C. L. (2010). Pharmacological effects of Salvia miltiorrhiza (Danshen) on cerebral infarction. *Chin. Med.* 5, 22. doi:10.1186/1749-8546-5-22

Liu, W., Gao, R., Yang, C., Feng, Z., Ou-Yang, W., Pan, X., et al. (2022). ECM-mimetic immunomodulatory hydrogel for methicillin-resistant Staphylococcus aureus-infected chronic skin wound healing. *Sci. Adv.* 8 (27), eabn7006. doi:10.1126/sciadv.abn7006

Mahdavian Delavary, B., van der Veer, W. M., van Egmond, M., Niessen, F. B., and Beelen, R. H. (2011). Macrophages in skin injury and repair. *Immunobiology* 216 (7), 753–762. doi:10.1016/j.imbio.2011.01.001

Meng, Z., Meng, L., Wang, K., Li, J., Cao, X., Wu, J., et al. (2015). Enhanced hepatic targeting, biodistribution and antifibrotic efficacy of tanshinone IIA loaded globin nanoparticles. *Eur. J. Pharm. Sci.* 73, 35–43. doi:10.1016/j.ejps.2015.03.002

Naderi, N., Karponis, D., Mosahebi,, A., and Seifalian, A. M. (2018). Nanoparticles in wound healing; from hope to promise, from promise to routine. *Front. Biosci.* 23, 1038–1059. doi:10.2741/4632

Naik, S., Larsen, S. B., Gomez, N. C., Alaverdyan, K., Sendoel, A., Yuan, S., et al. (2017). Inflammatory memory sensitizes skin epithelial stem cells to tissue damage. *Nature* 550 (7677), 475–480. doi:10.1038/nature24271

Narayanan, R., and El-Sayed, M. A. (2005). Catalysis with transition metal nanoparticles in colloidal solution: nanoparticle shape dependence and stability. *J. Phys. Chem. B* 109 (26), 12663–12676. doi:10.1021/jp051066p

Nestle, F. O., Di Meglio, P., Qin, J. Z., and Nickoloff, B. J. (2009). Skin immune sentinels in health and disease. *Nat. Rev. Immunol.* 9 (10), 679–691. doi:10.1038/nri2622

Proksch, E., Brandner, J. M., and Jensen, J. M. (2008). The skin: an indispensable barrier. *Exp. Dermatol* 17 (12), 1063–1072. doi:10.1111/j.1600-0625.2008.00786.x

Shi, R. F., Jin, Y., Zhao, S., Yuan, H., Shi, J., and Zhao, H. (2022). Hypoxic ADSC-derived exosomes enhance wound healing in diabetic mice via delivery of circ-Snhg11 and induction of M2-like macrophage polarization. *Biomed. and Pharmacother.* 153, 113463. doi:10.1016/j.biopha.2022.113463

Sorg, H., Tilkorn, D. J., Hager, S., Hauser, J., and Mirastschijski, U. (2017). Skin wound healing: an update on the current knowledge and concepts. *Eur. Surg. Res.* 58 (1-2), 81–94. doi:10.1159/000454919

Su, G., Miao, D., Yu, Y., Zhou, M., Jiao, P., Cao, X., et al. (2019). Mesoporous silica-coated gold nanostars with drug payload for combined chemo-photothermal cancer therapy. *J. Drug Target* 27 (2), 201–210. doi:10.1080/1061186x.2018.1499746

Sun, B. K., Siprashvili, Z., and Khavari, P. A. (2014). Advances in skin grafting and treatment of cutaneous wounds. *Science* 346 (6212), 941–945. doi:10.1126/science.1253836

Takeo, M., Lee, W., and Ito, M. (2015). Wound healing and skin regeneration. *Cold Spring Harb. Perspect. Med.* 5 (1), a023267. doi:10.1101/cshperspect.a023267

Wang, J., Yuan, S., Tu, Y., Lv, Z., Cheng, H., and Ding, X. (2024). Extracellular vesicles in skin health, diseases, and aging. *Interdiscip. Med.* 2 (3), e20240011. doi:10.1002/inmd.20240011

Wang, M., Muhammad, T., Gao, H., Liu, J., and Liang, H. (2023). Targeted pH-responsive chitosan nanogels with Tanshinone IIA for enhancing the antibacterial/anti-biofilm efficacy. *Int. J. Biol. Macromol.* 237, 124177. doi:10.1016/j.ijbiomac.2023.124177

Wolf, N. B., Küchler, S., Radowski, M. R., Blaschke, T., Kramer, K. D., Weindl, G., et al. (2009). Influences of opioids and nanoparticles on *in vitro* wound healing models. *Eur. J. Pharm. Biopharm.* 73 (1), 34–42. doi:10.1016/j.ejpb.2009.03.009

Xiao, T. F., Sun, M., Zhao, C., and Kang, J. (2023). TRPV1: a promising therapeutic target for skin aging and inflammatory skin diseases. *Front. Pharmacol.* 14, 1037925. doi:10.3389/fphar.2023.1037925

Xu, J. W., Yao, K., and Xu, Z. K. (2019). Nanomaterials with a photothermal effect for antibacterial activities: an overview. *Nanoscale* 11 (18), 8680–8691. doi:10.1039/c9nr01833f

Xu, T., Liu, W., Li, Z., Wang, B., Chitrakar, B., Xiong, W., et al. (2023). Photothermal and selective microbial inactivation behaviors of gluconamide-coated IR780 nanoparticles. *Colloids Surf. B Biointerfaces* 222, 113126. doi:10.1016/j.colsurfb.2023.113126

Xu, Z., Deng, B., Wang, X., Yu, J., Xu, Z., Liu, P., et al. (2021). Nanofiber-mediated sequential photothermal antibacteria and macrophage polarization for healing MRSA-infected diabetic wounds. *J. Nanobiotechnology* 19 (1), 404. doi:10.1186/s12951-021-01152-4

Yu, Y. Y., Zhou, M., Zhang, W., Huang, L., Miao, D., Zhu, H., et al. (2019). Rattle-type gold nanorods/porous-SiO2 nanocomposites as near-infrared light-activated drug delivery systems for cancer combined chemo-photothermal therapy. *Mol. Pharm.* 16 (5), 1929–1938. doi:10.1021/acs.molpharmaceut.8b01298

Zegadlo, K., Gieroń, M., Żarnowiec, P., Durlik-Popińska, K., Kręcisz, B., Kaca, W., et al. (2023). Bacterial motility and its role in skin and wound infections. *Int. J. Mol. Sci.* 24 (2), 1707. doi:10.3390/ijms24021707

Zhang, E., Luo, S., Tan, X., and Shi, C. (2014). Mechanistic study of IR-780 dye as a potential tumor targeting and drug delivery agent. *Biomaterials* 35 (2), 771–778. doi:10.1016/j.biomaterials.2013.10.033

Zhang, H., Zhou, P., Jiang, Y., Li, L., Ju, F., Cheng, Q., et al. (2023). Sustained-release esketamine based nanoparticle-hydrogel delivery system for neuropathic pain management. *Int. J. Nanomedicine* 18, 1131–1143. doi:10.2147/ijn.s400798

Zhang, J., Cai, Z., Yang, M., Tong, L., and Zhang, Y. (2020). Inhibition of tanshinone IIA on renin activity protected against osteoporosis in diabetic mice. *Pharm. Biol.* 58 (1), 219–224. doi:10.1080/13880209.2020.1738502

Zhang, Y., Won, S. H., Jiang, C., Lee, H. J., Jeong, S. J., Lee, E. O., et al. (2012). Tanshinones from Chinese medicinal herb Danshen (Salvia miltiorrhiza Bunge) suppress prostate cancer growth and androgen receptor signaling. *Pharm. Res.* 29 (6), 1595–1608. doi:10.1007/s11095-012-0670-3

Zhou, L., Zuo, Z., and Chow, M. S. (2005). Danshen: an overview of its chemistry, pharmacology, pharmacokinetics, and clinical use. *J. Clin. Pharmacol.* 45 (12), 1345–1359. doi:10.1177/0091270005282630

Zhou, S., Xie, M., Su, J., Cai, B., Li, J., and Zhang, K. (2023). New insights into balancing wound healing and scarless skin repair. *J. Tissue Eng.* 14, 20417314231185848. doi:10.1177/20417314231185848

frontiers | Frontiers in Bioengineering and Biotechnology

TYPE Original Research
PUBLISHED 06 January 2025
DOI 10.3389/fbioe.2024.1500343

OPEN ACCESS

EDITED BY
Yao Luo,
Sichuan University, China

REVIEWED BY
Gautam Pareek,
University of Washington, United States
Shangguo Hou,
Shenzhen Bay Laboratory, China
Yan Zhao,
Shenzhen Bay Laboratory, China

*CORRESPONDENCE
Yingke Xu,
yingkexu@zju.edu.cn

†These authors have contributed equally to this work

RECEIVED 23 September 2024
ACCEPTED 04 December 2024
PUBLISHED 06 January 2025

CITATION
Zhang L, Liu X, Zhu M, Yao Y, Liu Z, Zhang X, Deng X, Wang Y, Duan L, Guo X, Fu J and Xu Y (2025) Optogenetic control of mitochondrial aggregation and function.
Front. Bioeng. Biotechnol. 12:1500343.
doi: 10.3389/fbioe.2024.1500343

Optogenetic control of mitochondrial aggregation and function

Luhao Zhang[1,2,3†], Xuechun Liu[2†], Min Zhu[2,4†], Yuanfa Yao[2], Zhichao Liu[2], Xianming Zhang[2], Xin Deng[1], Yi Wang[5], Liting Duan[6], Xiaogang Guo[4], Junfen Fu[1] and Yingke Xu[1,2,3*]

[1]Department of Endocrinology, Children's Hospital of Zhejiang University School of Medicine, National Clinical Research Center for Children's Health, Hangzhou, China, [2]Department of Biomedical Engineering, Key Laboratory of Biomedical Engineering of Ministry of Education, Zhejiang Provincial Key Laboratory of Cardio-Cerebral Vascular Detection Technology and Medicinal Effectiveness Appraisal, Zhejiang University, Hangzhou, China, [3]Innovation Center for Smart Medical Technologies and Devices, Binjiang Institute of Zhejiang University, Hangzhou, China, [4]Department of Cardiology, The First Affiliated Hospital, School of Medicine, Zhejiang University, Hangzhou, China, [5]Pharmaceutical Informatics Institute, College of Pharmaceutical Sciences, Zhejiang University, Hangzhou, China, [6]Department of Biomedical Engineering, The Chinese University of Hong Kong, Sha Tin, Hong Kong SAR, China

The balance of mitochondrial fission and fusion plays an important role in maintaining the stability of cellular homeostasis. Abnormal mitochondrial fission and fragmentation have been shown to be associated with oxidative stress, which causes a variety of human diseases from neurodegeneration disease to cancer. Therefore, the induction of mitochondrial aggregation and fusion may provide an alternative approach to alleviate these conditions. Here, an optogenetic-based mitochondrial aggregation system (Opto-MitoA) developed, which is based on the CRY2clust/CIBN light-sensitive module. Upon blue light illumination, CRY2clust relocates from the cytosol to mitochondria where it induces mitochondrial aggregation by CRY2clust homo-oligomerization and CRY2clust-CIBN hetero-dimerization. Our functional experiments demonstrate that Opto-MitoA-induced mitochondrial aggregation potently alleviates niclosamide-caused cell dysfunction in ATP production. This study establishes a novel optogenetic-based strategy to regulate mitochondrial dynamics in cells, which may provide a potential therapy for treating mitochondrial-related diseases.

KEYWORDS

optogenetics, mitochondria, aggregation, ATP, imaging

Introduction

Interactions among intracellular organelles are increasingly considered important regulators for many cellular processes, such as metabolite exchange (Helle et al., 2013), organelle remodeling (Guo et al., 2018), growth and organelle biogenesis (Friedman et al., 2011; Cohen et al., 2018). Among various subcellular organelles, the dynamic processes of mitochondrial fission and fusion, and its interactions with other organelles mediate many physiological processes, such as energy output (Seidlmayer et al., 2019), reactive oxygen species (ROS) production (Yu et al., 2006), lipid synthesis, calcium homeostasis (Cohen et al., 2018; Twig et al., 2008; Giacomello and Pellegrini, 2016), and cell death. For example, the bioenergetic roles of mitochondrial fusion have been identified. Knockout of mitofusins has been shown to impair ATP biosynthesis (Seidlmayer et al., 2019). Furthermore, the dysfunction of mitochondria and its interplay with other organelles such as endoplasmic reticulum (ER) has been demonstrated to be associated with neurodegenerative and metabolic

disorders (Rieusset et al., 2016; Area-Gomez and Schon, 2016), cancer cell growth (Huang et al., 2023), and migration (Morciano et al., 2018).

Recently, the manipulation of organelle interactions and positioning has increasingly attracted the attention of researchers. Those techniques can be classified into chemical and genetic induction. Some chemicals can directly interact with protein complexes residing in organelle–organelle membrane contact sites (MCSs), influencing protein expression and regulating organelle interactions. For instance, LDC3/Dynarrestin, an aminothiazole derivative, has been demonstrated to enhance the interaction between mitochondria and ER via action on the tethering complex which consists of the ER protein vesicle-associated membrane protein-associated protein B (VAPB) and the mitochondrial protein tyrosine phosphatase-interacting protein 51 (PTPIP51) (Dietel et al., 2019). Chemically induced crosslinking of supramolecules artificially added onto the mitochondrial surface can also promote mitochondrial aggregation and fusion (Sun et al., 2020), while niclosamide has been shown to break intact mitochondria into fragments (Park et al., 2011). Genetic strategies take longer to function, regulating key proteins involving in organelle interaction such as mitofusins, dynamin-related protein1 (DRP1), VAPB, and PTPIP51 (Stoica et al., 2014) by gene silencing or overexpression.

In contrast to these strategies, optogenetics has been shown to be a promising approach in its rapid and reversible regulation of cellular processes with high spatial–temporal resolution. Optogenetic tools have been developed to control organelle interactions, positioning, and deformation in cells (van Bergeijk et al., 2015; Duan et al., 2015; Shi et al., 2018; Song et al., 2022). For example, the improved light-induced dimer (iLID) and stringent starvation protein B (SspB) system has been shown to tether the ER and mitochondria together (Tkatch et al., 2017). The co-expression of optogenetic elements, such as cryptochromes 2 (CRY2) and cryptochrome-interacting basic helix–loop–helix (CIB1), with specific targeting on organelle and molecular motors, have been used to control organelle trafficking and positioning (Berry and Wojtovich, 2020; Rensvold et al., 2022). Previous studies have used optogenetic modules to regulate the mitochondrial function by modulating iron pump activity, which ultimately controls mitochondrial membrane potential and perturbs ATP synthesis (Tkatch et al., 2017; Berry and Wojtovich, 2020). However, all these tools cannot control mitochondrial dynamics and make it hard to interpret the connection between mitochondrial morphology and function.

In this study, we present a novel optogenetic-based mitochondrial aggregation system (Opto-MitoA) that is based on the CRY2clust/CIBN light-sensitive module. We demonstrate that this optogenetic tool can rapidly control mitochondrial aggregation in cells and that its induced effects increase the energy-generating function of mitochondria and alleviate niclosamide-caused cell dysfunction. The Opto-MitoA may thus provide a new strategy for light-induced mitochondrial aggregation and fusion and for the potential treatment of mitochondrial-related diseases.

Materials and methods

Materials

Tom20-CIBN-GFP, Tom20-CIBN, and mCherry-CRY2clust plasmids were generated as per Duan et al. (2015). Niclosamide was purchased from Sigma Aldrich (St. Louis, MO, United States, No. N3510). 2′,7′-Dichlorofluorescin diacetate (DCFH-DA) for the assay of reactive oxygen species was purchased from Sigma Aldrich (St. Louis, MO, United States, No. D6883). CellTiter-Glo Luminescent Cell Viability Assay was purchased from Promega (Madison, WI, United States, No. G7571). Hoechst 33342 was purchased from Sigma Aldrich (St. Louis, MO, United States, No. 14533).

Cell culture and transfection

The COS-7 cells were cultured in high-glucose Dulbecco′s modification Eagle′s medium (DMEM, Corning) with 10% fetal bovine serum (FBS, Gibco) and 1% penicillin G/streptomycin (Beyotime) at 37°C in a humidified 5% CO_2 incubator. The cells grown at 70%–90% confluency were transiently transfected with Lipofectamine 3000 (Thermo Fisher) according to the manufacturer′s instructions. After 18–24 h of transfection, the cells were used for imaging or functional evaluation experiments.

Live cell imaging

Live cell imaging was performed as per Xu et al. (2016). COS-7 cells were cultured on 35-mm glass bottom dishes and imaged 18–24 h after transfection. The cells were imaged in pH 7.4 Krebs–Ringer bicarbonate HEPES imaging buffer (KRBH) containing 125 mM NaCl, 5 mM KCl, 1.3 mM $CaCl_2$, 1.2 mM $MgSO_4$, 20 mM D-Glucose, 25 mM HEPES, and 0.2% bovine serum albumin. Cells were kept in a thermostat-controlled chamber at 37°C throughout the imaging process. An FV3000 confocal microscope (Olympus) with a 100 × NA 1.4 oil object was used for imaging. A 488-nm laser was used for visualizing GFP-tagged mitochondria and inducing CRY2clust oligomerization, and a 561-nm laser was employed to screen the oligomerization process of mCherry-labeled CRY2clust.

Cellular ATP assay

The COS-7 cells were cultured in an opaque-walled 96-well plate overnight, with 100 μL cell culture per well. Both CellTiter-Glo Reagent and the plate were prepared and equilibrated to room temperature for 30 min. CellTiter-Glo Reagent was then added to the cell culture plate at 100 μL per well. An orbital shaker was used to mix the contents and induce cell lysis. The plate was incubated at room temperature for 10 min before record luminescence.

Cellular ROS assay

The COS-7 cells were transplanted to a 96-well plate and cultured overnight. Cells were washed with PBS before incubation with 10 mM DCFH-DA for 30 min at 37°C. After rinsing with PBS three times, the plate was analyzed by a fluorescence microplate reader with excitation/emission at 485 nm/535 nm.

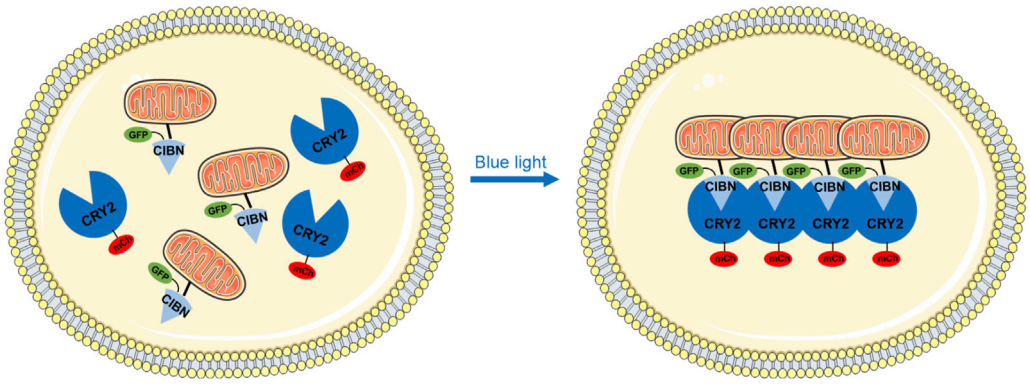

FIGURE 1
Schematic diagram depicting the optogenetic-based mitochondrial aggregation system (Opto-MitoA) in cells. In this schematic illustration, CIBN-GFP is specifically targeted at the mitochondria via the Tom20 domain. CRY2clust (CRY2) tagged with mCherry (mCh) is expressed in the cytosol. Upon blue-light illumination, CRY2clust formed protein clusters by homo-oligomerization, which further interacts with the CIBN to induce mitochondrial aggregation in the cell.

Image analysis and statistics

Stacks of time-lapse images were processed and analyzed using ImageJ 1.51 s (National Institutes of Health). To quantify the degree of mitochondrial aggregation, the entropy of each image was normalized by the first frame of the time-lapse image sequences. All data were presented as the mean ± SEM and statistically tested by using Student's t-test unless otherwise indicated. All analyzed experiments used biological replicates to compute statistical significance. In all statistical analyses, $P < 0.05$ was considered statistically significant.

Results and discussion

Rapid optogenetic control of mitochondrial aggregation in cells

Mitochondria are highly dynamic cellular organelles that play an active role in calcium and damage-associated signaling, amino acids, and lipid metabolism and apoptosis (Rensvold et al., 2022; Araiso et al., 2022). The maintenance of mitochondrial integrity and homeostasis is extremely critical and is achieved through constant fusion and fission when exposed to metabolic and environmental stress (Adebayo et al., 2021). We proposed a novel system that employs blue light to rapidly control mitochondrial aggregation and to study how that perturbation affects cell function. This optogenetics-based mitochondrial aggregation system (Opto-MitoA) is based on blue-light-induced homo-oligomerization of CRY2clust (Park et al., 2017) and simultaneous hetero-dimerization between the CRY2clust and CIBN (Figure 1). CRY2clust is a C-terminal extension of CRY2PHR with nine-residue peptide, and CIBN is the N-terminal region of CIB1 (amino acids 1–170). Opto-MitoA consists of mCherry (mCh)-CRY2clust and Tom20-CIBN-GFP. We chose red fluorescent protein mCherry to track CRY2clust while not activating it. Tom20-CIBN-GFP is reported as targeting mitochondria and interacting with CRY2clust. Upon blue-light illumination, the CRY2clust forms protein clusters in the cytosol and interacts with the Tom20-CIBN-GFP to rapidly induce the aggregation of mitochondria in the cell (Figure 1).

First, we confirmed the specific mitochondrial localization of Tom20-CIBN-GFP by performing co-localization experiments with MitoTracker Orange (Supplementary Figure S1). We then transfected COS-7 cells with only Tom20-CIBN-GFP plasmid or with both Tom20-CIBN-GFP and mCherry-CRY2clust plasmids to examine whether it induces mitochondrial aggregation. The cells were illuminated with a 488-nm laser (2 ms exposure time per pixel; 0.1 mW/cm^2) at 10-s intervals to stimulate the oligomerization of CRY2clust and the dimerization of CRY2clust-CIBN, and the distribution and dynamics of mitochondria in cells were imaged by confocal microscopy. For cells only transfected with Tom20-CIBN-GFP, the GFP-labeled mitochondria rarely changed before and after 60 min of blue light illumination (Figure 2A, Supplementary Video S1). However, in the COS-7 cells co-transfected with Tom20-CIBN-GFP and mCherry-CRY2clust, we detected upon blue light illumination the robust formation of mCherry-CRY2 protein clusters in the cytosol and the concomitant formation of mitochondrial aggregation after 60 min of light activation (Figure 2B, Supplementary Video S2).

To quantify mitochondrial aggregation, we employed image entropy (Shannon, 1948) to measure the chaotic degree of mitochondrial distribution at different time points. The values of image entropy were calculated using a custom-written MATLAB program (Supplementary Figure S2). Image entropy is negatively correlated with the chaotic degree of mitochondrial distribution; thus, the induced mitochondrial aggregation would decrease the value of image entropy. Our results showed that the image entropy of the Opto-MitoA group had reduced nearly 20% compared with the control group after 60 min of blue light stimulation (Figures 2C,D). In summary, we demonstrated that our developed Opto-MitoA module is capable of promoting mitochondrial aggregation by using light.

10.3389/fbioe.2024.1500343

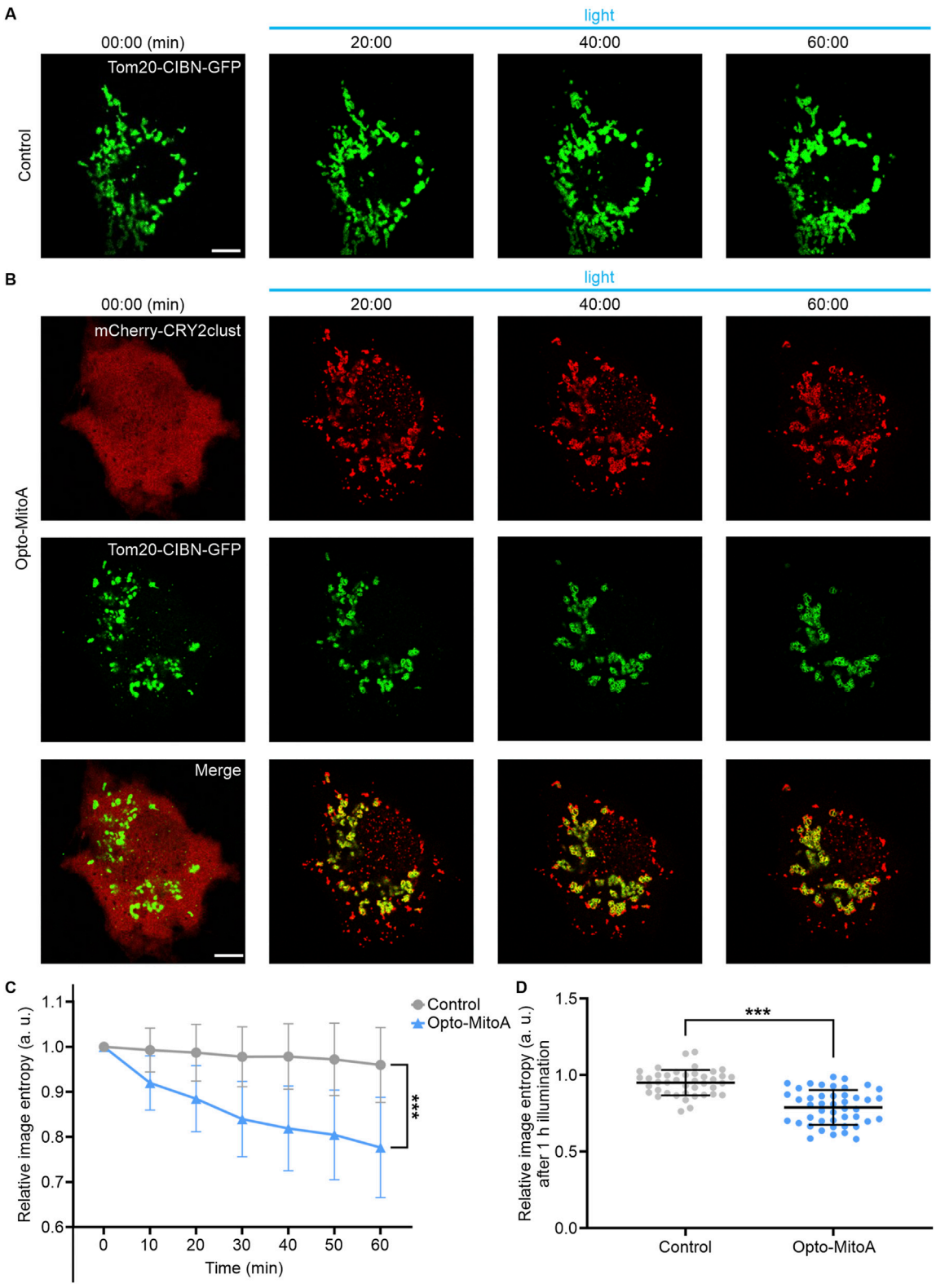

FIGURE 2
Rapid light-induced mitochondrial aggregation. The COS-7 cells were transfected either with Tom20-CIBN-GFP (Control group) or with both Tom20-CIBN-GFP and mCherry-CRY2clust (Opto-MitoA group). **(A)** Confocal images of COS-7 cells transfected with Tom20-CIBN-GFP before and after blue light illumination (representative time points shown). **(B)** Confocal images of COS-7 cells co-transfected with Tom20-CIBN-GFP and mCherry-CRY2clust before and after blue light illumination (representative time points shown). Scale bars: 10 μm. **(C)** Quantification of mitochondrial distribution at different time points by image entropy analysis. Data were statistically tested using one-way ANOVA. **(D)** Image entropy of mitochondrial distribution after 60 min of blue light illumination. Gray: control group. Blue: opto-MitoA group. n = 45 cells, *** indicates $P < 0.001$.

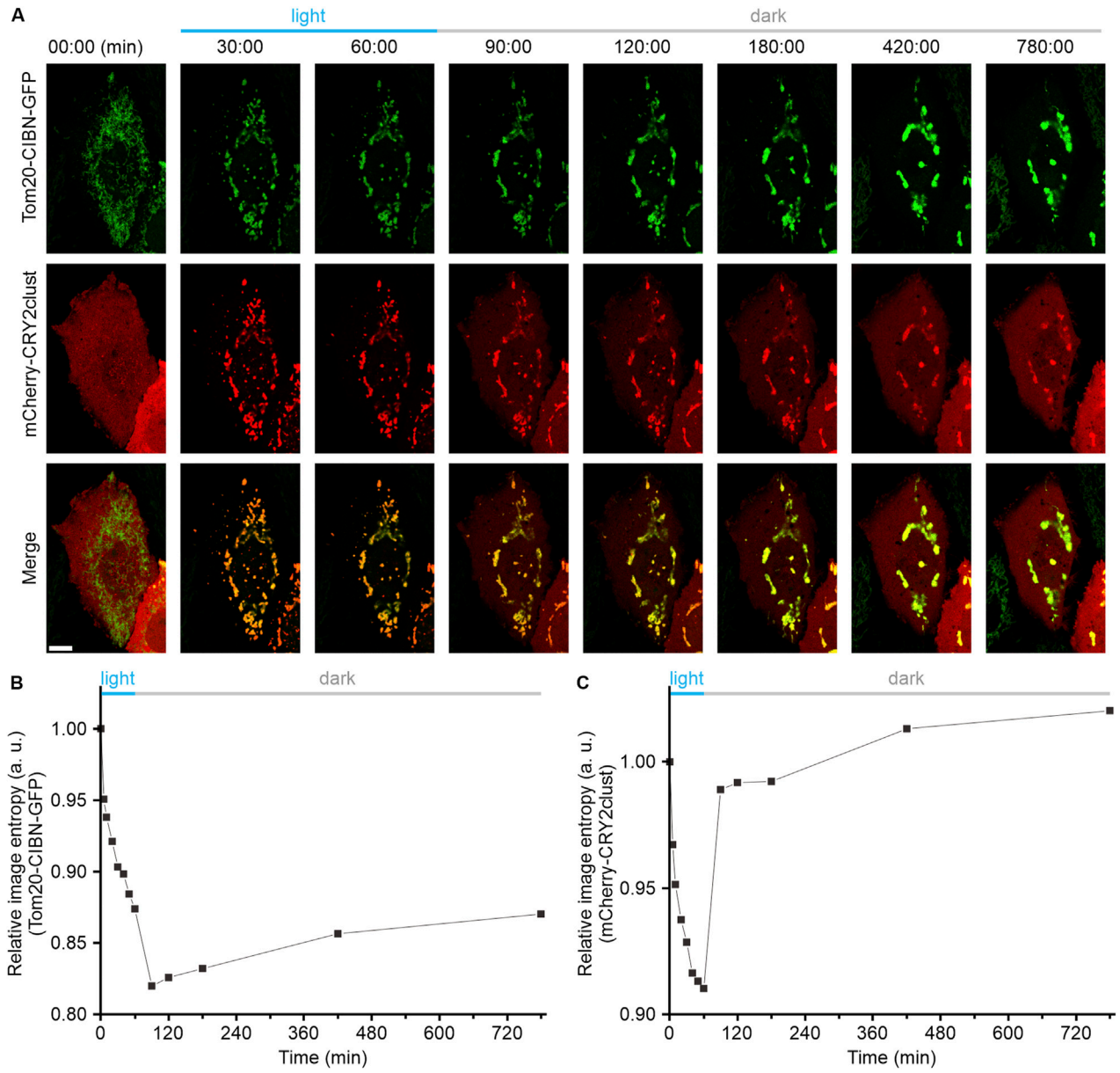

FIGURE 3
Light-induced mitochondrial aggregation is irreversible. COS-7 cells were transfected with both Tom20-CIBN-GFP and mCherry-CRY2clust (Opto-MitoA). The dynamics of mitochondria were imaged by confocal microscopy. **(A)** Representative confocal images showing the dynamics of mCherry-CRY2clust and the Tom20-CIBN-GFP-labeled mitochondria before and after blue light illumination, and recovery in dark conditions as time indicated. Scale bar: 10 μm. **(B)** Quantitative image entropy analysis of mitochondrial (GFP) aggregation before and after blue light illumination and recovery in dark conditions at different time points. **(C)** Quantitative image entropy analysis of CRY2clust (mCherry) aggregation before and after blue light illumination and recovery in dark conditions at different time points.

Opto-MitoA-induced mitochondrial aggregation is irreversible

It has been well established that both light-induced homo-oligomerization of CRY2clust and hetero-dimerization between the CRY2 and CIBN are highly reversible (Park et al., 2017; Li et al., 2020; Xu et al., 2016). Hence, we performed experiments to determine whether Opto-MitoA-induced mitochondrial aggregation is reversible. The COS-7 cells were co-transfected with Tom20-CIBN-GFP and mCherry-CRY2clust plasmids, and the dynamics of mitochondria were imaged by confocal microscopy. As we previously demonstrated, blue light illumination rapidly induces the formation of mCherry-CRY2 protein clusters in the cytosol, and the dimerization of CRY2 and CIBN further promotes mitochondrial aggregation (Figure 3A). After 60 min of blue light exposure, we turned off the blue light. After another 30 min of recovery in the dark, we observed an increase of dispersed mCherry fluorescence in the cytosol, which indicates the reversibility of the CRY2clust and CRY2-CIBN modules. Images at 90 min show some red fluorescence still

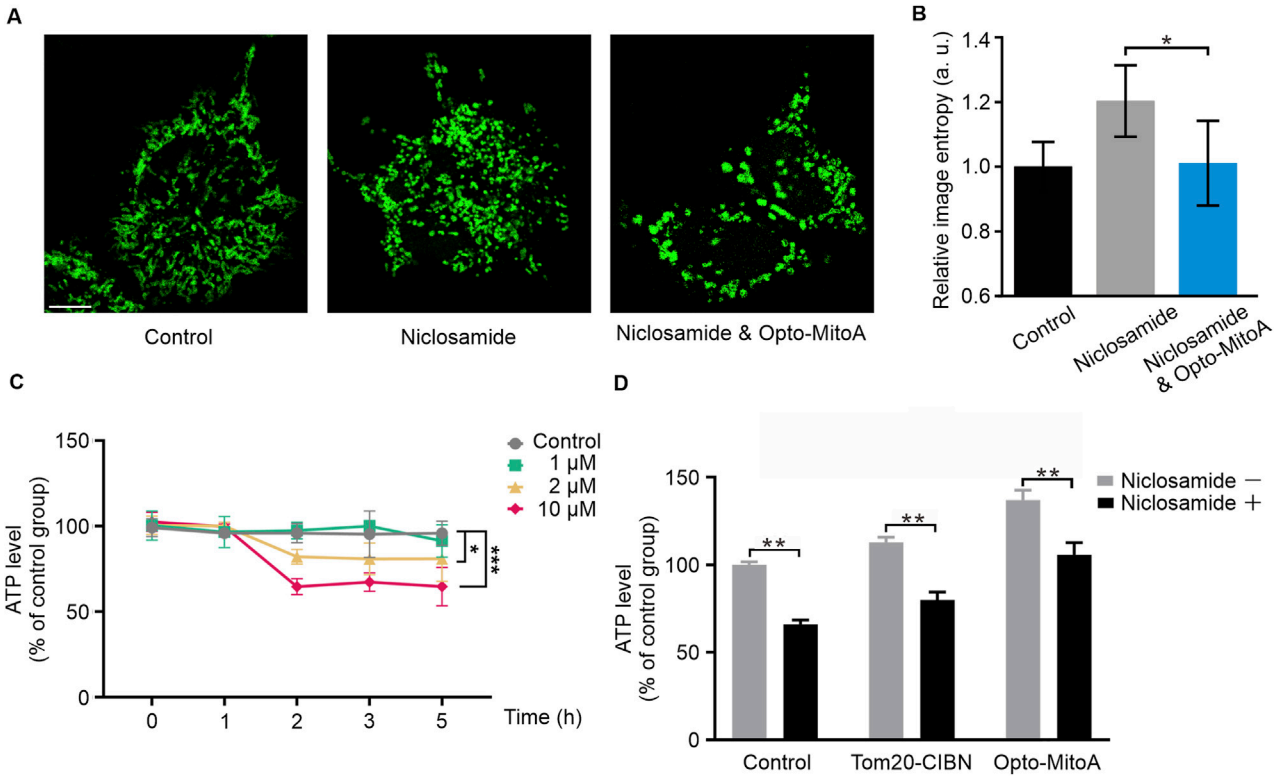

FIGURE 4
Opto-MitoA alleviates niclosamide-induced cell dysfunction. COS-7 cells were transfected either with Tom20-CIBN-GFP only or with both Tom20-CIBN-GFP and mCherry-CRY2clust (Opto-MitoA). The cells were treated with niclosamide or together with blue light activation, and the ATP production in cells was measured. **(A)** Confocal image samples of Tom20-CIBN-GFP-labeled mitochondria of control group, 10 μM niclosamide treatment group, rescue group with 10 μM niclosamide, and Opto-MitoA treatment. Scale bar: 10 μm. **(B)** Histogram of the image entropy of the control group, niclosamide group, and niclosamide and Opto-MitoA group. n = 5 cells. **(C)** ATP production in COS-7 cells treated with different concentrations of niclosamide and different incubation time. Data were statistically tested using one-way ANOVA. **(D)** Histogram of ATP production in control COS-7 cells with or without niclosamide treatment and in COS-7 cells expressing either Tom20-CIBN-GFP or with Opto-MitoA module, exposed with both niclosamide and light. Data are statistically tested using two-way ANOVA. *p*-value differences between each group are < 0.01. * indicates P < 0.05, ** indicates $P < 0.01$, *** indicates $P < 0.001$.

colocalized with green fluorescence (Figure 3A). We speculate that the aggregation of mitochondria increases the spatial hindrance of proteins, leading to a slower dissociation rate of the CRY2 and CIBN. Astonishingly, we found that the Opto-MitoA-induced mitochondrial aggregation was not reversible after recovery, although the expressed protein modules have been shown to be fully reversible. The mitochondria, as labeled with Tom20-CIBN-GFP, were still forming aggregates even after 720 min of recovery in the dark, and some proteins of mCherry-CRY2clust were trapped in aggregated mitochondria (Figure 3A). The image entropy analysis results demonstrated the progress of light-induced mitochondrial aggregation, clearly showing the irreversibility of Opto-MitoA-induced mitochondrial aggregation (Figure 3B), the reversibility of the homo-oligomerization of CRY2clust, and the hetero-dimerization between the CRY2 and CIBN (Figure 3C). The underlying mechanism of these interesting phenomena is not clear, and we suspect that the light-induced mitochondrial aggregation may directly promote mitochondrial fusion. Indeed, studies have shown that supramolecular crosslinking would induce mitochondrial aggregation and fusion, and the possibility of changes in mitofusion protein conformations would also affect mitochondrial fusion (Franco et al., 2016).

Light-induced mitochondrial aggregation alleviates niclosamide-caused cell dysfunction

Mitochondrial dynamics and morphology are closely related to their functions. Chemically or genetically mediated structural perturbations of mitochondria would cause energy deficit, impair calcium ion homeostasis, and induce oxidative stress (Chinopoulos and Adam-Vizi, 2010). Niclosamide (5-chloro-N-(2-chloro-4-nitro-phenyl)-2-hydroxybenzamide) has been shown to modulate mitochondrial dynamics via the promotion of Drp1-dependent mitochondrial fragmentation (Park et al., 2011), which eventually increases cellular reactive oxygen species (ROS) content (Peng et al., 2023) and reduces ATP production (Sun et al., 2020; Zuo et al., 2024). Here, we sought to understand whether Opto-MitoA-induced mitochondrial aggregation could alleviate mitochondrial dysfunction caused by niclosamide treatment.

We found that of COS-7 cells with 10 μM niclosamide for 1 h caused mitochondrial fragmentation (Figure 4A). We then measured the ATP levels in these cells treated with different concentrations of niclosamide at different incubation times. Our results showed that niclosamide treatment caused ATP production

to decrease in a concentration- and time-dependent manner (Figure 4D; Supplementary Figure S3). Treatment of COS-7 cells with 10 μM niclosamide for only 2 h reduced ATP production nearly 50% compared with untreated control cells (Figure 4D). Collectively, these results indicate that niclosamide treatment induces mitochondrial fragmentation and reduces ATP production in COS-7 cells.

We sought to investigate whether Opto-MitoA could improve mitochondrial functions and rescue mitochondrial dysfunctions induced by niclosamide. COS-7 cells were transfected with Tom20-CIBN-GFP and mCherry-CRY2clust plasmids. The cells were exposed with both niclosamide and blue light to induce the aggregation of fragmentated mitochondria in the cells. By using confocal microscopy, a higher density of mitochondria of both niclosamide and blue light groups was observed compared to the niclosamide-treated group (Figure 4A). Image entropy of both the niclosamide and blue light groups was significantly lower than the niclosamide-treated group (Figure 4B). These indicate the successful aggregation of fragmentated mitochondria. In the Opto-MitoA expressing cells, we found a higher basal concentration of ATP production compared with control cells and cells expressing Tom20-CIBN-GFP (Figure 4D). Although niclosamide treatment reduces ATP production in Opto-MitoA-expressing cells, its production is still at a level comparable to the control cells without drug treatment (Figure 4D). We further employed a fluorometric assay using dichlorofluorescein (DCF) to measure ROS levels in our samples. We found that cells treated with Opto-MitoA and niclosamide had a significant decrease in ROS production compared to cells treated with niclosamide after blue light illumination, indicating that the drug has the potential to rescue mitochondrial function (Supplementary Figure S4). Our results thus demonstrate that Opto-MitoA elevates the energy-generating function and decreases ROS production of mitochondria by promoting mitochondrial aggregation, which also functions to alleviate niclosamide-induced cell dysfunction in cells.

In summary, we developed a novel optogenetic-based mitochondrial aggregation system (Opto-MitoA) based on the CRY2clust/CIBN light-sensitive module. We validated its functionality of rapidly controlling mitochondrial aggregation in cells with its induced beneficial effects of increasing the energy-generating function of mitochondria and alleviating niclosamide-caused cell dysfunction. This tool seems to enable light-induced mitochondrial aggregation and fusion in cells and may have the potential for treating mitochondrial-related diseases.

Data availability statement

The original contributions presented in the study are included in the article/Supplementary Material; further inquiries can be directed to the corresponding author.

Ethics statement

Ethical approval was not required in accordance with local legislation and institutional requirements because only commercially available established cell lines were used.

Author contributions

LZ: conceptualization, data curation, formal analysis, funding acquisition, investigation, methodology, validation, visualization, writing–original draft, and writing–review and editing. XL: conceptualization, data curation, formal analysis, investigation, methodology, validation, writing–original draft, and writing–review and editing. MZ: data curation, formal analysis, methodology, validation, and writing–review and editing. YY: conceptualization, data curation, formal analysis, investigation, and writing–review and editing. ZL: data curation, formal analysis, and writing–review and editing. XZ: data curation, formal analysis, and writing–review and editing. XD: data curation, formal analysis, and writing–review and editing. YW: conceptualization, investigation, project administration, resources, and writing–review and editing. LD: project administration, resources, visualization, and writing–review and editing. XG: project administration, supervision, and writing–review and editing. JF: project administration, supervision, and writing–review and editing. YX: conceptualization, funding acquisition, investigation, methodology, resources, supervision, validation, and writing–review and editing.

Funding

The authors declare that financial support was received for the research, authorship, and/or publication of this article. This work was supported by the Zhejiang Provincial Natural Science Foundation (LZ23H180002), the National Natural Science Foundation of China (62105288 and 22104129), the National Key Research and Development Program of China (2021YFF0700305), the Zhejiang Province Science and Technology Research Plan (2024C03056), and the Fundamental Research Funds for the Central Universities (226-2024-00059).

Conflict of interest

The authors declare that the research was conducted in the absence of any commercial or financial relationships that could be construed as a potential conflict of interest.

Publisher's note

Supplementary material

The Supplementary Material for this article can be found online at: https://www.frontiersin.org/articles/10.3389/fbioe.2024.1500343/full#supplementary-material

References

Adebayo, M., Singh, S., Singh, A. P., and Dasgupta, S. (2021). Mitochondrial fusion and fission: the fine-tune balance for cellular homeostasis. *FASEB J.* 35, e21620. doi:10.1096/fj.202100067r

Araiso, Y., Imai, K., and Endo, T. (2022). Role of the TOM complex in protein import into mitochondria: structural views. *Annu. Rev. Biochem.* 91, 679–703. doi:10.1146/annurev-biochem-032620-104527

Area-Gomez, E., and Schon, E. A. (2016). Mitochondria-associated ER membranes and Alzheimer disease. *Curr. Opin. Genet. Dev.* 38, 90–96. doi:10.1016/j.gde.2016.04.006

Berry, B. J., and Wojtovich, A. P. (2020). Mitochondrial light switches: optogenetic approaches to control metabolism. *FEBS J.* 287, 4544–4556. doi:10.1111/febs.15424

Chinopoulos, C., and Adam-Vizi, V. (2010). Mitochondria as ATP consumers in cellular pathology. *Biochim. Biophys. Acta, Mol. Basis Dis.* 1802, 221–227. doi:10.1016/j.bbadis.2009.08.008

Cohen, S., Valm, A. M., and Lippincott-Schwartz, J. (2018). Interacting organelles. *Curr. Opin. Cell Biol.* 53, 84–91. doi:10.1016/j.ceb.2018.06.003

Dietel, E., Brobeil, A., Delventhal, L., Tag, C., Gattenlohner, S., and Wimmer, M. (2019). Crosstalks of the PTPIP51 interactome revealed in Her2 amplified breast cancer cells by the novel small molecule LDC3/Dynarrestin. *PLoS One* 14, e0216642. doi:10.1371/journal.pone.0216642

Duan, L. T., Che, D., Zhang, K., Ong, Q. X., Guo, S. L., and Cui, B. X. (2015). Optogenetic control of molecular motors and organelle distributions in cells. *Cell Chem. Biol.* 22, 671–682. doi:10.1016/j.chembiol.2015.04.014

Franco, A., Kitsis, R. N., Fleischer, J. A., Gavathiotis, E., Kornfeld, O. S., Gong, G., et al. (2016). Correcting mitochondrial fusion by manipulating mitofusin conformations. *Nature* 540, 74–79. doi:10.1038/nature20156

Friedman, J. R., Lackner, L. L., West, M., DiBenedetto, J. R., Nunnari, J., and Voeltz, G. K. (2011). ER tubules mark sites of mitochondrial division. *Science* 334, 358–362. doi:10.1126/science.1207385

Giacomello, M., and Pellegrini, L. (2016). The coming of age of the mitochondria-ER contact: a matter of thickness. *Cell Death Differ.* 23, 1417–1427. doi:10.1038/cdd.2016.52

Guo, Y. T., Li, D., Zhang, S. W., Yang, Y. R., Liu, J. J., Wang, X. Y., et al. (2018). Visualizing intracellular organelle and cytoskeletal interactions at nanoscale resolution on millisecond timescales. *Cell* 175, 1430–1442.e17. doi:10.1016/j.cell.2018.09.057

Helle, S. C., Kanfer, G., Kolar, K., Lang, A., Michel, A. H., and Kornmann, B. (2013). Organization and function of membrane contact sites. *Biochim. Biophys. Acta, Mol. Cell Res.* 1833, 2526–2541. doi:10.1016/j.bbamcr.2013.01.028

Huang, H., Dong, C. H., Chang, M. Q., Ding, L., Chen, L., Feng, W., et al. (2023). Mitochondria-specific nanocatalysts for chemotherapy-augmented sequential chemoreactive tumor therapy. *Exploration* 3, 50–60. doi:10.1002/exp.20210149

Li, H. B., Shentu, P., Xiao, M., Zhao, X. Q., Fan, J. N., Liu, X. C., et al. (2020). Dual function of PI(4,5)P-2 in insulin-regulated exocytic trafficking of GLUT4 in adipocytes. *J. Mol. Biol.* 432, 4341–4357. doi:10.1016/j.jmb.2020.06.019

Morciano, G., Marchi, S., Morganti, C., Sbano, L., Bittremieux, M., Kerkhofs, M., et al. (2018). Role of mitochondria-associated ER membranes in calcium regulation in cancer-specific settings. *Neoplasia* 20, 510–523. doi:10.1016/j.neo.2018.03.005

Park, H., Kim, N. Y., Lee, S., Kim, N., Kim, J., and Heo, W. D. (2017). Optogenetic protein clustering through fluorescent protein tagging and extension of CRY2. *Nat. Commun.* 8, 30. doi:10.1038/s41467-017-00060-2

Park, S. J., Shin, J. H., Kang, H., Hwang, J. J., and Cho, D. H. (2011). Niclosamide induces mitochondria fragmentation and promotes both apoptotic and autophagic cell death. *BMB Rep.* 44, 517–522. doi:10.5483/bmbrep.2011.44.8.517

Peng, H. B., Yao, F. B., Zhao, J. X., Zhang, W., Chen, L. C., Wang, X., et al. (2023). Unraveling mitochondria-targeting reactive oxygen species modulation and their implementations in cancer therapy by nanomaterials. *Exploration* 3, 20220115. doi:10.1002/exp.20220115

Rensvold, J. W., Shishkova, E., Sverchkov, Y., Miller, I. J., Cetinkaya, A., Pyle, A., et al. (2022). Defining mitochondrial protein functions through deep multiomic profiling. *Nature* 606, 382–388. doi:10.1038/s41586-022-04765-3

Rieusset, J., Fauconnier, J., Paillard, M., Belaidi, E., Tubbs, E., Chauvin, M. A., et al. (2016). Disruption of calcium transfer from ER to mitochondria links alterations of mitochondria-associated ER membrane integrity to hepatic insulin resistance. *Diabetologia* 59, 614–623. doi:10.1007/s00125-015-3829-8

Seidlmayer, L. K., Mages, C., Berbner, A., Eder-Negrin, P., Arias-Loza, P. A., Kaspar, M., et al. (2019). Mitofusin 2 is essential for IP3-mediated SR/mitochondria metabolic feedback in ventricular myocytes. *Front. Physiol.* 10, 733. doi:10.3389/fphys.2019.00733

Shannon, C. E. (1948). A mathematical theory of communication. *Bell Syst. Tech. J.* 27, 379–423. doi:10.1002/j.1538-7305.1948.tb01338.x

Shi, F., Kawano, F., Park, S. H. E., Komazak, S., Hirabayashi, Y., Polleux, F., et al. (2018). Optogenetic control of endoplasmic reticulum-mitochondria tethering. *ACS Synth. Biol.* 7, 2–9. doi:10.1021/acssynbio.7b00248

Song, Y. T., Huang, P. Y., Liu, X. Y., Zhao, Z. H., Wang, Y. J., Cui, B. X., et al. (2022). Light-inducible deformation of mitochondria in live cells. *Cell Chem. Biol.* 29, 109–119.e3. doi:10.1016/j.chembiol.2021.05.015

Stoica, R., De Vos, K. J., Paillusson, S., Mueller, S., Sancho, R. M., Lau, K. F., et al. (2014). ER-mitochondria associations are regulated by the VAPB-PTPIP51 interaction and are disrupted by ALS/FTD-associated TDP-43. *Nat. Commun.* 5, 3996. doi:10.1038/ncomms4996

Sun, C., Wang, Z. Y., Yue, L. D., Huang, Q. X., Cheng, Q., and Wang, R. B. (2020). Supramolecular induction of mitochondrial aggregation and fusion. *J. Am. Chem. Soc.* 142, 16523–16527. doi:10.1021/jacs.0c06783

Tkatch, T., Greotti, E., Baranauskas, G., Pendin, D., Roy, S., Nita, L. I., et al. (2017). Optogenetic control of mitochondrial metabolism and Ca^{2+} signaling by mitochondria-targeted opsins. *Proc. Natl. Acad. Sci. U. S. A.* 114, E5167–E5176. doi:10.1073/pnas.1703623114

Twig, G., Elorza, A., Molina, A. J., Mohamed, H., Wikstrom, J. D., Walzer, G., et al. (2008). Fission and selective fusion govern mitochondrial segregation and elimination by autophagy. *EMBO J.* 27, 433–446. doi:10.1038/sj.emboj.7601963

van Bergeijk, P., Adrian, M., Hoogenraad, C. C., and Kapitein, L. C. (2015). Optogenetic control of organelle transport and positioning. *Nature* 518, 111–114. doi:10.1038/nature14128

Xu, Y. K., Nan, D., Fan, J. N., Bogan, J. S., and Toomre, D. (2016). Optogenetic activation reveals distinct roles of PIP3 and Akt in adipocyte insulin action. *J. Cell Sci.* 129, 2085–2095. doi:10.1242/jcs.174805

Yu, T. Z., Robotham, J. L., and Yoon, Y. (2006). Increased production of reactive oxygen species in hyperglycemic conditions requires dynamic change of mitochondrial morphology. *Proc. Natl. Acad. Sci. U. S. A.* 103, 2653–2658. doi:10.1073/pnas.0511154103

Zuo, T. T., Li, X. D., Ma, X., Zhang, Y., Li, X. R., Fan, X. H., et al. (2024). Engineering tumor-oxygenated nanomaterials: advancing photodynamic therapy for cancer treatment. *Front. Bioeng. Biotechnol.* 12, 1383930. doi:10.3389/fbioe.2024.1383930

frontiers | Frontiers in Bioengineering and Biotechnology

TYPE Original Research
PUBLISHED 08 January 2025
DOI 10.3389/fbioe.2024.1480573

OPEN ACCESS

EDITED BY
Yao Luo,
Sichuan University, China

REVIEWED BY
Huangfan Xie,
Southwest Medical University, China
Yan Zhao,
Shenzhen Bay Laboratory, China
Min Wei,
Dalian Medical University, China

*CORRESPONDENCE
Bingyin Su,
subingyinn@163.com
Shurong Li,
lsrsus@163.com

†These authors have contributed equally to this work and share first authorship

RECEIVED 14 August 2024
ACCEPTED 20 December 2024
PUBLISHED 08 January 2025

CITATION
Han Y, Yao Y, Wen X, Wang H, Li S and Su B (2025) Nanodiamond-mediated delivery of microRNA-7 for the neuroprotection of dopaminergic neurons.
Front. Bioeng. Biotechnol. 12:1480573.
doi: 10.3389/fbioe.2024.1480573

Nanodiamond-mediated delivery of microRNA-7 for the neuroprotection of dopaminergic neurons

Yuping Han†, Yue Yao†, Xinyi Wen, Hao Wang, Shurong Li* and Bingyin Su*

Development and Regeneration Key Lab of Sichuan Province, Department of Histology and Embryology, Department of Pathology, Chengdu Medical College, Chengdu, China

Parkinson's disease (PD) is a neurodegenerative disorder characterized by the gradual loss of dopaminergic neurons in the substantia nigra and the accumulation of α-synuclein aggregates known as Lewy bodies. MicroRNA-7 (miR-7) targets the gene *SNCA*, which encodes α-synuclein, reducing its expression and alleviating neuronal damage in PD. Regulating the post-transcriptional levels of α-synuclein through miR-7 effectively inhibits its production. Herein, we use nanodiamonds as carriers to deliver miR-7 (N-7), which can effectively protect dopaminergic neurons. Dopaminergic neurons efficiently take up N-7 and express miR-7. N-7 inhibits the expression of α-synuclein, reduces oxidative stress and restores dopamine levels effectively. These findings suggest that nanocomposites have significant potential in treating PD.

KEYWORDS

nanodiamonds, microRNA-7, Parkinson's disease, dopaminergic neurons, oxidative stress

1 Introduction

Parkinson's disease (PD) is a common neurodegenerative disorder that primarily affects the elderly. Its main pathological feature is the degeneration and death of dopaminergic neurons in the substantia nigra, as well as the formation of Lewy bodies, leading to clinical symptoms such as resting tremor, bradykinesia, and rigidity (Bloem et al., 2021). The primary component of Lewy bodies and Lewy neurites is aggregated α-synuclein (α-syn) (Aarsland et al., 2021). The pathogenesis of PD involves mutations and aggregation of α-synuclein, oxidative stress, and mitochondrial damage (Hansson, 2021). Mutations in the α-synuclein gene can lead to structural changes in the α-synuclein protein, causing dopaminergic neuron death (Iranzo et al., 2021). Environmental toxins like 1-methyl-4-phenyl-1,2,3,6-tetrahydro-pyridine (MPTP) and rotenone, along with mutations in genes like DJ-1 and PINK-1, cause mitochondrial damage, further contributing to dopaminergic neuron death (Malpartida et al., 2021). Oxidative stress and abnormal phosphorylation of proteins can also lead to misfolding and subsequent dopaminergic neuron death (Jomova et al., 2023). Clinically, treatments for PD include dopamine precursors such as levodopa, dopamine receptor agonists, monoamine oxidase inhibitors, anticholinergics, and excitatory amino acid inhibitors (Vijiaratnam et al., 2021). Levodopa remains the most effective drug for PD treatment but can lead to long-term side effects like dyskinesia (Ogawa

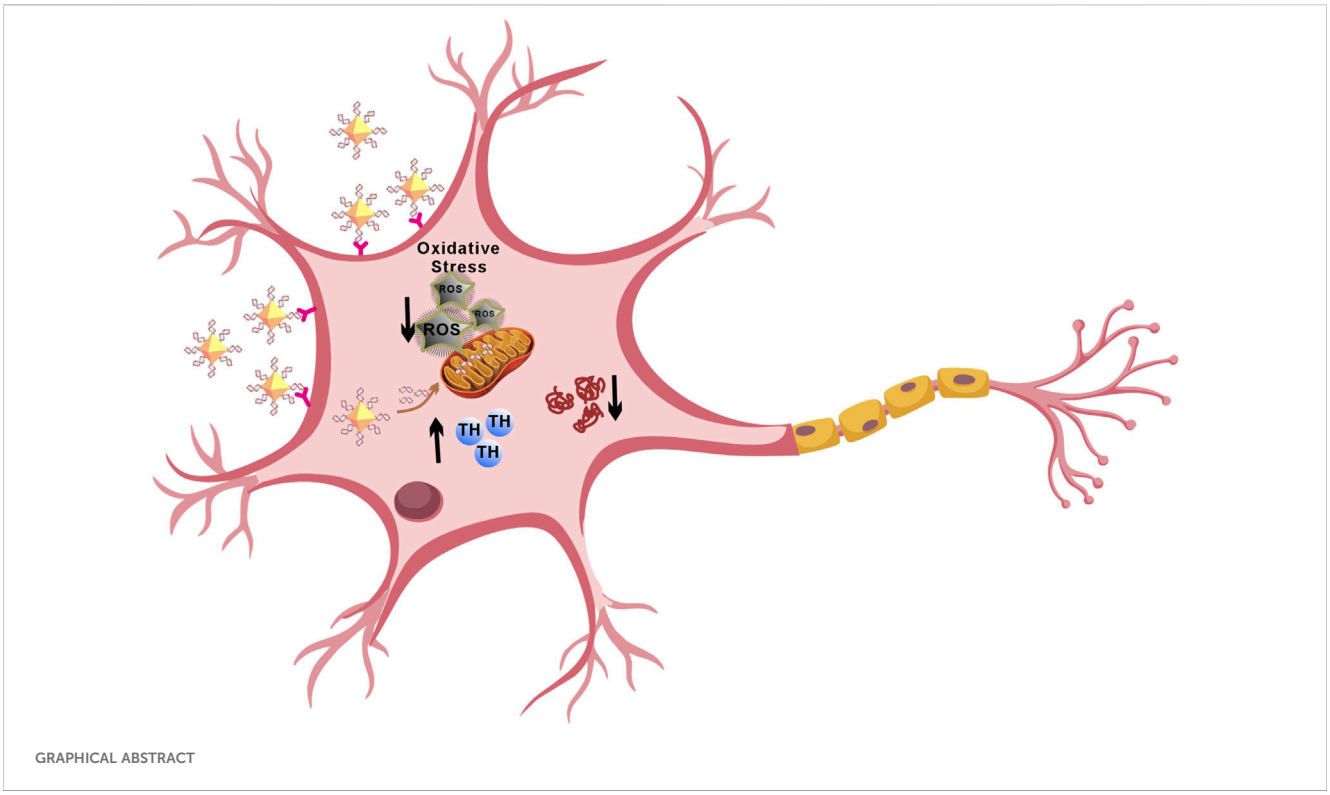

GRAPHICAL ABSTRACT

et al., 2022). Current treatments only alleviate symptoms and do not address the underlying degenerative process.

Gene therapy targeting specific proteins could provide neuroprotection and restoration by correcting the underlying disease mechanisms. miR-7, an endogenous single-stranded non-coding small RNA of 23 nucleotides, targets the SNCA gene encoding α-synuclein (Barrie et al., 2018). Physiologically, miR-7 expression levels are inversely correlated with α-synuclein levels, maintaining them within physiological ranges (Zhang et al., 2021). Reduced levels of miR-7 in PD patients' brains correlate with α-synuclein accumulation, DA neuron damage, and reduced striatal dopamine (McMillan et al., 2017). Our data suggest that miR-7 can reduce oxidative stress and inhibit SNCA gene translation, thereby protecting dopaminergic neurons. This suggests that targeted delivery of miR-7 to dopaminergic neurons may have therapeutic potential for PD.

However, naked miRNAs face several challenges due to their negative charge, off-target effects, short half-life in circulation, and instability. Cationic liposomes like Lipofectamine RNAiMAX have been used for gene therapy delivery but can be deactivated in the presence of serum (Tenchov et al., 2012) and are unstable during storage. Adeno-associated virus (AAV) can be used to deliver microRNA, but most often involves intracranial stereotactic injection. Nanoparticles are widely used in the biomedical industry due to their excellent physical and chemical properties (Gong et al., 2022; Cui et al., 2022; Meng et al., 2024; Xie and Xie, 2024). Numerous studies have reported the therapeutic effects of nanocarrier-RNA drug delivery systems for treating diseases, such as using polyethyleneimine, chitosan, silica nanoparticles, Au nanoparticles and cationic lipid nanoparticles to deliver RNA to target regions (Liu et al., 2023). From a delivery perspective, they have achieved expected outcomes in experimental settings; however, further investigation into drug targeting accuracy and long-term delivery safety is required. Nanodiamonds (NDs) possess ideal characteristics for nanocarrier functionality, including: nanoscale size, stable and inert core, tunable surface modifications, intrinsic fluorescence without photobleaching, minimal toxicity (Li et al., 2019) and ability to form complexes with drugs (Liu et al., 2015). Compared to other carbon-based nanomaterials, NDs have unique abilities to dissolve hydrophobic drugs, increasing stability and prolonging circulation time (Fujiwara et al., 2020). Given their inherent biocompatibility, structural stability, and nontoxic nature, NDs have broad applications in biomedicine and have been used to deliver various therapeutic molecules-including drugs, RNAs, hormones, proteins, and vitamins (Chen et al., 2018; Yang et al., 2020). Numerous studies have demonstrated their efficacy as drug carriers, such as for paclitaxel and cetuximab in the treatment of colorectal cancer (Lin et al., 2017), G9a inhibitors for hepatocellular carcinoma (Gu et al., 2019), doxorubicin for glioblastoma (Li et al., 2017), prostate cancer (Salaam et al., 2014), and alendronate for osteoporosis (Ahn et al., 2021), showing superior therapeutic effects compared to the use of the drugs alone.

To overcome the challenges of delivering miR-7 to dopaminergic neurons, we propose using NDs as carriers to create a nanocomplex (N-7) for PD treatment. Results show that N-7 has good biocompatibility. Dopaminergic neurons rapidly take up N-7 and express miR-7. Furthermore, the transfection efficiency of miR-7 when complexed with NDs outperforms that of Lipofectamine RNAiMAX. Importantly, N-7 can rescue the loss of tyrosine hydroxylase (TH) in PD cell models. Further research indicates that the therapeutic effect of N-7 is achieved through

inhibition of abnormal α-synuclein aggregation, promotion of TH expression, and antioxidant activity. In summary, these findings demonstrate the potential of N-7 for neuroprotective effects in PD treatment.

2 Materials and methods

2.1 Materials

Nanodiamonds were purchased from Sigma-Aldrich (USA). miR-7 was obtained from GenePharma (Shanghai, China). SH-SY5Y, MN9D and HEK293T cell lines were purchased from Cell Bank of Chinese Academy of Sciences (Shanghai, China). Dulbecco's Modified Eagle's Medium (DMEM), Dulbecco's Modified Eagle Medium/Nutrient Mixture F-12 (DMEM/F12) and fetal bovine serum (FBS) were from Gibco, ThermoFisher. Cell Counting Kit-8 was purchased from Beyotime (Shanghai, China). The miR-7 used in the article is an artificially synthesized short double-stranded RNA. The sequence of miR-7 and NC are in Supplementary Table S1.

2.2 Cell culture

SH-SY5Y and MN9D cells were cultured in DMEM/F12 medium, and HEK293T cells were cultured in DMEM medium. Both media were supplemented with 10% heat-inactivated fetal bovine serum (FBS) and antibiotics (1% streptomycin and 1% penicillin). Cells were maintained at 37°C in a humidified atmosphere with 5% CO_2.

2.3 Preparation of N-7

2.3.1 NDs and miR-7 complex ratio

We used RNase-free water to dilute NDs (10 mg/mL) 10–100 times and mix them with miR-7 at mass ratios of NDs: miR-7 of 0, 0.5, 1, 2, 5, 5, 10, 20, 30. Leave the mixture at room temperature for 30 min after mixing uniformly. Set the naked miR-7 as the control group. After 30 min, load the samples onto an agarose gel for electrophoresis.

2.3.2 NDs and miR-7 complexation time

Mix NDs and miR-7 at the optimal ratio determined in the previous step. Set different incubation times: 2 h, 1 h, 30 min, 15 min, 5 min, 1 min, and 0 min. Set the naked miR-7 and naked NDs as the control groups. Load all samples simultaneously onto an agarose gel for electrophoresis.

2.3.3 Complex strength of NDs and miR-7

Prepare two sets of NDs-miR-7 complexes at the optimal ratio and incubation time determined in steps 1 and 2. Centrifuge one set of complexes using a simple mini centrifuge for 1 min and then load the supernatant. Load the other set without centrifugation. Set the supernatants of naked miRNA and empty NDs after centrifugation as the control groups. Load all samples onto an agarose gel for electrophoresis.

2.3.4 Drug loading efficiency

Drug Loading Efficiency (%) = m (miR-7) / [m (miR-7) + m (NDs)] × 100%

2.4 Agarose gel electrophoresis

Prepare a 1% agarose gel. Add 1× TAE electrophoresis buffer to completely immerse the gel. In the top left well, add 5 μL of marker. Mix RNA samples with loading buffer and sequentially add them to the wells. Place the gel with the sample side towards the negative electrode and run at 100 V for approximately 20 min. Place the gel in a gel imaging system, set parameters, and perform imaging. miRNA should appear as a single band.

2.5 Dynamic light scattering (DLS)

Dilute the samples in DEPC-treated water to an appropriate concentration and measure at 25°C. Fit the correlation function using the cumulant method to obtain the hydrodynamic diameter (Z-average, nm) and its polydispersity index (PDI). Repeat three times.

2.6 Transmission electron microscopy (TEM)

Place a copper grid coated with a continuous carbon film on a 10 μL drop of sample solution and leave it for 5 min to adsorb the nanomaterial. Stain the grid by placing it in an equal volume of 2% phosphotungstic acid for 2 min, then dry it. Observe the morphology under TEM. Use ImageJ software for size analysis.

2.7 Biocompatibility analysis

We set up a blank group (NDs), a control group (miR-7), and experimental groups with varying mass ratios of NDs to miR-7 (0–30) and different mixing times (0–120 min). After mixing NDs and miR-7 for 10 min, the mixture was centrifuged at 6,000 rpm for 1 min, and the supernatant was collected. SH-SY5Y cells in the logarithmic growth phase were digested with 0.25% trypsin and seeded at 5 × 10^4 cells per well in a 96-well plate, with five replicates per group, and incubated overnight. The culture medium was then removed. The blank group received no treatment, the control group had its medium replaced with fresh culture medium, and the experimental groups were treated with different concentrations of NDs (0, 5, 25, 50, 100, 200 μg/mL) and miR-7 (0, 5, 10, 50, 100 mM), as well as N-7 complexes and other groups (Ctrl, miR-7, NC, L-7, L-NC, N-NC) (with miR-7 at 10 nM, where NC is a negative control miRNA). Solutions were prepared by mixing NDs and miR-7 for N-7, and Lipofectamine RNAiMAX and miR-7 for L-7, followed by incubation and addition to the cell culture medium. Cells were further incubated for 48 h. A CCK-8 assay was performed by adding 100 μL of a 10% CCK-8 reagent mixture to each well, incubating in the dark for 1–2 h until the medium turned orange-red, and measuring absorbance at 450 nm. Cell viability was calculated using the formula: Cell Viability (%) = (A (Experimental

Group) − A (Blank Group)) / (A (Control Group) − A (Blank Group)) × 100%.

2.8 Confocal fluorescence microscopy

Cells expressing fluorescent protein markers or cells immunostained for microtubule were imaged using confocal microscope. CY5 was excited with a 561 nm helium-neon laser and Hoechst 33258-labeled nuclei were excited with a 405 nm diode laser, respectively. The imaging channels were set at 570–620 and 450–500 nm, respectively.

2.9 Western blot

Separate protein samples using SDS-PAGE (Sodium Dodecyl Sulfate Polyacrylamide Gel Electrophoresis). Transfer the proteins onto a PVDF (Polyvinylidene Fluoride) membrane. Block the membrane with 5% non-fat milk in Tris Buffered Saline with Tween 20 (TBST) at room temperature. Incubate with primary antibodies overnight at 4°C. Wash the membrane with PBS (Phosphate Buffered Saline). Incubate with the secondary antibody conjugated to a reporter molecule at room temperature for 2 h. Visualize the proteins using an enhanced chemiluminescence kit.

2.10 Flow cytometry

Before measurements, cell media was removed and cells were washed for three times with PBS. Next, 0.2 mL trypsin (Invitrogen) was added to each sample and incubated for 1 min at 37°C before 0.5 mL DMEM/F12 was added. Cell suspensions were transferred into tubes before analyzed using a FACS Calibur flow cytometer. Consistent gating based on cell size and granularity (forward and side scatter) was applied to select the fluorescence signals of counted cells. At least 10,000 cells were counted for each sample and experiments were performed in triplicates.

2.11 qRT-PCR analysis

Extract RNA from cells using Trizol reagent. Following the instructions provided with the Vazyme miRNA 1st Strand cDNA Synthesis Kit (by stem-loop), reverse transcribe RNA into cDNA. Conduct real-time quantitative PCR using the Vazyme miRNA Universal SYBR qPCR Master Mix kit according to the manufacturer's instructions. The primer sequences used are detailed in Supplementary Table S2.

2.12 Detection of reactive oxygen species (ROS) levels

Dilute DCFH-DA in serum-free medium to a final concentration of 10 μM. Remove the cell culture medium from adherent cells in the dish and add 200 μL of the diluted probe to cover the cells fully. For the positive control group, add 0.2 μL of Rosup along with the probe. Incubate at 37°C for 20 min. Stain with Hoechst 33342 (1:100 dilution) for 10 min. Gently wash the cells three times with serum-free medium, leaving a small amount of medium on the culture insert to keep it moist. Observe under a confocal laser scanning microscope with excitation wavelengths of 350 nm (for Hoechst 33342) and 488 nm (for DCF).

2.13 Statistical analysis

Data analysis and statistical graph creation were performed using GraphPad Prism 8 software. Independent samples t-tests were used to compare differences between two groups. One-way ANOVA was used to compare differences among groups. Data are presented as mean ± standard deviation. A p-value less than 0.05 indicates statistically significant difference ($^{*}P < 0.05$; $^{**}P < 0.01$; $^{***}P < 0.001$).

3 Results and discussion

3.1 Preparation, characterization and biocompatibility of N-7

We conjugated miR-7 to the NDs through electrostatic adsorption (Figure 1A). Gel retardation experiments showed that when the mass ratio of NDs to miR-7 is 20:1, miR-7 is completely bound to the NDs (Supplementary Figure S1A), with a drug loading of 4.7 wt.%. Binding is complete within 10 min of co-incubation, whereas when NDs mixed with miR-7 are immediately loaded onto the gel, very little miR-7 binds to the NDs (Supplementary Figure S1B). After centrifugation of the synthesized N-7 complex, agarose gel electrophoresis of the supernatant did not show any miR-7 (Supplementary Figure S1C), indicating that miR-7 is stably bound to the NDs.

Transmission electron microscopy (TEM) images show that NDs appear as spherical particles with some aggregation, with diameters of approximately 5–10 nm. After complexing with miR-7, the solution becomes more viscous, and the material appears as aggregated clusters with scattered particles around them, with diameters of approximately 15–20 nm (Figure 1B). Dynamic light scattering (DLS) measurements show an average particle size of 47.6 nm for NDs with a polydispersity index (PDI) of 0.23; after complexing with miR-7, the particle size increases to 225.4 nm with a PDI of 0.77 (Figure 1C). The difference in particle sizes measured by DLS and TEM may be due to the hydrated state of the particles in DLS measurements and possible aggregation of NDs in the liquid medium. DLS results also show that the zeta potential of NDs decreases from 31.3 mV to 22.2 mV after complexing with miR-7 (Supplementary Figure S2). The positive zeta potential of the N-7 complex facilitates interaction with negatively charged components of the cell membrane, such as heparan sulfate proteoglycans, promoting uptake through endocytosis, phagocytosis, or pinocytosis.

Compared to the control group, the cell survival rate gradually decreases with increasing concentrations of NDs, but the survival rate remains above 50% across all tested concentrations; low concentration NDs (5 μg/mL) have almost no effect on cell survival (Figure 1D). These results indicate that nanodiamonds possess good biocompatibility, as shown in other studies (Chen

10.3389/fbioe.2024.1480573

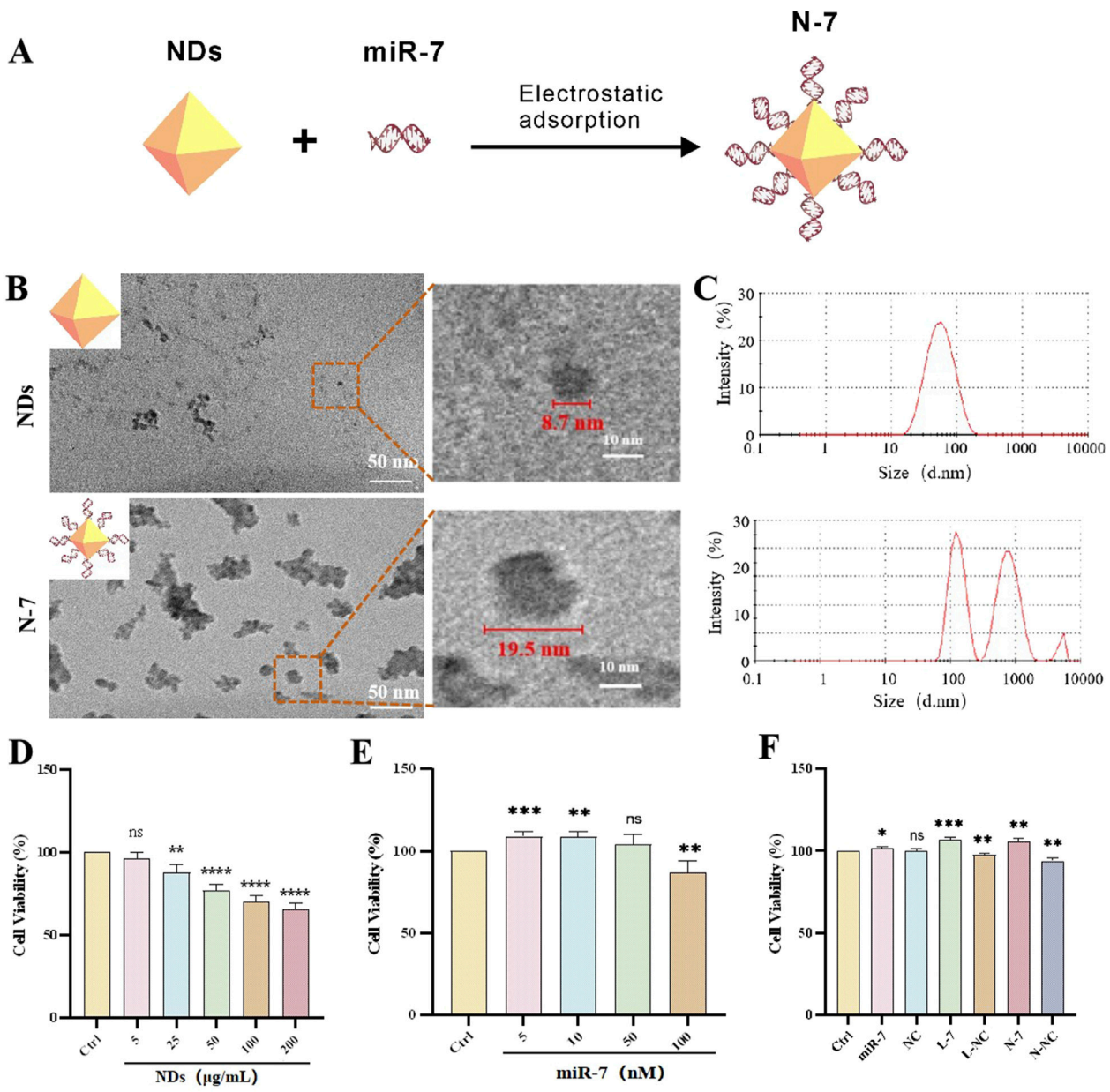

FIGURE 1
Characterization and biocompatibility of NDs and N-7. **(A)** Schematic diagram illustrates the synthesis of the N-7 complex using the electrostatic adsorption method. **(B)** Transmission Electron Microscopy of NDs and N-7. **(C)** Dynamic light scattering analysis of NDs and N-7. CCK-8 detection of the effects of different concentrations of NDs **(D)** or miR-7 **(E)** on the cell viability of SH-SY5Y cells (n = 3). **(F)** CCK-8 detection of the effects on the cell viability of SH-SY5Y cells under different conditions. NDs, nanodiamonds. N-7, the complex of nanodiamonds and microRNA-7. NC, nonsense microRNA. L-7, Lipofectamine RNAiMAX transfection of microRNA-7 (n = 3). L-NC, Lipofectamine RNAiMAX transfection of nonsense microRNA. N-NC, the complex of nanodiamonds and nonsense microRNA. ns means no statistical significance, $^{*}P < 0.05$, $^{**}P < 0.01$, $^{***}P < 0.001$ and $^{****}P < 0.0001$ with respect to the control group.

et al., 2018). Liposome-transfected miR-7 at low concentrations (5 nM, 10 nM, 50 nM) does not harm cell viability and is even beneficial at 5 nM and 10 nM (Figure 1E). N-7 nanocomplexes and L-7 (miR-7 concentration 10 nM) significantly increase cell survival rates after 48 h of co-incubation with SH-SY5Y cells. In comparison, free miR-7 benefits cell survival, while NC has no effect, and both liposome transfection and ND-mediated delivery slightly decrease cell survival (Figure 1F). These data suggest that N-7 complexes protect dopaminergic neurons.

3.2 The internalization of NDs both *in vitro* and *in vivo*

Confocal laser scanning microscopy was used to observe the uptake of red fluorescent NDs by MN9D cells at different time points ranging from 1 h to 48 h, and at both low (5 μg/mL) and high (20 μg/mL) concentrations. (Figure 2A). At a low concentration (5 μg/mL), NDs are observed to be evenly distributed in the cells after 1 h of incubation, with a tendency to accumulate around the

10.3389/fbioe.2024.1480573

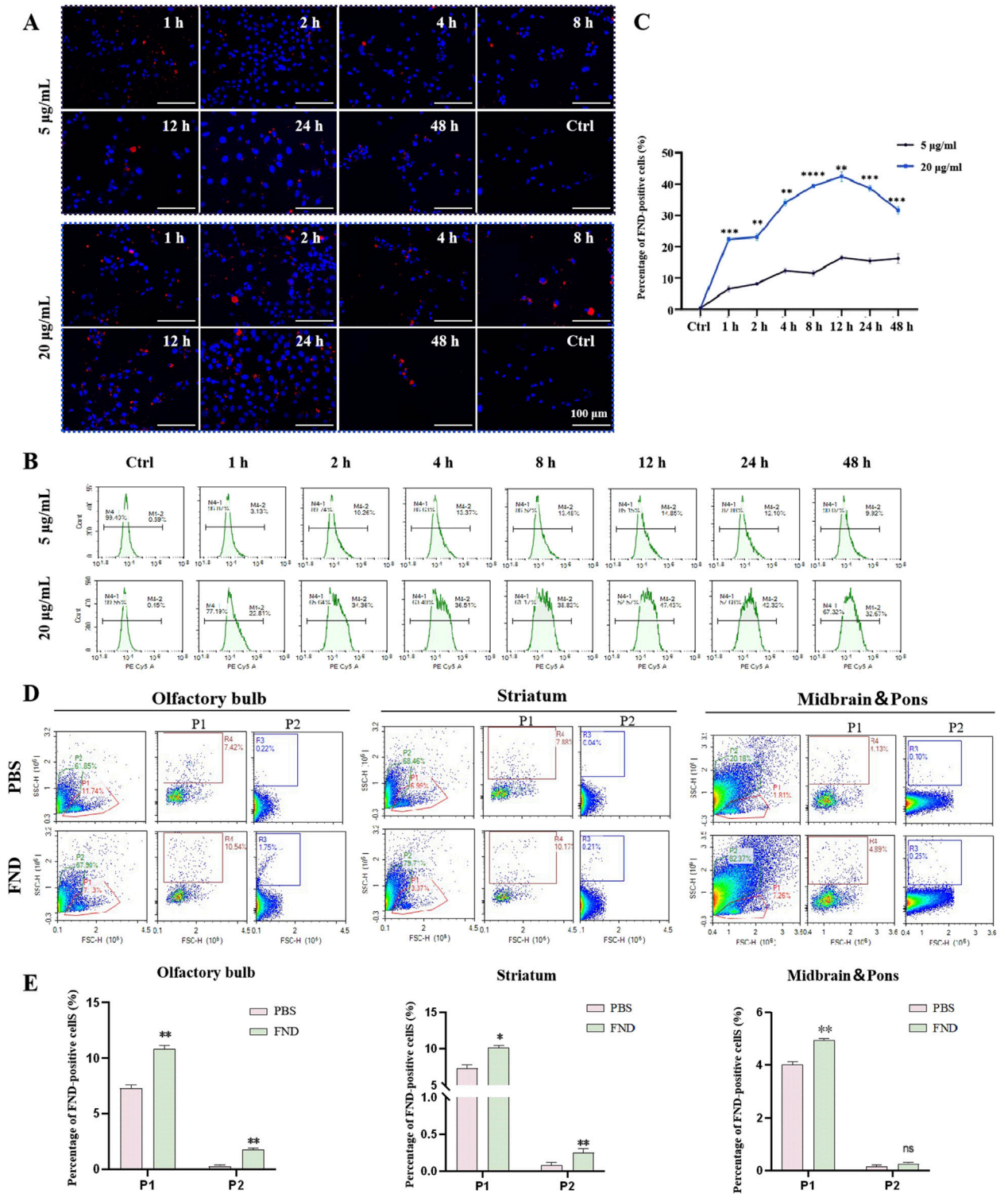

FIGURE 2
The internalization of NDs both *in vitro* and *in vivo*. **(A)** MN9D cells were incubated with different concentrations of NDs for up to 48 h. At indicated time points, intracellular fluorescence was observed using confocal laser scanning microscopy. **(B)** and **(C)** Fluorescence of internalized NDs were quantified using flow cytometry analysis (n = 3). $^{**}P < 0.01$, $^{***}P < 0.001$ and $^{****}P < 0.0001$ with respect to the control group. **(D)** and **(E)** Flow cytometric analysis of the distribution of fluorescent nanodiamonds in the olfactory bulb, striatum, midbrain and pons (n = 3). P1 represents neurons, and P2 represents glial cells. ns means no statistical significance, $^{*}P < 0.05$ and $^{**}P < 0.01$ with respect to the PBS group.

10.3389/fbioe.2024.1480573

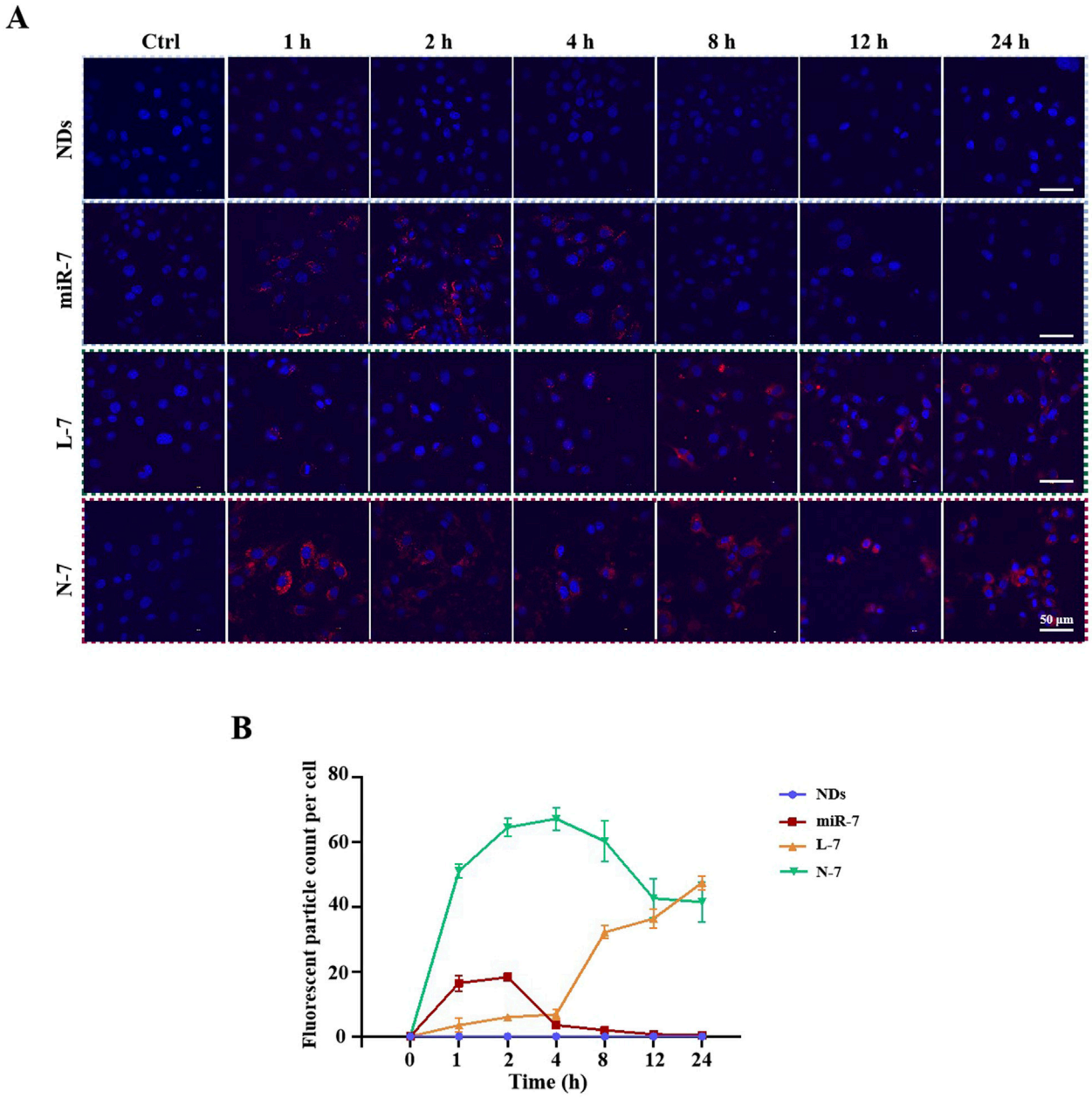

FIGURE 3
Uptake of N-7 by MN9D cells. **(A)** Imaging the uptake of Cy5-miR-7 by MN9D cells under different conditions using confocal laser scanning microscopy. **(B)** Fluorescent particle count per cell (n = 20).

nucleus at 8 h, and remain in the perinuclear region up to 48 h. At a high concentration (20 μg/mL), NDs are seen to accumulate around the nucleus after 8 h, and remain in the cytoplasm up to 48 h, although fewer cells are visible at this time point.

Flow cytometry results (Figures 2B, C) show that the uptake rate of NDs by MN9D cells at a low concentration (5 μg/mL) increases gradually from 1 to 4 h, stabilizes from 4 to 24 h, and then decreases, with 9.34% of cells having internalized NDs at 48 h. At a high concentration (20 μg/mL), the uptake rate is faster, reaching 21.98% at 1 h, with the highest uptake (46.59%) at 12 h, followed by a gradual decline to 31.86% at 48 h. This indicates that NDs are taken up by cells in a concentration-dependent and time-dependent manner, and that over time, nanodiamonds may be expelled from cells via exocytosis. Nanodiamonds were administered intranasally to mice, and their distribution in the olfactory bulbs and striatum was detected using flow cytometry (Figures 2D, E). Thus, nanodiamonds can be internalized both *in vitro* and *in vivo*.

3.3 NDs-mediated cellular uptake and expression of miR-7

Cy5-labeled miR-7 (Cy5-miR-7) was transfected into MN9D cells using NDs and Lipofectamine RNAiMAX. Confocal laser scanning

10.3389/fbioe.2024.1480573

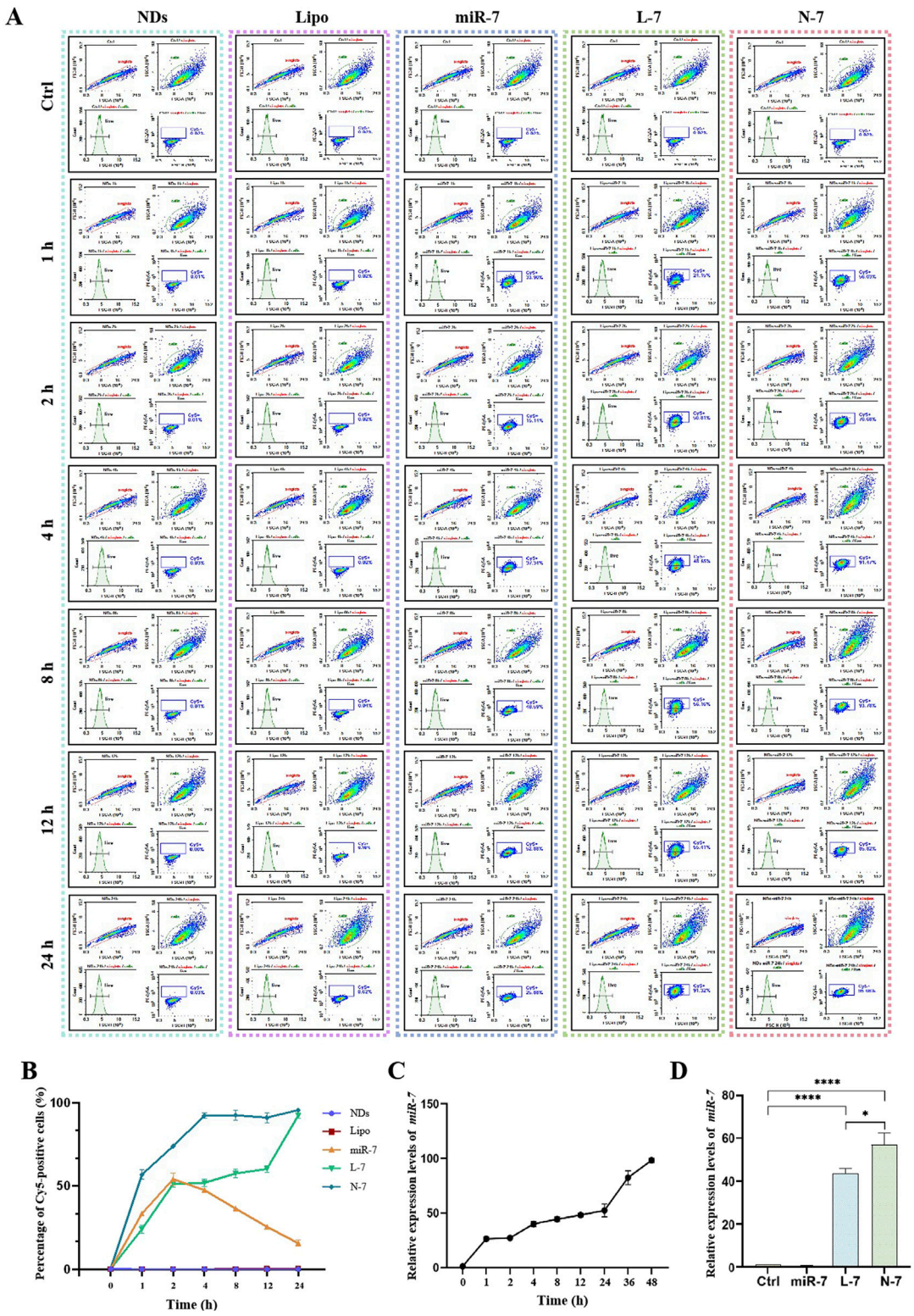

FIGURE 4
Expression of N-7 by MN9D and SH-SY5Y cells. **(A)** and **(B)** Fluorescence of internalized NDs by MN9D cells were quantified using flow cytometry analysis. **(C)** Relative expression levels of miR-7 in SH-SY5Y cells at different times post-transfection with Lipofectamine RNAiMAX. **(D)** Relative expression levels of miR-7 in SH-SY5Y cells after 24 h of incubation with naked miR-7, L-7, and N-7. U6 as the internal reference gene in **(C)** and **(D)** (n = 3). $^{*}P < 0.05$, $^{****}P < 0.0001$.

10.3389/fbioe.2024.1480573

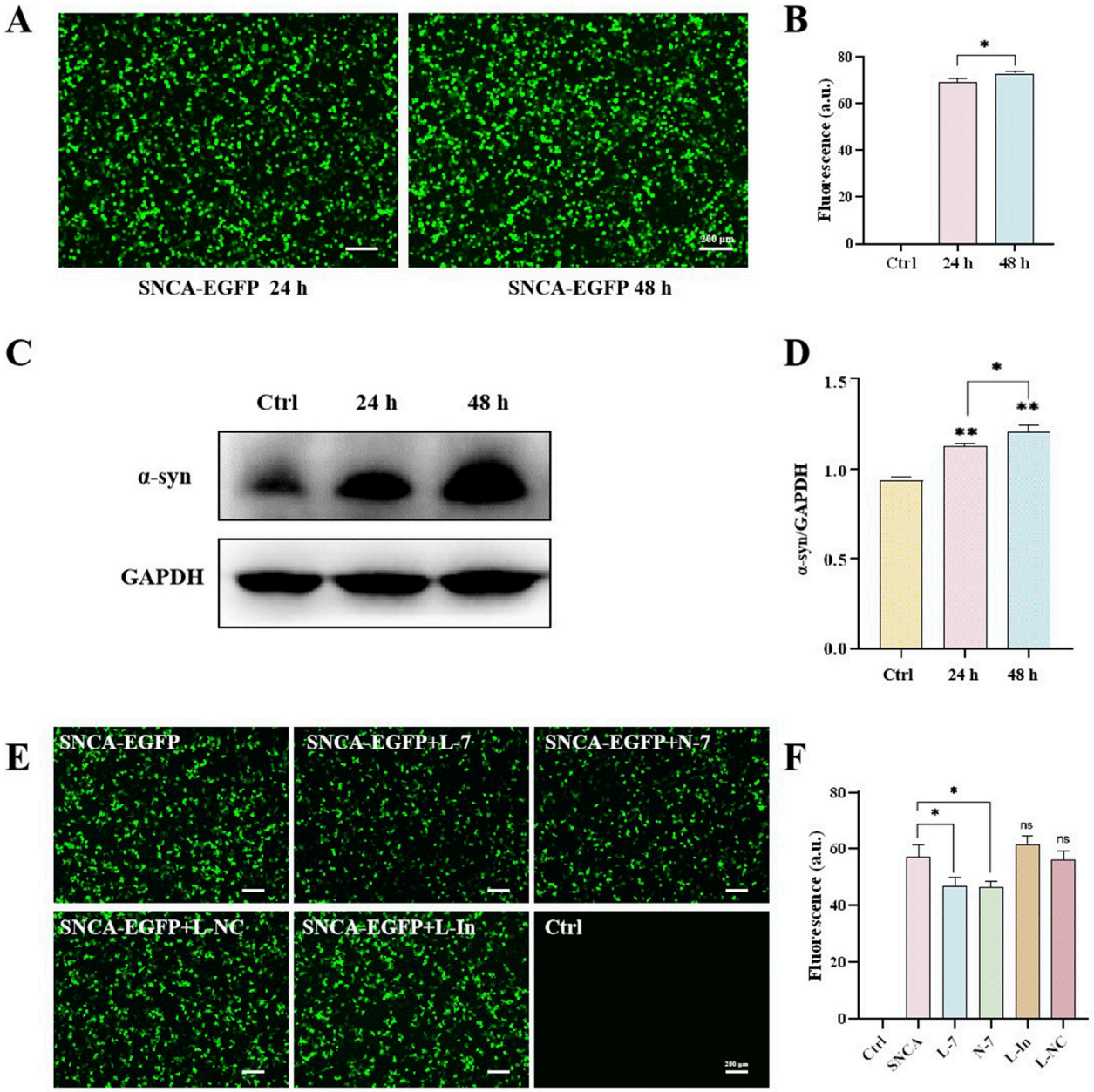

FIGURE 5
N-7 targets the mRNA of α-synuclein. **(A)** Protein levels of α-synuclein were analyzed by Western blotting and its intensity is quantified in **(B)**. **(C)** EGFP fluorescence in HEK293T cells after transfection with the SNCA-EGFP plasmid for 24 or 48 h and quantified in **(D)**. **(E)** EGFP fluorescence in HEK293T cells under different conditions and quantified in **(F)**. L-In, Lipofectamine RNAiMAX transfection of mimic miR-7 inhibitors. ns means no significant difference, $^{*}P < 0.05$ and $^{**}P < 0.01$.

microscopy observations (Figure 3) showed that naked Cy5-miR-7 displays strong red fluorescence in cells from 1 to 4 h post-incubation, with a tendency to accumulate around the nucleus at 2 h and decreasing fluorescence intensity at 4 h. For Lipofectamine RNAiMAX-transfected Cy5-miR-7 (L-7), the intensity of red fluorescence increases over time, peaking at 24 h. For Cy5-miR-7 complexed with NDs (N-7), strong red fluorescence is observed from 1 to 24 h, with a significant amount of punctate accumulation in the cytoplasm at 1 h, and stable fluorescence intensity from 2 to 24 h.

Flow cytometry analysis (Figures 4A, B) showed that neither NDs nor Lipofectamine RNAiMAX alone display any fluorescence signal. Naked Cy5-miR-7 shows an increase in the number of Cy5-positive cells from 1 to 8 h, peaking at 8–12 h and declining at 24 h, with only about 50% of cells being Cy5-positive at the peak. For Lipofectamine RNAiMAX-transfected Cy5-miR-7, the number of Cy5-positive cells increases to about 50% at 1–2 h and remains stable until 12 h, reaching a peak of approximately 90% at 24 h. For NDs-mediated Cy5-miR-7, over 50% of MN9D cells are Cy5-positive at 1 h, and the uptake continues to rise until it reaches a maximum of 96% at 24 h.

The expression of miR-7 within cells increases over time after transfection with Lipofectamine RNAiMAX (Figure 4C). Naked

10.3389/fbioe.2024.1480573

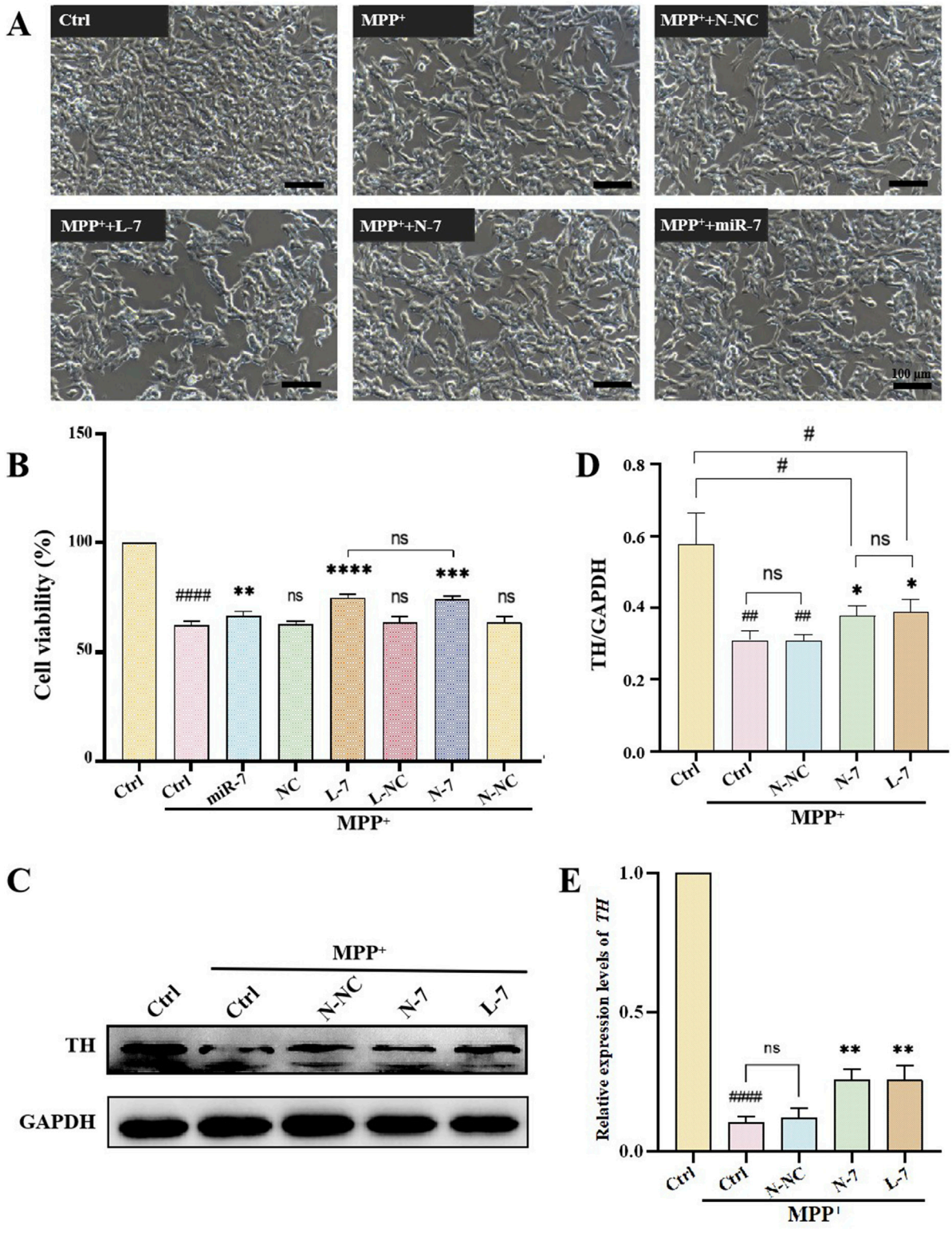

FIGURE 6
The effect of N-7 on MPP+-induced PD model. **(A)** SH-SY5Y cells were photographed with an inverted microscope in white light. **(B)** CCK-8 detection of the effects on the cell viability of SH-SY5Y cells under different conditions (n = 3). $^{\#\#\#\#}P < 0.0001$ with respect to the control group. ns means no statistical significance, $^{**}P < 0.01$, $^{***}P < 0.001$ and $^{****}P < 0.0001$ with respect to the MPP+ Ctrl group. **(C)** Protein levels of TH were analyzed by Western blotting and quantified in **(D)** (n = 3). $^{\#\#}P < 0.01$ with respect to the control group. $^{*}P < 0.05$ with respect to the MPP+ Ctrl group. **(E)** qRT-PCR analysis of relative expression levels of TH (n = 3). $^{\#\#\#\#}P < 0.0001$ with respect to the control group. $^{**}P < 0.01$ with respect to the MPP+ Ctrl group.

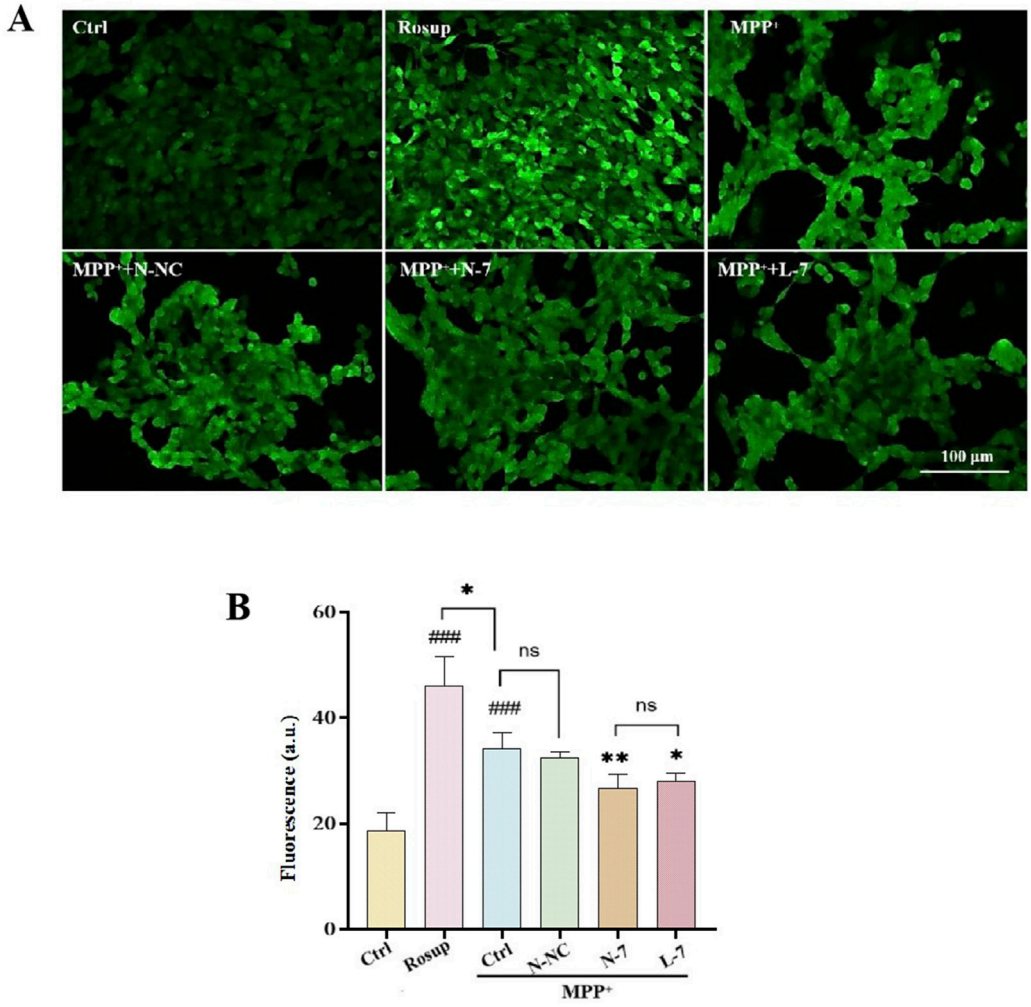

FIGURE 7
N-7 inhibits MPP⁺-induced oxidative stress in SH-SY5Y cells. **(A)** DCFH-DA probe fluorescence was imaged under different conditions using confocal laser scanning microscopy. **(B)** Statistical analysis of the average fluorescence intensity in Figure **(A)**, with Rosup serving as the positive control. $^{###}P < 0.001$ with respect to the control group. $^{*}P < 0.05$ and $^{**}P < 0.01$ with respect to the MPP⁺ Ctrl group.

miR-7 co-incubated with SH-SY5Y cells for 24 h does not differ significantly in relative expression compared to the control group, while L-7 and N-7 co-incubated with SH-SY5Y cells for 24 h show significantly higher miR-7 expression. Furthermore, miR-7 complexed with NDs demonstrates superior transfection efficiency compared to Lipofectamine RNAiMAX, with statistically significant differences ($P < 0.05$) (Figure 4D).

Studies have shown that NDs are primarily internalized via clathrin-mediated endocytosis and can bind serum proteins to enhance receptor-mediated endocytosis (Igarashi et al., 2012). Using polyethylenimine-modified diamond nanoparticles (50 nm) increased DNA delivery efficiency by 70-fold. This suggests that nucleic acids carried by NDs can be efficiently taken up by cells. In this study, we confirmed that Cy5-labeled miRNAs complexed with NDs enter cells rapidly, with over 50% of cells showing Cy5 fluorescence after 1 h, reaching 90% by 4 h and maintaining this level up to 24 h. Compared to Lipofectamine RNAiMAX, NDs deliver miR-7 faster and achieve 1.5 times higher intracellular expression of miR-7 after 24 h.

3.4 N-7 targets the mRNA of α-synuclein

The motor symptoms of PD are largely due to the loss of dopaminergic neurons in the substantia nigra and the resulting dysregulation of basal ganglia activity (Russo et al., 2021). Neuropathologically, PD is characterized by protein inclusions known as Lewy bodies (LBs), with α-synuclein being the major protein component of these inclusions (Cascella et al., 2021). To examine the effect of N-7 on *SNCA* expression, we transfected the human embryonic kidney cell line 293T (HEK293T) with the pLenti-DsRed_IRES_SNCA:EGFP plasmid using TransIntro EL reagent. After 24 h of transfection, a significant number of cells expressing EGFP green fluorescence were observed under the microscope. The expression level of α-synuclein was found to be approximately 65 times higher than in the control group. By 48 h post-transfection, both the fluorescence intensity and α-synuclein expression had further increased, reaching about 70 times that of the control (Figures 5A, B). This indicates the successful establishment of an α-synuclein overexpression model. Western blot analysis

revealed an increase in α-synuclein protein expression levels 24 h post-transfection with the SNCA-EGFP plasmid. Additionally, a significant enhancement in fluorescence intensity was observed at the 48-h mark following transfection (Figures 5C, D).

After overexpressing or inhibiting miR-7 for 24 h and then transfecting the SNCA-EGFP plasmid for another 24 h, the expression of EGFP green fluorescence was observed under confocal microscopy in HEK293T. Approximately 50% of the cells expressed SNCA-EGFP in the SNCA-EGFP group. Both the Lipofectamine RNAiMAX-transfected miR-7 overexpression (L-7) group and the nanodiamond-loaded miR-7 (N-7) group showed a decrease in SNCA-EGFP fluorescence expression. Cells treated with the negative control Lipofectamine RNAiMAX-transfected non-targeting miRNA (L-NC) showed no significant changes in fluorescence expression. Cells treated with the Lipofectamine RNAiMAX-transfected miR-7 mimic inhibitor (L-In) showed a slight increase in fluorescence expression, but the difference was not statistically significant (Figures 5E, F), demonstrating the suppressive effect of miR-7 on *SNCA* gene translation.

3.5 Protection of dopaminergic neurons by N-7

1-Methyl-4-phenylpyridinium (MPP^+) is an inhibitor of mitochondrial complex I that leads to the depletion of cellular ATP and loss of membrane potential, ultimately causing mitochondrial dysfunction and increased production of ROS (Prasad and Hung, 2020). It is commonly used as an inducer for PD cell models. By exposing SH-SY5Y cells to a gradient of MPP^+ concentrations and analyzing their cell viability, the optimal experimental concentration for creating PD models was determined. Results showed that cell viability decreased with increasing MPP^+ concentration; at 100 μM MPP^+, cells exhibited damage and death, which was statistically significant; at 1 mM MPP^+, there was a substantial cell death, with a survival rate of approximately 50%, reaching the half-maximal lethal concentration, suggesting that this concentration could be used as the MPP^+ treatment dose in this study (Supplementary Figure S3).

An important neurochemical abnormality in PD is the degeneration of dopaminergic neurons in the substantia nigra, leading to reduced striatal dopamine (DA) levels. TH is the rate-limiting enzyme of DA biosynthesis, catalyzing the hydroxylation of tyrosine to L-DOPA (Du et al., 2022). After 48 h of 1 mM MPP^+ treatment, the cell viability of SH-SY5Y cells was approximately 60%. Treatment with naked miR-7 led to a significant recovery in cell viability ($P < 0.01$). Cells treated with NC, L-NC, or N-NC had cell viabilities similar to the model group, showing no therapeutic effect. After treatment with L-7, cell viability significantly increased compared to the model group ($P < 0.0001$), and after treatment with N-7, cell viability also significantly increased ($P < 0.001$); there was no statistical difference between the L-7 and N-7 groups (Figure 6B). The results indicate that N-7 does not induce changes in the density or morphology of SH-SY5Y cells.

After pre-treatment with N-NC, L-7, or N-7 for 12 h, MPP^+ was added to achieve a final concentration of 1 mM, and samples were collected after 24 h for observation under inverted microscopy. Results showed that the control group had a high cell density with neurite-like cell projections; after MPP^+ treatment, cell density decreased to approximately 50%, with no significant change in cell morphology; the density of treated cells did not change significantly, and cell morphology remained unchanged (Figure 6A). Western blot results showed that TH protein levels significantly decreased in the PD model group ($P < 0.0001$), while TH protein levels did not change in the negative control (N-NC) group. TH protein levels significantly increased in the positive control (L-7) group ($P < 0.01$), and the increase in the N-7 group ($P < 0.01$) was slightly higher than in the L-7 group (Figures 6C, D). qRT-PCR results were similar to those of the Western blot (Figure 6E). These data indicate that the N-7 nanocomplex not only prevents the MPP^+-induced decrease in TH protein levels but also prevents the MPP^+-induced decrease in TH RNA levels, demonstrating protective effects on dopaminergic neurons.

In this study, we used MPP^+ to induce a PD cell model and used nanodiamonds (NDs) loaded with miR-7 to target the SNCA gene, providing protection against PD cell models. The results show that N-7 can improve the viability of cells damaged by MPP^+ and can increase TH protein expression and RNA levels, demonstrating protective effects on dopaminergic neurons.

3.6 Reduction of cellular oxidative stress levels by N-7

Oxidative stress is a prominent feature of PD and is closely associated with neuronal death and neurological dysfunction, playing a key pathogenic role in PD (Gao et al., 2024). Excessive generation of ROS caused by oxidative stress can lead to apoptosis of dopaminergic neurons, which is one of the primary causes of PD (Fan et al., 2023). As a complex I inhibitor, MPP^+ inhibits ATP production and stimulates the formation of superoxide and peroxynitrite, thus damaging proteins through oxidative and nitrosative stress (Ghosh et al., 2016). Therapies aimed at reducing cellular ROS levels may provide neuroprotective treatment for PD. In the experiment, we used the DCFH-DA probe to detect intracellular ROS levels. Results showed weak ROS in the control group, high fluorescence intensity and high ROS levels in the positive control group (Rosup). After MPP^+ treatment, ROS levels significantly increased compared to the control group. After treatment with N-NC, there was no significant change in ROS levels. After treatment with N-7 and L-7, ROS levels decreased, and there was no statistical difference between N-7 and L-7 (Figures 7A, B).

4 Conclusion

In this study, we designed a nanocomplex (N-7) for the treatment of PD. Compared to traditional RNA transfection reagents like Lipofectamine RNAiMAX, nanodiamonds (NDs) were able to more rapidly and efficiently deliver miR-7 to dopaminergic neurons. In MPP^+-induced PD cell models, N-7 exhibited neuroprotective effects, not only improving the survival rate of dopaminergic neurons in PD models but also alleviating the pathological reduction in TH levels, inhibiting α-synuclein expression, and reducing oxidative stress. N-7 demonstrated

excellent biocompatibility. In summary, the results of this study indicate that N-7 represents a promising strategy for drug delivery in the treatment of PD and other neurodegenerative diseases.

Data availability statement

The raw data supporting the conclusions of this article will be made available by the authors, without undue reservation.

Ethics statement

Ethical approval was not required for the studies on humans in accordance with the local legislation and institutional requirements because only commercially available established cell lines were used. The animal study was approved by The Experimental Animal Welfare and Ethics Committee of Chengdu Medical College. The study was conducted in accordance with the local legislation and institutional requirements.

Author contributions

YH: Conceptualization, Data curation, Formal Analysis, Funding acquisition, Investigation, Methodology, Project administration, Resources, Software, Supervision, Validation, Visualization, Writing–original draft, Writing–review and editing. YY: Conceptualization, Data curation, Formal Analysis, Investigation, Methodology, Project administration, Software, Supervision, Validation, Writing–original draft, Writing–review and editing, Resources. XW: Resources, Visualization, Writing–review and editing. HW: Methodology, Software, Writing–review and editing. SL: Funding acquisition, Writing–original draft, Writing–review and editing, Investigation, Resources. BS: Data curation, Formal Analysis, Funding acquisition, Methodology, Project administration, Resources, Writing–original draft, Writing–review and editing, Conceptualization, Investigation, Software, Supervision, Validation, Visualization.

Funding

The author(s) declare that financial support was received for the research, authorship, and/or publication of this article. This research was supported by the Natural Science Foundation of Sichuan Province (2022NSFSC0807), Young Elite Scientist Sponsorship Program from China Association for Science and Technology (2019QNRC001) and Foundation of Chengdu Medical College (CYZZD22-02).

Conflict of interest

The authors declare that the research was conducted in the absence of any commercial or financial relationships that could be construed as a potential conflict of interest.

Publisher's note

Supplementary material

The Supplementary Material for this article can be found online at: https://www.frontiersin.org/articles/10.3389/fbioe.2024.1480573/full#supplementary-material

References

Aarsland, D., Batzu, L., Halliday, G. M., Geurtsen, G. J., Ballard, C., Chaudhuri, K. R., et al. (2021). Parkinson disease-associated cognitive impairment. *Nat. Rev. Dis. Prim.* 7 (1), 47. doi:10.1038/s41572-021-00280-3

Ahn, G. Y., Kim, S. E., Yun, T. H., Choi, I., Park, D., and Choi, S. W. (2021). Enhanced osteogenic differentiation of alendronate-conjugated nanodiamonds for potential osteoporosis treatment. *Biomaterials Res.* 25 (1), 28. doi:10.1186/s40824-021-00231-9

Barrie, E. S., Lee, S. H., Frater, J. T., Kataki, M., Scharre, D. W., and Sadee, W. (2018). Alpha-synuclein mRNA isoform formation and translation affected by polymorphism in the human *SNCA* 3′UTR. *Mol. Genet. and Genomic Med.* 6 (4), 565–574. doi:10.1002/mgg3.407

Bloem, B. R., Okun, M. S., and Klein, C. (2021). Parkinson's disease. *Lancet* 397 (10291), 2284–2303. doi:10.1016/s0140-6736(21)00218-x

Cascella, R., Chen, S. W., Bigi, A., Camino, J. D., Xu, C. K., Dobson, C. M., et al. (2021). The release of toxic oligomers from α-synuclein fibrils induces dysfunction in neuronal cells. *Nat. Commun.* 12 (1), 1814. doi:10.1038/s41467-021-21937-3

Chen, N., Han, Y. P., Luo, Y., Zhou, Y. F., Hu, X. J., Yu, Y., et al. (2018). Nanodiamond-based non-canonical autophagy inhibitor synergistically induces cell death in oxygen-deprived tumors. *Mater. Horizons* 5 (6), 1204–1210. doi:10.1039/c8mh00993g

Cui, X., Zhang, Z., Yang, Y., Li, S., and Lee, C. S. (2022). Organic radical materials in biomedical applications: state of the art and perspectives. *Explor. (Beijing, China)* 2 (2), 20210264. doi:10.1002/exp.20210264

Du, D., Su, Y. L., Shang, Q., Chen, C., Tang, W. K., Zhang, L., et al. (2022). Biomimetic synthesis of L-DOPA inspired by tyrosine hydroxylase. *J. Inorg. Biochem.* 234, 111878. doi:10.1016/j.jinorgbio.2022.111878

Fan, Z. X., Jin, H., Tan, X. F., Li, Y., Shi, D., Wang, Q. L., et al. (2023). ROS-responsive hierarchical targeting vehicle-free nanodrugs for three-pronged Parkinson's disease therapy. *Chem. Eng. J.* 466, 143245. doi:10.1016/j.cej.2023.143245

Fujiwara, M., Sun, S. M., Dohms, A., Nishimura, Y., Suto, K., Takezawa, Y., et al. (2020). Real-time nanodiamond thermometry probing *in vivo* thermogenic responses. *Sci. Adv.* 6 (37), eaba9636. doi:10.1126/sciadv.aba9636

Gao, Y. F., Zhai, L. M., Chen, J. P., Lin, D. M., Zhang, L. K., Yang, H., et al. (2024). Focused ultrasound-mediated cerium-based nanoreactor against Parkinson's disease via ROS regulation and microglia polarization. *J. Control. Release* 368, 580–594. doi:10.1016/j.jconrel.2024.03.010

Ghosh, A., Langley, M. R., Harischandra, D. S., Neal, M. L., Jin, H. J., Anantharam, V., et al. (2016). Mitoapocynin treatment protects against neuroinflammation and dopaminergic neurodegeneration in a preclinical animal model of Parkinson's disease. *J. Neuroimmune Pharmacol.* 11 (2), 259–278. doi:10.1007/s11481-016-9650-4

Gong, B., Zhang, X., Zahrani, A. A., Gao, W., Ma, G., Zhang, L., et al. (2022). Neural tissue engineering: from bioactive scaffolds and *in situ* monitoring to regeneration. *Explor. (Beijing, China)* 2 (3), 20210035. doi:10.1002/exp.20210035

Gu, M. J., Toh, T. B., Hooi, L., Lim, J. J., Zhang, X. Y., and Chow, E. K. H. (2019). Nanodiamond-mediated delivery of a G9a inhibitor for hepatocellular carcinoma

therapy. *Acs Appl. Mater. and Interfaces* 11 (49), 45427–45441. doi:10.1021/acsami.9b16323

Hansson, O. (2021). Biomarkers for neurodegenerative diseases. *Nat. Med.* 27 (6), 954–963. doi:10.1038/s41591-021-01382-x

Igarashi, R., Yoshinari, Y., Yokota, H., Sugi, T., Sugihara, F., Ikeda, K., et al. (2012). Real-time background-free selective imaging of fluorescent nanodiamonds *in vivo*. *Nano Lett.* 12 (11), 5726–5732. doi:10.1021/nl302979d

Iranzo, A., Fairfoul, G., Ayudhaya, A. C. N., Serradell, M., Gelpi, E., Vilaseca, I., et al. (2021). Detection of α-synuclein in CSF by RT-QuIC in patients with isolated rapid-eye-movement sleep behaviour disorder: a longitudinal observational study. *Lancet Neurol.* 20 (3), 203–212. doi:10.1016/s1474-4422(20)30449-x

Jomova, K., Raptova, R., Alomar, S. Y., Alwasel, S. H., Nepovimova, E., Kuca, K., et al. (2023). Reactive oxygen species, toxicity, oxidative stress, and antioxidants: chronic diseases and aging. *Archives Toxicol.* 97 (10), 2499–2574. doi:10.1007/s00204-023-03562-9

Li, T. F., Li, K., Wang, C., Liu, X., Wen, Y., Xu, Y. H., et al. (2017). Harnessing the cross-talk between tumor cells and tumor-associated macrophages with a nano-drug for modulation of glioblastoma immune microenvironment. *J. Control. Release* 268, 128–146. doi:10.1016/j.jconrel.2017.10.024

Li, T. F., Xu, Y. H., Li, K., Wang, C., Liu, X., Yue, Y., et al. (2019). Doxorubicin-polyglycerol-nanodiamond composites stimulate glioblastoma cell immunogenicity through activation of autophagy. *Acta Biomater.* 86, 381–394. doi:10.1016/j.actbio.2019.01.020

Lin, Y. W., Raj, E. N., Liao, W. S., Lin, J., Liu, K. K., Chen, T. H., et al. (2017). Co-delivery of paclitaxel and cetuximab by nanodiamond enhances mitotic catastrophe and tumor inhibition. *Sci. Rep.* 7, 9814. doi:10.1038/s41598-017-09983-8

Liu, B., Qi, Z., and Chao, J. (2023). Framework nucleic acids directed assembly of Au nanostructures for biomedical applications. *Interdiscip. Med.* 1 (1), e20220009. doi:10.1002/inmd.20220009

Liu, Y. M., Chen, S., Quan, X., and Yu, H. T. (2015). Efficient electrochemical reduction of carbon dioxide to acetate on nitrogen-doped nanodiamond. *J. Am. Chem. Soc.* 137 (36), 11631–11636. doi:10.1021/jacs.5b02975

Malpartida, A. B., Williamson, M., Narendra, D. P., Wade-Martins, R., and Ryan, B. J. (2021). Mitochondrial dysfunction and mitophagy in Parkinson's disease: from mechanism to therapy. *Trends Biochem. Sci.* 46 (4), 329–343. doi:10.1016/j.tibs.2020.11.007

McMillan, K. J., Murray, T. K., Bengoa-Vergniory, N., Cordero-Llana, O., Cooper, J., Buckley, A., et al. (2017). Loss of MicroRNA-7 regulation leads to α-synuclein accumulation and dopaminergic neuronal loss *in vivo*. *Mol. Ther.* 25 (10), 2404–2414. doi:10.1016/j.ymthe.2017.08.017

Meng, Z., Zhang, Y., Yang, L., Yuan, F., Wang, J., Chen, J., et al. (2024). Application of advanced biosensors in nervous system diseases. *Interdiscip. Med.* 2, e20240024. doi:10.1002/inmd.20240024

Ogawa, M., Murae, M., Gemba, R., Irie, T., Shimojima, M., Saijo, M., et al. (2022). L-DOPA, a treatment for Parkinson's disease, and its enantiomer D-DOPA inhibit severe fever with thrombocytopenia syndrome virus infection *in vitro*. *J. Infect. Chemother.* 28 (3), 373–376. doi:10.1016/j.jiac.2021.11.005

Prasad, E. M., and Hung, S. Y. (2020). Behavioral tests in neurotoxin-induced animal models of Parkinson's disease. *Antioxidants* 9 (10), 1007. doi:10.3390/antiox9101007

Russo, M. J., Orru, C. D., Concha-Marambio, L., Giaisi, S., Groveman, B. R., Farris, C. M., et al. (2021). High diagnostic performance of independent alpha-synuclein seed amplification assays for detection of early Parkinson's disease. *Acta Neuropathol. Commun.* 9 (1), 179. doi:10.1186/s40478-021-01282-8

Salaam, A. D., Hwang, P. T. J., Poonawalla, A., Green, H. N., Jun, H. W., and Dean, D. (2014). Nanodiamonds enhance therapeutic efficacy of doxorubicin in treating metastatic hormone-refractory prostate cancer. *Nanotechnology* 25 (42), 425103. doi:10.1088/0957-4484/25/42/425103

Tenchov, B., Sugimoto, Y., Koynova, R., Brueggemeier, R. W., and Lee, R. J. (2012). Highly efficient cationic ethylphosphatidylcholine siRNA carrier for GFP suppression in modified breast cancer cells. *Anticancer Res.* 32 (7), 2563–2566. doi:10.1093/annonc/mds166

Vijiaratnam, N., Simuni, T., Bandmann, O., Morris, H. R., and Foltynie, T. (2021). Progress towards therapies for disease modification in Parkinson's disease. *Lancet Neurol.* 20 (7), 559–572. doi:10.1016/s1474-4422(21)00061-2

Xie, B., and Xie, H. (2024). Application of stimuli-responsive hydrogel in brain disease treatment. *Front. Bioeng. Biotechnol.* 12, 1450267. doi:10.3389/fbioe.2024.1450267

Yang, T. C., Chang, C. Y., Yarmishyn, A. A., Mao, Y. S., Yang, Y. P., Wang, M. L., et al. (2020). Carboxylated nanodiamond-mediated CRISPR-Cas9 delivery of human retinoschisis mutation into human iPSCs and mouse retina. *Acta Biomater.* 101, 484–494. doi:10.1016/j.actbio.2019.10.037

Zhang, J., Zhao, M. Y., Yan, R., Liu, J., Maddila, S., Junn, E. S., et al. (2021). MicroRNA-7 protects against neurodegeneration induced by α-synuclein preformed fibrils in the mouse brain. *Neurotherapeutics* 18 (4), 2529–2540. doi:10.1007/s13311-021-01130-6

frontiers | Frontiers in Bioengineering and Biotechnology

TYPE Review
PUBLISHED 01 April 2025
DOI 10.3389/fbioe.2025.1553653

OPEN ACCESS

EDITED BY
Donglin Xia,
Nantong University, China

REVIEWED BY
Chao Wang,
Johns Hopkins University, United States
Jianqiang Liu,
Guangdong Medical University, China

*CORRESPONDENCE
Yongfang Zhou,
zhouyongfang0117@163.com
Bin Li,
1libin@163.com
Pan Shang,
shangpan20230419@njmu.edu.cn

†These authors have contributed equally to this work

RECEIVED 31 December 2024
ACCEPTED 04 March 2025
PUBLISHED 01 April 2025

CITATION
He J, Wang G, Zhou Y, Li B and Shang P (2025) Recent advances in polydopamine-coated metal–organic frameworks for cancer therapy. *Front. Bioeng. Biotechnol.* 13:1553653. doi: 10.3389/fbioe.2025.1553653

Recent advances in polydopamine-coated metal–organic frameworks for cancer therapy

Jingchao He[1,2†], Guangtian Wang[3†], Yongfang Zhou[4*], Bin Li[5*] and Pan Shang[6*]

[1]Institute of Translational Medicine, Medical College, Yangzhou University, Yangzhou, China, [2]Key Laboratory of the Jiangsu Higher Education Institutions for Nucleic Acid and Cell Fate Regulation, Yangzhou University, Yangzhou, China, [3]Teaching Center of Pathogenic Biology, School of Basic Medical Sciences, Harbin Medical University, Harbin, China, [4]Department of Oncology, Jining Cancer Hospital, Jining, China, [5]Department of Biochemistry and Molecular Biology, Medical College, Guangxi University of Science and Technology, Liuzhou, China, [6]Department of Obstetrics and Gynecology, The Affiliated Taizhou People's Hospital of Nanjing Medical University, Taizhou, China

The creation and development of classical multifunctional nanomaterials are crucial for the advancement of nanotherapeutic treatments for tumors. Currently, metal–organic frameworks (MOFs) modified with polydopamine (PDA) are at the forefront of nanomedicine research, particularly in tumor diagnostics and therapy, owing to their exceptional biocompatibility, expansive specific surface area, multifaceted functionalities, and superior photothermal properties, which led to significant advancements in anti-tumor research. Consequently, a range of anti-cancer strategies has been devised by leveraging the exceptional capabilities of MOFs, including intelligent drug delivery systems, photodynamic therapy, and photothermal therapy, which are particularly tailored for the tumor microenvironment. In order to gain deeper insight into the role of MOFs@PDA in cancer diagnosis and treatment, it is essential to conduct a comprehensive review of existing research outcomes and promptly analyze the challenges associated with their biological applications. This will provide valuable perspectives on the potential of MOFs@PDA in clinical settings.

KEYWORDS

metal–organic frameworks, polydopamine, metal–organic frameworks modified with polydopamine, cancer, diagnosis and therapy

1 Introduction

Nanomedicine protects drugs, improves drug targeting, enables intelligent drug release, and overcomes drug resistance (Wang and Zhang, 2023). Nanomedicine utilizes the tumor microenvironment to treat tumors and enables comprehensive treatment and diagnosis of tumors, improving the efficiency of tumor treatment (Wang and Zhang, 2023). Nanomedicine plays a pivotal role in tumor diagnosis and therapy, emerging as a frontier for the discovery of innovative diagnostic and therapeutic approaches that are increasingly attracting research interest (Wang and Zhang, 2023; Zhang J. et al., 2023; Forgham et al., 2024). It has enhanced the efficacy of cancer treatment and reduced treatment-associated toxicities, markedly improving the quality of life and survival rates for cancer patients and contributing to the advancement of precision medicine (Sandbhor et al., 2024). Multifunctional nanomaterials are the main elements of nanomedicine and are the

carriers of nanomedicine for the diagnosis and treatment of tumors (Zhou L. L. et al., 2024). The design and fabrication of these multifunctional nanomaterials are crucial for achieving efficient and safe tumor treatment and represent a central milestone in the progression of nanomedicine, which can catalyze the development of new diagnostic and therapeutic strategies (Sharma and Otto, 2023; Zhou Z. et al., 2021; Lan et al., 2023). Consequently, the pursuit of multifunctional nanomaterials in the domain of tumor diagnostics and therapeutics, through a comprehensive review, holds the potential to offer insights for the creation of novel multifunctional nanomaterials and foster the discovery of innovative anti-tumor strategies, thus proving to be of significant value.

Metal–organic frameworks (MOFs) with excellent properties are mesoporous crystalline materials composed of metal ions and organic ligands, which have become leading materials in the field of tumor diagnosis and therapy and have received increasing attention (Ma et al., 2023; Binaeian et al., 2023; Wang Y. et al., 2025a). Compared with traditional nanomaterials, MOFs mainly have the following advantages (Wang S. et al., 2024; Shi P. et al., 2023; Gulati et al., 2023; Moharramnejad et al., 2023; Mehata et al., 2023): (1) MOFs possess abundant mesopores and a high specific surface area, enabling efficient drug loading. Some MOFs can degrade within the tumor microenvironment to realize the precise release of drugs at the tumor site. Therefore, MOFs are highly efficient carriers for the construction of nano-drug delivery systems. (2) Some MOFs are composed of metal ions that are essential to the human body and low-toxicity organic ligands, which exhibit good biocompatibility. Some MOFs are degradable, which reduces the long-term toxicity of the nanoparticles. Thus, MOFs have good biosafety, which is the basis for anti-tumor applications. (3) Due to the diverse and multifunctional nature of the metal ions and organic ligands, MOFs exhibit highly efficient imaging properties [computed tomography (CT) imaging, magnetic resonance imaging (MRI), and fluorescence imaging (FI), among others] and therapeutic properties [chemodynamic therapy (CDT), photodynamic therapy (PDT), and sonodynamic therapy (SDT), among others]; their rich and adjustable functions make them an efficient platform for achieving diagnostic and therapeutic integration and comprehensive treatment. (4) MOFs have nano-enzymatic activity, which can scavenge the highly expressed glutathione (GSH) in the tumor microenvironment and catalyze the generation of reactive oxygen species (ROS) and O_2 from endogenous highly expressed H_2O_2 to improve the hypoxic state of the tumor microenvironment. Therefore, MOFs can regulate the characteristics of the tumor microenvironment and enhance the tumor therapeutic effect. Therefore, MOFs have important research significance and can promote the development of novel tumor diagnostic and therapeutic strategies.

Polydopamine (PDA), which is produced from dopamine by self-polymerization reaction under oxygen and an alkaline environment, has excellent properties and is a classical nanomaterial that has been widely studied and highly regarded in the field of tumor diagnosis and therapy (Zhao X. et al., 2024; Mao et al., 2024; Menichetti et al., 2024). Compared with other functional materials, PDA has the following main advantages (Wu H. et al., 2022a; Li M. et al., 2023; Acter et al., 2023; Witkowska et al., 2023; Li H. et al., 2021): (1) PDA not only has good biocompatibility but also has degradability. Therefore, PDA has superior biosafety, which is the basis for its wide application. (2) PDA is an excellent photothermal agent, with high photothermal conversion efficiency and high photothermal stability, demonstrating high efficiency of photothermal performance. (3) PDA has high adhesion and could be coated on the surface of a variety of functional materials, making it an ideal unit for the preparation of multifunctional nanomaterials. (4) The surface of PDA is rich in reactive groups such as catechol, amine, and amino, which not only chelate metal ions (Gd^{3+}, Mn^{2+}, and Fe^{3+}, etc.) to produce T_1-weighted MRI but also facilitate surface modification. (5) The preparation process of PDA is simple, making it easy to obtain samples for biomedical applications. Therefore, PDA is of great research significance and has broad applications in tumor therapy and diagnosis.

MOFs@PDA could combine the advantages of MOFs and PDA, which is a classic multifunctional material for achieving a good synergistic effect of "1 + 1>2." MOFs and PDA have both advantages and disadvantages. Some MOFs have problems such as poor water solubility, unstable physiological environments, and lack of active groups on the surface, which limit their biological applications (Zhou et al., 2022). By virtue of its strong adhesion properties, PDA can grow on the surface of MOFs and improve the water solubility, stability, and biocompatibility of MOFs (Zhou et al., 2022). PDAs alone are relatively monofunctional and cannot provide highly efficient tumor diagnosis and treatment. However, PDA can chelate the metal ions that compose MOFs, leading to the growth of MOFs with multiple functions on its surface; this process endows PDA with multifunctionality to meet high clinical therapeutic requirements (Chen L. et al., 2019). Therefore, MOFs@PDA is a classical combination that can overcome the inherent defects of MOFs and PDA and produce new physicochemical properties, which is more suitable for tumor diagnosis and treatment. For example, PDA is coated on the surface of MOFs that are efficiently loaded with drugs, placing the drugs inside the composite material, avoiding the problem of drug leakage in the bloodstream that exists with most carriers, and mitigating the toxic side effects of the drugs (Huang et al., 2023).

Currently, MOFs@PDA has achieved a series of breakthrough research results in the field of tumor diagnosis and treatment by virtue of its excellent performance, which is useful for reference. Unfortunately, no review on MOFs@PDA in the field of tumor diagnosis and therapy has been reported. In this paper, we summarized the application of MOFs@PDA in tumor monotherapy and combination therapy (Figure 1) and analyzed the challenges of MOFs@PDA in oncology applications in a timely manner to deepen the understanding of MOFs@PDA, which is expected to be useful for the construction of new classical multifunctional nanomaterials and the development of novel anti-tumor strategies.

2 Application of polydopamine-coated metal–organic frameworks in cancer therapy

MOFs@PDA combine the unique advantages of both MOFs and PDA, overcoming the inherent limitations of each while acquiring

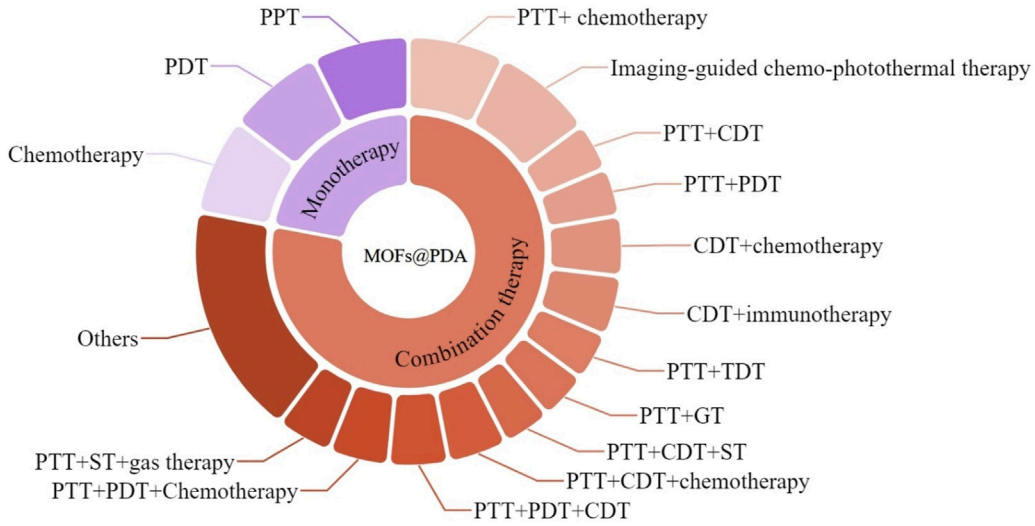

FIGURE 1
Schematic illustration showing the application of MOFs@PDA in tumor therapy.

new physicochemical properties. This results in a highly efficient and safe classical multifunctional nanomaterial. MOFs@PDA can act as a contrast agent and be used for photodynamic and photothermal therapy, thus achieving the integration of diagnosis and treatment (Guo et al., 2020). MOFs@PDA can efficiently load proteases and drugs, which could achieve comprehensive treatment, and it has made significant breakthroughs in addressing drug resistance, tumor microenvironment-induced therapeutic resistance, and the low efficiency of low-temperature PTT (Li J. M. et al., 2023; Liu G. et al., 2020; Yu H. et al., 2022; Deng X. et al., 2023). The application of MOFs@PDA in cancer diagnosis and therapy is shown in Table 1.

2.1 Polydopamine-coated metal–organic frameworks in monotherapy for tumor

2.1.1 Chemotherapy

At present, chemotherapy is still one of the main clinical treatments for tumors. However, there are some problems such as the non-specific distribution of chemotherapeutic drugs, premature degradation during circulation, and poor water solubility, which limit the efficient application of chemotherapy in clinics (Wang P. et al., 2024). Therefore, it is of great research value to use a simple method to construct a nano-drug delivery system to overcome the abovementioned shortcomings. Shu et al. (2018) encapsulated DOX inside ZIF-8 by the one-step method, coated ZIF-8 surface with PDA, chelated Fe^{3+} with shell PDA, and connected hyaluronic acid (HA) to the surface of the prepared material by the coordination between the carboxyl group of HA and Fe^{3+}, resulting in the preparation of DOX@ZIF-HA Due to the presence of HA, DOX@ZIF-HA could actively target tumor tissues with high CD44 receptor expression and become specifically distributed at the tumor site. DOX@ZIF-HA loaded DOX inside the material to prevent premature degradation and leakage of the drug during circulation. Because PDA chelated Fe^{3+}, DOX@ZIF-HA had a relaxation rate (R_1) of 5.57 mM^{-1} s^{-1}, which was higher than that of Gd-DTPA, a clinical MRI contrast agent, and it showed excellent T_1-weighted MRI performance. DOX@ZIF-HA, with a drug-loading capacity of approximately 8.92%, exhibited good stability and pH-responsive drug release performance, which achieved T_1-weighted MRI-guided active targeted chemotherapy (Shu et al., 2018). Zhou C. et al. (2022) coated the surface of MIL-53 (Fe) loaded with camptothecin (CPT) by PDA to prepare PDA@CPT@MIL-53 (Fe). The surface modification of PDA not only improved the stability, hydrophilicity, and biocompatibility of MIL-53 (Fe) but also prevented the leakage of CPT in blood circulation. PDA@CPT@MIL-53 (Fe) has a drug-loading capacity of 43.07%, and it showed a pH-responsive drug release, which reduced the side effects of chemotherapy. Due to the presence of MIL-53 (Fe), PDA@CPT@MIL-53 (Fe) possessed a transverse relaxation rate of 50 $mM^{-1}s^{-1}$ and showed good T2-weighted MRI performance, which achieved imaging-guided chemotherapy (Zhou C. et al., 2022).

2.1.2 Photodynamic therapy

Photodynamic therapy (PDT) can be divided into type I PDT and type II PDT, which has advantages such as non-invasiveness, low side effects, and high tumor specificity, serving as an efficient method for the clinical treatment of tumors (Hsia et al., 2023; Jiang et al., 2023). Most PDT belongs to type II PDT, where the main mechanism consists of photosensitizers converting O_2 into ROS under light irradiation, which, in turn, destroys tumor cells (Sun et al., 2023; Yu Q.et al., 2024; Yu L. et al., 2024). Tumor hypoxia is the basic feature of a tumor microenvironment and is mainly caused by the rapid increase of tumors and abnormal vascular systems in the tumor, resulting in abnormal blood supply and local hypoxia, which can not only promote the development of tumors but also reduce the efficacy of PDT, chemotherapy, and radiation therapy (Zhang C. et al., 2023; Liu Z. et al., 2024). MOFs@PDA has nano-enzyme activity or can combine with nano-enzyme to catalyze the high concentration of H_2O_2 in the tumor to produce O_2, which

TABLE 1 Application of MOFs@PDA in cancer diagnosis and therapy.

MOFs@PDA-based nano-system	Surface modification of MOFs@PDA	Imaging performance	Treatment mode	Reference
DOX@ZIF-HA	HA	T_1-weighted MRI	Chemotherapy	Shu et al. (2018)
PDA@CPT@MIL-53 (Fe)	_	T_2-weighted MRI	Chemotherapy	Zhou et al. (2022)
UIO@Ca-Pt	_	_	PDT	Ren et al. (2021)
MnCoO-PDA-PEG-Ce6	PEG	T_2-weighted MRI and FI	PDT	Wang et al. (2019a)
PDA-Pt@PCN-FA	FA	FI	PDT	Wang D. et al. (2018)
Cu-BTC@PDA	_	T_1-weighted MRI	PTT	Thirumurugan et al. (2023)
MCP-PEG-RGD	PEG and cRGD	T_1-weighted MRI	PTT	Wang X. S. et al. (2018)
SOR@ZIF-8@PDA	_	_	PTT + chemotherapy	Hu et al. (2023)
BA@ZIF-8-PDA-PEG	PEG-NH_2	_	PTT + chemotherapy	Gao S. S. et al. (2023)
DOX/Pd@ZIF-8@PDA	_	PAI	PTT + chemotherapy	Zhu et al. (2019)
PDA-PCM@ZIF-8/DOX	Tetradecanol	_	PTT + chemotherapy	Wu et al. (2018)
PDA/MTX@ZIF-8	_	_	PTT + chemotherapy	Yin et al. (2022)
IDa-PRMSs@ZF	FA	_	PTT + chemotherapy	Zhang W. et al. (2023)
DOX@MoS_2-PMA	HA	T_1-weighted MRI and PAI	PTT + chemotherapy	Yang et al. (2021)
DI@HMONs-PMOFs	PEG-NH_2	T_1-weighted MRI and PAI	PTT + chemotherapy	Chen et al. (2019)
ZIF-8/DMPP	PEG	T_1-weighted MRI and PAI	PTT + chemotherapy	Guo et al. (2020)
Fe3O4-NH_2@PDA@Au@MIL101-NH_2-DOX	_	T_2-weighted MRI	PTT + chemotherapy	Li S. et al. (2021)
Gd/Tm- PB@ZIF-8/PDA-DOX	_	T_1–T_2 weighted MRI and FI	PTT + chemotherapy	Xu et al. (2020)
BTTP-MOF@PDA/DOX	BTTP	T_1-weighted MRI	PTT + chemotherapy	Wang Y. T. et al. (2022)
Cu-BTC@PDA	_	_	CDT + PTT	Liu L.et al. (2023)
PDA@Cu/ZIF-8	_	_	CDT + PTT	An et al. (2020)
HG-MIL@PDA	HA	_	CDT + PTT	Wu et al. (2021)
MP@PI	_	FI	CDT + PTT	Deng et al. (2022)
Gd-PDA-Ce6@Gd-MOF	_	T_1–T_2 weighted MRI and PAI	PTT + PDT	Pu et al. (2021)
PDA-MB-CAT-ZIF-8	_	_	PTT + PDT	Feng et al. (2020a)
MCDP@Bif	_	PET/CT	CDT + chemotherapy	Li J. M. et al. (2023)
CQ/FA-PDA@MOF	FA	_	CDT + immunotherapy	Chiang B. et al. (2023)
MPDA/AIPH@ZIF-8/GA	_	_	PTT + TDT	Deng et al. (2023)
PDAs-siRNA-ZIF-8	_	PAI and near-infrared imaging	PTT + GT	Feng et al. (2020b)
Zr/Ce-MOFs/GOx/PDA	_	_	PTT + catalytic therapy	You et al. (2024)
TPZ/PFA@UiO-66@PDA	_	PAI	PTT + hypoxia-activated chemotherapy	Chen et al. (2021)
MPDA@ZIF-8/DOX + GOx	_	_	PTT + starvation therapy	Liu et al. (2020)
ZDZP@PP	mPEG-NH_2	_	PDT + chemotherapy	Ren et al. (2020)
PDA-MOF-E-M	Osteosarcoma cell membranes	T_1-weighted MRI	PTT + ferroptosis	Liu Y. J. et al. (2024)

(Continued on following page)

TABLE 1 (*Continued*) Application of MOFs@PDA in cancer diagnosis and therapy.

MOFs@PDA-based nano-system	Surface modification of MOFs@PDA	Imaging performance	Treatment mode	Reference
PDA@C3N4@MIL/GOx@HA	HA	_	PTT + ST + CDT	Yu et al. (2022)
MGH	HA	PAI	PTT + ST + CDT	Zhang et al. (2019)
Oxa@MIL-PDA-PEGTK	NH_2-PEGTK-COOH	_	PTT + CDT + chemotherapy	Huang et al. (2022)
RBCM-HCPT@Cu/ZIF-8@PDA	Erythrocyte membrane	_	PTT + CDT + chemotherapy	Ren et al. (2024)
CMC/OSA/PCN-224 (Cu) at PDA	_	_	PTT + PDT + CDT	Zhang and Yuan. (2024)
AIPH/PDA@CuS/ZIF-8	_	PAI	PTT + PDT + CDT	Zhang et al. (2021)
PCN-DOX@PDA	_	T_2-weighted MRI	PTT + PDT + chemotherapy	Chen B. et al. (2023)
Ini@PM-HP	HA	FI + photothermal imaging	PTT + PDT + chemotherapy	Feng et al. (2022)
PCoA@M	Macrophage membranes	_	PTT + ST + GT	Cheng K. et al. (2022)
DGZPNs	_	_	PTT + ST + chemotherapy	Zhan et al. (2023)
Cu@MIL-101@PMTPC	_	_	CDT + PDT immunotherapy + chemotherapy	An et al. (2024)
d-Arg/GOX/TPZ@MOF (Fe)-PDA/Fe^{3+}/FA-BSA	FA-BSA	T_1-weighted MRI	ST + CDT + RT + GT + chemotherapy	Wang et al. (2023)

significantly improves the photodynamic effect (Ren et al., 2021; Wang D. et al., 2019a; Wang X. S. et al., 2018). Ren et al. (2021) used PDA and CaO_2 to coat the surface of UIO-66-NH_2 loaded with photosensitizer TCPP through stirring and applied a Pt nano-enzyme, which grew on the surface of the prepared material by a reduction reaction, resulting in the construction of UIO@Ca-Pt. CaO_2 reacted with water to form calcium hydroxide and H_2O_2, which overcame the deficiency of endogenous H_2O_2. Pt could catalyze H_2O_2 to produce a large amount of O_2 and increase the level of O_2 in the tumor site, thus improving the effect of TCPP-mediated PDT (Ren et al., 2021). The researchers made rational use of nano-enzymes to generate a large amount of O_2 at the tumor site in a cascade enzyme reaction, alleviating the lack of oxygen at the tumor site and significantly improving the efficiency of PDT, which provided an effective way to overcome the problem of lack of oxygen in the tumor environment. Wang D. et al. (2019a) obtained well-dispersed MnCoO by a one-step method, coated the surface of MnCoO with PDA, modified the shell PDA with PEG, and used the prepared material to load photosensitizer Ce6 through Mn^{2+} and deprotonated COO^- coordination, resulting in the preparation of MnCoO-PDA-PEG-Ce6. Due to the presence of PDA and PEG, MnCoO-PDA-PEG-Ce6 showed excellent biocompatibility and good physiological stability, which could be enriched at tumor sites. MnCoO not only had T2-weighted MRI performance but also was a type of nano-enzyme that could continuously catalyze endogenous high concentrations of H_2O_2 to produce a large amount of O_2, thus improving the efficacy of PDT mediated by Ce6. MnCoO-PDA-PEG-Ce6 had a drug-loading capacity of 13.8% and could lead to continuous production of O_2 *in situ* to improve the state of hypoxia, showing a good effect of PDT on both hypoxic and normoxic tumors (Wang D. et al., 2019a). Wang X. S. et al. (2018) synthesized Pt on the surface of PDA, coated PCN on the surface of PDA, and connected FA with shell PCN, leading to the formation of PDA-Pt@PCN-FA. Because of the stable properties of PDA, researchers could synthesize Pt on the surface of PDA via a reduction reaction. Pt was a type of nano-enzyme that could catalyze the infiltration of H_2O_2 into the inner layer of the material and produce a large amount of O_2, thus improving the efficacy of PDT and inhibiting tumor metastasis. When O_2 entered the shell PCN, PCN generated a large amount of ROS under laser irradiation, showing highly efficient PDT. PDA-Pt@PCN-FA used nano-enzymes to continuously produce O_2, which showed high efficiency of PDT for both hypoxic and normoxic tumors (Figure 2) (Wang X. S. et al., 2018). In this study, a core-shell multi-functional complex was reasonably designed, and the different parts of the material had a clear division of labor, performed their own duties, and did not interfere with each other, thus providing a large amount of oxygen for PDT, solving the problem of low efficiency of PDT caused by hypoxia, and inhibiting tumor metastasis (Wang X. S. et al., 2018). The abovementioned studies used nano-enzymes to catalyze the formation of O_2 from endogenous H_2O_2, which improved the efficacy of PDT. However, the insufficient content of endogenous H_2O_2 at the tumor site could limit the efficiency of O_2 production.

2.1.3 Photothermal therapy

Photothermal therapy (PTT) uses photothermal agents to absorb the energy of laser light and convert it into heat, which uses high temperatures to destroy tumor cells (Li N. et al., 2024). PTT has the advantages of high specificity, fewer side effects, high efficiency, and simple operation (Zhang S. et al., 2024; Duan et al., 2023). The multi-functional photothermal agent that integrates diagnosis and photothermal performance can monitor the effect of photothermal therapy and delimit the area of photothermal therapy, which improves photothermal efficiency and is a hot spot in the field of photothermal research (Chen X. et al., 2024; Liu S. et al., 2024; He et al., 2023). Some MOFs have excellent imaging performance, and PDA has excellent photothermal

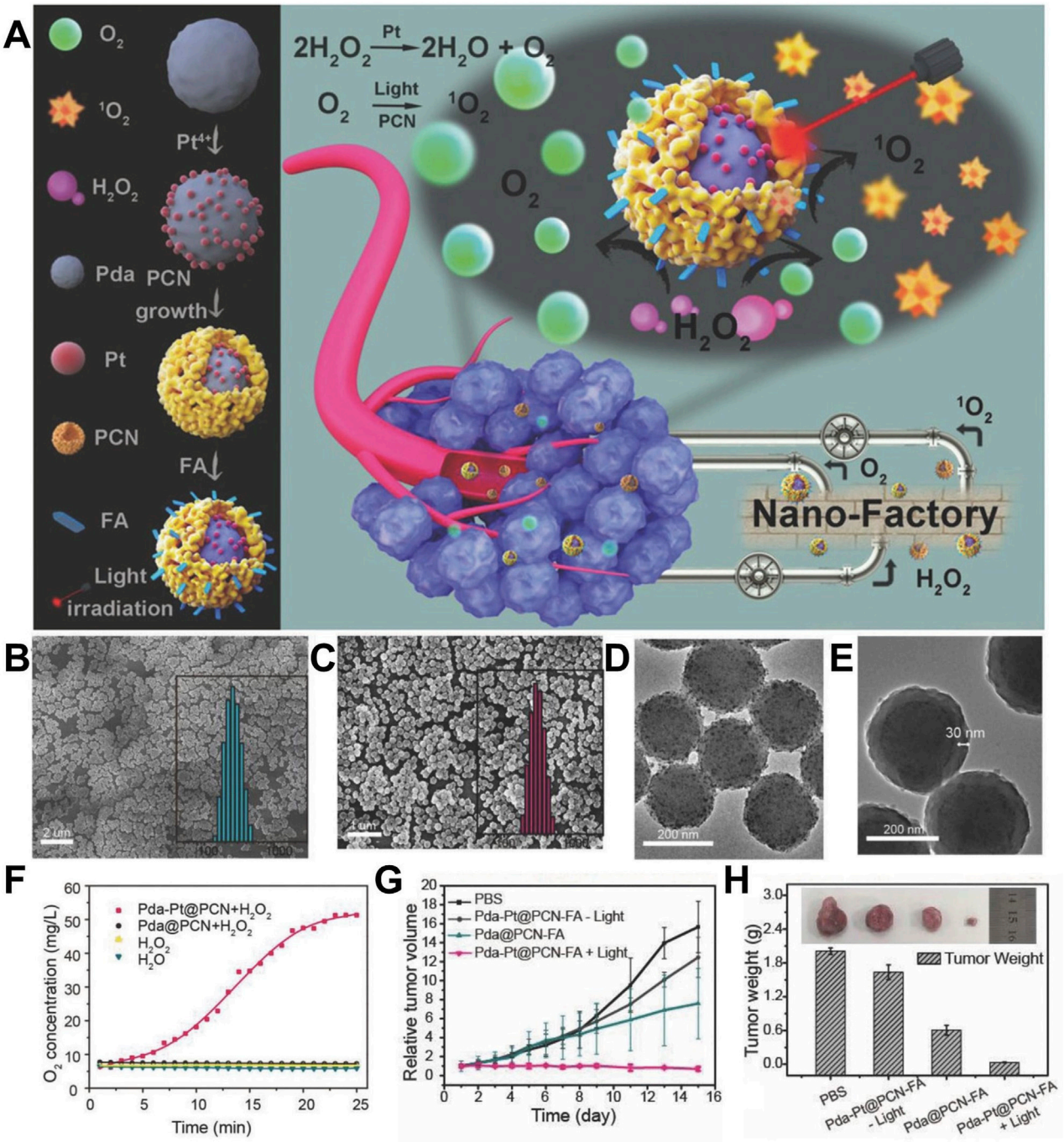

FIGURE 2
(A) Schematic illustration of experimental procedure for preparing PDA-Pt@PCN-FA and anti-tumor mechanisms of PDA-Pt@PCN-FA. DLS and SEM images of **(B)** PDA-Pt and **(C)** PDA-Pt@PCN. TEM images of **(D)** PDA-Pt and **(E)** PDA-Pt@PCN. **(F)** O_2 generation properties in different groups. **(G)** Relative tumor volume changes in different treatment groups. **(H)** Representative tumor images and average tumor weight of tumor-bearing mice in different treatment groups. Copyright 2018, with permission from Wiley-VCH GmbH and Wang X. S. et al. (2018).

performance. Therefore, MOFs@PDA can serve as a multi-functional photothermal agent, enriching the variety of multi-functional photothermal agents (Thirumurugan et al., 2023; Wang et al., 2018). Thirumurugan et al. (2023) synthesized Cu-BTC by the hydrothermal method and coated the surface of Cu-BTC with PDA to prepare Cu-BTC@PDA. Due to the paramagnetism of Cu^{2+} in Cu-BTC, Cu-BTC@PDA possessed an R_1 value of 3.01 mg^{-1} s^{-1} and exhibited excellent T_1-weighted MRI performance *in vitro*. Due to the presence of PDA, Cu-BTC@PDA not only exhibited good biocompatibility but also had 13.32% photothermal conversion efficiency, showing superior photothermal effect (Thirumurugan et al., 2023). Wang et al. (2018) combined Mn_3 [Co. (CN) $_6]_2$ and PDA into a hybrid nanogel (MCP) by the one-pot method and used MCP to connect PEG and cRGD, thus preparing MCP-PEG-RGD .

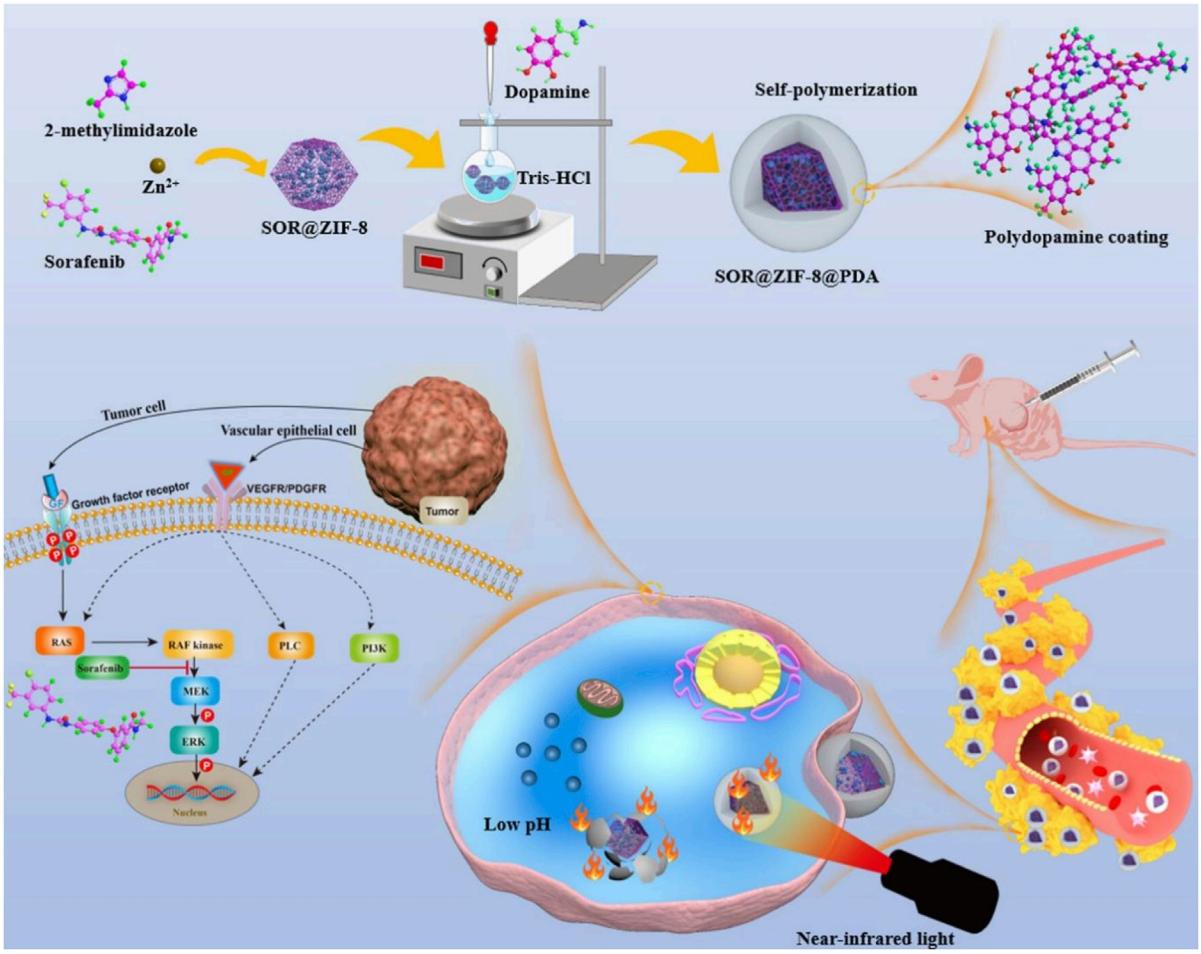

FIGURE 3
Schematic illustration of the experimental procedure for preparing SOR@ZIF-8@PDA and the combination of photothermal therapy and chemotherapy induced by SOR@ZIF-8@PDA; copyright 2023, with permission from American Chemical Society and Hu et al. (2023).

Due to the presence of PEG and RGD with active targeting performance, MCP-PEG-RGD exhibited good stability, biocompatibility, and long blood circulation time, which could accumulate in large quantities at the tumor site. MCP-PEG-RGD had a photothermal conversion efficiency of 41.3% and possessed an R_1 value of 5.175 $mM^{-1}S^{-1}$, which achieved the active-targeting PTT guided by T_1-weighted MRI (Wang et al., 2018).

2.2 Polydopamine-coated metal–organic frameworks in combination therapy

Because of the heterogeneity, complexity, and diversity of tumors, comprehensive treatment has the advantages of different treatment methods, which is the focus of research in the field of tumor therapy (Turkmen et al., 2024; Yang et al., 2024). MOFs@PDA are multifunctional nanomaterials that combine diagnostic and therapeutic functions, and they are highly efficient platforms for comprehensive treatment, providing a vehicle for exploring novel strategies for tumor diagnosis and treatment and promoting the development of tumor diagnosis and treatment.

2.2.1 MOFs@PDA integrated photothermal therapy and chemotherapy for anti-tumor effects

Chemotherapy can enhance the efficacy of PTT, and PTT promotes drug release and enhances the ability of drugs to enter cells (Yang K. et al., 2023). Therefore, PTT combined with chemotherapy is an efficient combination therapy (Wang X. et al., 2023). At present, liver cancer, with high incidence and mortality, still lacks effective treatment (Ladd et al., 2024). Sorafenib (SOR) is a clinically approved HCC treatment drug, which prolongs the survival time and improves the quality of life of patients (Chon et al., 2024). However, SOR has some problems, such as short half-life, low solubility, easy drug resistance, and adverse side effects, which limit its clinical application (Liu X. et al., 2024). Therefore, many nanomaterials are used to load SOR to improve the therapeutic efficiency of SOR (Wang L. et al., 2023a). However, many nanomaterials load SOR on their surface, which cannot prevent SOR leakage into bloodstream or its toxicity to normal tissues (Kong et al., 2021). In view of this, Hu et al. (2023) encapsulated SOR inside ZIF-8 by a simple one-pot method and coated ZIF-8 with PDA to prepare SOR@ZIF-8@PDA. PDA not only improved the biocompatibility and stability of ZIF-8 but also

prevented drug leakage in blood circulation and reduced adverse drug reactions. Due to the presence of PDA, SOR@ZIF-8@PDA had a photothermal conversion efficiency of 23.95%, showing a good photothermal effect. Because ZIF-8 has the characteristics of acid-responsive degradation and PDA accelerated degradation at high temperatures, SOR@ZIF-8@PDA showed pH- and light-stimulated responsive drug release, with the most drug release under both acidic and light conditions. SOR@ZIF-8@PDA exhibited a drug-loading capacity of 7.3% and excellent biosafety, enabling the combination of chemotherapy and PTT, which significantly inhibited tumor growth (Figure 3) (Hu et al., 2023). Due to the self-polymerization of dopamine in an alkaline solution and the coordination between zinc ion (Zn^{2+}) and PDA, Gao S. S. et al. (2023) coated PDA on the surface of ZIF-8 loaded with baicalein (BA) and modified PEG-NH_2 on the surface of shell PDA by electrostatic action to prepare BA@ZIF-8-PDA-PEG. Due to the presence of PDA and PEG-NH_2, BA@ZIF-8-PDA-PEG possessed good stability, dispersion, and biocompatibility. In an acidic environment, the protonation of the imidazolium group in ZIF-8 resulted in the destruction of coordination between the zinc ion and the imidazole ring, which led to the degradation of ZIF-8. PDA can also undergo degradation through depolymerization under weakly acidic conditions. Therefore, BA@ZIF-8-PDA-PEG showed pH-responsive drug release, facilitating precise drug delivery in the slightly tumor acidic environment of the tumor while reducing the adverse effects of chemotherapy. BA@ZIF-8-PDA-PEG improved the stability and solubility of BA, with a drug-loading capacity of 70.4% and a photothermal conversion efficiency of 39.48%, enabling chemotherapy combined with PTT (Gao S. S. et al., 2023). This study provided a reference for the construction of a nano-drug delivery system based on traditional Chinese medicine and provided a method for the rational use of traditional Chinese medicine. Zhu et al. (2019) encapsulated two-dimensional Pd nanowires and DOX inside ZIF-8 by the one-step method and coated ZIF-8 surface with PDA to prepare DOX/Pd@ZIF-8@PDA. Due to the presence of two photothermal agents, Pd and PDA, DOX/Pd@ZIF-8@PDA had a photothermal conversion efficiency of up to 45% and an excellent photothermal effect. DOX/Pd@ZIF-8@PDA had a drug-loading capacity of 12% and showed pH- and light-stimulated responsive drug release, enabling the combination of PTT and chemotherapy (Zhu et al., 2019). In this study, two-dimensional materials, MOFs, and PDA were combined to obtain novel composites, which improved the drug-loading performance and intelligent drug release ability of two-dimensional materials and made use of the efficient photothermal properties of two-dimensional materials, providing an efficient platform for the realization of comprehensive treatment. Wu Q. et al. (2018) encapsulated DOX inside ZIF-8 by the one-pot method, coated the ZIF-8 surface with phase change materials (tetradecanol and PCM), and applied PDA to coat the surface of PCM@ZIF-8/DOX, leading to the preparation of PDA-PCM@ZIF-8/DOX. Due to the presence of PDA, PDA-PCM@ZIF-8/DOX exhibited good biocompatibility, low toxicity, and high stability, overcoming the problem of rapid degradation of ZIF-8 in an acidic environment. PDA-PCM@ZIF-8/DOX possessed the characteristics of degradation in an acidic environment, showing the pH-responsive release of drugs. PDA-mediated PTT led to local high temperature, resulting in the dissolution of PCM and promoting drug release, which resulted in heat-responsive drug release. Therefore, PDA-PCM@ZIF-8/DOX achieved pH- and thermal-responsive release of drugs, which could enable accurate treatment of tumors and avoid damage to normal tissues. PDA-PCM@ZIF-8/DOX had a drug-loading capacity of 37.86% and a photothermal conversion efficiency of 30.61%, enabling the combination of PTT and chemotherapy (Wu Q. et al., 2018). PDA-PCM@ZIF-8/DOX prepared in this study had pH-responsive degradation properties, which avoided long-term toxicity accumulation of nanomaterials. The thermo-responsive degradation of PCM was used to modify the surface of the material, which enabled the precise release of the drug at the irradiation site of the tumor, promoting the development of precision medicine. Yin et al. (2022) encapsulated methotrexate (MTX) in the inner part of ZIF-8 by the one-pot method and coated ZIF-8 with PDA to prepare PDA/MTX@ZIF-8. PDA/MTX@ZIF-8 had a drug-loading capacity of 16.45% and showed drug release in response to pH and light stimulation, enabling the combination of chemotherapy and PTT (Yin et al., 2022). These studies suggested that ZIF-8@PDA, with its intelligent drug release capability, served as an excellent photothermal agent and an ideal drug carrier, enabling the efficient combination of chemotherapy and PTT. Zhang W. et al. (2023) loaded ammonium bicarbonate (NH_4HCO_3) and DOX with rod-shaped mesoporous silica nanoparticles (RMSs), applied PDA to coat RMSs and load photosensitizer ICG, and synthesized ZIF-8 modified with FA on the PDA surface to prepare IDa-PRMSs@ZF. IDa-PRMSs@ZF not only had a photothermal conversion efficiency of 26.06%, showing a good photothermal effect, but also showed drug release in response to pH and light stimulation. FA-ZIF-8 endowed the composites with active tumor targeting and improved their biocompatibility. In an acidic environment and at high temperatures, NH_4HCO_3 readily decomposed, producing a large amount of CO_2, which promoted the rapid release of DOX at the tumor site. This enabled DOX to reach the therapeutic concentration in a short time, thereby improving the effectiveness of chemotherapy. IDa-PRMSs@ZF could actively target the tumor tissue and release several chemotherapeutic drugs within the tumor, thus achieving a highly efficient combination of chemotherapy and PTT. This provided an ideal nano-platform for the construction of a nano-drug delivery system with active targeting capabilities and the ability to trigger drug release in large quantities at the tumor site (Zhang W. et al., 2023).

2.2.2 Imaging-guided chemo-photothermal therapy

Yang S. et al. (2021) synthesized MoS_2 with photothermal therapy and PA imaging ability by the one-pot method, applied PDA to coat the surface of MoS_2, used Fe-MOFs consisting of Fe^{3+} and trimesic acid (H_3BTC) to grow layer-by-layer through self-assembly on the PDA surface, and utilized the Fe-MOFs for DOX-loading and connecting with HA, leading to the preparation of DOX@MoS_2-PMA. Because the active group of PDA could chelate Fe^{3+}, Fe-MOFs could grow on the surface of MoS_2@PDA, which showed T_1-weighted MRI properties. The DOX@MoS_2-PMA could actively target breast cancer cells with high HA receptor expression and had a drug-loading capacity of 21.46%, enabling drug release in response to both pH and light stimulation. DOX@MoS_2-PMA achieved MRI and PAI-guided the combination of chemotherapy

and PTT, which significantly inhibited tumor growth (Yang S. et al., 2021). MoS_2, as a non-mesoporous material, was combined with mesoporous MOFs to form a composite that leveraged the photothermal properties of MoS_2 and the drug-carrying capacity of MOFs; this combination compensated for the low drug-carrying efficiency of MoS_2, enabling highly efficient combination therapy. Chen L. et al. (2019) used PDA to coat hollow mesoporous organosilica nanoparticles (HMONs) loaded with DOX to synthesize Fe-MOFs consisting of Fe^{3+} and H_3BTC on the surface of PDA through the layer-by-layer self-assembly technique and used Fe-MOFs to connect PEG-NH2 and load ICG, leading to the preparation of DI@HMONs-PMOFs. Because of the coordination between PDA and Fe^{3+} and the PAI performance of ICG, DI@HMONs-PMOFs had T_1-weighted MRI and PAI performance, which was helpful in achieving accurate diagnosis and imaging-guided treatment. DI@HMONs-PMOFs had a drug-loading capacity of 11.88% for DOX and a drug-loading capacity of 19.52% for ICG, and it showed drug release in response to pH and light stimulation, achieving an efficient combination of PTT and chemotherapy (Chen L. et al., 2019). In this study, taking advantage of the fact that PDA was easy to coat on the surface of functional materials and chelate metal ions, HMONs and MOFs were combined to achieve efficient loading of drugs and photothermal agents, achieving comprehensive treatment guided by imaging, which provided a novel idea for the construction of a multi-functional complex. Guo et al. (2020) encapsulated DOX inside ZIF-8 by the one-pot method, coated the ZIF-8 surface with PDA, chelated Mn^{2+}, and connected PEG with shell PDA, leading to the preparation of ZIF-8/DMPP. Due to the chelation of Mn^{2+} by PDA, ZIF-8/DMPP exhibited T_1-weighted MRI and PAI performance, improving imaging accuracy. ZIF-8/DMPP with a drug-loading capacity of 18.9% exhibited pH-responsive degradation and showed pH- and light stimulation-responsive drug release, achieving a combination of chemotherapy and PTT (Guo et al., 2020). This study illustrated that MOFs@PDA, with PDA as the shell, could directly chelate metal ions to achieve imaging capabilities through a simple method; this provided a simple and rational strategy for preparing multifunctional nano-platforms with integrated diagnostic and therapeutic functions. Li S. et al. (2021) used Au nanocages, a photothermal agent, to adhere to the core-shell structure of Fe_3O_4-NH_2@PDA through physical stirring; they then synthesized MIL-101-NH_2 on the surface of the synthetic material by the microwave thermal method and loaded DOX into the MIL-101-NH_2 shell, leading to the preparation of Fe_3O_4-NH_2@PDA@Au@MIL101-NH_2-DOX. Fe_3O_4-NH_2@PDA@Au@MIL101-NH_2-DOX exhibited good biocompatibility, exhibited drug release in response to light stimulation, and enabled T_2-weighted MRI-guided chemotherapy combined with PTT (Li S. et al., 2021). These studies suggest the correctness of the following. Due to its strong adhesive properties, PDA can be easily coated on the surface of different types of materials (Wu H. et al., 2022a; Li M. et al., 2023; Acter et al., 2023; Witkowska et al., 2023; Li H. et al., 2021). Since PDA could chelate the metal ions that constitute MOFs, MOFs easily grow on the PDA surface. Through the bridge action of PDA, MOFs were easy to combine with different types of nanomaterials to form a complex, which provided multi-functional platforms for the integration of diagnosis and treatment. Xu et al. (2020) synthesized ZIF-8 on the Gd^{3+}- and Tm^{3+}-doped Prussian blue (Gd/Tm-PB) surface, coated the ZIF-8 surface with PDA, and loaded DOX with shell PDA, leading to the preparation of Gd/Tm-PB@ZIF-8/PDA-DOX. Due to the presence of Gd^{3+} and Tm^{3+}, Gd/Tm-PB showed the performance of T_1–T_2-weighted MRI and fluorescence imaging (FI), leveraging the complementary advantages of different imaging modes to improve diagnostic accuracy. Due to the degradation of PDA at high GSH concentration and the degradation of ZIF-8 in acidic environments, the complex achieved drug release in response to GSH and pH. Gd/Tm-PB@ZIF-8/PDA-DOX enabled the combination of chemotherapy and PTT guided by multimodal imaging (Xu et al., 2020). Given the tumor microenvironment's characteristics—low pH and high GSH concentration—the complex demonstrated potential for accurate drug release at the tumor site, thus reducing the toxicity of chemotherapy (Xu et al., 2020). The bone microenvironment also provided a "barrier" for malignant bone tumors, preventing chemotherapeutic drugs and tumor-targeting molecules from entering bone tumor cells (Natoni et al., 2019; Liu et al., 2014; Chen et al., 2017; Tian et al., 2021). Therefore, it is of great research value to develop new efficient and safe methods for the treatment of bone tumors. Wang et al. (2022a) prepared the complex of Mn–Co MOFs and PDA by the one-step method, used PDA to connect bone-targeted small molecule BTTP through the Michael addition reaction, and applied PDA to efficiently load DOX through π–π stacking, leading to the preparation of BTTP-MOF@PDA/DOX. Due to the presence of BTTP, BTTP-MOF@PDA/DOX could actively target bone tumors and efficiently enrich nanomaterials and DOX at bone tumor sites. BTTP-MOF@PDA/DOX had a drug-loading capacity of 9.23%, showed pH-responsive drug release, and possessed a photothermal conversion efficiency of 42.67%, showing a good photothermal effect. Due to the Mn^{2+} in the Mn–Co MOFs, the BTTP-MOF@PDA/DOX had excellent T_1-weighted MRI performance, enabling the integration of diagnosis and treatment. BTTP-MOF@PDA/DOX could actively target bone tumors, and it achieved an efficient combination of PTT and chemotherapy to inhibit bone tumor growth and bone destruction, which provided ideas for overcoming low treatment efficacy caused by the bone microenvironment (Figure 4) (Wang et al., 2022a).

2.2.3 MOFs@PDA integrate photothermal therapy and chemodynamic therapy to enhance anti-tumor effects

Chemodynamic therapy (CDT) involves metal ions reacting with H_2O_2 in the tumor through the Fenton reaction to generate toxic hydroxyl radicals (•OH), which destroy tumor cells (Cheng B. et al., 2023). Insufficient intracellular H_2O_2 concentration leads to less ROS production, and high GSH expression in tumor cells scavenged ROS, which reduced the efficiency of CDT (Cheng B. et al., 2023). The combination of PTT and CDT is an excellent therapeutic modality (Cheng B. et al., 2023; Yan et al., 2024; Gao Q. et al., 2023). PTT generated high temperatures that increased the efficacy of the Fenton reaction and promoted the effect of CDT, and CDT generated ROS that inhibited the activity of heat shock proteins and enhanced the sensitivity of PTT (Yan et al., 2024; Gao Q. et al., 2023). Liu L. et al. (2023) coated PDA on the surface of Cu-BTC composed of Cu^{2+} and H_3BTC to prepare Cu-BTC@PDA. The shell PDA improved the stability and biocompatibility of Cu-

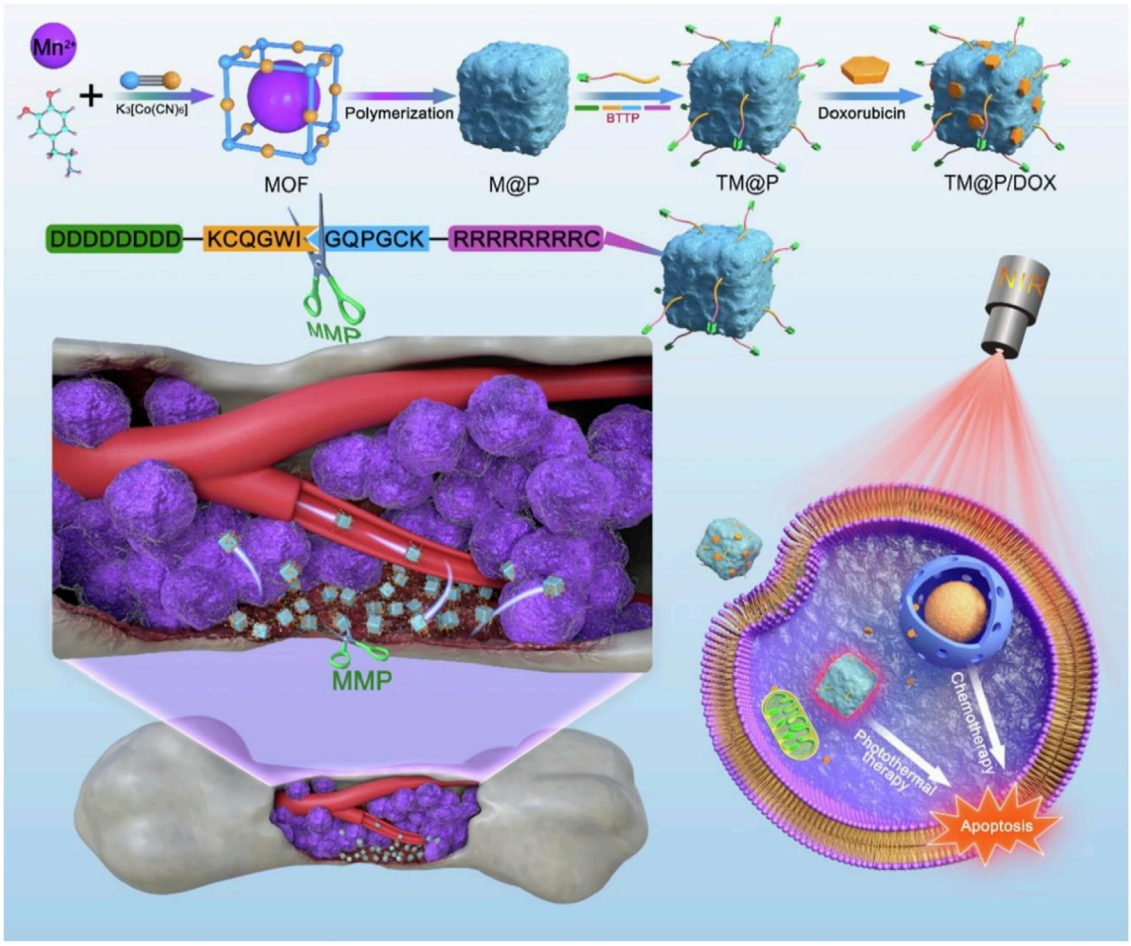

FIGURE 4
Schematic illustration of experimental procedure for preparing BTTP-MOF@PDA/DOX (TM@P/DOX) and the combination of photothermal therapy and chemotherapy induced by TM@P/DOX with the property of bone tumor cell targeting; copyright 2022, with permission from Elsevier and Wang Y. T. et al. (2022).

BTC. The photothermal conversion efficiency of Cu-BTC@PDA was 49.38%, which was significantly higher than that of PDA (36.12%). The photothermal performance of Cu-BTC@PDA was enhanced by the plasma generated by the d–d leap of Cu^{2+} in Cu-BTC. Cu-BTC@PDA released Cu^{2+} in the acidic microenvironment. Cu^{2+} consumed GSH and generated Cu^{+}, which reduced the clearance of OH. Cu^{+} reacted with H_2O_2 in tumor cells to generate OH, which produced CDT. Cu-BTC@PDA achieved highly efficient PTT combined with CDT, which significantly inhibited the growth of melanoma (Liu L. et al., 2023). An P. et al. (2020) applied Cu^{2+}-doped ZIF-8 to grow on the surface of PDA, leading to the preparation of PDA@Cu/ZIF-8. Cu^{2+} released by PDA@Cu/ZIF-8 could scavenge GSH and produce Cu^{+}, which could react with H_2O_2 through the Fenton reaction to form OH, resulting in CDT. PDA-mediated PTT promoted GSH depletion and enhanced Fenton reaction efficiency, thereby disrupting intracellular redox balance and improving the efficacy of CDT. PDA@Cu/ZIF-8 could effectively deplete GSH, facilitating strong energy between PTT and CDT (An P. et al., 2020). In view of the low efficiency of CDT caused by the insufficient concentration of endogenous H_2O_2, Wu et al. (2021) synthesized MIL-101-NH_2 composed of Fe^{3+} and 2-aminoterephthalic acid on the surface of PDA modified by PVP and applied shell MIL-101-NH_2 to load GOx and connect HA, leading to the preparation of HG-MIL@PDA. Due to the presence of HA, HG-MIL@PDA could actively target tumor cells with high expression of CD44 receptors and prolong blood circulation time, thus efficiently enriching the tumor site. Due to the degradability of shell MIL-101-NH_2, HG-MIL@PDA has the dual stimulation of pH and light to release Fe^{3+} and GOx. GOx could catalyze glucose to produce H_2O_2 and gluconic acid in the presence of O_2, which could compensate for the deficiency of endogenous H_2O_2. Fe^{3+} could react with GSH to deplete it and generate Fe^{2+}, which inhibited the antioxidant system and reduced ROS clearance. Fe^{2+} reacted with a large amount of H_2O_2 to produce a large amount of ROS, thus achieving high-efficiency CDT. Gluconic acid could reduce the acidic environment of the tumor site, which promoted the efficiency of the Fenton reaction and improved the effect of CDT. HG-MIL@PDA had a photothermal conversion efficiency of 26.03%, showed a good photothermal effect, and enabled an efficient combination of CDT and PTT (Wu et al., 2021). In this study, HG-MIL@PDA had the ability to generate a large amount of H_2O_2 and remove GSH, solving the problem of CDT inefficiency

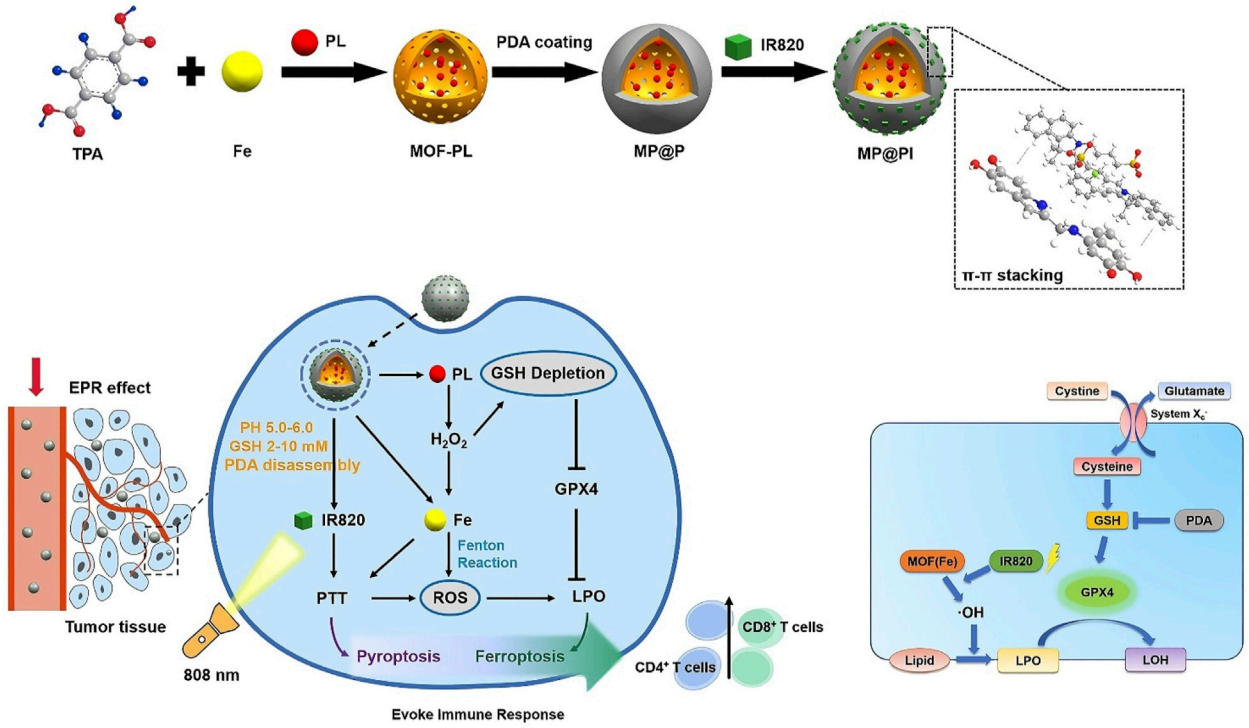

FIGURE 5
Schematic illustration of the fabrication of MP@PI and the combination of photothermal therapy and chemodynamic therapy induced by MP@PI with the mechanism of ferroptosis; copyright 2022, with permission from the American Chemical Society and Deng H. et al. (2022).

due to the insufficient endogenous H_2O_2 and high expression of GSH, which could provide a new idea for the efficient use of CDT in the treatment of tumors (Wu et al., 2021). Different from apoptosis, necrosis, and pyroptosis, ferroptosis has a mode of death characterized by iron-dependent lipid peroxidation and the accumulation of large amounts of reactive oxygen species, which can promote the efficacy of chemotherapy, radiotherapy, PDT, and PTT (Ye et al., 2024). Studies have shown that the inhibition of cystine/glutamate transporter (System xc-) and glutathione peroxidase 4 (GPX4) is the main mechanism leading to ferroptosis (Song et al., 2024). The inhibition of GSH, that is, the GPX4 cofactor, leads to the suppression of the GPX4 expression, which leads to lipid peroxidation and the generation of ferroptosis (Song et al., 2024; Yang et al., 2025; Nie et al., 2024). Deng H. et al. (2022) coated PDA on the surface of MOFs loaded with piperlongumine (PL) and incorporated IR 820 using shell PDA, leading to the formation of MP@PI. PDA could consume GSH and reduce the expression of GPX4, which was beneficial for the occurrence of ferroptosis and enhanced the efficacy of CDT. PI produced a large amount of H_2O_2 in the tumor site, which could overcome the problem of poor efficacy of CDT caused by the deficiency of endogenous H_2O_2. A large number of iron ions in MOFs could react with H_2O_2 to produce a large amount of ROS, which led to lipid peroxidation, promoted the generation of ferroptosis, and produced efficient CDT. PTT mediated by PDA and IR820 not only promoted the efficiency of CDT but also produced the effect of pyroptosis. Under laser irradiation, MP@PI could clear GSH and downregulate the expression of GPX4, resulting in lipid peroxidation, the generation of ferroptosis, and CDT. MP@PI showed pH-responsive drug release and FI capability, and it effectively combined ferroptosis and pyroptosis to eliminate tumors, achieving an efficient combination of PTT and CDT (Figure 5) (Deng H. et al., 2022).

2.2.4 PTT + PDT

Both PTT and PDT are effective local therapies, which can produce a good synergistic anti-tumor effect (Zhang M. et al., 2024a). Pu et al., (2021) synthesized gadolinium (III) ion-doped PDA using a simple hydrothermal method, loaded photosensitizer Ce6 onto Gd-PDA by electrostatic interaction and π–π interaction, and coated Gd-MOF on the surface of Gd-PDA NPs using layer-by-layer self-assembly technology, leading to the preparation of Gd-PDA-Ce6@Gd-MOF. Due to the presence of shell Gd-MOF, Gd-PDA-Ce6@Gd-MOF exhibited good stability, enabled pH- and light-stimulated drug release, and prevented premature drug leakage in blood circulation. Gd-PDA-Ce6@Gd-MOF had a photothermal conversion efficiency of 39.14% and a drug-loading capacity of 7.4%, and it possessed longitudinal proton relaxation time of 13.72 mM^{-1} S^{-1} and transverse proton relaxation time of 216.14 mM^{-1} S^{-1}, enabling PDT and PTT guided by MRI and PAI (Pu et al., 2021). Feng J. et al. (2020a) coated ZIF-8 on the surface of PDA and encapsulated photosensitizer MB and catalase (CAT) inside the shell ZIF-8 by the one-step method, leading to the preparation of PDA-MB-CAT-ZIF-8. PDA-MB-CAT-ZIF-8 prevented the leakage of MB and CAT in blood circulation and achieved the responsive drug release of pH, which facilitated precise

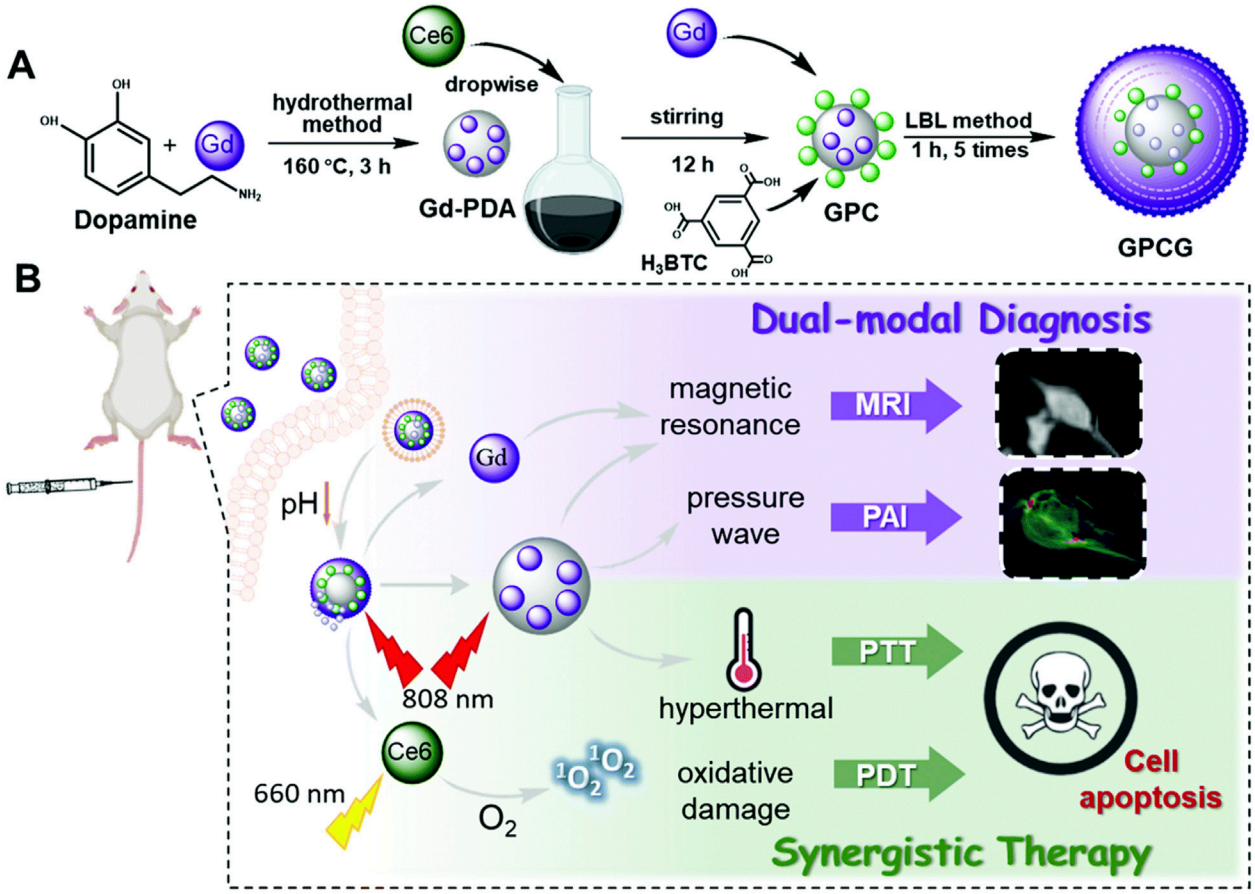

FIGURE 6
(A) Schematic representation of synthesis of Gd-PDA-Ce6@Gd-MOF. **(B)** the application of Gd-PDA-Ce6@Gd-MOF for efficient combination of photodynamic therapy and photothermal therapy guided by MR/PA imaging. copyright 2021, with permission from the Royal Society of Chemistry and Pu et al. (2021).

drug release at the tumor site. CAT catalyzed endogenous H_2O_2 to produce a large amount of O_2, which improved the effect of MB-mediated PDT. PDA-MB-CAT-ZIF-8 has a drug-loading capacity of 3.4% for CAT and 5% for MB, and it solved the problem of lack of oxygen at the tumor site by the rational use of biological enzymes, achieving PTT–PDT combination therapy (Figure 6) (Feng J. et al., 2020a).

2.2.5 CDT+ chemotherapy

Due to the lack of targeting and abnormal blood supply in the tumor site, traditional chemotherapeutic drugs or nanomaterials could not penetrate the hypoxic area of the solid tumor and accumulate in the hypoxic area at high concentrations, which strongly limited the therapeutic effect of the hypoxic area (Li J. M. et al., 2023). Therefore, the therapeutic effect of tumors could be improved by efficiently and accurately delivering therapeutic drugs or nanomaterials to the tumor area of hypoxia (Li J. M. et al., 2023). Li et al. loaded CaO_2 and DOX with MIL, coated the surface of the preparation material with PDA, and used shell PDA to adhere to anaerobic *Bifidobacterium infantis* (Bif), leading to the preparation of MCDP@Bif. The PDA coating on the shell could not only prevent the leakage of encapsulated CaO_2 and DOX but also promote the adhesion of the composite material to Bif. Due to the presence of Bif, MCDP@Bif could actively target the hypoxic area of the tumor and enrich the hypoxic area of the tumor with high concentrations, thus reducing the systemic adverse reactions of DOX. Shell PDA was degraded in a tumor microenvironment of high GSH, low pH, and high ROS, leading to the release of CaO_2@MIL-DOX from MCDP@Bif. In the tumor acidic microenvironment, CaO_2@MIL-DOX released CaO_2, Fe^{3+}, and DOX. Fe^{3+} depleted GSH and generated Fe^{2+}, which reduced ROS consumption and improved the efficacy of CDT. CaO_2 produced a large amount of H_2O_2 and Ca^{2+} in the tumor acidic microenvironment. Fe^{2+} reacted with H_2O_2 to produce a large amount of ROS, resulting in efficient CDT. A large amount of Ca^{2+} released by CaO_2 caused calcium overload in tumor cells, increased the level of oxidative stress in tumor cells, and promoted apoptosis, thus enhancing the chemotherapeutic effect of DOX. MCDP@Bif utilized anaerobic bacteria to target hypoxic tumor areas, exhibited pH-responsive drug release, and generated large amounts of H_2O_2 at the tumor site; this enabled highly effective, low-toxicity CDT-combined chemotherapy, providing novel therapeutic strategies for overcoming treatment resistance caused by hypoxia (Figure 7) (Li J. M. et al., 2023).

2.2.6 CDT + immunotherapy

In immunotherapy, immunogenic cell death (ICD) can activate T cells, thereby destroying tumor cells. ICD results in the release of

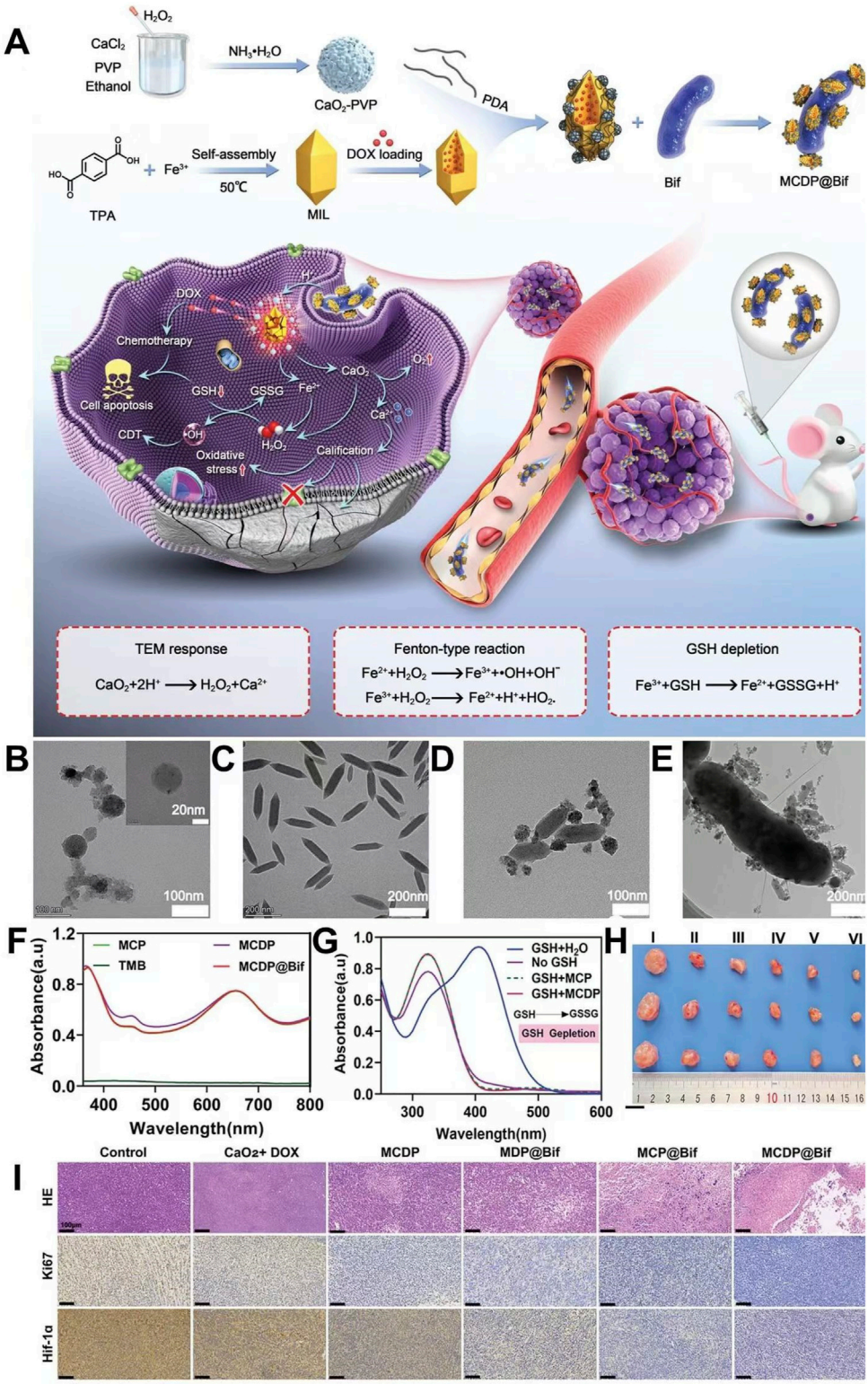

FIGURE 7
(A) Schematic representation of synthesis of MCDP@Bif and synergistic therapy induced by MCDP@Bif. **(B)** TEM image of CaO_2. **(C)** TEM image of MIL. **(D)** TEM image of MCDP. **(E)** TEM image of the MCDP@Bif biohybrid. **(F)** OH generation in different groups. **(G)** GSH depletion performance in different groups. **(H)** Representative tumor images in different groups. **(I)** HE staining, Ki67 staining, and HIF-1α staining of tumor tissues in different groups. Copyright 2023, with permission from Wiley-VCH GmbH and Li J. M. et al. (2023).

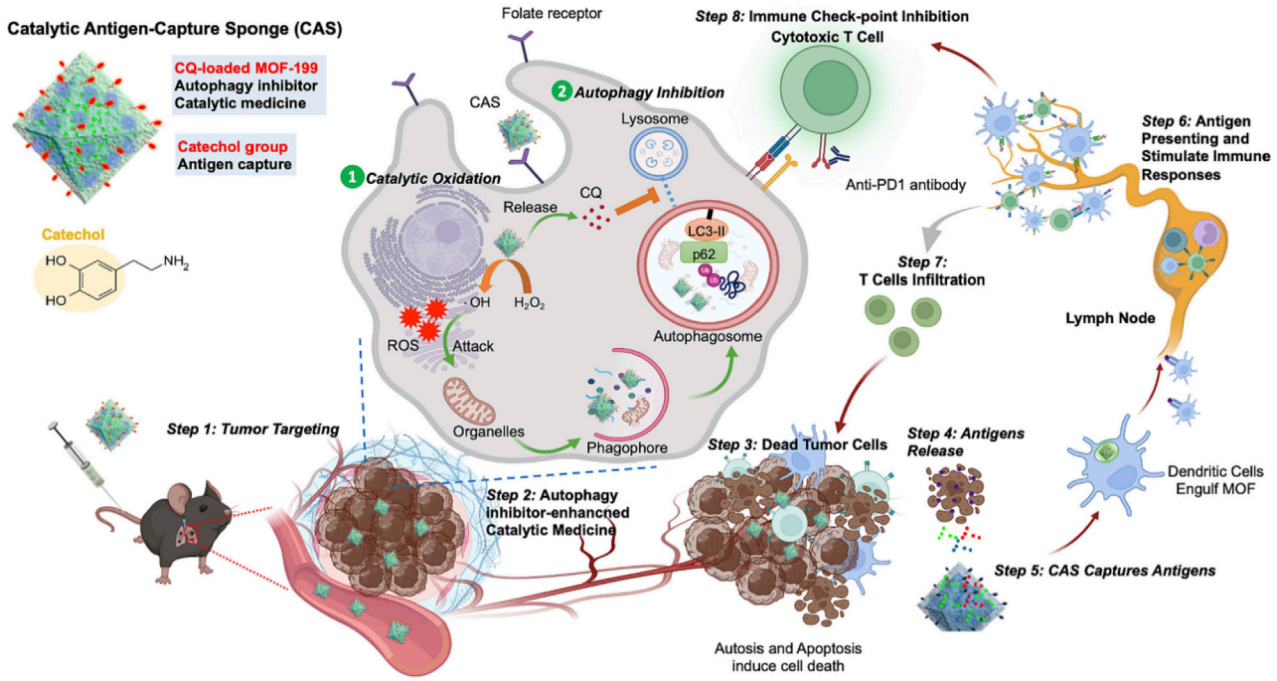

FIGURE 8
Schematic representation of the high efficacy of immunotherapy induced by catalytic antigen capture sponges (CASs) serving as immunostimulants; copyright 2023, with permission from Elsevier and Chiang et al. (2023). CAS was efficiently enriched at the tumor site by the folate receptor, which led to chemodynamic therapy and inhibited autophagy to generate immunogenic cell death, improving T-cell infiltration. Tumor antigens were presented by dendritic cells, leading to activation of T cells. The immune checkpoint inhibitors were efficiently combined with CAS, improving the efficacy of inhibiting tumor growth.

several damage-related molecular patterns (DAMPs), including high mobility group protein 1 (HMGB1), adenosine triphosphate (ATP), and calmodulin (CRT) from cancer cells (Alavijeh and Akhbari, 2024). Dendritic cells (DCs) can phagocytize and present DAMP and further activate T lymphocytes for immunotherapy (Alavijeh and Akhbari, 2024). The low immunogenicity of tumors and the low efficiency of antigen delivery strongly limited the effect of immunotherapy (Li Q. et al., 2022; Cheng W. et al., 2022). In view of this, Chiang et al. (2023) synthesized MOF-199 using a hydrothermal method, used MOF-199 to load chloroquine (CQ) via π–π interaction, and used PDA to coat on the outside of MOF-199 and attach it with folic acid (FA), leading to the preparation of CQ/FA-PDA@MOF. Cu^{2+} in the complex reacted with GSH to form Cu^{+}, which reduced ROS clearance caused by GSH. Cu^{+} reacted with H_2O_2 via the Fenton reaction to generate large amounts of ROS, causing CDT and immunogenic death of several tumor cells, which led to the release of DAMP. CQ inhibited protective autophagy generated by CDT, leading to the collapse of cellular self-defense mechanisms, exacerbating cytotoxicity, and promoting the release of tumor-associated antigens. CQ/FA-PDA@MOF could absorb a large number of tumor-associated antigens released by the abovementioned process and transfer them to dendritic cells to induce cytotoxic T-lymphocyte infiltration, enabling efficient delivery of antigens, which resulted in efficient immunotherapy and inhibition of tumor metastasis. CQ/FA-PDA@MOF efficiently produced tumor-associated antigens by CDT, enabled efficient antigen delivery, and achieved a highly efficient combination of CDT and immunotherapy, providing a novel approach to overcome the low immunogenicity and heterogeneity of tumors that resulted in low immunotherapeutic efficacy (Figure 8) (Chiang et al., 2023).

2.2.7 PTT + TDT

Traditional high-temperature PTT (>50°C) can cause skin damage and induce inflammation, which limits the clinical application of PTT (Li K.et al., 2023). Low-temperature PTT (≤45°C) can avoid potential damage to normal tissues, which has great potential clinical value (Liu W. et al., 2023). However, a large number of heat shock proteins are produced during PTT, which can repair cell thermal damage and significantly reduce the efficiency of low-temperature PTT (Fan et al., 2023). Inhibiting the expression of heat shock protein to achieve low-temperature PTT meets the clinical requirements for efficient and low toxicity treatment, which has important research value (Li X. et al., 2021). Deng X. et al. (2023) prepared MPDA/AIPH@ZIF-8/GA by coating ZIF-8 on the surface of mesoporous dopamine (MPDA) loaded with 2,2-azobis [2-(2-imidazolin-2-yl) propane]-dihydrochloride (AIPH) and using ZIF-8 to load gambogic acid (GA). MPDA/AIPH@ZIF-8/GA improved the stability of AIPH and prevented the leakage of AIPH in blood circulation. Due to the degradation of ZIF-8 in the acidic environment and the degradation of ZIF-8 promoted by high temperature, MPDA/AIPH@ZIF-8/GA achieved drug release in response to pH and light, which reduced the side effects of chemotherapy. Due to the presence of PDA, the complex had a photothermal conversion efficiency of 24.7%, showing a good photothermal effect. The released GA inhibited the expression of HSP90 and reversed the thermotolerance of tumor cells to achieve low-temperature PTT. Under laser irradiation, the large amount of heat

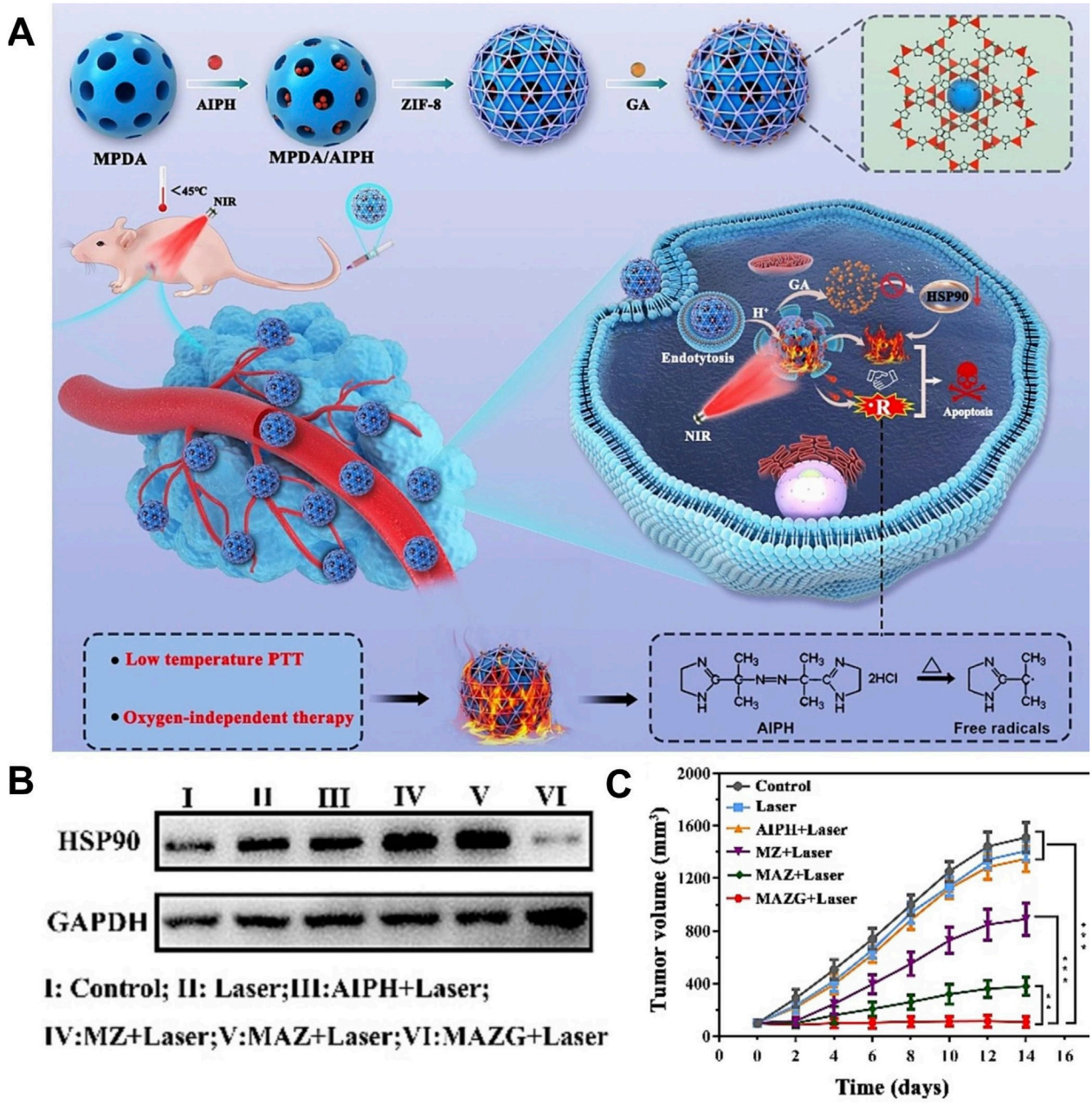

FIGURE 9
(A) Schematic illustration of the synthesis of MPDA/AIPH@ZIF-8/GA and the combination of thermodynamic therapy and photothermal therapy induced by MPDA/AIPH@ZIF-8/GA. **(B)** Inhibition of HSP90 protein expression properties in different treatment groups. **(C)** Tumor volume changes in different treatment groups. Copyright 2023, with permission from Elsevier and Deng X. et al. (2023).

generated by the complex led to the rapid decomposition of AIPH to produce oxygen-independent cytotoxic alkyl radicals, which caused oxidative damage to cancer cells, resulting in tumor cell destruction and enabling thermodynamic therapy (TDT). The MPDA/AIPH@ZIF-8/GA exhibited good therapeutic safety and realized low-temperature PTT combined with TDT, which had a significant inhibitory effect on both hypoxic and normoxic tumors (Figure 9) (Deng X. et al., 2023). This study utilized traditional Chinese medicine to efficiently inhibit the expression of heat shock proteins, enabling low-temperature PTT. This approach provides a potential strategy for achieving low-temperature PTT and holds significant reference value. In addition, this study provided an O_2-independent free radical generation scheme, which enriched the methods of tumor treatment based on free radicals and provided an effective solution for the treatment of hypoxic tumors.

2.2.8 PTT+ GT

Small interfering RNA (siRNA)-induced cancer gene therapy (GT), which inhibits the expression of specific genes, has promising applications (Jadhav et al., 2024). However, there are some problems with siRNA, such as nuclease degradation, low cell uptake efficiency, and non-specific biological distribution and immune response, which hinder the clinical application of siRNA (Tao et al., 2024).

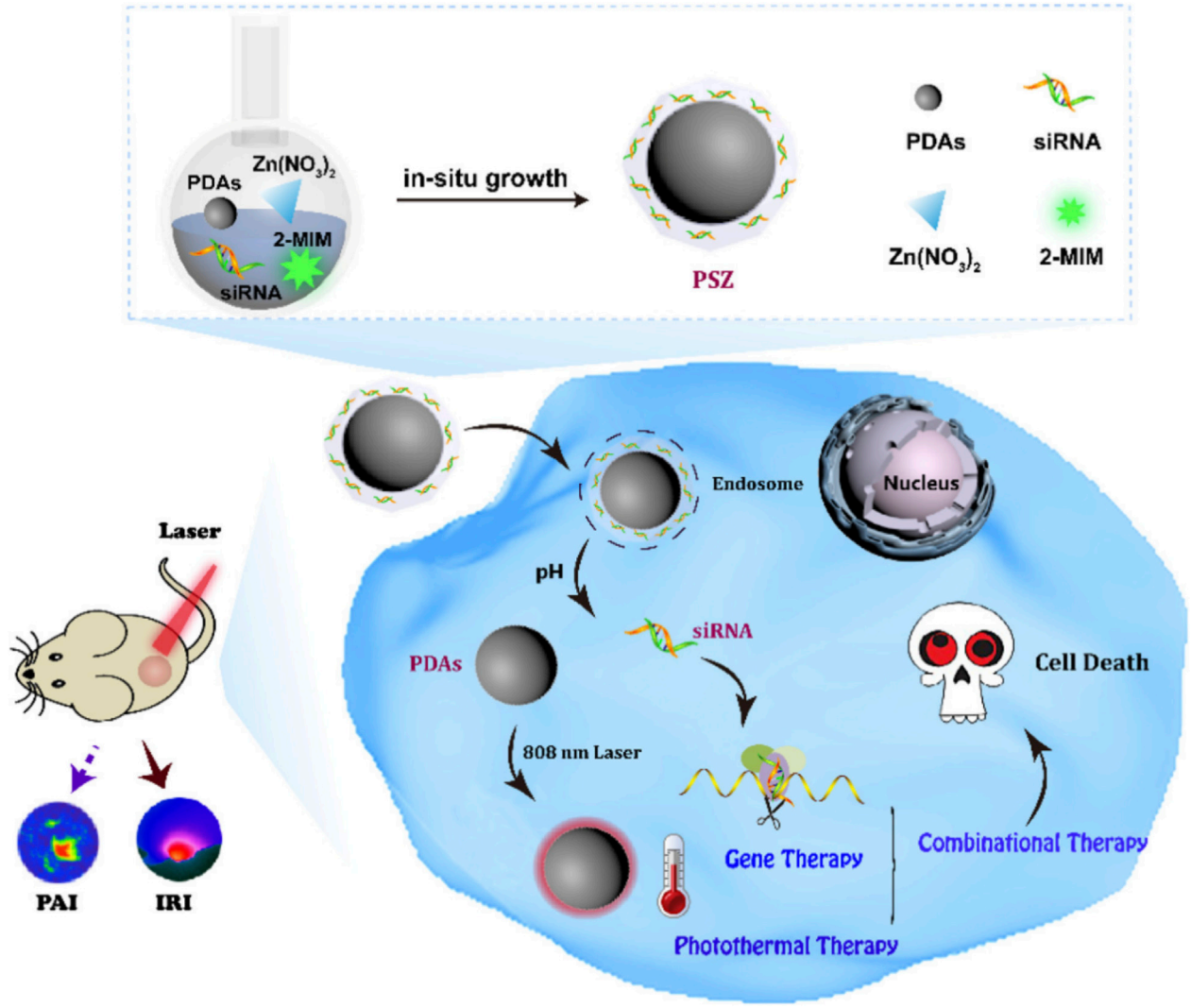

FIGURE 10
Schematic illustration of the synthesis of PDAs-siRNA-ZIF-8 and the combination of gene therapy and photothermal therapy generated by PDAs-siRNA-ZIF-8; copyright 2020, with permission from the American Chemical Society and Feng J. et al. (2020b).

Therefore, the development of novel nano-carriers for the efficient delivery of siRNA to tumor sites has important research value (Kandasamy and Maity, 2024; Moazzam et al., 2024). Feng J. et al. (2020b) prepared PDA-siRNA-ZIF-8 by coating ZIF-8 on the surface of PDA and encapsulating siRNA inside the shell ZIF-8 by the one-step method. Because the siRNA was inside ZIF-8, PDA-siRNA-ZIF-8 avoided the enzymatic degradation of siRNA and prevented the leakage of siRNA in blood circulation. Due to the acid-responsive degradation of ZIF-8, the complex was not only enriched in the tumor site by the enhanced permeability and retention (EPR) effect but also had the ability to accurately release siRNA in the tumor acidic microenvironment, reducing the adverse side effects of gene therapy. PDA-siRNA-ZIF-8 had a photothermal conversion efficiency of 39%, showed a good photothermal effect, and enabled the combination of PTT and gene therapy guided by PAI (Figure 10) (Feng J. et al., 2020b). In this study, siRNA was encapsulated in nanomaterials, which solved the problems of siRNA and enabled the efficient delivery of siRNA and the accurate release at the tumor site, providing a potential strategy for the construction of a novel siRNA delivery system.

2.2.9 Combination of the other two treatment methods

Catalytic therapy mainly regulates the tumor microenvironment (TME) through specific catalytic reactions, leading to the depletion of GSH and the production of ROS and oxygen, leading to tumor cell death, which has the advantages of high specificity and low toxicity (Zheng et al., 2025; Bonet-Aleta et al., 2024). However, the high expression of GSH in tumor cells and the insufficient supply of endogenous H_2O_2 limit the efficiency of catalytic therapy (Xiong et al., 2024). In view of this, You et al. (2024) loaded glucose oxidase (GOx) with Zr/Ce-MOFs and coated Zr/Ce-MOFs with PDA to prepare Zr/Ce-MOFs/GOx/PDA. GOx catalyzed glucose to produce a large amount of H_2O_2, which compensated for the insufficient supply of endogenous H_2O_2. Ce^{3+} in the Zr/Ce-MOFs catalyzed H_2O_2 to produce highly toxic OH and Ce^{4+}. Ce^{4+} could consume GSH and generate Ce^{3+}. A large amount of GSH

consumption could avoid the consumption of OH produced by catalytic reaction. Due to the presence of PDA, Zr/Ce-MOFs/GOx/PDA had a photothermal conversion efficiency of 26.2% and produced a good photothermal effect, which promoted the efficiency of the catalytic reaction mentioned above. Zr/Ce-MOFs/GOx/PDA achieved a cascade catalytic reaction within the tumor microenvironment to regulate H_2O_2 and GSH, enabling PTT combined with catalytic therapy with high efficacy and low toxicity, which provided ideas for designing nano-enzymes to regulate the TME to improve therapeutic efficacy (You et al., 2024). In order to solve the problem of hypoxia in the tumor microenvironment, improving hypoxia is a challenging task (Shen et al., 2023). Researchers can also take advantage of the characteristics of the tumor hypoxic microenvironment to use hypoxia-activated toxic drugs to destroy hypoxic tumors (Zhao L. et al., 2024). Chen H. et al. (2021) used the large surface area and high porosity of UiO-66 to efficiently load perfluorotributylamine (PFA) and tirapazamine(TPZ) and coated PDA on the surface of UiO-66, leading to the preparation of TPZ/PFA@UiO-66@PDA (Chen H. et al., 2021). TPZ/PFA@UiO-66@PDA remained stable in PBS and the culture medium for 24 h and could be enriched in the tumor site by the permeability and retention effect. Due to the presence of PDA, TPZ/PFA@UiO-66@PDA not only exhibited a good photothermal effect but could also prevent early leakage of TPZ and PFA in blood circulation. PFA adsorbed O_2 in the tumor site, resulting in significant hypoxia of tumor cells and the upregulation of the oxygen-dependent HIF-1α pathway, which led to tumor cell apoptosis. The significant hypoxic environment induced by PFA activated the conversion of TPZ to highly toxic benzotriazine (BTZ), resulting in efficient chemotherapy. TPZ/PFA@UiO-66@PDA exhibited good biocompatibility and enabled the combination of PTT and hypoxia-activated chemotherapy, which effectively inhibited the growth of hypoxic tumors (Chen H. et al., 2021). This study made use of the hypoxia characteristics of the tumor microenvironment and used PFA to adsorb O_2 from the tumor site to create a significant hypoxia environment, leading to the efficient activation of hypoxia-sensitive drugs and effectively eliminated hypoxia tumors, which provided a strategy for solving the problem of treatment resistance caused by hypoxia (Chen H. et al., 2021). Liu G. et al. (2020) prepared MPDA@ZIF-8/DOX + GOx by growing ZIF-8 *in situ* on the surface of MPDA loaded with DOX and encapsulating GOx inside ZIF-8. The shell ZIF-8 encapsulated GOx inside, which prevented the leakage of GOx in blood circulation, improved the stability of GOx, and ensured the efficient catalytic activity of GOx. In an acidic environment, the outer shell ZIF-8 degraded and released GOx, which consumed glucose and inhibited ATP production, inhibiting the function of ATP-dependent P-glycoprotein (P-gp) transporter proteins. MPDA@ZIF-8/DOX + GOx released GOx and DOX in a sequential manner and released GOx first to inhibit Pgp function and limit the drug efflux, which led to a large accumulation of DOX at the tumor site, thus reversing the resistance. MPDA@ZIF-8/DOX + GOx with a drug-loading capacity of 68.3% showed pH-responsive release of GOx and DOX, which significantly inhibited the growth of breast cancer resistant to DOX and reversed drug resistance (Liu G. et al., 2020). This study constructed a novel nano-drug delivery system that could efficiently load P-gp inhibitors and chemotherapeutic drugs, release P-gp inhibitors and chemotherapeutic drugs sequentially, and effectively reverse drug resistance by inhibiting ATP production, providing a new strategy for overcoming chemotherapeutic drug resistance. Ren et al. (2020) synthesized ZIF-8 on the surface of ZIF-67 loaded with DOX, encapsulated PpIX inside ZIF-8, and used PDA to wrap ZIF-8 and connect mPEG-NH_2, leading to the preparation of ZDZP@PP. Due to the presence of PDA and mPEG-NH_2, ZDZP@PP remained stable in PBS and DMEM culture medium for a week and showed excellent biocompatibility, which facilitated the accumulation of nanomaterials at the tumor site. Different parts of ZDZP@PP were loaded with different drugs, which enabled the sequential release of DOX and PpIX and avoided the reaction between different drugs. Because the complex had the characteristics of acid-responsive degradation, ZDZP@PP showed pH-responsive drug release, which was conducive to accurate drug release in the tumor acidic microenvironment. ZIF-67 had the function of nano-enzyme, which could catalyze endogenous H_2O_2 to produce O_2, improving PpIX-mediated PDT. ZDZP@PP utilized nano-enzymes to overcome the problem of oxygen deprivation at the tumor site and achieved a highly effective combination of PDT and chemotherapy (Ren et al., 2020). The combination of PTT and ferroptosis showed excellent synergistic effects, and PTT could enhance the sensitivity of cells to ferroptosis (Zeng et al., 2022; Wu et al., 2022b). Iron ions released by Fe-MOF could catalyze H_2O_2 to produce OH through the Fenton reaction, resulting in cell oxidative damage and lipid peroxidation, which promoted the generation of ferroptosis (Zhang M. et al., 2024b; Rao et al., 2023; Bai et al., 2024). Liu Y. J. et al. (2024) embedded PDA into the Fe-MOF by physical mixing, applied the prepared material to load erastin by Michael's addition reactions, and used osteosarcoma cell membranes to wrap the surface of PDA-MOF-E, leading to the preparation of PDA-MOF-E-M. Due to the presence of the osteosarcoma cell membrane, PDA-MOF-E-M showed high biocompatibility and homologous targeting. PDA-MOF-E-M showed good stability in an acid–base environment (pH = 5.0 and pH = 9.0) and thermal environment (35°C and 42°C), indicating that it could have favorable chemical stability in various humoral environments of the human body. Fe-MOF releases a large amount of iron ions, creating an iron-rich environment in the tumor, which resulted in lipid peroxidation and promoted the generation of ferroptosis. Erastin inhibited the expression of the SLC7A11 protein, resulting in the decrease of the intracellular cysteine level and inhibition of GSH synthesis, which indirectly inhibited the activity of GPX4, led to the accumulation of lipid peroxides, and finally induced ferroptosis. Fe-MOF and erastin cooperate to promote the occurrence of ferroptosis through different mechanisms. PDA-MOF-E-M showed excellent T_1-weighted MRI performance and enabled the combination of PTT and ferroptosis, which inhibited osteoclast differentiation and significantly inhibited the growth of osteosarcoma, providing a novel therapeutic option for the treatment of osteosarcoma (Figure 11) (Liu Y. J. et al., 2024). This study suggests that Fe-MOF@PDA was a potential ferroptosis inducer and provided a large amount of Fe^{3+}, which cooperated with ferroptosis inducers that inhibit GPX4 activity to enhance ferroptosis, leading to a highly efficient anti-tumor effect.

2.3 Polydopamine-coated metal–organic frameworks in multimodal combination therapy

2.3.1 PTT + CDT + ST

GOx catalyzed glucose to produce H_2O_2 in the presence of O_2, which blocked the energy supply and produced starvation therapy (ST) (Fu et al., 2023). However, the characteristics of hypoxia in the tumor microenvironment strongly restrict the therapeutic efficiency

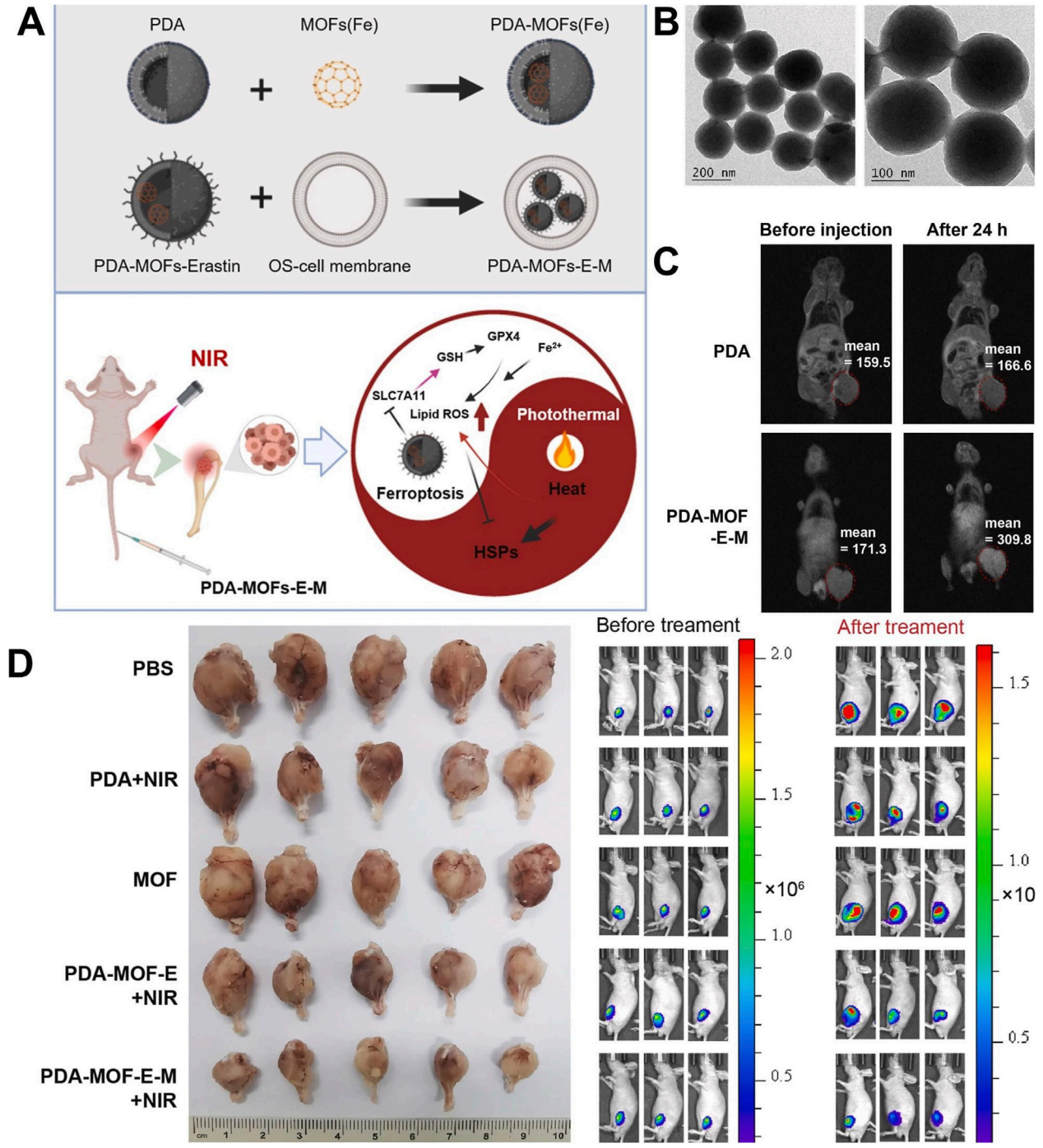

FIGURE 11
(A) Schematic illustration of experimental procedure for preparing PDA-MOF-E-M and the combination of ferroptosis and photothermal therapy generated by PDA-MOF-E-M. **(B)** SEM images of PDA-MOF-E-M. **(C)** T_1-weighted MRI images of PDA/Fe and PDA-MOF-erastin-M *in vivo*. **(D)** Luminescence images of mice in different treatment groups and tibial tumor images in different treatment groups. Copyright 2024, with permission from KeAi Communications and Liu Y. J. et al. (2024).

of GOx (Fu et al., 2023). The efficiency of CDT is limited due to the insufficient concentration of endogenous H_2O_2, which makes it impossible to use the Fenton reaction to produce a large amount of OH (Hao et al., 2023). Yu H. et al. (2022). coated carbon nitride (C_3N_4) on PDA by physical stirring, modified PDA@C_3N_4 surface with polyacrylic acid (PAA), used MIL-100 to grow on the PAA-modified PDA@C_3N_4 surface through layer-by-layer self-assembly, loaded GOx with shell MIL-100, and connected HA to the surface of GOx by amide bond, leading to the preparation of PDA@C_3N_4@MIL/GOx@HA. C_3N_4 cleaved water to produce O_2, which could

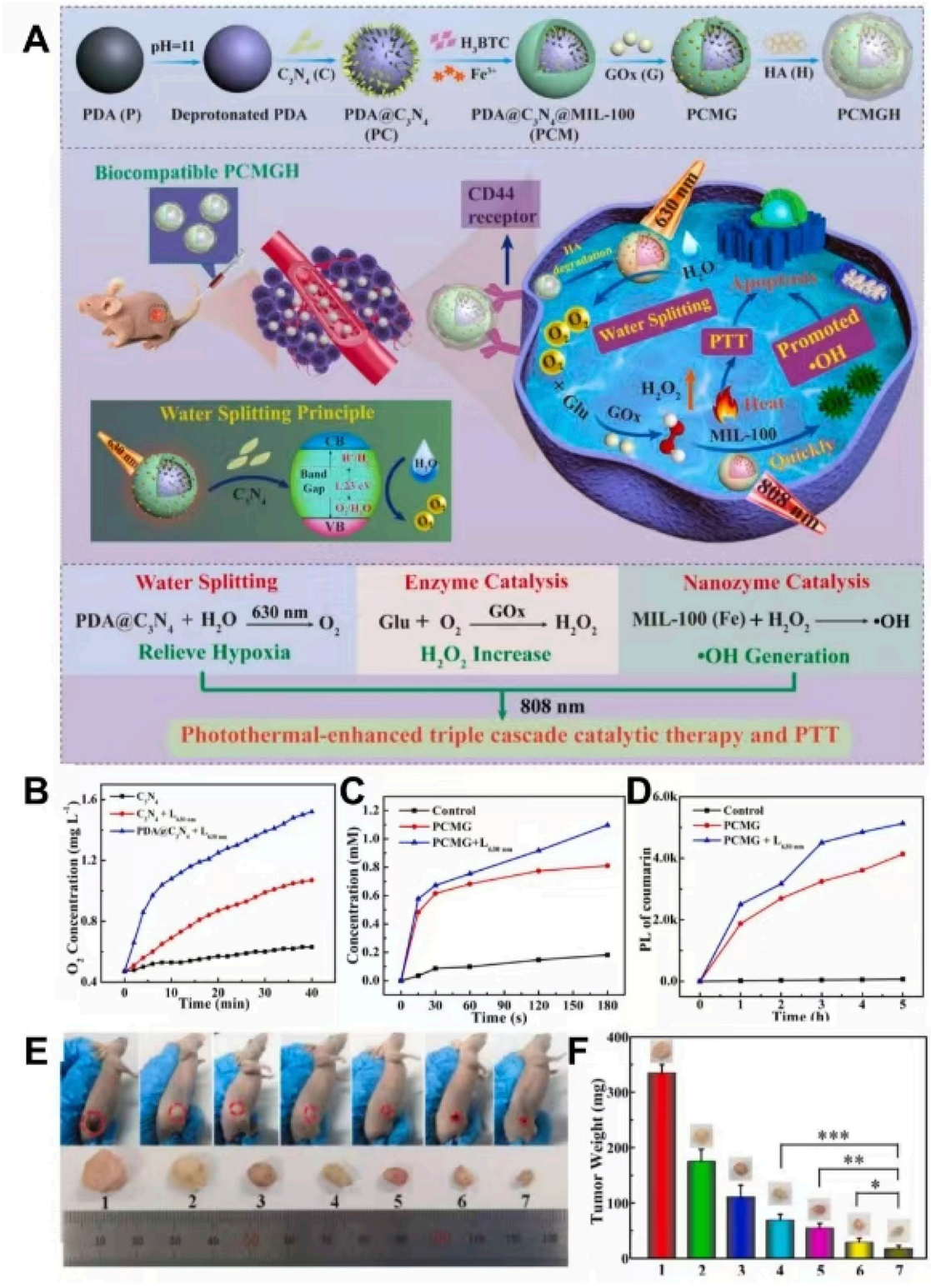

FIGURE 12
(A) Schematic illustration of the synthesis and anti-cancer mechanisms of PDA@C_3N_4@MIL@GOx@HA (PCMGH). **(B)** O_2 generation performance in different groups. **(C)** H_2O_2 generation performance in different groups. **(D)** OH generation performance in different groups. **(E)** Tumor images in different treatment groups. **(F)** Tumor weight in different treatment groups. Copyright 2022, with permission from Elsevier and Yu H. et al. (2022).

improve the hypoxia state of the tumor microenvironment and improve the efficiency of glucose catalyzed by GOx. GOx catalyzed glucose to produce a large amount of H_2O_2 in the presence of O_2 to overcome the problem of insufficient endogenous H_2O_2. The iron ion in MIL-100 had peroxidase-like activity, which could catalyze H_2O_2 to produce toxic OH, resulting in efficient CDT. The abovementioned process was triple cascade catalysis that relieved hypoxia and produced efficient ST and CDT. PDA not only improved the O_2 production efficiency of C_3N_4 but also produced a good photothermal effect, which promoted the triple cascade catalytic reaction. Due to the presence of HA, PDA@C_3N_4@MIL/GOx@HA could actively target tumor tissue and reduce side effects. PDA@C_3N_4@MIL/GOx@HA showed good biocompatibility, achieved photothermal enhanced triple cascade catalysis, and improved tumor hypoxia, enabling an efficient combination of PTT, ST, and CDT and achieving a significant inhibitory effect on hypoxic tumors (Figure 12) (Yu H. et al., 2022). This study utilized nano-enzymes to achieve a triple cascade reaction that improved hypoxia in the tumor site and overcame insufficient endogenous H_2O_2, which achieved highly efficient ST and CDT, acquiring a safe and efficient method of tumor therapy. Zhang et al. prepared MGH by coating hyaluronic acid-modified dopamine (HA-PDA) on the surface of MIL-100 loaded with GOx (Zhang Y.et al., 2019). Due to the presence of HA-PDA, MGH could actively target tumor tissues with high CD44 receptor expression, exhibit good biocompatibility and stability, and prevent the leakage of GOx in blood circulation. GOx catalyzed glucose in the presence of O_2, which not only inhibited energy production and produced ST but also produced gluconic acid and H_2O_2. MIL-100 catalyzed H_2O_2 to produce OH and O_2 through the Fenton-like reaction, which produced CDT and improved the hypoxia state of tumors. Gluconic acid deepened the local acidity of the tumor and promoted the efficiency of the Fenton-like reaction. Generated O_2 enhanced the efficiency of glucose catalyzed by GOx. MGH produced a large amount of OH and O_2 by cascade catalytic reaction, which enabled the efficient combination of PTT, ST, and CDT guided by PAI (Zhang Y. et al., 2019). In this study, a positive feedback cascade catalytic reaction was achieved through the combination of a nano-enzyme and a biological enzyme, resulting in the production of a large amount of H_2O_2 and O_2; this approach overcame the inefficiency of CDT caused by the lack of endogenous H_2O_2 and the inefficiency of GOx-mediated ST caused by hypoxia, enabling the effective coordination of ST and CDT.

2.3.2 PTT + CDT + chemotherapy

Huang et al. (2023) coated PDA on the surface of MIL-100 loaded with oxaliplatin (Oxa) and connected the shell PDA to NH_2-PEGTK-COOH by amide bond to prepare Oxa@MIL-PDA-PEGTK. Oxa@MIL-PDA-PEGTK had the characteristic of acid-responsive degradation and a drug-loading capacity of 5.34%, and it enabled drug release in response to the double irritation of pH and H_2O_2, which was conducive to the precise release of drugs in the tumor microenvironment. Fe^{2+} in MIL-100 could react with the high concentration of H_2O_2 in cells to produce a large number of OH for destroying tumors, which led to CDT. Oxa@MIL-PDA-PEGTK could efficiently deliver drugs and accurately release drugs at the tumor site, enabling the combination of CDT, chemotherapy, and PTT, which significantly inhibited the growth of liver cancer (Figure 13) (Huang et al., 2023). Wang et al. synthesized Cu^{2+}/ZIF-8 using a simple ion-doping method, loaded DOX with Cu^{2+}/ZIF-8, and coated shell PDA on the surface of Cu^{2+}/ZIF-8, leading to the preparation of DOX@Cu^{2+}/ZIF-8@PDA (Wang L.et al., 2022b). DOX@Cu^{2+}/ZIF-8@PDA possessed a drug-loading capacity of 9%, and it exhibited pH- and light-stimulated drug release, which reduced the side effects of chemotherapy. Released Cu^{2+} could oxidize GSH, break the redox homeostasis of tumors, and produce Cu+ to overcome the low efficiency of CDT caused by high GSH expression in the tumor microenvironment. Cu^{+} catalyzed the formation of OH from H_2O_2 in tumors to produce effective CDT. Due to the presence of PDA, DOX@Cu^{2+}/ZIF-8@PDA had a photothermal conversion efficiency of 34.6% and showed a good photothermal effect, which enhanced the effect of CDT and chemotherapy. DOX@Cu^{2+}/ZIF-8@PDA depleted GSH and achieved an efficient combination of PTT, chemotherapy, and CDT (Wang L. et al., 2022). Ren et al. (2024) coated PDA on Cu/ZIF-8 with hydroxycamptothecin (HCPT) and used erythrocyte membrane to coat on the surface of PDA, leading to the preparation of RBCM-HCPT@Cu/ZIF-8@PDA. Due to the presence of the erythrocyte membrane, RBCM-HCPT@Cu/ZIF-8@PDA could achieve immune escape and prolong blood circulation in the body, which could be efficiently enriched at the tumor site. Due to the acid-responsive degradation of ZIF-8, RBCM-HCPT@Cu/ZIF-8@PDA effectively releases copper ions and HCPT in the tumor microenvironment, thus enabling safe and effective CDT and chemotherapy. RBCM-HCPT@Cu/ZIF-8@PDA with a drug-loading capacity of 19.1% showed excellent biosafety, had acid- and light-responsive drug release, and enabled an efficient combination of CDT, chemotherapy, and PTT (Ren et al., 2024).

2.3.3 PTT + PDT + CDT

Due to the problems such as poor targeting, side effects, and poor accuracy of traditional treatment methods such as chemotherapy, it is very valuable to develop a non-chemotherapy system to achieve accurate and effective tumor treatment (Zhang and Yuan, 2024). Drugs or nanoparticles are usually injected into the body by subcutaneous or vascular injection and enter the tumor site through systemic blood circulation (Tu et al., 2024; Dash et al., 2024; Zuo et al., 2024). The successful enrichment of nanomaterials at tumor sites poses a significant challenge to the stability of nanoparticles *in vivo* and their tumor-targeting performance (Wang Q. et al., 2024; Zhang X. et al., 2024). Meanwhile, nanoparticles are easily cleared by the immune system, and drugs tend to leak into the bloodstream during circulation (Wang Q. et al., 2024; Zhang X. et al., 2024). Therefore, it is difficult to achieve accurate treatment of tumors. In view of the above, Zhang et al. synthesized PCN-224 (Cu) by chelating Cu^{2+} with TCPP (ligand of PCN-22) and used PDA to coat on the surface of PCN-224 (Cu) to prepare PCN-224 (Cu) @ PDA (PCP). Zhang et al. dispersed PCP into disodium alginate (OSA) and carboxymethyl chitosan (CMC) and synthesized nanocomposite self-healing hydrogels by Schiff base bonding. The complex was injected into the tumor site through intra-tumoral injection to release PCP slowly, which avoided the toxicity caused by the non-specific distribution of nanomaterials caused by systemic circulation and facilitated precise treatment. Cu^{2+} in PCN-224(Cu) reacted with GSH to produce Cu^{+}, which

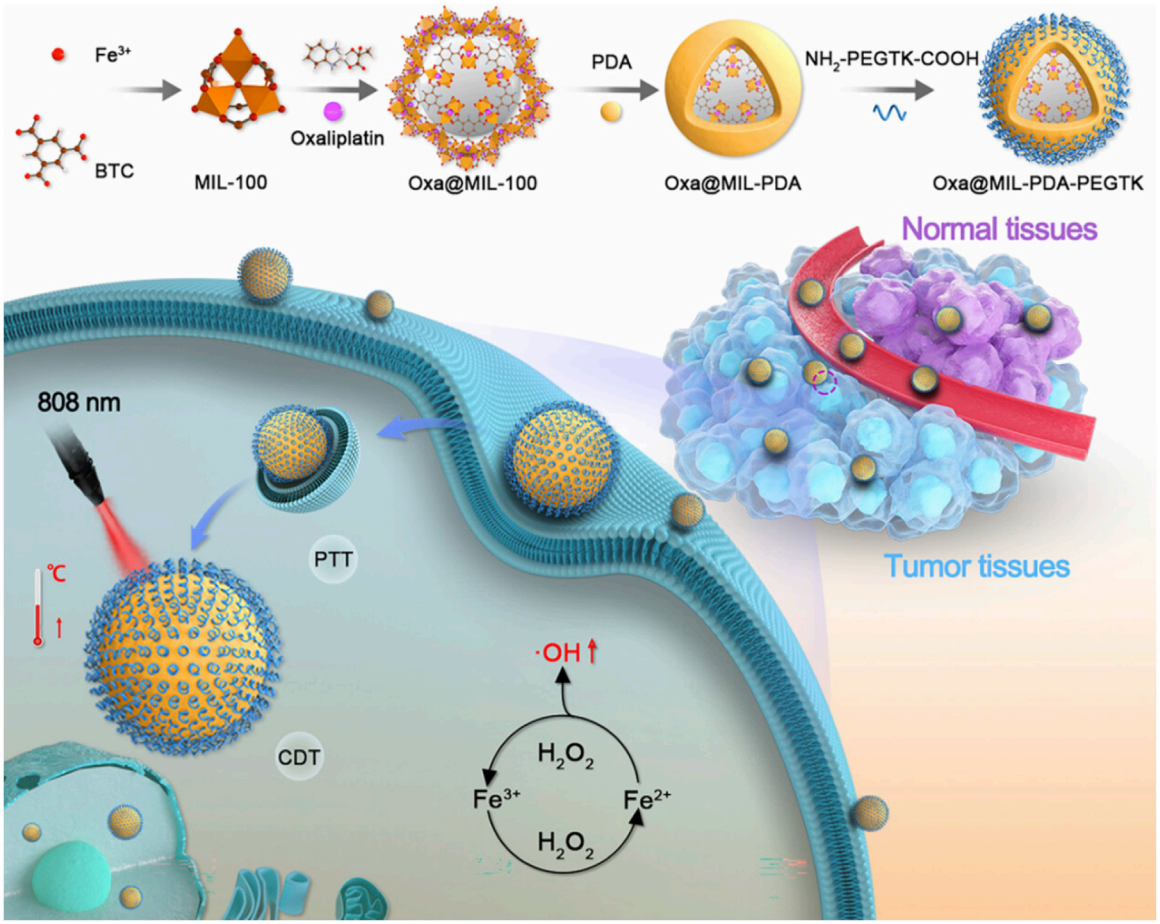

FIGURE 13
Schematic illustration of the experimental procedure for preparing Oxa@MIL-PDA-PEGTK and its applications for the efficient combination of chemodynamic therapy, chemotherapy, and photothermal therapy; copyright 2023, with permission from the American Chemical Society and Huang et al. (2023).

reduced ROS scavenging and improved the efficacy of CDT and PDT. Cu^+ reacted with a high concentration of H_2O_2 in tumor cells to form ROS, which could be used for CDT. PCN-224 (Cu) showed excellent performance of PDT, and PDA exhibited good photothermal performance. The complex integrated a variety of non-chemotherapy treatment methods into one platform to achieve the combined effects of PTT, PDT, and CDT, which provided a reference for the establishment of efficient, accurate, and non-chemotherapy treatment of tumors (Figure 14A) (Zhang and Yuan, 2024). The self-healing hydrogel in the study not only had superior biosafety but also had injectability, which could enter the tumor tissue through intra-tumoral injection, enabling precise drug release at the tumor site and avoiding the toxicity of drugs or nanoparticles to normal tissues during systemic circulation (Zhang and Yuan, 2024). Zhang L. et al. (2021) synthesized ZIF-8 on the surface of PDA loaded with AIPH and encapsulated PVP-modified CuS inside ZIF-8 to prepare AIPH/PDA@CuS/ZIF-8. Due to the degradation of shell ZIF-8 in an acidic environment, AIPH/PDA@CuS/ZIF-8 could accurately release CuS and AIPH in the tumor site. CuS could clear GSH and produce Cu^+, which could react with H_2O_2 to form ROS through the Fenton reaction, resulting in CDT. Due to the presence of CuS, AIPH/PDA@CuS/ZIF-8 possessed a photothermal conversion efficiency of 28.05% and produced a good photothermal effect. High temperatures generated by PTT led to the decomposition of AIPH to O_2-independent alkyl free radicals for oxygen-independent PDT. Both PDA and CuS could scavenge GSH, which reduced ROS scavenging, and disrupt the oxidative stress balance in tumor cells, improving the efficacy of PDT and CDT based on ROS as a therapeutic mechanism. AIPH/PDA@CuS/ZIF-8 achieved PAI-guided combination therapy, integrating PTT, O_2-independent PDT, and CDT, which produced efficient anti-tumor effects on both hypoxic and normoxic tumors (Figure 14B) (Zhang L. et al., 2021). This study utilized the high temperature generated by PTT to lead to the decomposition of AIPH, resulting in the production of a large number of highly toxic alkyl radicals without the involvement of O_2 to generate highly efficient O_2-independent PDT, which provided a new method to overcome the inefficiency of PDT due to the lack of oxygen at the tumor site.

2.3.4 PTT + PDT+ chemotherapy

An intelligent response drug release system can improve treatment efficiency and reduce adverse reactions, which has great application potential in the accurate treatment of tumors

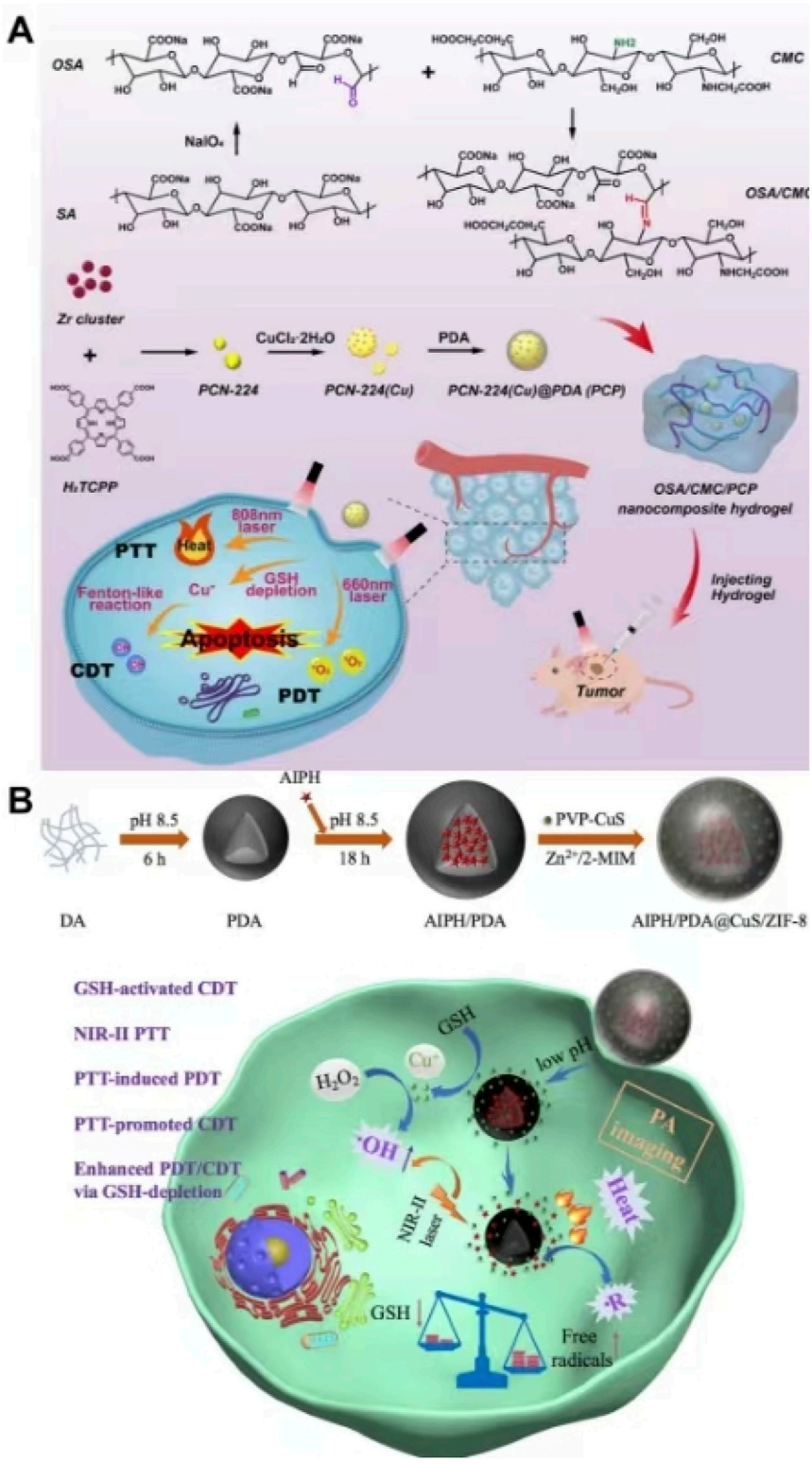

FIGURE 14
(A) Schematic illustration of the synthesis of OSA/CMC@PCP and its application for the synergistic therapy of breast cancer with chemodynamic therapy, photodynamic therapy, and photothermal therapy; copyright 2024, with permission from Elsevier and Zhang and Yuan (2024). **(B)** Schematic illustration of the synthesis and synergistic therapy of AIPH/PDA@CuS/ZIF-8; copyright 2022, with permission from Wiley-VCH GmbH and Zhang et al. (2021).

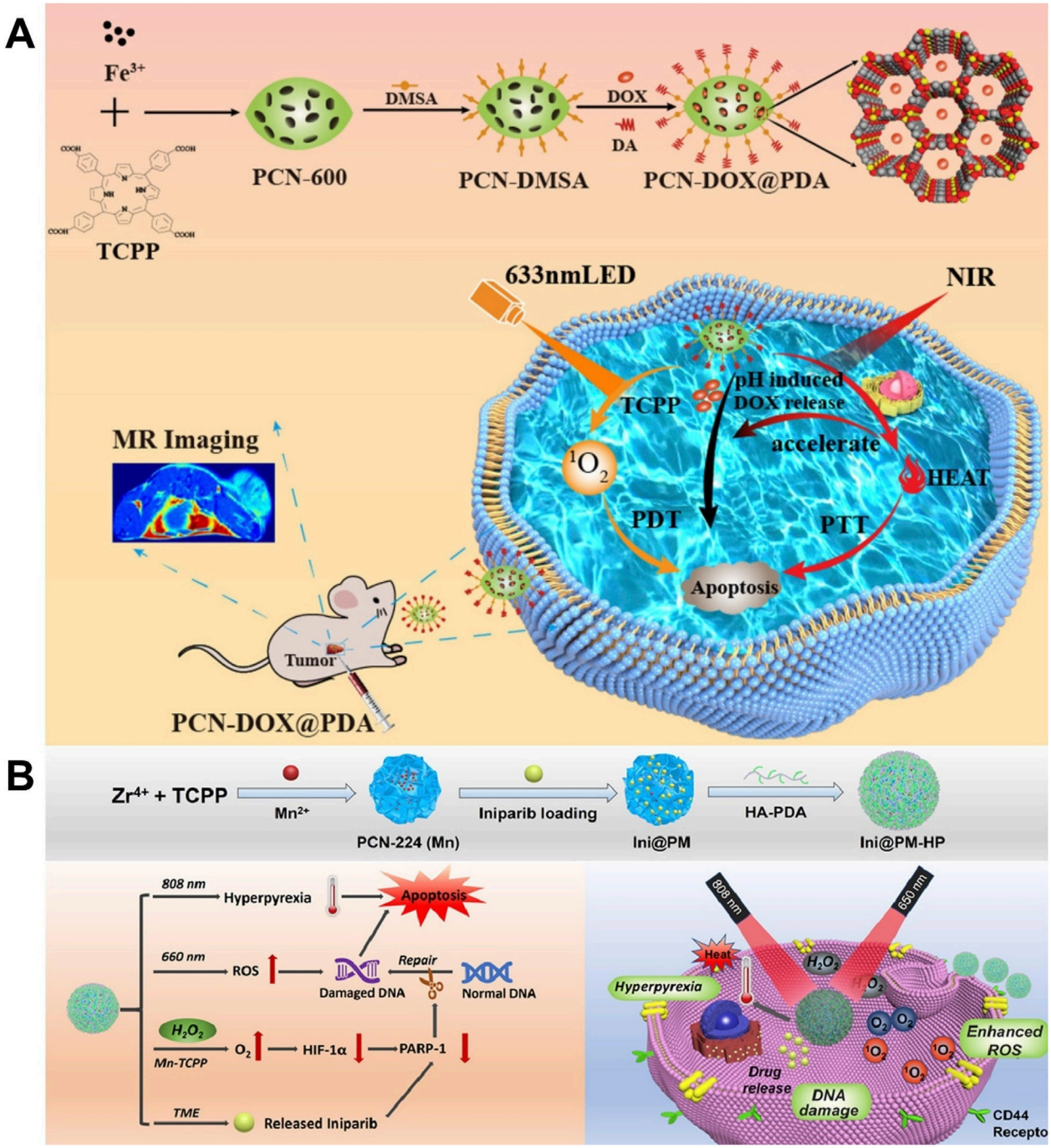

FIGURE 15
(A) Schematic representation of the synthesis of PCN-DOX@PDA and its application for the combined therapy of breast cancer with chemotherapy, photodynamic therapy, and photothermal therapy; copyright 2023, with permission from the American Chemical Society and Chen Z. et al. (2023). **(B)** Schematic representation of the synthesis and combined therapy of Ini@PM-HP; copyright 2022, with permission from Elsevier and Feng L. et al. (2022).

(Zhao H. et al., 2024). Chen Z. et al. (2023) prepared PCN-DOX@PDA by loading DOX on PCN-600 assembled through the coordination of Fe^{3+} and TCPP and utilizing PDA to coat the surface of PCN-600. Due to the degradation of shell PDA in an acidic environment and the heat-promoted thermal movement of the molecules, PCN-DOX@PDA showed pH- and light-stimulation-responsive drug release, which achieved precise drug release at the tumor site and reduced the side effects of chemotherapy, promoting the implementation of precision medicine. Due to the presence of Fe^{3+} and photosensitizer TCPP, PCN-DOX@PDA exhibited superior T_2-weighted MRI performance and efficient PDT. PCN-DOX@PDA, with a drug-loading capacity of 78%, demonstrated dual stimuli-responsive drug release and excellent biocompatibility, and it enabled an MRI-guided combination of PDT, PTT, and chemotherapy, which provided a reference for the construction of a multi-functional

intelligent response drug delivery system (Figure 15A) (Chen Z. et al., 2023). Feng L. et al. (2022) prepared PCN-224 (Mn) by chelating TCPP with Mn^{2+}, applied PCN-224 (Mn) to load the hydrophobic chemotherapeutic drug iniparib through electrostatic interaction, and applied HA-PDA to modify the surface of PCN-224 (Mn), leading to the preparation of Ini@PM-HP. Ini@PM-HP had a drug-loading capacity of 29.38% and could be degraded in a phosphate environment, showing phosphate-responsive drug release, which was expected to be accurately released in the tumor microenvironment with a high phosphate concentration. The released iniparib causes DNA damage and repair dysfunction, and it promoted tumor apoptosis, producing chemotherapy and improving the efficacy of PDT. Released Mn^{2+} had peroxidase-like activity, which could catalyze the high concentration of H_2O_2 in the tumor to produce O_2, improving the anoxic state of the tumor and enhancing the efficacy of PDT and chemotherapy. Due to the presence of HA-PDA, Ini@PM-HP could actively target tumor tissues with high CD44 receptor expression and possessed a photothermal conversion efficiency of 19.5%, showing good photothermal performance. Ini@PM-HP used nano-enzyme to generate O_2 *in situ*, which improved the hypoxia state of tumors and enabled a highly efficient combination of chemotherapy, PDT, and PTT, providing a multi-functional nano-platform and a reference for improving hypoxia and combined therapy (Figure 15B) (Feng L. et al., 2022).

2.3.5 PTT + ST+ gas therapy

H_2S-based gas therapy is an effective anti-tumor modality, which can hinder the cell cycle, induce apoptosis of tumor cells, enhance immunotherapy, and inhibit tumor metastasis, showing a promising application (Ghaffari-Bohlouli et al., 2024; Wu G. L. et al., 2023; Li S. et al., 2023; Cheng J. et al., 2023). H_2S has a short blood half-life and poor stability and could not specifically target tumor tissue, which severely limits the effectiveness of H_2S treatment (Rong et al., 2022; Ge et al., 2022; Cheng K. et al., 2022). Therefore, it is of great significance to construct a multi-functional nano-platform to achieve the targeted enrichment of H_2S at the tumor site and the accurate release of H_2S at the tumor site (Cheng K. et al., 2022). PTT could upregulate the expression of the heat shock protein, which caused heat tolerance of tumor cells and limited the efficiency of PTT (Premji et al., 2024). Therefore, the inhibition of heat shock proteins produced during PTT is an important method to improve the efficiency of PTT (Chang et al., 2022). Due to the strong chelation of the catechol group of PDA with metal ions, Cheng K. et al. (2022) synthesized Co-MOF on the surface of PDA using the one-pot method, loaded triethole (ADT) into mesoporous Co-MOF, and coated it with a macrophage membrane, leading to the preparation of PCoA@M. Due to the expression of integrin on the membrane of macrophages, PCoA@M could recognize tumorous cells with high expression of vascular cell adhesion molecules, efficiently enrich tumor tissues, show high stability, and reduce phagocytosis of the immune system. PCoA@M was degraded in an acidic environment to achieve pH-responsive release of Co^{2+} and ADT, which facilitated accurate drug release in the acidic microenvironment of the tumor. Co^{2+} downregulated the expression of HSP90 and inhibited heat shock protein-mediated thermo-resistance in tumor cells, which increased the sensitivity of PTT. The precise release of ADT at the tumor site was catalyzed by enzymes highly expressed in the tumor cells to generate high concentrations of H_2S, producing gas therapy. ADT reacted with nicotinamide adenine dinucleotide (NADH), leading to a reduction in the content of NADH and resulting in a dynamic imbalance in the nicotinamide adenine dinucleotide/lutein adenine dinucleotide (NADH/FAD) ratio; this disruption ultimately reduced ATP production, thereby inducing ST. NADH/FAD-mediated autofluorescence showed that the content of PCoA@M reached the maximum at 8 h after tail vein injection. PCoA@M, with a drug-loading capacity of 3.4%, showed good biosafety and enabled the combination of PTT, gas therapy, and ST, which significantly inhibited the growth and lung metastasis of breast cancer (Figure 16) (Cheng K. et al., 2022). This study utilized the Co^{2+} in PCoA@M to inhibit the expression of heat shock proteins and improve the efficiency of PTT, which suggested that Co^{2+}-containing MOFs@PDA may act as a heat shock protein inhibitor, showing promising applications. This study achieved efficient enrichment of H_2S-producing drugs at the tumor site and precise release of H_2S-producing drugs at the tumor site, and it applied the enzymes in tumor cells to catalyze drugs to generate H_2S, which facilitated the efficient enrichment and precise release of H_2S at the tumor site and improved the effectiveness of H_2S-based gas therapy, providing ideas for the efficient use of H_2S in the treatment of tumors.

2.3.6 Others

Zhan et al. (2023) encapsulated GOx and DOX in the inner part of ZIF-8 using the one-pot method and coated ZIF-8 with PDA to prepare DGZPNs . Because PDA and ZIF-8 were stable in a neutral environment and degraded in an acidic environment, DGZPNs not only prevented the premature release of GOx and DOX in blood circulation but also achieved acid-responsive release of GOx and DOX in the tumor microenvironment, which reduced the toxicity of drugs to normal tissues. GOx consumed glucose to disrupt the metabolic pathway of cancer cells, which led to ST. DGZPNs possessed a drug-loading capacity of 14.6% and a photothermal conversion efficiency of 36.9%, enabling the combination of chemotherapy, ST, and PTT, which could inhibit tumor growth in a safe and efficient way (Zhan et al., 2023). An G. et al. (2024) prepared MIL-101 by the solvothermal method, applied Cu nanoparticles to grow on MIL-101 through the reduction reaction, and applied Cu@MIL-101 to load cisplatin (Pt) and 1-methyl-D-tryptophan (1-MT) and connect TCPP by the amide bond, leading to the preparation of Cu@MIL-101@PMT. An et al. prepared Cu@MIL-101@PMTPC by coating PDA on the surface of Cu@MIL-101@PMT and coating CaO_2 on the surface of PDA through physical stirring. Because PDA was coated on the surface of Cu@MIL-101 loaded with drugs, the composite avoided drug leakage in the process of blood circulation and enriched the tumor site through EPR, reducing the toxicity of drugs to normal tissues. Cu@MIL-101@PMTPC possessed a drug-loading capacity of 40.5% for Pt and 9.5% for 1-MT, and it showed pH-responsive drug release. Fe^{3+} in MIL-101 (Fe) and Cu nanoparticles could react with intracellular GSH, leading to GSH depletion, and the production of Fe^{2+} and Cu^{+}, improving the efficacy of CDT and PDT. Fe^{2+} and Cu^{+} could interact with H_2O_2 by the Fenton-like reaction to produce ROS, which produced the effect of CDT. Outer CaO_2 reacted with water to produce O_2 and H_2O_2, which enhanced

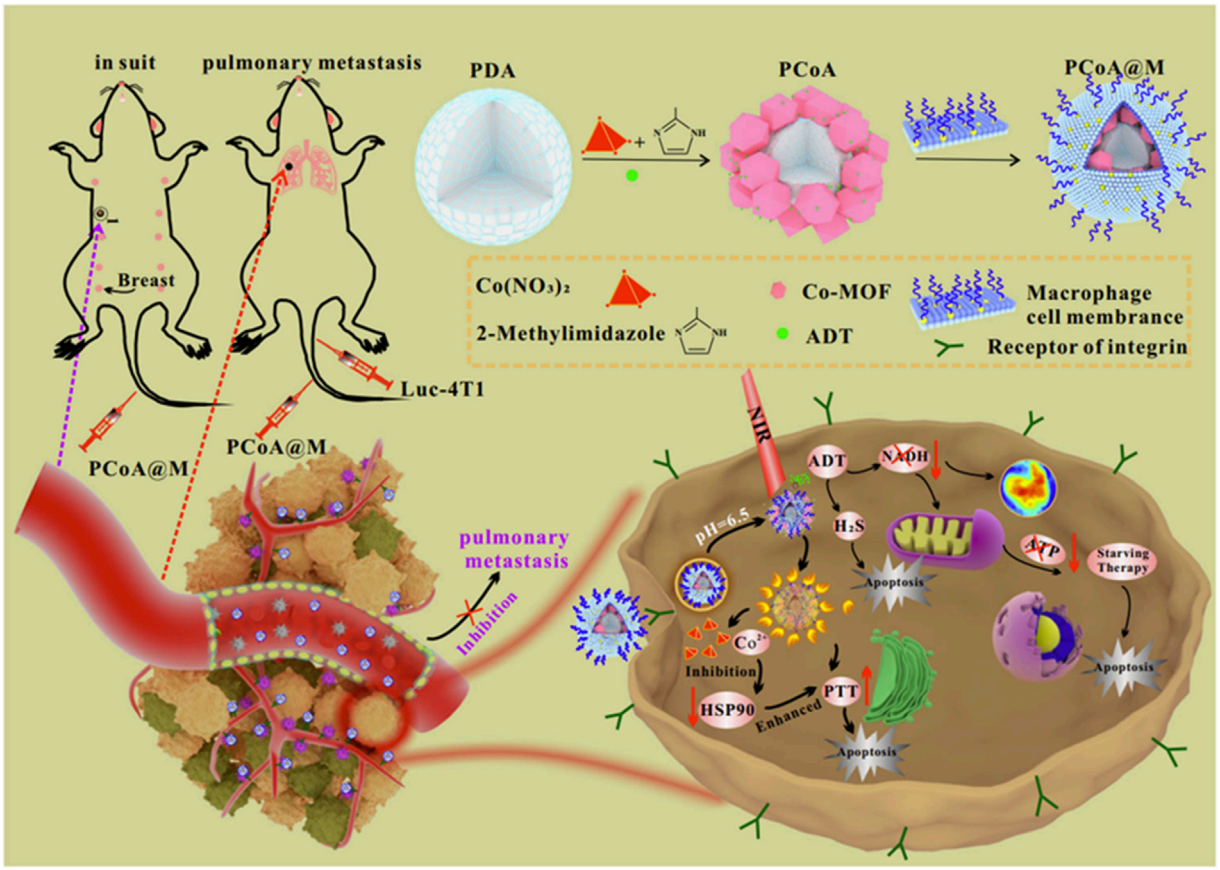

FIGURE 16
Schematic illustration of the experimental procedure for preparing PCoA@M and synergistic treatment of breast cancer induced by PCoA@M; copyright 2022, with permission from Springer Nature and Cheng K. et al. (2022). PCoA@M could be efficiently enriched at tumor sites by integrin on the membrane of macrophages. PCoA@M inhibited HSPs to enhance photothermal therapy and inhibited NADH generation, which achieved the combination of starvation therapy, gas therapy, and photothermal therapy, inhibiting tumor growth and metastasis.

the effect of PDT and provided a continuous supply of H_2O_2 for Fenton-like reactions, enhancing the effect of CDT. 1-MT was an indoleamine 2-dioxygenase (IDO) inhibitor, which could enhance the expression of $CD8^+$ and $CD4^+$ T cells and accelerate immunogenic cell death, and it can overcome the immune escape caused by cisplatin, producing immunotherapy. Cu@MIL-101@PMTPC had cascade catalysis to achieve self-supply of O_2 and H_2O_2, improving the poor efficacy of PDT caused by hypoxia and overcoming the poor efficacy of CDT caused by insufficient H_2O_2 in tumors. Cu@MIL-101@PMTPC enabled high-efficiency combination of CDT, PDT immunotherapy, and chemotherapy, enriching the types of multi-functional nano-platforms and providing a new strategy for cancer treatment (An G. et al., 2024). TPZ is a biological reductant with selective hypoxia cytotoxicity, which could produce highly active free radicals in a hypoxic environment, resulting in tumor cell death (Shi Q. et al., 2024; Chen Y. et al., 2024). Wang Y. et al. (2023b) used MIL-88B-NH_2 to load D-arginine (D-Arg), GOx, and TPZ, then coated PDA on the surface of MIL-88B-NH_2, and used shell PDA to chelate Fe^{3+} and link with folic acid-modified bovine serum albumin (FA-BSA), leading to the preparation of D-Arg/GOx/TPZ@MOF(Fe)-PDA/Fe^{3+}/FA-BSA. Due to the presence of FA-BSA, the complex could actively target osteosarcoma and prolong the blood circulation time. GOx catalyzed endogenous glucose to produce H_2O_2 and gluconic acid, which cuts off cell energy supply, producing ST. As gluconic acid led to acidification of the tumor site, MIL-88B-NH_2 degraded and released TPZ and Fe^{3+}. Fe^{3+} reacted with H_2O_2 to produce ROS, which catalyzed D-Arg to produce NO, enhancing the efficacy of radiotherapy (RT) and generating gas therapy. Endogenous glucose catalyzed by GOx consumed O_2 and RT consumed O_2, resulting in serious hypoxia of the tumor microenvironment. The serious hypoxia in the tumor site could activate TPZ, resulting in efficient chemotherapy. The shell PDA could not only seal the MIL-88B-NH_2 pores loaded with drugs but also chelate Fe^{3+} to produce superior T_1-weighted MRI performance. The complex showed pH- responsive drug release and enabled the combination of ST, gas therapy, CDT, low-dose RT, and chemotherapy, which significantly inhibited tumor growth and lung metastasis (Figure 17) (Wang Y. et al., 2023b). This study utilized ST and RT to lead to significant hypoxia at the tumor site, which activated hypoxia-activated drugs to produce highly effective anti-tumor effects, providing a new strategy for treating tumors by making use of the characteristics of hypoxia at the tumor site and offering an effective method to overcome treatment resistance due to hypoxia.

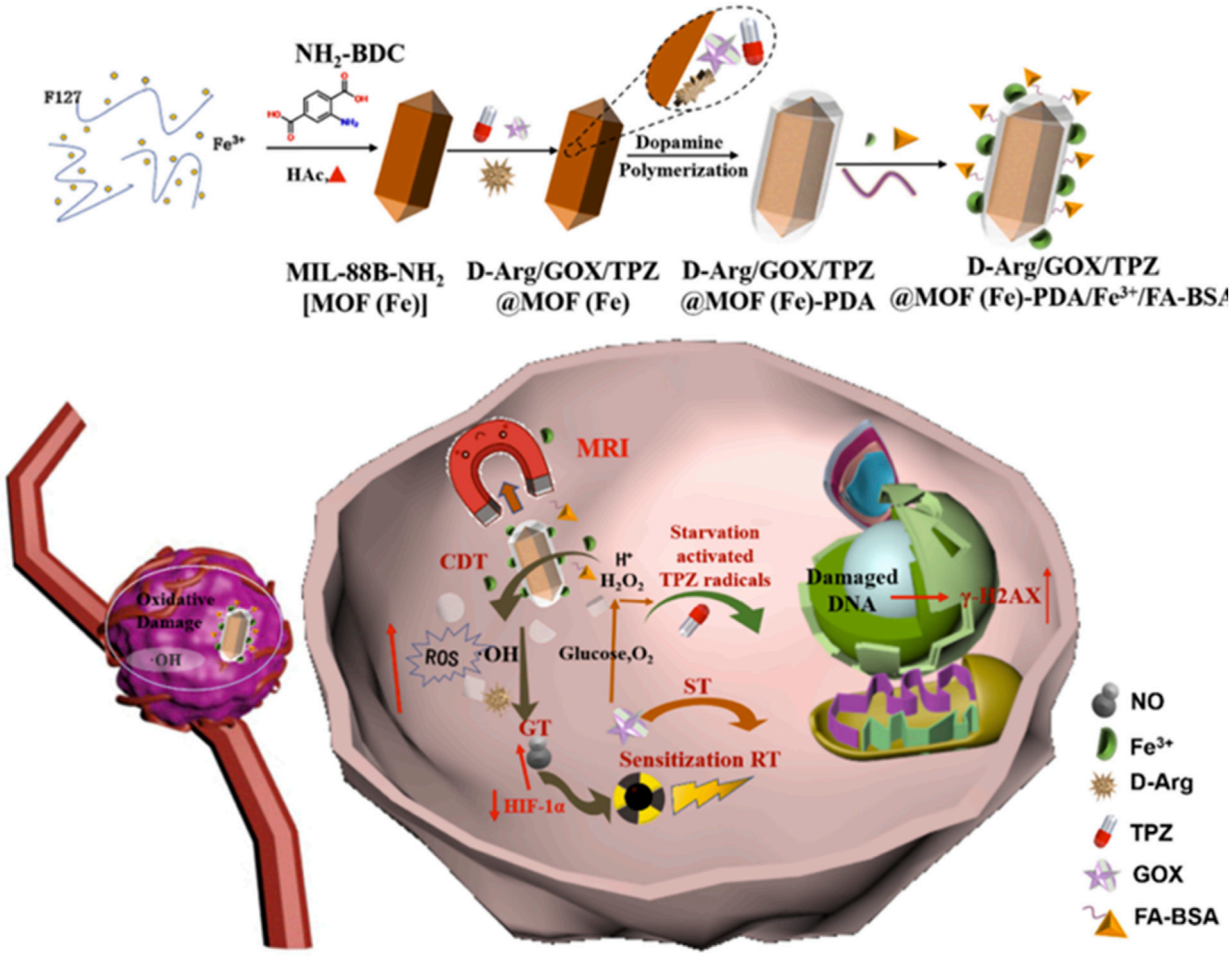

FIGURE 17
Schematic illustration of the experimental procedure for preparing D-Arg/GOX/TPZ@MOF(Fe)-PDA/Fe^{3+}/FA-BSA and its application for the combined therapy of osteosarcoma with chemotherapy, starvation therapy, gas therapy, chemodynamic therapy, and radiotherapy; copyright 2023, with permission from Elsevier and Wang Y. et al. (2023b).

3 Summary and challenges

MOFs@PDA are classical multifunctional nanomaterials and ideal carriers for constructing nano-drug delivery systems, achieving integrated diagnosis and treatment and comprehensive treatment. MOFs@PDA have made breakthrough progress in solving problems such as treatment resistance caused by hypoxia at the tumor site, low efficiency of low-temperature PTT caused by the upregulation of heat shock proteins, chemotherapy resistance, and low efficiency of CDT caused by high GSH expression inside the tumor. MOFs@PDA could internally encapsulate drugs and efficiently load drugs on the surface using various mechanisms and could achieve pH- and light-stimulation-responsive drug release, which facilitated the precise release of drugs at the tumor site, improved the efficiency of chemotherapy, and reduced the side effects of chemotherapy. Due to the excellent photothermal properties of PDA and the good imaging properties of MOFs, MOFs@PDA are not only excellent multifunctional photothermal agents that combine diagnostic and photothermal properties but can also be loaded with drugs or enzymes, which makes it easy to achieve comprehensive treatment. MOFs@PDA not only scavenge GSH to break redox homeostasis but also catalyze the generation of ROS from H_2O_2, which sensitize the effects of various tumor-treatment modalities. Therefore, MOFs@PDA are of great value for biomedical applications.

MOFs@PDA also face great challenges in clinical translation. First, the safety of MOFs@PDA is the basis for its clinical translational application. However, the current safety assessment of MOFs@PDA is mostly limited to short-term toxicity, such as the effect on body weight and pathological changes in major organs in animals. The lack of assessment of long-term toxicity of MOFs@PDA limits the clinical translational application of MOFs@PDA. When selecting metal ions and organic ligands to compose MOFs, we can pick the metal ions essential for the human body and FDA-approved organic ligands, thus guaranteeing the safety of MOFs@PDA from the beginning of the experiment. Second, the preparation process of MOFs@PDA is relatively complex, which is not conducive to the reproducibility of samples and could not provide the availability of a large number of samples for biomedical applications. The optimization of experimental parameters and the standardization of experimental steps for the preparation of simple and multifunctional MOFs@PDA are of great value for the diagnosis and treatment of tumors. Third, some MOFs@PDA with PDA as nuclei and MOFs as shells may be unstable in the

physiological environment, which can be easily aggregated and phagocytosed after the conditioning effect of the immune system and are unable to be effectively enriched at the tumor site. Researchers can utilize active targeting molecules, cell membranes, and albumin for the surface modification of MOFs@PDA to improve the water solubility and targeting of MOFs@PDA. Fourth, the lack of in-depth and systematic studies on the degradation mechanism and pharmacokinetic characteristics of MOFs@PDA *in vivo* is not conducive to selecting the optimal therapeutic dosage of MOFs@PDA and understanding the *in vivo* clearance of MOFs@PDA, which makes it impossible to rationally utilize MOFs@PDA to treat tumors. Researchers need to monitor the metabolism of MOFs@PDA in large primates for a long time and carefully study the specific degradation mechanism of MOFs@PDA. Fifth, the specific molecular mechanisms and signaling pathways of MOFs@PDA's anti-tumor effects are not clear, which is not conducive to guiding clinical medication. Researchers can explore the specific molecular mechanism of MOFs@PDA's anti-tumor effects by sequencing the genome of MOFs@PDA-treated cells and employing a large number of biological experiments. For the clinical translation of MOFs@PDA, researchers need to take a rational approach to address the safety, stability, and targeting and scale-up preparation of MOFs@PDA and deeply investigate the metabolic mechanism and specific anti-tumor mechanism of MOFs@PDA.

In summary, this paper summarized the progress made by MOFs@PDA in the field of tumor diagnosis and treatment in a timely manner, with the expectation of promoting the biomedical application of MOFs@PDA, increasing the development of novel strategies for tumor diagnosis and treatment, and inspiring researchers to explore the clinical translational applications of MOFs@PDA. Despite the significant challenges, MOFs@PDA will continue to make groundbreaking research advances in tumor diagnosis and treatment and promote the clinical translational application of nanomedicine.

Author contributions

JH: conceptualization, data curation, formal analysis, investigation, methodology, project administration, resources, software, supervision, visualization, writing–original draft, and writing–review and editing. GW: conceptualization, data curation, investigation, methodology, validation, and writing–review and editing. YZ: investigation, methodology, and writing–review and editing. BL: conceptualization, funding acquisition, investigation, project administration, supervision, and writing–review and editing. PS: methodology, project administration, validation, and writing–review and editing.

Funding

The author(s) declare that financial support was received for the research and/or publication of this article. This work was supported by Guangxi Science and Technology Bases and Talents (AD21238014).

Conflict of interest

The authors declare that the research was conducted in the absence of any commercial or financial relationships that could be construed as a potential conflict of interest.

Generative AI statement

The author(s) declare that no Generative AI was used in the creation of this manuscript.

Publisher's note

References

Acter, S., Moreau, M., Ivkov, R., Viswanathan, A., and Ngwa, W. (2023). Polydopamine nanomaterials for overcoming current challenges in cancer treatment. *Nanomater. (Basel)* 13 (10), 1656. doi:10.3390/nano13101656

Alavijeh, R. K., and Akhbari, K. (2024). Cancer therapy by nano MIL-n series of metal-organic frameworks. *Coord. Chem. Rev.* 15, 503. doi:10.1016/j.ccr.2023.215643

An, G., Zheng, H., Guo, L., Huang, J., Yang, C., Bai, Z., et al. (2024). A metal-organic framework (MOF) built on surface-modified Cu nanoparticles eliminates tumors via multiple cascading synergistic therapeutic effects. *J. Colloid. Interface. Sci.* 662, 298–312. doi:10.1016/j.jcis.2024.02.055

An, P., Fan, F., Gu, D., Gao, Z., Hossain, A. M. S., and Sun, B. (2020). Photothermal-reinforced and glutathione-triggered *in situ* cascaded nanocatalytic therapy. *J. Control. Release.* 321, 734–743. doi:10.1016/j.jconrel.2020.03.007

Bai, T., Xue, P., Shao, S., Yan, S., and Zeng, X. (2024). Cholesterol depletion-enhanced ferroptosis and immunotherapy via engineered nanozyme. *Adv. Sci. (Weinh)* 11 (38), e2405826. doi:10.1002/advs.202405826

Binaeian, E., Nabipour, H., Ahmadi, S., and Rohani, S. (2023). The green synthesis and applications of biological metal-organic frameworks for targeted drug delivery and tumor treatments. *J. Mat. Chem. B* 11 (48), 11426–11459. doi:10.1039/d3tb01959d

Bonet-Aleta, J., Alegre-Requena, J. V., Martin-Martin, J., Encinas-Gimenez, M., Martín-Pardillos, A., Martin-Duque, P., et al. (2024). Nanoparticle-catalyzed transamination under tumor microenvironment conditions: anovel tool to disrupt the pool of amino acids and GSSG in cancer cells. *Nano. Lett.* 15, 4091–4100. doi:10.1021/acs.nanolett.3c04947

Chang, M., Hou, Z., Wang, M., Wen, D., Li, C., Liu, Y., et al. (2022). Cu single atom nanozyme based high-efficiency mild Photothermal therapy through cellular metabolic regulation. *Angew. Chem. Int. Ed. Engl.* 61 (50), e202209245. doi:10.1002/anie.202209245

Chen, H., Fu, Y., Feng, K., Zhou, Y., Wang, X., Huang, H., et al. (2021). Polydopamine-coated UiO-66 nanoparticles loaded with perfluorotributylamine/tirapazamine for hypoxia-activated osteosarcoma therapy. *J. Nanobiotechnology* 19 (1), 298. doi:10.1186/s12951-021-01013-0

Chen, L., Zhang, J., Zhou, X., Yang, S., Zhang, Q., Wang, W., et al. (2019). Merging metal organic framework with hollow organosilica nanoparticles as a versatile nanoplatform for cancer theranostics. *Acta Biomater.* 86, 406–415. doi:10.1016/j.actbio.2019.01.005

Chen, W., Ouyang, J., Liu, H., Chen, M., Zeng, K., Sheng, J., et al. (2017). Black phosphorus nanosheet-based drug delivery system for synergistic photodynamic/

photothermal/chemotherapy of cancer. *Adv. Mater* 29 (5). doi:10.1002/adma.201603864

Chen, X., Ma, X., Yang, G., Huang, G., Dai, H., Yu, J., et al. (2024). Chalcogen atom-modulated croconaine for efficient NIR-II photothermal theranostics. *Acs. Appl. Mat. Interfaces* 16 (10), 12332–12338. doi:10.1021/acsami.4c02254

Chen, Y., Zou, T., Xin, G., Liu, X., Yang, Y., Wei, L., et al. (2024). Oxygen-independent synchronized ROS generation and hypoxia prodrug activation with Z-scheme heterostructure sonosensitizer. *Adv. Mat.* 36 (3), e2307929. doi:10.1002/adma.202307929

Chen, Z., Sun, Y., Wang, J., Zhou, X., Kong, X., Meng, J., et al. (2023). Dual-responsive triple-synergistic Fe-MOF for tumor theranostics. *Acs. Nano.* 17 (10), 9003–9013. doi:10.1021/acsnano.2c10310

Cheng, B., Li, D., Li, C., Zhuang, Z., Wang, P., and Liu, G. (2023). The application of biomedicine in chemodynamictherapy: from material design to improved strategies. *Bioeng. (Basel)* 10 (8), 925. doi:10.3390/bioengineering10080925

Cheng, J., Zhu, Y., Dai, Y., Li, L., Zhang, M., Jin, D., et al. (2023). Gas-mediated tumor energy remodeling for sensitizing mild photothermal therapy. *Angew. Chem. Int. Ed. Engl.* 62 (27), e202304312. doi:10.1002/anie.202304312

Cheng, K., Liu, B., Zhang, X. S., Zhang, R. Y., Zhang, F., Ashraf, G., et al. (2022). Biomimetic material degradation for synergistic enhanced therapy by regulating endogenous energy metabolism imaging under hypothermia. *Nat. Commun.* 13 (1), 4567. doi:10.1038/s41467-022-32349-2

Cheng, W., Su, Y. L., Hsu, H. H., Lin, Y. H., Chu, L. A., Huang, W. C., et al. (2022). Rabies virus glycoprotein-mediated transportation and T cell infiltration to brain tumor by magnetoelectric gold yarnballs. *ACS Nano* 16 (3), 4014–4027. doi:10.1021/acsnano.1c09601

Chiang, M. R., Shen, W. T., Huang, P. X., Wang, K. L., Weng, W. H., Chang, C. W., et al. (2023). Programmed T cells infiltration into lung metastases with harnessing dendritic cells in cancer immunotherapies by catalytic antigen-capture sponges. *J. Control. Release.* 360, 260–273. doi:10.1016/j.jconrel.2023.06.033

Chon, Y. E., Kim, D. Y., Kim, M., Kim, B. K., Kim, S. U., Park, J. Y., et al. (2024). Sorafenib vs. Lenvatinib in advanced hepatocellular carcinoma after Atezolizumab/Bevacizumab Failure: a real-world study. *Clin. Mol. Hepatol.* 12, 345–359. doi:10.3350/cmh.2023.0553

Dash, B. S., Lu, Y. J., and Chen, J. P. (2024). Enhancing photothermal/photodynamic therapy for glioblastoma by tumor hypoxia alleviation and heat shock protein inhibition using IR820-conjugated reduced graphene oxide quantum dots. *Acs. Appl. Mat. Interfaces* 16 (11), 13543–13562. doi:10.1021/acsami.3c19152

Deng, H., Zhang, J., Yang, Y., Yang, J., Wei, Y., Ma, S., et al. (2022). Chemodynamic and photothermal combination therapy based on dual-modified metal-organic framework for inducing tumor ferroptosis/pyroptosis. *Acs. Appl. Mat. Interfaces* 14 (21), 24089–24101. doi:10.1021/acsami.2c00574

Deng, X. T., Zhao, R. L., Tang, Y. F., Ge, Z. L., Wang, D., Xiong, Z. C., et al. (2023). NIR laser-activated multifunctional nanocomposites for cascade low-temperature photothermal and oxygen-irrelevant thermodynamic therapy. *Mater. and Des.* 233, 112206. doi:10.1016/j.matdes.2023.112206

Duan, H., Wang, F., Xu, W., Sheng, G., Sun, Z., and Chu, H. (2023). Recent advances in the nanoarchitectonics of metal-organic frameworks for light-activated tumor therapy. *Dalton. Trans.* 52 (44), 16085–16102. doi:10.1039/d3dt02725b

Fan, R., Chen, C., Hu, J., Mu, M., Chuan, D., Chen, Z., et al. (2023). Multifunctional gold nanorods in low-temperature photothermal interactions for combined tumor starvation and RNA interference therapy. *Acta. Biomater.* 159, 324–337. doi:10.1016/j.actbio.2023.01.036

Feng, J., Yu, W., Xu, Z., Hu, J., Liu, J., and Wang, F. (2020b). Multifunctional siRNA-laden hybrid nanoplatform for noninvasive PA/IR dual-modal imaging-guided enhanced photogenetherapy. *Acs. Appl. Mat. Interfaces* 12 (20), 22613–22623. doi:10.1021/acsami.4c18256

Feng, J., Yu, W., Xu, Z., and Wang, F. (2020a). An intelligent ZIF-8-gated polydopamine nanoplatform for*in vivo*cooperatively enhanced combination phototherapy. *Chem. Sci.* 11 (6), 1649–1656. doi:10.1039/c9sc06337d

Feng, L., Chen, M., Li, R., Zhou, L., Wang, C., Ye, P., et al. (2022). Biodegradable oxygen-producing manganese-chelated metal organic frameworks for tumor-targeted synergistic chemo/photothermal/photodynamic therapy. *Acta. Biomater.* 138, 463–477. doi:10.1016/j.actbio.2021.10.032

Forgham, H., Zhu, J., Huang, X., Zhang, C., Biggs, H., Liu, L., et al. (2024). Multifunctional fluoropolymer-engineered magnetic nanoparticles to facilitate blood-brain barrier penetration and effective gene silencing in medulloblastoma. *Adv. Sci. (Weinh)* 22, e2401340. doi:10.1002/advs.202401340

Fu, Y., Sun, J., Wang, Y., and Li, W. (2023). Glucose oxidase and metal catalysts combined tumor synergistic therapy: mechanism, advance and nanodelivery system. *J. Nanobiotechnology* 21 (1), 400. doi:10.1186/s12951-023-02158-w

Gao, Q., He, X., He, L., Lin, J., Wang, L., Xie, Y., et al. (2023). Hollow $Cu_{2-x}Se$-based nanocatalysts for combined photothermal and chemodynamic therapy in the second near-infrared window. *Nanoscale* 15 (44), 17987–17995. doi:10.1039/d3nr03260d

Gao, S. S., Lv, R. H., Hao, N., Wang, H. H., Lv, Y. N., Li, Y. C., et al. (2023). Fabrication of pH/photothermal-responsive ZIF-8 nanocarriers loaded with baicalein for effective drug delivery and synergistic chem-photothermal effects. *Colloids. And. Surfaces. A Physicochemical.And. Eng. Aspects.* 668, 131401. doi:10.1016/j.colsurfa.2023.131401

Ge, Y., Rong, F., Li, W., and Wang, Y. (2022). On-demand therapeutic delivery of hydrogen sulfide aided by biomolecules. *J. Control. Release.* 352, 586–599. doi:10.1016/j.jconrel.2022.10.055

Ghaffari-Bohlouli, P., Jafari, H., Okoro, O. V., Alimoradi, H., Nie, L., Jiang, G., et al. (2024). Gas therapy: generating, delivery, and biomedical applications. *Small. Methods.* 9, e2301349. doi:10.1002/smtd.202301349

Gulati, S., Choudhury, A., Mohan, G., Katiyar, R., Kurikkal, M. P. M. A., Kumar, S., et al. (2023). Metal-organic frameworks (MOFs) as effectual diagnostic and therapeutic tools for cancer. *J. Mater Chem. B* 11 (29), 6782–6801. doi:10.1039/d3tb00706e

Guo, H., Xia, Y., Feng, K., Qu, X., Zhang, C., and Wan, F. (2020). Surface engineering of metal-organic framework as pH-/NIR-responsive nanocarrier for imaging-guided chemo-photothermal therapy. *Int. J. Nanomedicine.* 15, 3235–3250. doi:10.2147/IJN.S239910

Hao, J. N., Ge, K., Chen, G., Dai, B., and Li, Y. (2023). Strategies to engineer various nanocarrier-based hybrid catalysts for enhanced chemodynamic cancer therapy. *Chem. Soc. Rev.* 52 (22), 7707–7736. doi:10.1039/d3cs00356f

He, J., Ramachandraiah, K., Huang, T., Yuan, T., Liu, X., Zhang, H., et al. (2023). Core-shell structured hollow copper sulfide@metal-organic framework for magnetic resonance imaging guided photothermal therapy in second near-infrared biological window. *Biochem. Biophys. Res. Commun.* 638, 51–57. doi:10.1016/j.bbrc.2022.11.036

Hsia, T., Small, J. L., Yekula, A., Batool, S. M., Escobedo, A. K., Ekanayake, E., et al. (2023). Systematic review of photodynamic therapy in gliomas. *Cancers (Basel)* 15 (15), 3918. doi:10.3390/cancers15153918

Hu, Q., Xu, L., Huang, X., Duan, Y., Sun, D., Fu, Z., et al. (2023). Polydopamine-modified zeolite imidazole framework drug delivery system for photothermal chemotherapy of hepatocellular carcinoma. *Biomacromolecules* 24 (12), 5964–5976. doi:10.1021/acs.biomac.3c00971

Huang, R., Liu, W., Zhang, Q., Zhu, G., Qu, W., Tao, C., et al. (2023). Laser-induced combinatorial chemotherapeutic, chemodynamic, and photothermal therapy for hepatocellular carcinoma based on oxaliplatin-loaded metal-organic frameworks. *Acs. Appl. Mat. Interfaces* 15 (3), 3781–3790. doi:10.1021/acsami.2c19305

Jadhav, V., Vaishnaw, A., Fitzgerald, K., and Maier, M. A. (2024). RNA interference in the era of nucleic acid therapeutics. *Nat. Biotechnol.* 42 (3), 394–405. doi:10.1038/s41587-023-02105-y

Jiang, X., Zhao, Y., Sun, S., Xiang, Y., Yan, J., Wang, J., et al. (2023). Research development of porphyrin-based metal-organic frameworks: targeting modalities and cancer therapeutic applications. *J. Mater Chem. B* 11 (27), 6172–6200. doi:10.1039/d3tb00632h

Kandasamy, G., and Maity, D. (2024). Inorganic nanocarriers for siRNA delivery for cancer treatments. *Biomed. Mat.* 19 (2), 022001. doi:10.1088/1748-605X/ad1baf

Kong, F. H., Ye, Q. F., Miao, X. Y., Liu, X., Huang, S. Q., Xiong, L., et al. (2021). Current status of sorafenib nanoparticle delivery systems in the treatment of hepatocellular carcinoma. *Theranostics* 11 (11), 5464–5490. doi:10.7150/thno.54822

Ladd, A. D., Duarte, S., Sahin, I., and Zarrinpar, A. (2024). Mechanisms of drug resistance in HCC. *Hepatology* 79 (4), 926–940. doi:10.1097/HEP.0000000000000237

Lan, H. R., Zhang, Y. N., Han, Y. J., Yao, S. Y., Yang, M. X., Xu, X. G., et al. (2023). Multifunctional nanocarriers for targeted drug delivery and diagnostic applications of lymph nodes metastasis: a review of recent trends and future perspectives. *J. Nanobiotechnology* 21 (1), 247. doi:10.1186/s12951-023-01990-4

Li, H., Yin, D., Li, W., Tang, Q., Zou, L., and Peng, Q. (2021). Polydopamine-based nanomaterials and their potentials in advanced drug delivery and therapy. *Colloids. Surf. B. Biointerfaces.* 199, 111502. doi:10.1016/j.colsurfb.2020.111502

Li, J. M., Dai, J., Zhao, L., Lin, S., Wen, Q. L., Wen, Q., et al. (2023). Bioactive bacteria/MOF hybrids can achieve targeted synergistic chemotherapy and chemodynamic therapy against breast tumors. *Materials.* 33 (42), 114–125. doi:10.1002/adfm.202303254

Li, K., Xu, K., Liu, S., He, Y., Tan, M., Mao, Y., et al. (2023). All-in-One engineering multifunctional nanoplatforms for sensitizing tumor low-temperature photothermal therapy *in vivo*. *ACS Nano* 17 (20), 20218–20236. doi:10.1021/acsnano.3c05991

Li, M., Xuan, Y., Zhang, W., Zhang, S., and An, J. (2023). Polydopamine-containing nano-systems for cancer multi-mode diagnoses and therapies: a review. *Int. J. Biol. Macromol.* 247, 125826. doi:10.1016/j.ijbiomac.2023.125826

Li, N., Wang, Y., Li, Y., Zhang, C., and Fang, G. (2024). Recent advances in photothermal therapy at near-infrared-II based on 2D mXenes. *Small* 20 (6), e2305645. doi:10.1002/smll.202305645

Li, Q., Liu, Y., Zhang, Y., and Jiang, W. (2022). Immunogenicity-boosted cancer immunotherapy based on nanoscale metal-organic frameworks. *J. Control. Release*. 347, 183–198. doi:10.1016/j.jconrel.2022.05.003

Li, S., Shi, X., Wang, H., and Xiao, L. (2021). A multifunctional dual-shell magnetic nanocomposite with near-infrared light response for synergistic chemo-thermal tumor therapy. *J. Biomed. Mat. Res. B. Appl.Biomater.* 109 (6), 841–852. doi:10.1002/jbm.b.34749

Li, S., Xu, F., Ren, X., Tan, L., Fu, C., Wu, Q., et al. (2023). H_2S-reactivating antitumor immune response after microwave thermal therapy for long-term tumor suppression. *ACS Nano* 17 (19), 19242–19253. doi:10.1021/acsnano.3c05936

Li, X., Pan, Y., Chen, C., Gao, Y., Liu, X., Yang, K., et al. (2021). Hypoxia-responsive gene editing to reduce tumor thermal tolerance for mild-photothermal therapy. *Angew. Chem. Int. Ed. Engl.* 60 (39), 21200–21204. doi:10.1002/anie.202107036

Liu, G., Wang, L., Liu, J., Lu, L., Mo, D., Li, K., et al. (2020). Engineering of a core-shell nanoplatform to overcome multidrug resistance via ATP deprivation. *Adv. Healthc. Mat.* 9 (20), e2000432. doi:10.1002/adhm.202000432

Liu, L., Zhang, H., Peng, L., Wang, D., Zhang, Y., Yan, B., et al. (2023). A copper-metal organic framework enhances the photothermal and chemodynamic properties of polydopamine for melanoma therapy. *Acta. Biomater.* 158, 660–672. doi:10.1016/j.actbio.2023.01.010

Liu, S., Tian, L., Mu, M., Liu, Z., Dong, M., Gong, Y., et al. (2024). Platinum nanoparticles-enhanced ferritin-Mn^{2+}interaction for magnetic resonance contrast enhancement and efficient tumor photothermal therapy. *Adv. Healthc. Mat.* 6, e2303939. doi:10.1002/adhm.202303939

Liu, T., Wang, C., Gu, X., Gong, H., Cheng, L., Shi, X., et al. (2014). Drug delivery with PEGylated MoS_2 nano-sheets for combined photothermal and chemotherapy of cancer. *Adv. Mat.* 26 (21), 3433–3440. doi:10.1002/adma.201305256

Liu, W., Di, J., Ma, Y., Wang, S., Meng, M., Yin, Y., et al. (2023). Mitochondria-mediated HSP inhibition strategy for enhanced low-temperature photothermal therapy. *Acs. Appl. Mat. Interfaces* 15 (22), 26252–26262. doi:10.1021/acsami.3c00870

Liu, Y. J., Dong, S. H., Hu, W. H., Chen, Q. L., Zhang, S. F., Song, K., et al. (2024). A multifunctional biomimetic nanoplatform for image-guideded photothermal-ferroptotic synergistic osteosarcoma therapy. *Bioact. Mater* 36, 157–167. doi:10.1016/j.bioactmat.2024.02.007

Liu, Z., Liu, X., Zhang, W., Gao, R., Wei, H., and Yu, C. Y. (2024). Current advances in modulating tumor hypoxia for enhanced therapeutic efficacy. *Acta. Biomater.* 176, 1–27. doi:10.1016/j.actbio.2024.01.010

Liu X., X., Hu, T., Jia, Y., Yang, S., Yang, Y., Cui, Z., et al. (2024). A MgAl-LDH-CuS nanosheet-based thermo-responsive composite hydrogel with nir-responsive angiogenesis inhibitor releasing capability for multimode starvation therapy. *J. Nanobiotechnology* 22 (1), 127. doi:10.1186/s12951-024-02384-w

Ma, D., Wang, G., Lu, J., Zeng, X., Cheng, Y., Zhang, Z., et al. (2023). Multifunctional nano MOF drug delivery platform in combination therapy. *Eur. J. Med. Chem.* 261, 115884. doi:10.1016/j.ejmech.2023.115884

Mao, D., Dong, Z., Liu, X., Li, W., Li, H., Gu, C., et al. (2024). An intelligent DNA nanoreactor for easy-to-read *in vivo*tumor imaging and precise therapy. *Angew. Chem. Int. Ed. Engl.* 63 (7), e202311309. doi:10.1002/anie.202311309

Mehata, A. K., Vikas, K., Viswanadh, M. K., and Muthu, M. S. (2023). Theranostics of metal-organic frameworks: image-guided nanomedicine for clinical translation. *Nanomedicine (Lond).* 18 (8), 695–703. doi:10.2217/nnm-2022-0278

Menichetti, A., Mordini, D., and Montalti, M. (2024). Polydopamine nanosystems in drug delivery: effect of size, morphology, and surface charge. *Nanomater. (Basel)* 14 (3), 303. doi:10.3390/nano14030303

Moazzam, M., Zhang, M., Hussain, A., Yu, X., Huang, J., and Huang, Y. (2024). The landscape of nanoparticle-based siRNA delivery and therapeutic development. *Mol. Ther.* 32 (2), 284–312. doi:10.1016/j.ymthe.2024.01.005

Moharramnejad, M., Malekshah, R. E., Ehsani, A., Gharanli, S., Shahi, M., Alvan, S. A., et al. (2023). A review of recent developments of metal-organic frameworks as combined biomedical platforms over the past decade. *Adv. Colloid. Interface. Sci.* 316, 102908. doi:10.1016/j.cis.2023.102908

Natoni, A., Bohara, R., Pandit, A., and O'Dwyer, M. (2019). Targeted approaches to inhibit sialylation of multiple myeloma in the bone marrow microenvironment. *Front.Bioeng. Biotechnol.* 7, 252. doi:10.3389/fbioe.2019.00252

Nie, A., Shen, C., Zhou, Z., Wang, J., Sun, B., and Zhu, C. (2024). Ferroptosis: potential opportunities for natural products in cancer therapy. *Phytother. Res.* 38 (3), 1173–1190. doi:10.1002/ptr.8088

Premji, T. P., Dash, B. S., Das, S., and Chen, J. P. (2024). Functionalized nanomaterials for inhibiting ATP-dependent heat shock proteins in cancer photothermal/photodynamic therapy and combination therapy. *Nanomater. (Basel).* 14 (1), 112. doi:10.3390/nano14010112

Pu, Y., Zhu, Y., Qiao, Z., Xin, N., Chen, S., Sun, J., et al. (2021). A Gd-doped polydopamine (PDA)-based theranostic nanoplatform as a strong MR/PA dual-modal imaging agent for PTT/PDT synergistic therapy. *J. Mat. Chem. B* 9 (7), 1846–1857. doi:10.1039/d0tb02725a

Rao, Z., Xia, Y., Jia, Q., Zhu, Y., Wang, L., Liu, G., et al. (2023). Iron-based metal-organic framework co-loaded with buthionine sulfoximine and oxaliplatin for enhanced cancer chemo-ferrotherapy via sustainable glutathione elimination. *J. Nanobiotechnology* 21 (1), 265. doi:10.1186/s12951-023-01998-w

Ren, L., Sun, Y., Zhang, J., Nie, L., Shavandi, A., Yunusov, K. E., et al. (2024). Red blood cell membrane-coated functionalized Cu-doped metal organic framework nanoformulations as a biomimetic platform for improved chemo-/chemodynamic/photothermal synergistic therapy. *Int. J. Pharm.* 652, 123811. doi:10.1016/j.ijpharm.2024.123811

Ren, S. Z., Wang, B., Zhu, X. H., Zhu, D., Liu, M., Li, S. K., et al. (2020). Oxygen self-sufficient core-shell metal-organic framework-based smart nanoplatform for enhanced synergistic chemotherapy and photodynamic therapy. *Acs. Appl. Mat. Interfaces* 12 (22), 24662–24674. doi:10.1021/acsami.0c08534

Ren, S. Z., Zhu, X. H., Wang, B., Liu, M., Li, S. K., Yang, Y. S., et al. (2021). A versatile nanoplatform based on multivariate porphyrinic metal-organic frameworks for catalytic cascade-enhanced photodynamic therapy. *J. Mat. Chem. B* 9 (23), 4678–4689. doi:10.1039/d0tb02652b

Rong, F., Wang, T., Zhou, Q., Peng, H., Yang, J., Fan, Q., et al. (2022). Intelligent polymeric hydrogen sulfide delivery systems for therapeutic applications. *Bioact. Mat.* 19, 198–216. doi:10.1016/j.bioactmat.2022.03.043

Sandbhor, P., Palkar, P., Bhat, S., John, G., and andGoda, J. S. (2024). Nanomedicine as a multimodal therapeutic paradigm against cancer: on the way forward in advancing precision therapy. *Nanoscale* 16 (13), 6330–6364. doi:10.1039/d3nr06131k

Sharma, P., and Otto, M. (2023). Multifunctional nanocomposites modulating the tumor microenvironment for enhanced cancer immunotherapy. *Bioact. Mat.* 31, 440–462. doi:10.1016/j.bioactmat.2023.08.022

Shen, J., Chen, G., Zhao, L., Huang, G., Liu, H., Liu, B., et al. (2023). Recent advances in nanoplatform construction strategy for alleviating tumor hypoxia. *Adv. Healthc. Mat.* 12 (21), e2300089. doi:10.1002/adhm.202300089

Shi, P., Sun, X., Yuan, H., Chen, K., Bi, S., and andZhang, S. (2023). Nanoscale metal-organic frameworks combined with metal nanoparticles and metal oxide/peroxide to relieve tumor hypoxia for enhanced photodynamic therapy. *Acs. Biomater. Sci. Eng.* 9 (10), 5441–5456. doi:10.1021/acsbiomaterials.3c00509

Shi, Q., Zhang, W., Zhou, Y., Huang, S., Yu, J., Yang, M., et al. (2024). Hypoxia-activated cascade nanovaccine for synergistic chemoembolization-immune therapy of hepatocellular carcinoma. *Biomaterials* 306, 122480. doi:10.1016/j.biomaterials.2024.122480

Shu, F., Lv, D., Song, X. L., Huang, B., Wang, C., Yu, Y., et al. (2018). Fabrication of a hyaluronic acid conjugated metal organic framework for targeted drug delivery and magnetic resonance imaging. *RSC Adv.* 8 (12), 6581–6589. doi:10.1039/c7ra12969f

Song, Y., Xu, X., Wang, Z., and Zhao, Y. (2024). Metal-organic framework-based nanomedicines for ferroptoticcancer therapy. *Adv. Healthc. Mat.* 14, e2303533. doi:10.1002/adhm.202303533

Sun, Z., Liu, J., Li, Y., Lin, X., Chu, Y., Wang, W., et al. (2023). Aggregation-induced-emission photosensitizer-loaded nano-superartificialdendritic cells with directly presenting tumor antigens and reversed immunosuppression for photodynamically boosted immunotherapy. *Adv. Mater* 35 (3), e2208555. doi:10.1002/adma.202208555

Tao, T., Rehman, S. U., Xu, S., Zhang, J., Xia, H., Guo, Z., et al. (2024). A biomimetic camouflaged metal organic framework for enhanced siRNA delivery in the tumor environment. *J. Mater Chem. B* 12 (17), 4080–4096. doi:10.1039/d3tb02827e

Thirumurugan, S., Samuvel, M. K., Sakthivel, R., Liao, M. Y., Kasai, H., and Chung, R. J. (2023). Polydopamine-coated Cu-BTC nanowires for effective magnetic resonance imaging and photothermal therapy. *Pharmaceutics* 15 (3), 822. doi:10.3390/pharmaceutics15030822

Tian, Z., Wu, L., Yu, C., Chen, Y., Xu, Z., Bado, I., et al. (2021). Harnessing the power of antibodies to fight bone metastasis. *Sci. Adv.* 7 (26), eabf2051. doi:10.1126/sciadv.abf2051

Tu, L., Chen, S., Yuan, Z., Xiong, Y., Luo, B., Chen, Y., et al. (2024). Amino acid-based metallo-supramolecular nanoassemblies capable of regulating cellular redox homeostasis for tumoricidal chemo-/photo-/catalytic combination therapy. *J. Colloid. Interface. Sci.* 663, 810–824. doi:10.1016/j.jcis.2024.02.197

Turkmen, K. S. N., Rezaei, B. S., Aral, I. P., Shahbazi, R., and Ulubayram, K. (2024). Gold nanoparticles-mediated photothermal and photodynamic therapies for cancer. *Int. J. Pharm.* 655, 124057. doi:10.1016/j.ijpharm.2024.124057

Wang, C., and Zhang, S. (2023). Advantages of nanomedicine in cancer therapy: areview. *Acs. Appl. Nano. Mater.* 6 (24), 22594–22610. doi:10.1021/acsanm.3c04487

Wang, D., Wu, H., Lim, W. Q., Phua, S. Z. F., Xu, P., Chen, Q., et al. (2019a). A mesoporous nanoenzymederived from metal-organic frameworks with endogenous oxygen generation to alleviate tumor hypoxia for significantly enhanced photodynamic therapy. *Adv. Mater* 31 (27), e1901893. doi:10.1002/adma.201901893

Wang, D., Wu, H., Zhou, J., Xu, P., Wang, C., Shi, R., et al. (2018). *In situ* one-pot synthesis of MOF-polydopamine hybrid nanogels with enhanced photothermal effect for targeted cancer therapy. *Adv. Sci. (Weinh)* 5 (6), 1800287. doi:10.1002/advs.201800287

Wang, L., Chen, M., Ran, X., Tang, H., and Cao, D. (2023a). Sorafenib-based drug delivery systems: applications and perspectives. *Polym. (Basel)* 15 (12), 2638. doi:10.3390/polym15122638

Wang, L., Xu, Y. T., Liu, C., Si, W. L., Wang, W. J., Zhang, Y. W., et al. (2022). Copper-doped MOF-based nanocomposite for GSH depleted chemo/photothermal/chemodynamic combination therapy. *Chem. Eng. J.* 438, 135567. doi:10.1016/j.cej.2022.135567

Wang, P., Sun, S., Bai, G., Zhang, R., Liang, F., and Zhang, Y. (2024). Nanosized Prussian blue and its analogs for bioimaging and cancer theranostics. *Acta. Biomater.* 176, 77–98. doi:10.1016/j.actbio.2023.12.047

Wang, X., Zhang, Y., Li, T., and Liu, Y. (2023). Bioorthogonalglycoengineering-mediated multifunctional liquid metal nanoprobes for highly efficient photoacoustic imaging-guided photothermal/chemotherapy of tumor. *Acs. Appl. Bio. Mat.* 6 (8), 3232–3240. doi:10.1021/acsabm.3c00348

Wang, X. S., Zeng, J. Y., Zhang, M. K., Zeng, X., and Zhang, X. Z. (2018). A versatile Pt-based core–shell nanoplatform as a nanofactory for enhanced tumor therapy. *Adv. Funct. Mater.* 28, 1801783. doi:10.1002/adfm.201801783

Wang, Y., Tang, Y., Guo, L., Yang, X., Wu, S., Yue, Y., et al. (2025a). Recent advances in zeolitic imidazolate frameworks as drug delivery systems for cancer therapy. *Asian. J. Pharm. Sci.* 20 (1), 101017. doi:10.1016/j.ajps.2025.101017

Wang, Y., Williams, G. R., Zheng, Y., Guo, H., Chen, S., Ren, R., et al. (2023b). Polydopamine-cloaked Fe-based metal organic frameworks enable synergistic multidimensional treatment of osteosarcoma. *J. Colloid. Interface. Sci.* 651, 76–92. doi:10.1016/j.jcis.2023.07.146

Wang, Y. T., Cui, J. J., Chen, J. J., Wan, J. Y., Liang, Y. K., Qi, M., et al. (2022). Novel bone tumor cell targeting nanosystem for chemo-photothermal therapy of malignant bone tumors. *Chem. Eng. J.* 446, 136905. doi:10.1016/j.cej.2022.136905

Wang Q., Q., Li, S., Xu, C., Wang, X., Yang, T., Wang, C., et al. (2024). Glutaminolysis inhibition boosts photodynamic therapy to eliminate cancer stem cells. *Biomaterials* 306, 122497. doi:10.1016/j.biomaterials.2024.122497

Wang S., S., Liu, Y., Quan, C., Luan, S., Shi, H., and Wang, L. (2024). A metal-organic framework-integrated composite for piezocatalysis-assisted tumour therapy: design, related mechanisms, and recent advances. *Biomater. Sci.* 12 (4), 896–906. doi:10.1039/d3bm01944f

Witkowska, M., Golusińska-Kardach, E., Golusiński, W., and Florek, E. (2023). Polydopamine-based material and their potential in head and neck cancer therapy-current state of knowledge. *Int. J. Mol. Sci.* 24 (5), 4890. doi:10.3390/ijms24054890

Wu, F., Chen, H., Liu, R., Suo, Y., Li, Q., Zhang, Y., et al. (2022b). An active-passive strategy for enhanced synergistic photothermal-ferroptosis therapy in the NIR-I/II biowindows. *Biomater. Sci.* 10 (4), 1104–1112. doi:10.1039/d1bm01908b

Wu, G. L., Liu, F., Li, N., Fu, Q., Wang, C. K., Yang, S., et al. (2023). Trisulfide bond-mediated molecular phototheranostic platform for "Activatable" NIR-II imaging-guided enhanced gas/chemo-hypothermal photothermal therapy. *Adv. Sci. (Weinh)* 10 (36), e2304104. doi:10.1002/advs.202304104

Wu, H., Gu, D., Xia, S., Chen, F., You, C., and Sun, B. (2021). One-for-all intelligent core-shell nanoparticles for tumor-specific photothermal-chemodynamic synergistic therapy. *Biomater. Sci.* 9 (3), 1020–1033. doi:10.1039/d0bm01734e

Wu, H., Wei, M., Xu, Y., Li, Y., Zhai, X., Su, P., et al. (2022a). PDA-based drug delivery nanosystems: a potential approach for glioma treatment. *Int. J. Nanomedicine.* 17, 3751–3775. doi:10.2147/IJN.S378217

Wu, Q., Niu, M., Chen, X., Tan, L., Fu, C., Ren, X., et al. (2018). Biocompatible and biodegradable zeolitic imidazolate framework/polydopamine nanocarriers for dual stimulus triggered tumor thermo-chemotherapy. *Biomaterials* 162, 132–143. doi:10.1016/j.biomaterials.2018.02.022

Xiong, R., Zhu, X., Zhao, J., Ling, G., and Zhang, P. (2024). Nanozymes-mediated cascade reaction system for tumor-specific diagnosis and targeted therapy. *Small. Methods.* 13, e2301676. doi:10.1002/smtd.202301676

Xu, M., Chi, B., Han, Z., He, Y., Tian, F., Xu, Z., et al. (2020). Controllable synthesis of rare earth (Gd^{3+},Tm^{3+}) doped Prussian blue for multimode imaging guided synergistic treatment. *Dalton Trans.* 49 (35), 12327–12337. doi:10.1039/d0dt02152k

Yan, Z., Wu, X., Tan, W., Yan, J., Zhou, J., Chen, S., et al. (2024). Single-atom Cu nanozyme-loaded bone scaffolds for ferroptosis-synergized mild photothermal therapy in osteosarcoma treatment. *Adv.Healthc. Mat.* 29, e2304595. doi:10.1002/adhm.202304595

Yang, K., Dong, Y., Li, X., Wang, F., and Zhang, Y. (2023). Dual-targeted delivery of paclitaxel and indocyanine green with aptamer-modified ferritin for synergetic chemo-phototherapy. *Colloids. Surf. B. Biointerfaces.* 229, 113437. doi:10.1016/j.colsurfb.2023.113437

Yang, S., Li, D., Chen, L., Zhou, X., Fu, L., You, Y., et al. (2021). Coupling metal organic frameworks with molybdenum disulfide nanoflakes for targeted cancer theranostics. *Biomater. Sci.* 9 (9), 3306–3318. doi:10.1039/d0bm02012e

Yang, X., Sun, Y., Zhang, H., Liu, F., Chen, Q., Shen, Q., et al. (2024). CaCO3 nanoplatform for cancer treatment: drug delivery and combination therapy. *Nanoscale* 16 (14), 6876–6899. doi:10.1039/d3nr05986c

Yang, X., Wu, L., and Xu, S. (2025). An overview of GPX4-targeting TPDs for cancer therapy. *Bioorg. Med. Chem.* 118, 118046. doi:10.1016/j.bmc.2024.118046

Ye, L., Wen, X., Qin, J., Zhang, X., Wang, Y., Wang, Z., et al. (2024). Metabolism-regulated ferroptosis in cancer progression and therapy. *Cell. death. Dis.* 15 (3), 196. doi:10.1038/s41419-024-06584-y

Yin, X., Ran, S., Cheng, H., Zhang, M., Sun, W., Wan, Y., et al. (2022). Polydopamine-modified ZIF-8 nanoparticles as a drug carrier for combined chemo-photothermal osteosarcoma therapy. *Colloids. Surf. B. Biointerfaces.* 216, 112507. doi:10.1016/j.colsurfb.2022.112507

You, S. S., Lu, S., Gao, H. Q., Song, Q., and Li, L. (2024). Photothermal-enhanced multifunctional nanozyme for regulate GSH and H2O2 in tumor for improving catalytic therapy. *Phys. Scr.* 99, 025014. doi:10.1088/1402-4896/ad190b

Yu, H., Cheng, Y., Wen, C., Sun, Y. Q., and Yin, X. B. (2022). Triple cascade nanocatalyst with laser-activatable O2 supply and photothermal enhancement for effective catalytic therapy against hypoxic tumor. *Biomaterials* 280, 121308. doi:10.1016/j.biomaterials.2021.121308

Yu, L., Liu, Z., Xu, W., Jin, K., Liu, J., Zhu, X., et al. (2024). Towards overcoming obstacles of type II photodynamic therapy: endogenous production of light, photosensitizer, and oxygen. *Acta. Pharm. Sin. B* 14 (3), 1111–1131. doi:10.1016/j.apsb.2023.11.007

Yu, Q., Li, X., Wang, J., Guo, L., Huang, L., and Gao, W. (2024). Recent advances in reprogramming strategy of tumor microenvironment for rejuvenating photosensitizers-mediated photodynamic therapy. *Small* 20 (16), e2305708. doi:10.1002/smll.202305708

Zeng, F., Tang, L., Zhang, Q., Shi, C., Huang, Z., Nijiati, S., et al. (2022). Coordinating the mechanisms of action of ferroptosis and the photothermal effect for cancer theranostics. *Angew. Chem. Int. Ed. Engl.* 61 (13), e202112925. doi:10.1002/anie.202112925

Zhan, L., Yin, X., Zhang, Y., Ju, J., Wu, Y., Ding, L., et al. (2023). Polydopamine-guarded metal-organic frameworks as co-delivery systems for starvation-assisted chemo-photothermal therapy. *Biomater. Adv.* 146, 213306. doi:10.1016/j.bioadv.2023.213306

Zhang, C., Hu, X., Jin, L., Lin, L., Lin, H., Yang, Z., et al. (2023). Strategic design of conquering hypoxia in tumor for advanced photodynamic therapy. *Adv. Healthc. Mat.* 12 (24), e2300530. doi:10.1002/adhm.202300530

Zhang, H., and Yuan, W. (2024). Self-healable oxide sodium alginate/carboxymethyl chitosan nanocomposite hydrogel loading Cu2+-doped MOF for enhanced synergistic and precise cancer therapy. *Int. J. Biol. Macromol.* 262 (Pt 2), 129996. doi:10.1016/j.ijbiomac.2024.129996

Zhang, J., Yang, Y., Qin, F., Hu, T., Zhao, X., Zhao, S., et al. (2023). Catalyzing generation and stabilization of oxygen vacancies on CeO2-x nanorods by Pt nanoclusters as nanozymes for catalytic therapy. *Adv. Healthc. Mat.* 12 (31), e2302056. doi:10.1002/adhm.202302056

Zhang, L., Fan, Y., Yang, Z., Yang, M., and Wong, C. Y. (2021). NIR-II-driven and glutathione depletion-enhanced hypoxia-irrelevant free radical nanogenerator for combined cancer therapy. *J. Nanobiotechnology* 19 (1), 265. doi:10.1186/s12951-021-01003-2

Zhang, M., Wang, S., Bai, Y., Wang, D., Fu, Y., Su, Z., et al. (2024a). A dual-function hemicyaninematerial with highly efficient photothermal and photodynamic effect used for tumor therapy. *Adv. Healthc. Mat.* 13 (10), e2303432. doi:10.1002/adhm.202303432

Zhang, M., Yao, X., Xu, J., Song, J., Mai, S., Zhu, W., et al. (2024b). Biodegradable zwitterionic polymer-cloaked defective metal-organic frameworks for ferroptosis-inducing cancer therapy. *Int. J. Pharm.* 655, 124032. doi:10.1016/j.ijpharm.2024.124032

Zhang, S., Kong, N., Wang, Z., Zhang, Y., Ni, C., Li, L., et al. (2024). Nanochemistry of gold: from surface engineering to dental healthcare applications. *Chem. Soc. Rev.* 19, 3656–3686. doi:10.1039/d3cs00894k

Zhang, W., Chen, L., Zhang, X., Gong, P., Wang, X., Xu, Z., et al. (2023). Functionalized nanohybrids with rod shape for improved chemo-phototherapeutic effect against cancer by sequentially generating singlet oxygen and carbon dioxide bubbles. *Biomater. Sci.* 11 (20), 6894–6905. doi:10.1039/d3bm00541k

Zhang, X., Dou, Y., Liu, S., Chen, P., Wen, Y., Li, J., et al. (2024). Rationally designed benzobisthiadiazole-based covalent organic framework for high-performance NIR-II fluorescence imaging-guided photodynamic therapy. *Adv. Healthc. Mat.* 8, e2303842. doi:10.1002/adhm.202303842

Zhang, Y., Lin, L., Liu, L., Liu, F., Sheng, S., Tian, H., et al. (2019). Positive feedback nanoamplifier responded to tumor microenvironments for self-enhanced tumor imaging and therapy. *Biomaterials* 216, 119255. doi:10.1016/j.biomaterials.2019.119255

Zhao, H., Li, Y., Chen, J., Zhang, J., Yang, Q., Cui, J., et al. (2024). Environmental stimulus-responsive mesoporous silica nanoparticles as anticancer drug delivery platforms. *Colloids. Surf. B. Biointerfaces.* 234, 113758. doi:10.1016/j.colsurfb.2024.113758

Zhao, L., Tan, L., Wu, Q., Fu, C., Ren, X., Ren, J., et al. (2024). A two-stage exacerbated hypoxia nanoengineering strategy induced amplifying activation of tirapazamine for microwave hyperthermia-chemotherapy of breast cancer. *J. Colloid. Interface. Sci.* 659, 178–190. doi:10.1016/j.jcis.2023.12.149

Zhao, X., Wang, X., Zhang, W., Tian, T., Zhang, J., Wang, J., et al. (2024). A ferroptosis-inducing arsenene-iridium nanoplatform for synergistic immunotherapy in

pancreatic cancer. *Angew. Chem. Int. Ed. Engl.* 63 (15), e202400829. doi:10.1002/anie.202400829

Zheng, J., Peng, W., Shi, H., Zhang, J., Hu, Q., and Chen, J. (2025). Emerging engineered nanozymes: current status and future perspectives in cancer treatments. *Nanoscale. Adv.* 7 (5), 1226–1242. doi:10.1039/d4na00924j

Zhou, C., Yang, Q., Zhou, X., and Jia, N. (2022). PDA-coated CPT@MIL-53(Fe)-based theranostic nanoplatform for pH-responsive and MRI-guided chemotherapy. *J. Mat. Chem. B* 10 (11), 1821–1832. doi:10.1039/d1tb02339j

Zhou, L. L., Guan, Q., and Dong, Y. B. (2024). Covalent organic frameworks: opportunities for rational materials design in cancer therapy. *Angew. Chem. Int. Ed. Engl.* 63 (8), e202314763. doi:10.1002/anie.202314763

Zhou, Z., Wang, X., Zhang, H., Huang, H., Sun, L., Ma, L., et al. (2021). Activating layered metal oxide nanomaterials via structural engineering as biodegradable nanoagents for photothermal cancer therapy. *Small* 17 (12), e2007486. doi:10.1002/smll.202007486

Zhu, W., Chen, M., Liu, Y., Tian, Y., Song, Z., Song, G., et al. (2019). A dual factor activated metal-organic framework hybrid nanoplatform for photoacoustic imaging and synergetic photo-chemotherapy. *Nanoscale* 11 (43), 20630–20637. doi:10.1039/c9nr06349h

Zuo, Y. C., Huo, C. M., Chen, Y., Ding, P. L., Tong, S. Y., Xue, W., et al. (2024). Cancer-thylakoid hybrid membrane camouflaged thulium oxide Nanoparticles with oxygen self-supply capability for tumor-homing phototherapy. *Adv. Healthc. Mat.* 30, e2303779. doi:10.1002/adhm.202303779

frontiers | Frontiers in Bioengineering and Biotechnology

TYPE Original Research
PUBLISHED 04 April 2025
DOI 10.3389/fbioe.2025.1549101

OPEN ACCESS

EDITED BY
Donglin Xia,
Nantong University, China

REVIEWED BY
Chen Shen,
Hebei University of Science and Technology, China
Weiquan Xie,
Guilin Medical University, China

*CORRESPONDENCE
Yangbo Tan,
191575702@qq.com

RECEIVED 20 December 2024
ACCEPTED 19 March 2025
PUBLISHED 04 April 2025

CITATION
Bin L, Huang L, Chen A, Yang Y, Zheng Y, Zhang H, Zhang Q, Zheng J, Qiu M, Li X and Tan Y (2025) Inhibition of energy metabolism in macrophages to block MPS for enhancing the chemotherapy efficacy.
Front. Bioeng. Biotechnol. 13:1549101.
doi: 10.3389/fbioe.2025.1549101

Inhibition of energy metabolism in macrophages to block MPS for enhancing the chemotherapy efficacy

Li Bin[1,2], Linlin Huang[1], Aiyu Chen[1], Yinyi Yang[1], Yanmei Zheng[1], Hanwen Zhang[1], Qinfang Zhang[1], Jiahui Zheng[1], Meiting Qiu[1], Xiajin Li[1] and Yangbo Tan[1]*

[1]Department of Medical College, Guangxi University of Science and Technology, Liuzhou, China, [2]Laboratory animal Center, Liuzhou People's Hospital, Liuzhou, Guangxi, China

Various biological barriers hinder the effective use of administered nanoparticles, with the mononuclear phagocyte system (MPS) being a major obstacle to their *in vivo* efficacy. Glucose metabolism is an important factor for macrophages to perform MPS clearance *in vivo*. In this study, energy metabolism-blocking nanoparticles PEG-S-S-PLA@RGD @Dox@BAY876 (RPDB NPs) were developed to change drug distribution in the body, improving the efficacy of chemotherapy. First, BAY876 showed an excellent inhibition effects on macrophage energy metabolism *in vitro*. This inhibitory behavior of energy metabolism reduced the aggregation of nanoparticles in macrophages. Similarly, the migration capacity of macrophages was also limited by reduced energy metabolism. Second, the fluorescence distribution in the mice also showed that the fluorescence intensity of RPDB NPs in the liver was about 40% of that of RPD NPs, suggesting that reducing energy metabolism helps to downregulate the uptake of mononuclear phagocytic cell (MPS), and change the distribution of the drug *in vivo*. Furthermore, anti-tumor effects of RPDB NPs were evaluated both *in vivo* and *in vitro*. *In vivo*, RPDB nanomicelles inhibited breast cancer by up to 68.3%, higher than other administration groups. Moreover, the pathological section of tumor exhibited a significantly greater increase in cell apoptosis in RPDB NPs group. Hence, inhibition of macrophage energy metabolism is a promising approach to eliminate MPS effects, while also opening up a new window for the effective inhibition of tumors development and metastasis.

KEYWORDS

glucose transporter 1, energy metabolism, MPS, metastasis, chemotherapy

1 Introduction

Nanomedicine has emerged as a promising field in biomedicine over the past few decades, owing to the exceptional pharmacokinetics and high-contrast imaging capabilities of nanotherapeutics and diagnostic agents (Wang et al., 2011; Li and Lane, 2019). However, only 0.7% injected doses of nanoparticles (NPs) can reach solid tumors, which limits the therapeutic effect (Poon et al., 2020). The delivery inefficiency arises from the mononuclear phagocyte system (also called the reticuloendothelial system, RES), which was capable of rapidly recognizing and engulfing exogenous nanoparticles (Liu et al., 2017; Yang et al.,

2016; Wan et al., 2020). Under the influence of MPS, nanoparticles tend to accumulate in normal tissues, particularly in the liver, which may lead to potential adverse effects (Mirkasymov et al., 2021). Therefore, efficient strategies for regulating the mononuclear phagocyte system (MPS) are highly promising for improving tumor accumulation (Mirkasymov et al., 2022).

Numerous strategies have been devised and implemented to alleviate the influence of MPS (Mirkasymov et al., 2022). Obstructing the recognition of macrophages and nanoparticles can be achieved through various methods, such as reducing the immunogenicity of nanoparticles by modifying their surface with polymers or camouflaging them with biomimetic materials and "do not eat me" signal molecules to evade detection by macrophages (Yang et al., 2022; Wang et al., 2019; Belhadj et al., 2020). Blocking macrophages through saturation is a promising tactic that endows nanoparticles with several benefits, including an extended duration of blood circulation (Ngo et al., 2022; Li et al., 2023; Cheng et al., 2021; Ouyang et al., 2020). For instance, a considerable quantity of nanoparticles was phagocytosed by macrophages *in vivo*, surpassing the RES threshold and penetrating the immune barrier, thereby prolonging the circulation time of blood and facilitating accumulation in tumors (Ouyang et al., 2020). Furthermore, the blocking efficiency of RES showed a positive correlation with the administered dosage, and macrophage saturation occurred within 1.5 h following the injection of one trillion nanoparticles (Ouyang et al., 2020). However, the burden of eliminating nanoparticles in normal tissues was significantly increased at high dosages of administration, potentially leading to inflammation in the aggregation area.

The strategy of eliminating macrophages to obstruct the mononuclear phagocyte system (MPS) has attracted significant attention. These agents were taken up by MPS, resulting in macrophage blockade followed by an extension of the circulation time of nanoparticles *in vivo*. This is primarily attributed to the impairment of MPS-mediated immune clearance of exogenous substances, particularly the Kupffer cells in the liver which constitute a pivotal component of MPS (Tavares et al., 2017). The drug-induced blockage phenomenon *in vivo* is transient, and hepatic macrophages typically recover promptly (Hao et al., 2018). For instance, the administration of dextran sulfate 500, a polysaccharide compound, at a dosage of 50 mg/kg significantly reduced the level of liposomes in the liver and disappeared within 48 h (Patel et al., 1983). The clodronate was encapsulated in nanoparticles to achieve macrophage depletion, resulting in a remarkable 80% increase in the rate of tumor inhibition (Hao et al., 2018). In addition, liposomal encapsulation of methylpalmitate and gadolinium chloride demonstrated significant macrophage clearance effects by regulating the ATP levels, respectively, similar to clodronate (Yamada et al., 2003). Thus, the main metabolic process of numerous MPS blockers like clodronate used frequently for macrophage scavenging is their conversion through hydrolysis into an analog that hinders ATP synthesis. However, the complete elimination of macrophages will affect the body's immune function and even cause damage to the body.

Similarly, regulating glucose uptake to inhibit the energy metabolism of macrophages and reduce ATP production has become a feasible strategy for the drug development (Curi et al., 2017; Sakamoto et al., 2011; Jacobs et al., 2008). Glucose plays a crucial role in maintaining cellular activity and promoting nanoparticles phagocytosis by cells (Zhao et al., 2011; Bonamy et al., 2023; Venturelli et al., 2016). Glucose transporters, which are responsible for glucose uptake into cells, exhibit high levels of expression in macrophages, particularly in M2-like tumor-associated macrophages (Shi et al., 2022). Considering the propensity of nanoparticles to accumulate in the liver, with macrophages influencing up to 70% of them, it was hypothesized that the energy metabolism in macrophages may play a pivotal role in particle up-taken (Venturelli et al., 2016; Shi et al., 2022). As a proof of concept, the inhibition of glucose transporters 1 (GLUT1) protein in macrophages by a GLUT1 inhibitor was employed to curtail tricarboxylic acid cycle (TCA cycle) energy metabolism. Subsequently, MPS blockade was implemented to enhance nanoparticles aggregation within tumors. According to previous reports, BAY876, a GLUTs family inhibitor with a particular affinity for GLUT1, has demonstrated remarkable antitumor efficacy by reducing glucose levels and limiting glycolysis (Zhao et al., 2011; Chen et al., 2023).

Herein, tailor-made self-assembled nano-micelles of PEG-SS-PLA polymers containing disulfide bonds were used to improve the distribution of nanoparticles *in vivo* by interfering with the energy metabolism of macrophages in the liver. In addition, RGD peptides were introduced to prevent off-target phenomena and facilitate the investigation of drug distribution *in vivo*. Under the influence of MPS, the nanomicelles were internalized by liver macrophages and subsequently released BAY876 in lysosomes to inhibit GLUTs and ATP production. This macrophage blockade strategies reduced the persistent accumulation of nanomicelles in the liver. Therefore, this system effectively prolonged blood circulation time and enhanced the tumor accumulation of nanoparticles. Meanwhile, the utilization of nano-micelles integrated with macrophage elimination and chemotherapy strategy further enhanced the anti-tumor efficacy.

2 Materials and methods

2.1 Materials

All reagents without further purification were acquired from commercial corporations in this study. The paraformaldehyde (4%), phosphate buffer (PBS, pH7.4), doxorubicin (Dox), thiazolyl blue (MTT), and dimethyl sulfoxide (DMSO) were bought from Servicebio (Wuhan, China). The BAY-876 was obtained from MCE China (Shanghai). The Cy5.5-COOH was purchased from Aladdin (Shanghai, China). The RPMI-1640 complete medium and fetal serum (FBS) was purchased from KeyGen Biotech Co., Ltd. (Nanjing, China). Hoechst 33342, the nucleus-specific dye utilized in this study, was procured from Beyotime Biotechnology Ltd. (Shanghai, China). In addition, the GSH assay kit and Glucose assay kit and ATP assay kit were also acquired from Beyotime Biotechnology Ltd. (Shanghai, China). The mouse-derived 4T1 cancer cell was obtained from the Shanghai Institute of Cells (Shanghai, China). The polymer PEG2k-S-S-PLA2k (Polyethylene glycol-S-S-polylactic acid) was obtained from Chongqing Yusi Biotech Co. Ltd. (Chongqing, China). The SPF female mice (Balb/c, 5 weeks old) were purchased from SPF Biotechnology Co., Ltd. (Beijing, China) and maintained in a pathogen-free environment. The experiments protocols were reviewed and

approved by Institutional Animal Care and Use Committee of Liuzhou People`s Hospital (Liuzhou, China, IACUC No. Approved:LRYIACUC2023001). All experiments were performed with deionized water (Persee, 18.2 MΩ cm^{-1}).

2.2 Preparation of nano-micelle complexes

As previously described, a solution containing EDC and NHS was used to activate the carboxyl group of the target peptide (RGD) under pH5.8 for 30 min (molar ratio 1.2:1.2:1). Then, the NH2-PEG2k-PLA2k were added and incubated for 12 h. After that, the RGD-modified polymer (RP) were collected by centrifugation at 15000 RPM for 15 min. Similarly, Cy5.5-COOH reacted with EDC and NHS for 30 min under dark before adding RP. After 12 h, Cy5.5-labeled RP was centrifuged, purified, and stored at 4°C. Last, the nano-micelle complexes were prepared using the oil-in-water emulsion solvent diffusion method. To prepare the solution, 2.8 mg of Dox, 3.2 mg of BAY876, and 20.1 mg of the RGD-modified polymer (RP) were dissolved in 10 mL of chloroform. Removed the organic solvent by rotary evaporation in a 50°C water bath and collected the nano-micelle complexes (RPDB NPs) in an equal volume of PBS phosphate buffer solution. Encapsulation percentage=(1-The amount of free drug/The total amount of drug)*100%.

2.3 Characterization

To observe the morphology of RPDB NPs, a transmission electron microscope (HC-1, Hitachi, Japan) was used. The particle size and polydispersity were effectively determined by the dynamic light scattering (DLS) technique, which utilized Malvern Instruments. Then, the UV-2600 UV-vis spectrophotometer (Shimadzu, Japan) was successfully used for detecting absorbance and concentration. To study the release behavior of RPDB NPs in tumors, these particles were suspended in 1 mL of PBS with GSH (4 mM). In addition, the release behavior under pH 5.0 was further examined. Finally, the stability of nanoparticles in fetal bovine serum was monitored by DLS for 20 days under 37°C.

2.4 Evaluation of glucose uptake in macrophages

Macrophage RAW264.7 inoculated with 10% (v/v) FBS and DMEM incomplete medium under a humidified atmosphere (37°C) with 5% CO_2. When the density of macrophage cells reached 80%, the culture medium was discarded, and the dishes were washed three times with PBS phosphate buffer. The cells were digested by trypsin-EDTA and subsequently collected in a sterile centrifuge tube. After centrifugation, the macrophage cells were subcultured in a 6-well plate with 8×10^4 cells per well. Then, the cells were grouped as follows: RPD (50 μg mL^{-1}, according to the Dox concentration + LG (low glucose medium) group, RPD (50 μg mL^{-1}, according to the Dox concentration + HG (high glucose medium) group, RPDB(50 μg mL^{-1}, according to the Dox concentration + HG (high glucose medium) group and PBS group. The PBS group was incubated with high glucose (HG) DMEM. 24 h later, the dye was marked under fluorescence microscopy with different excitation wavelength (Hoechst 33342:350 nm, Dox: 488 nm).

2.5 Cytotoxicity assay

To evaluate cytotoxicity *in vitro*, 4T1 cells (5×10^3 cells per well) were inoculated into each well of a 96-well plate. After 12 h, the cells were grouped as follows: P, Dox (50 μg mL^{-1}), RPD (50 μg mL^{-1}, according to the Dox concentration + LG (low glucose medium) group, RPD (50 μg mL^{-1}, according to the Dox concentration + HG (high glucose medium) group, RPDB (50 μg mL^{-1}, according to the Dox concentration + HG (high glucose medium) group and PBS group. The PBS group was incubated with high glucose (HG) DMEM. Following a 24-h co-culture of nano-micelle complexes with cells, the living cell count was determined using MTT reagent. Then, the medium in each well was discarded, and 150 μL dimethyl sulfoxide (DMSO) was used to dissolve the crystals. Finally, the absorbance of each well at 490 nm was measured by the continuous wavelength multifunctional microplate reader (Victor Nivo 3S, United States). The cell viability (%) of nano-micelle complexes was calculated using the following method: OD treatment/OD control × 100%.

2.6 Glucose and ATP levels *in vitro*

To verify the effect of the GLUT1 inhibitor (BAY876), the cellular glucose uptake and ATP level was measured *in vitro*. Briefly, macrophage RAW264.7 and 4T1 cells were pre-cultured in 6-well plates (8×10^4 cells per well, 2 mL medium), respectively. Overnight, these cells were grouped and treated with the following samples: RPD (50 μg mL^{-1}, according to the Dox concentration + LG (low glucose medium) group, RPD (50 μg mL^{-1}, according to the Dox concentration + HG (high glucose medium) group, RPDB(50 μg mL^{-1}, according to the Dox concentration + HG (high glucose medium) group and PBS group. The PBS group was incubated with high glucose (HG) DMEM. After 24 h, all cells were treated with lysis buffer (containing Triton-X-100) and broken using ultrasonic (150 W, 30 s). After cracking, centrifuged at 4°C (12,000 g) for 5 min and collected supernatant. (1) ATP level: Added 100 μL of ATP test fluid to the plate. After 3 min at room temperature, added 20 μL of sample to each well, and tested with a multifunctional microplate reader. (2) The glucose level:Taken 5 μL sample to PCR tube and added 185 μL glucose assay reagent to make the final volume 190 μL. Placed on a PCR apparatus and heated at 95°C for 8 min, then cooled down to 4°C. Then 180 μL of liquid was sucked into the 96-well plate and absorbance was measured at 630 nm. The glucose concentration and ATP levels in the sample was calculated from the standard curve, respectively.

2.7 Detection of GSH level *in vitro*

4T1 cells were incubated with RPMI-1640 medium (including 10% (v/v) serum (FBS), 100 U/mL penicillin, and 100 μg/mL streptomycin). After overnight incubate, the samples were treated

with cells in the following order: RPD (50 μg mL^{-1}, according to the Dox concentration + LG (low glucose medium) group, RPD (50 μg mL^{-1}, according to the Dox concentration + HG (high glucose medium) group, RPDB(50 μg mL^{-1}, according to the Dox concentration + HG (high glucose medium) group and PBS group. The PBS group was incubated with high glucose (HG) DMEM. Then, the procedure was performed as described above. The GSH level was measured using an assay kit and the absorbance of GSH was recorded with a microplate reader.

2.8 Scratch assay *in vitro*

To assess the impact of a GLUT1 inhibitor on macrophage cell migration, an *in vitro* scratch assay was employed as a direct and cost-effective method. As previously described, RAW264.7 macrophage cells were seeded in a 6-well plate with DMEM (high glucose) containing 10% FBS for 12 h. Then, monolayer cells in a 6-well plate were scratched with a sterile pipette and washed with phosphate buffer to remove cell debris. After being cleaned, the samples were treated with macrophage cells for 24 h. These wounds were imaged using an inverted microscope, and the healing of wounds was evaluated by software ImageJ. The migration rate = (scratch width at 0 h - scratch width at 48 h)/scratch width at 0 h *100%

2.9 Tumor-bearing mice models

All healthy mice were purchased and housed for a week. Then, the 4T1 cells (5×10^6 cells/mouse, 100 μL) were injected into the right forelimb of each mouse to establish a solid tumor model. Thereafter, the mouse tumor volume was observed and measured every day using the formula length × $width^2$ × 0.5 to assess tumor volume.

2.10 *In vivo* distribution of nano-micelle complexes

To investigate the *in vivo* distribution of nano-micelle complexes, Cy5.5-labeled RPDB NPs and RPD NPs (100 μL, 2 mg/mL in PBS phosphate buffer) were tracked in tumor-bearing mice using IVIS Spectrum (Perkin Elmer, America). The excitation and emission wavelengths of Cy5.5 are 673 nm and 707 nm, respectively. These mice were then euthanized, the fluorescence intensity of their tumors was measured at various time points for 24 h, and the images were analyzed with ImageJ.

2.11 *In vivo* antitumor efficacy

After 5 days, when the tumor volume of mice ($n \geq 5$) reached approximately 100 mm^3, intravenous injections of PBS, Dox, RPD NPs, PDB NPs, and RPDB NPs were administered at a dose of 100 μL per mouse with a concentration of 5 mg/kg based on Dox concentration to the mice bearing the 4T1 tumors. Take an injection every 2 days. The body weight and tumor volume were measured and calculated to evaluate antitumor efficacy. After 13 days, the mice were humanely sacrificed, and their primary tumors, major organs, and blood samples were collected for further analysis.

2.12 Tumor metastasis model

In this anti-tumor metastasis, the mice were divided into the following groups: P1group (Each mouse was injected with 5×10^6 live cells), P2 group (Each mouse was injected with 5×10^6 dead cells), P3 (Each mouse was injected with 5×10^6 dead cells and 5×10^6 live cells), RPD NPs group (Each mouse was injected with 5×10^6 dead cells and 5×10^6 live cells) and RPDB NPs group (Each mouse was injected with 5×10^6 dead cells and 5×10^6 live cells). Then, 4T1 breast cancer cells were cultured and injected into mice tail vein for construct tumor metastasis model. RPD NPs was subsequently injected into RPD NPs group, RPDB NPs was subsequently injected into RPDB NPs group. After 14 days, the lung of mice were dissected to observe tumor metastasis.

2.13 Histopathology and routine blood analysis

In order to further investigate the effect and biosafety of nano-micelle complexes, major organs, and tumors were fixed in 4% paraformaldehyde at 4°C for 12 h. These slices were then prepared, including dehydration, embedding, and slicing, followed by dewaxing. Immediately, H&E staining and immunohistochemical analysis were performed, and all sections were observed under an inverted microscope. The blood samples of mice were collected for routine hematological analysis.

2.14 Statistical analysis

All data analyses were conducted using a T-test, and the results are presented as means ± standard deviation ($n \geq 3$, $^*p < 0.05$, $^{**}p < 0.01$ indicating significant differences).

3 Results and discussion

3.1 Characterization of nano-micelles

The clinical application of nanomedicine is hindered by various biological obstacles, particularly the mononuclear phagocyte system (MPS), which leads to particle accumulation in macrophages such as Kupffer cells and reduces anti-tumor efficacy. Therefore, various anti-tumor strategies targeting the MPS system, especially liver macrophages, have been proposed, such as utilizing low immunogenic vectors to avoid the accelerated blood clearance (ABC) effect, saturating macrophage, and even eliminating macrophage (Figure 1).

To further investigate the fundamental understanding of how glucose metabolism regulation affects the mononuclear phagocyte system (MPS) for enhancing tumor outcomes, nano-micelles were prepared in accordance with established protocols. In this study,

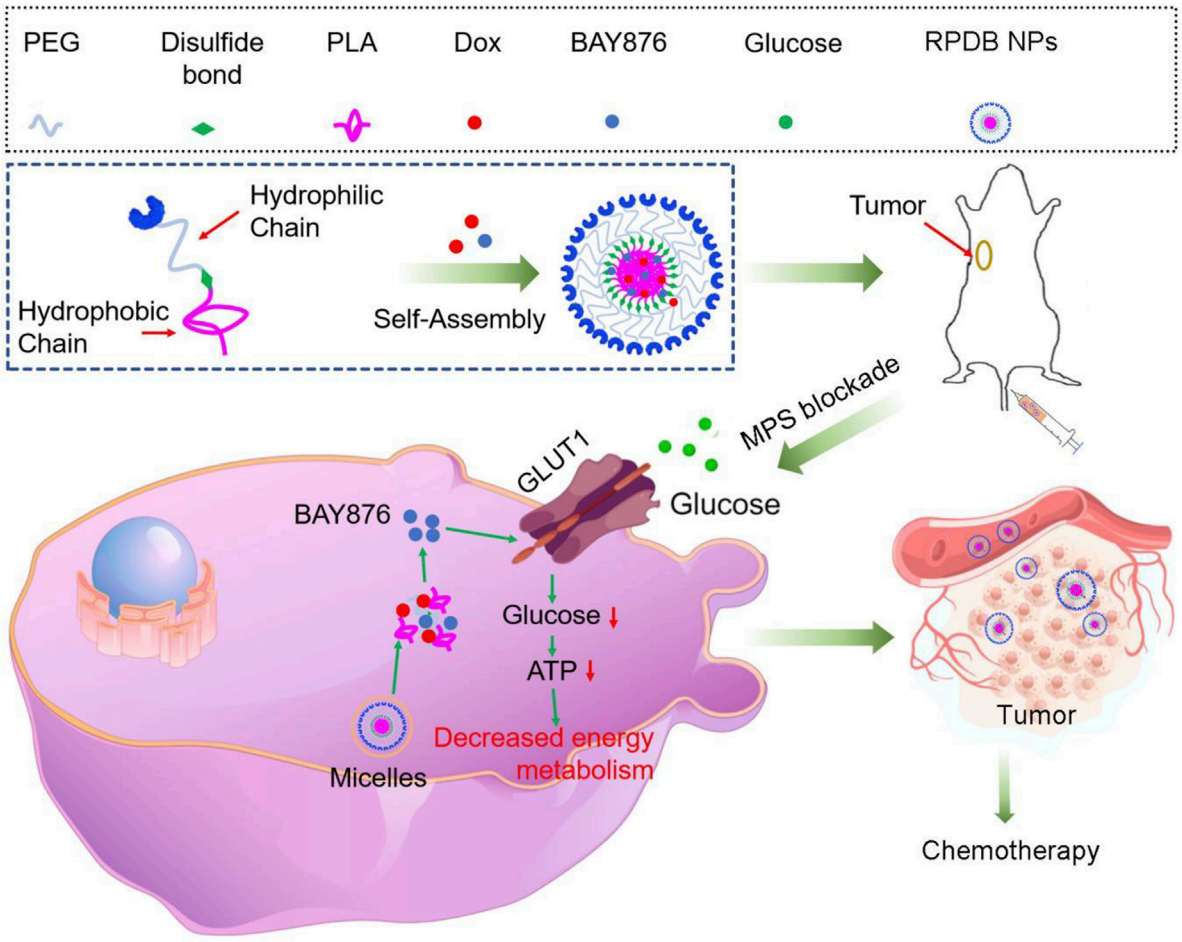

FIGURE 1
Schematics demonstrate the RPDB NPs blocking MPS for enhancing the antitumor efficacy. The intravenously injected nanoparticles were swallowed by macrophages, which release the GLUT1 inhibitor BAY876, reducing glucose entry into the cells. The phagocytic capacity of low-energy macrophages was downregulated, reducing the non-targeted effects and promoting drug aggregation in tumors.

drugs (Dox and BAY876 in chloroform) were encapsulated in PEG-PLA-based nano-micelles using the oil-in-water method. Subsequently, the nano-micelles were subjected to rigorous testing of their physical and chemical properties in order to ensure optimal drug loading efficacy. In Figure 2A, these nano-micelles were observed to have a spherical shape using transmission electron microscopy (TEM). The diameter distribution of the nano-micelles exhibited normality, with a mean value of approximately 61.6 ± 14.7 nm (Figure 2B). To further investigate size of nano-micelles, dynamic light scattering was utilized to characterize their mean hydrodynamic diameter (105.7 ± 15.7 nm, as illustrated in Figure 2C), which was consistent with the above data. For the formulation of nano-micelle complexes, the UV-vis spectrum analysis revealed that Dox and BAY876 exhibited strong absorption peaks at 480 nm and 320 nm, respectively (Figure 2D). After the synthesis of nano-micelles, the absorbance of these produces at 480 nm and 320 nm was detected, as shown in Figure2E. The encapsulation rate of Dox was 82.53% in RPD NPs and 55.12% in RPDB NPs. Similarly, the encapsulation rate of BAY876 was also evaluated to be 51.87% in RPDB NPs. Additionally, the biological efficacy of nano-micelles as an antitumor agent is hindered by their instability in blood. Therefore, we simulated the blood environment by incubating the sample in fetal bovine serum (FBS) at 37°C for a duration of 20 days. The hydrodynamic diameter mean did not exhibit significant alterations in Figure 2F when compared to Figure 2C. As previously reported, glutathione (GSH) can reduce disulfide bonds in tumor cells to form sulfhydryl groups, which not only depletes GSH but also facilitates drug release from PEG-S-S-PLA nano-micelles. Therefore, nano-micelles containing disulfide bonds were immersed in a 4 mM glutathione solution for varying durations to evaluate drug release. Compared to the absence of glutathione, it was observed that the release rate was significantly accelerated, with Dox and BAY876 releasing up to 45.3% and 47.1%, respectively, within 15 h (as depicted in Figures 2G, H). Considering the phagocytosis of macrophages, the release behavior of BAY876 was further explored under acidic conditions. As depicted in Figure 2I, the release of BAY876 from nano-micelles reached up to 35.7% within a time frame of 15 h, providing evidence for the potential inhibition of glucose transports in macrophages.

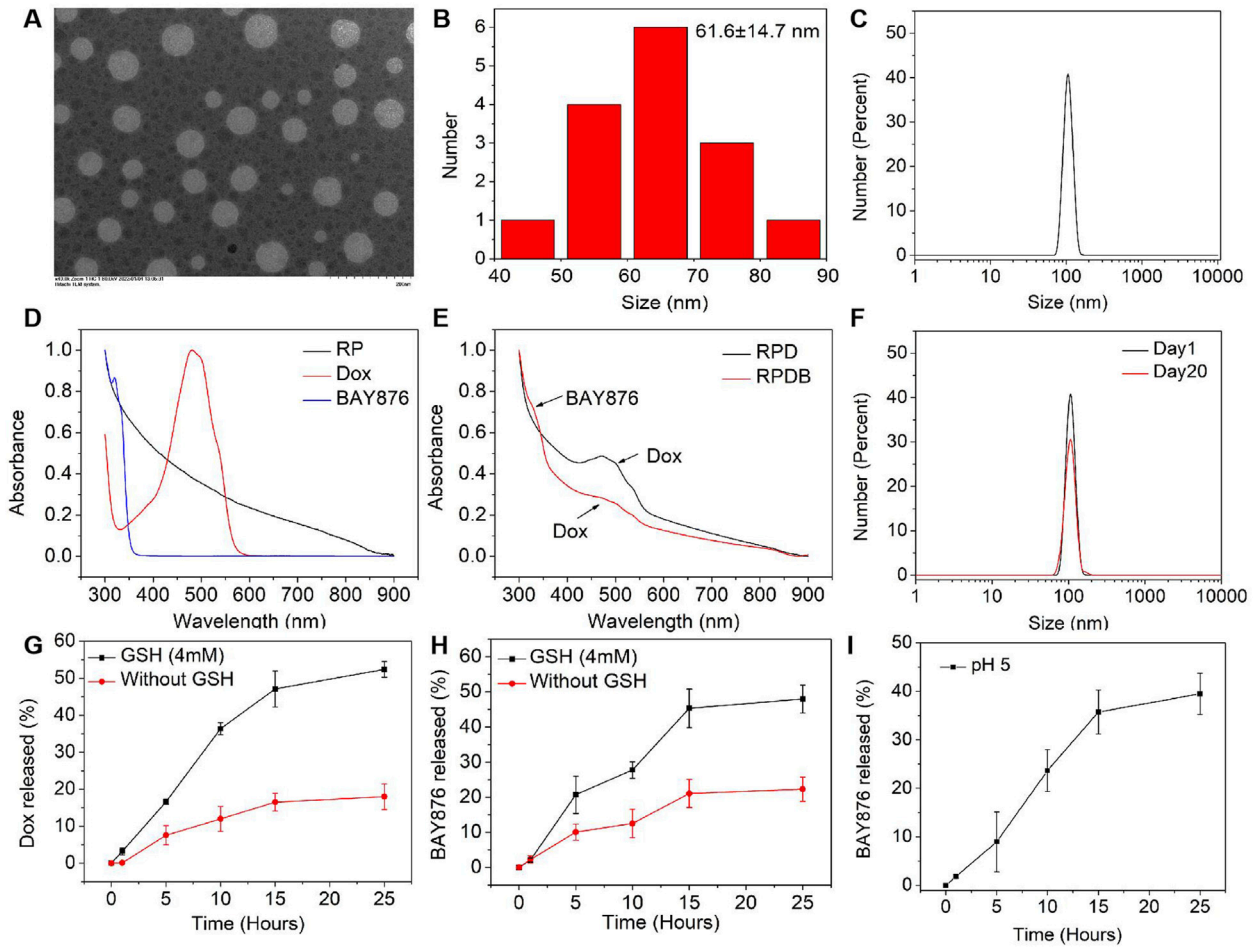

FIGURE 2
Characterization of RP-based nanoparticles. **(A)** TEM images of the RPDB NPs. **(B)** The size distribution of the RPDB NPs; **(C)** The mean hydrodynamic diameter distribution of RPDB NPs (105.7 ± 15.7 nm); **(D)** UV-vis spectra of BAY876, Dox and RP NPs; **(E)** UV-vis spectra of RPD NPs and RPDB NPs; **(F)** The stability of RPDB NPs was assessed by the mean hydrodynamic diameter distribution with FBS for 20 days. **(G)** The Dox release with and without GSH. **(H)** The BAY876 release with and without GSH. **(I)** The BAY876 release under different pH condition.

3.2 Inhibition of energy metabolism in macrophages

According to prior research, only 0.7% of ID nanoparticles were found to accumulate in tumors, primarily due to macrophage phagocytosis. Therefore, the regulation of macrophages has emerged as a promising strategy for cancer therapy and is receiving increasing attention. As a proof of concept, properties of constructing nano-micelles based on the energy metabolism of macrophages were verified here *in vitro*. As depicted in Figure 3A, macrophage RAW264.7 cells cultured in high glucose medium exhibited stronger fluorescence intensity compared to those cultured in low glucose medium, indicating the regulatory effect of glucose on macrophage endocytosis. However, incubation with the GLUT1 inhibitor BAY876 resulted in weaker fluorescence intensity of macrophages under high glucose conditions, indicating that the inhibitor reduced glucose uptake and subsequently minimized nanoparticle endocytosis. To further demonstrate this point, the glucose levels in macrophages from each group were assessed. The results indicated that the glucose level in group RPDB under high glucose conditions was significantly lower than that of group RPD, approaching levels observed in cells cultured with low glucose medium (as depicted in Figure 3B). Similarly, under high glucose conditions, group RPDB displayed lower ATP levels compared to group RPD, which is consistent with the glucose level trend (as shown in Figures 3B, C). At low glucose concentration, the cell survival rate was lower than that of group Dox. Similarly, under the same glucose concentration, the group RPDB with GULT1 inhibitor (BAY876) had lower vitality than that without GULT1 inhibitor, indicating that energy metabolism had an inhibitory effect on the viability of macrophages (as shown in Figure 3D). The decrease of glucose consumption leads to the slowing of aerobic respiration process and the increase of intracellular oxygen partial pressure, which may affect macrophage polarization and ROS production. Together with the aforementioned results, it was indicated that the effect of MPS was regulated by glucose metabolism for enhancing tumor outcomes.

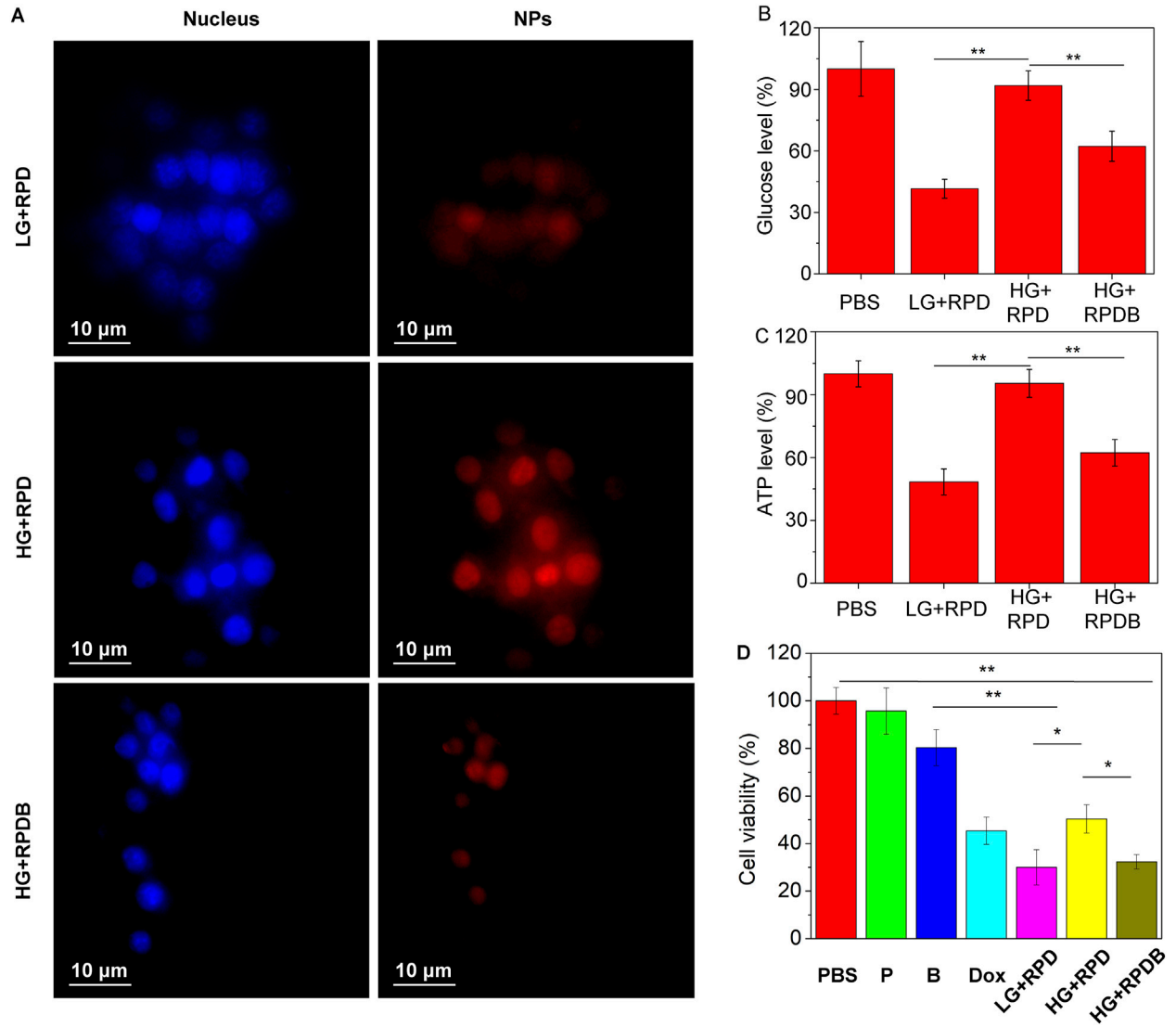

FIGURE 3
Evaluate the impact on energy metabolism inhibition in macrophages RAW264.7 cells. **(A)** Phagocytosis of nanoparticles by macrophages with different glucose concentrations. **(B)** The ratio of the glucose levels in nano-micelle-treated macrophages to those in the PBS group (n = 3, *p < 0.05, **p < 0.01). **(C)** The ratio of ATP levels between macrophages treated with nano-micelles and the PBS group (n = 3, *p < 0.05, **p < 0.01). The PBS group was incubated with high glucose (HG) DMEM. **(D)** The MTT assay was conducted for RAW264.7 cells viability, indicative of cytotoxicity. The PBS group was incubated with high glucose (HG) DMEM. The group LG + RPD represents the phagocytosis of RPD nanoparticles by macrophages under low glucose (LG) DMEM medium. Group HG + RPD represents the phagocytosis of RPD nanoparticles by macrophages under high glucose (HG) DMEM medium. Group HG + RPDB represents the phagocytosis of RPDB nanoparticles by macrophages under high glucose (HG) DMEM medium. Group P represents the addition of polymers alone; Group B represents the addition of BAY867 alone. (n = 3, *p < 0.05, **p < 0.01).

3.3 *In vitro* antitumor evaluation

Minimizing macrophage phagocytosis of inhibitor-loaded nano-micelles could reduce the MPS effect and prolong circulation time of blood for tumor therapy. Subsequently, the cytotoxicity of particles on tumor cells was evaluated *in vitro*, as displayed in Supplementary Figure S1A. The polymers demonstrated biocompatibility with 4T1 cells (as shown in Supplementary Figure S1A). Surprisingly, Dox-loaded polymers exhibited potent cytotoxicity surpassing that of injected Dox alone and BAY876. After 24 h of treatment, PDB NPs and RPDB NPs exhibited higher inhibition rates than other groups, indicating the GLUT1 inhibitor BAY876 blocked the glucose transport pathway. Among them, the RPDB NPs showed the higher inhibitory efficiency, which could be attributed to the expression of integrin on the cell membrane of 4T1. In Supplementary Figure S1B, cells were co-incubated with PDB NPs and RPDB NPs respectively, followed by staining with Hoechst33342. The fluorescent signal of RGD-modified nanoparticles was found to be stronger than that of PDB NPs, indicating the occurrence of RGD-mediated endocytosis process. This process facilitated the accumulation of nano-micelles in tumors, leading to glutathione (GSH) elimination and inhibition of energy metabolism. The downregulation of GSH levels in the polymer-treated groups, as demonstrated in Supplementary Figure S1C, was likely attributed to the presence of disulfide bonds within

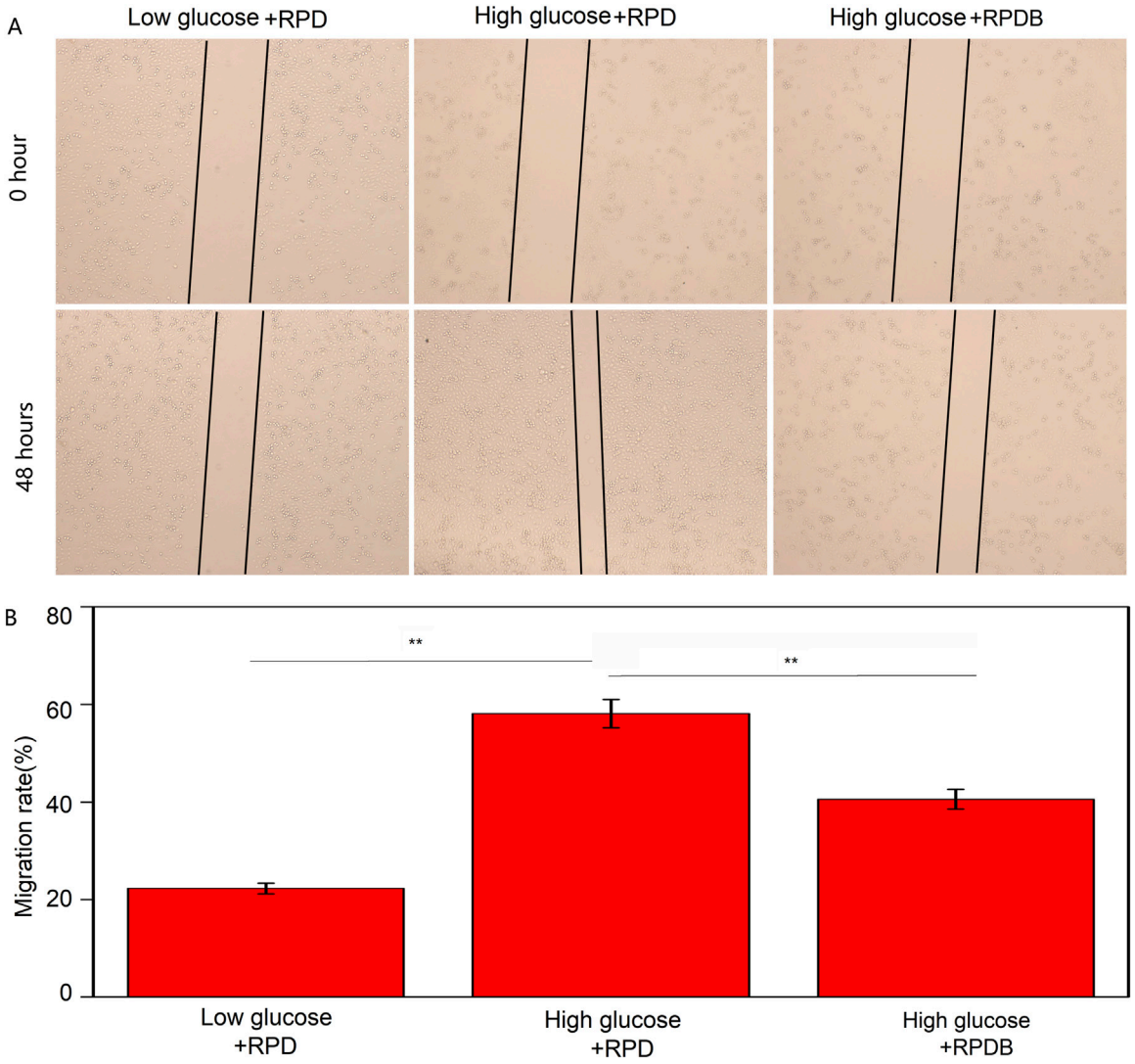

FIGURE 4
The migratory behavior was assessed by the scratch assay. **(A)** The impact of nano-micelle treatment on the migratory behavior of RAW264.7 cells was assessed within 0 and 48 h. **(B)** The migration rate was determined by administrating various nano-micelles.

the polymer. Previous reports have shown that the levels of GSH in tumors are overexpressed than that in normal cells, and a decrease in GSH levels can enhance ferroptosis within tumors by blocking the synthesis of the lipid repair enzyme glutathione peroxidase 4 (GPX4) (Xiao et al., 2011; Yang et al., 2014). Similarly, BAY876, a GLUT1 inhibitor, possesses excellent properties for regulating glucose uptake. Since glucose is the fundamental source for cell metabolism, tumor cells rely on the Warburg effect and thus consume large amounts of it. When PDB NPs and RPDB NPs were introduced, inhibitor BAY876 was released to block the GLUT1, thereby reducing glucose levels in cell. Therefore, the PDB NPs and RPDB NPs groups exhibited a significant decrease in glucose levels compared to the PBS and RPD NPs groups, as illustrated in Supplementary Figure S1D. Meanwhile, both PDB NPs and RPDB NPs demonstrated lower ATP levels than the other groups in Supplementary Figure S1E, which is consistent with the observations presented in Supplementary Figure S1D. Supplementary Figure S1F shows that RPDB has an inhibition effect on RAW264.7 cells, but there is no significant difference from group Dox; Group BAY876 showed the same toxicity as group P, basically had no effect on cells. In addition, the scratch assay was conducted to further assess the correlation between glucose and macrophage migration. As shown in Figures 4A, B, the migration rate of the RPDB group in low glucose medium was slower, similar to that of the RPD group in low glucose medium, compared to the RPD group in high glucose medium.

3.4 Distribution of nanoparticles *in vivo*

As previously reported, the majority of delivery systems encounter biological barriers that result in drug accumulation within the liver, particularly in macrophages, leading to a reduction in drug concentration at tumor sites. To monitor the *in vivo* distribution of nano-micelles, RPDB NPs were modified with Cy5.5 fluorescent dye. Fluorescence signals were detected in the

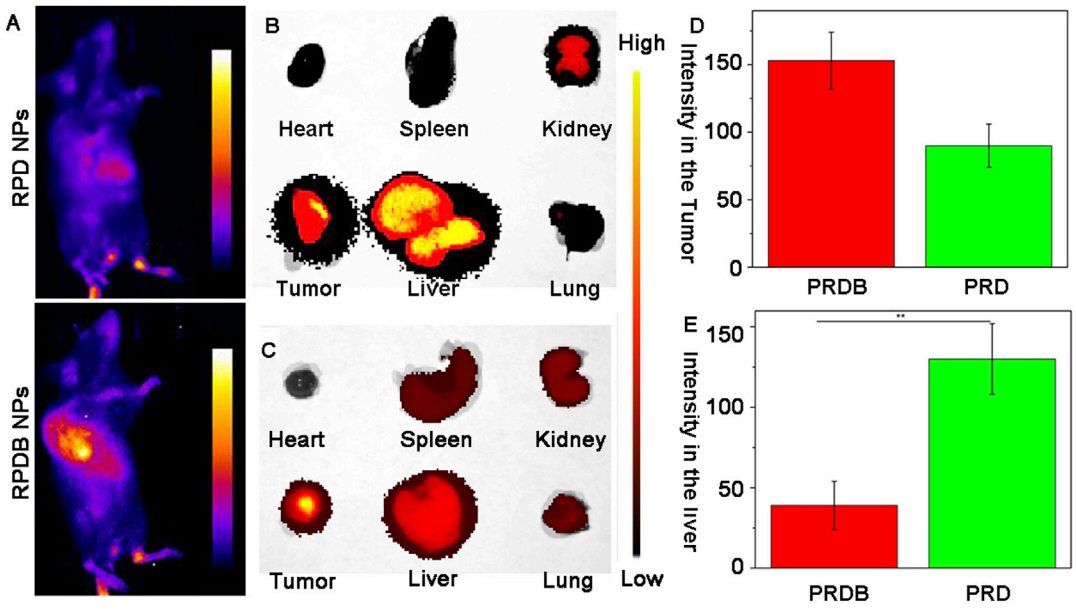

FIGURE 5
To assess the spatial distribution of fluorescently labeled nano-micelles in mice. **(A)** The fluorescence imaging of mice following intravenous injection *in vivo*. Blue indicates low fluorescence and yellow indicates high fluorescence; **(B)** The fluorescence images of major organs in group RPD NPs were collected; **(C)** The fluorescence images of major organs in group RPDB NPs were collected; **(D)** The fluorescence intensity of the tumor in mouse was semi-quantified using ImageJ software; **(E)** The fluorescence intensity of the liver in mouse was semi-quantified using ImageJ software.

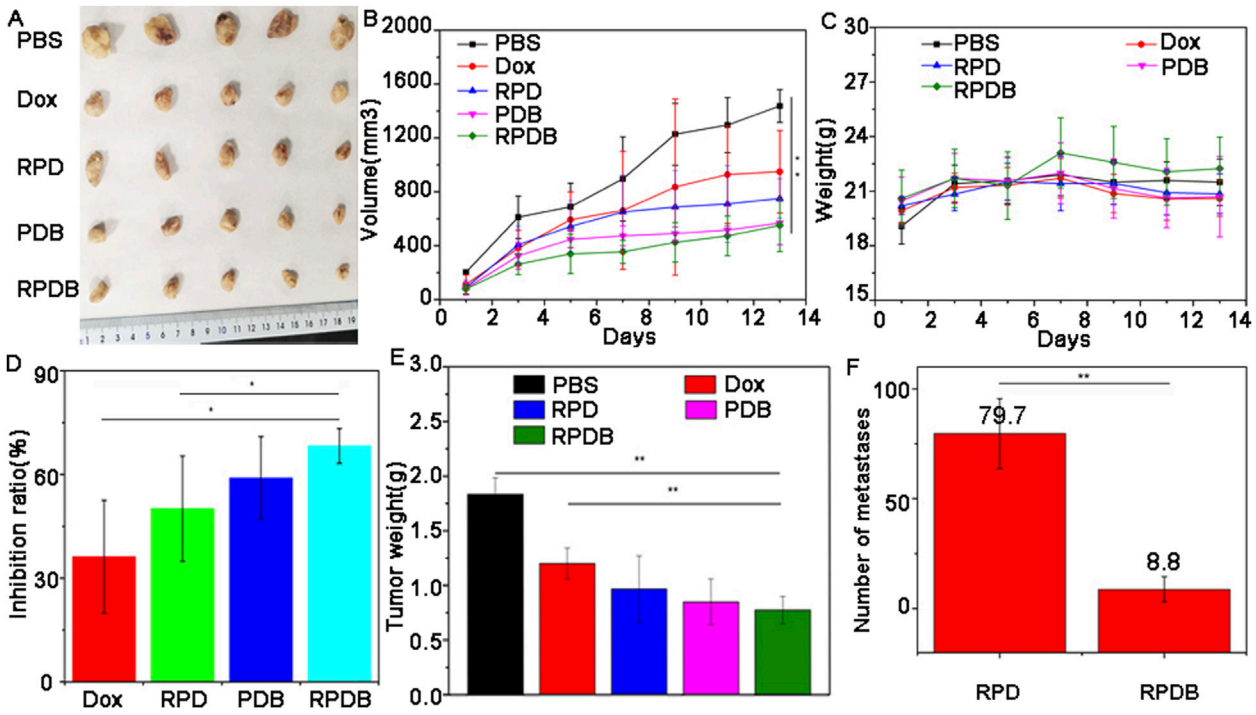

FIGURE 6
The *in vivo* antitumor efficacy of nano-micelles upon intravenous administration was evaluated. **(A)** The neoplasms were excised from the axillary region of the mouse forelimb on day 13 through surgical intervention; **(B)** The volume of tumor in mice injected with nano-micelles were meticulously measured for 13 days; **(C)** The weight trajectory of mice bearing tumors were meticulously recorded during the treatment period; **(D)** Inhibition rates of tumor growth across different groups of administration; **(E)** Tumor weights were meticulously recorded on day 13; **(F)** The number of metastases in mice of injected RPDB NPs and injected RPD NPs, and all data were presented as the mean ± standard deviation (n = 5, *p < 0.05, **p < 0.01). Number of metastases (Group RPD: 79.7 ± 15.9; Group RPDB: 8.8 ± 5.7).

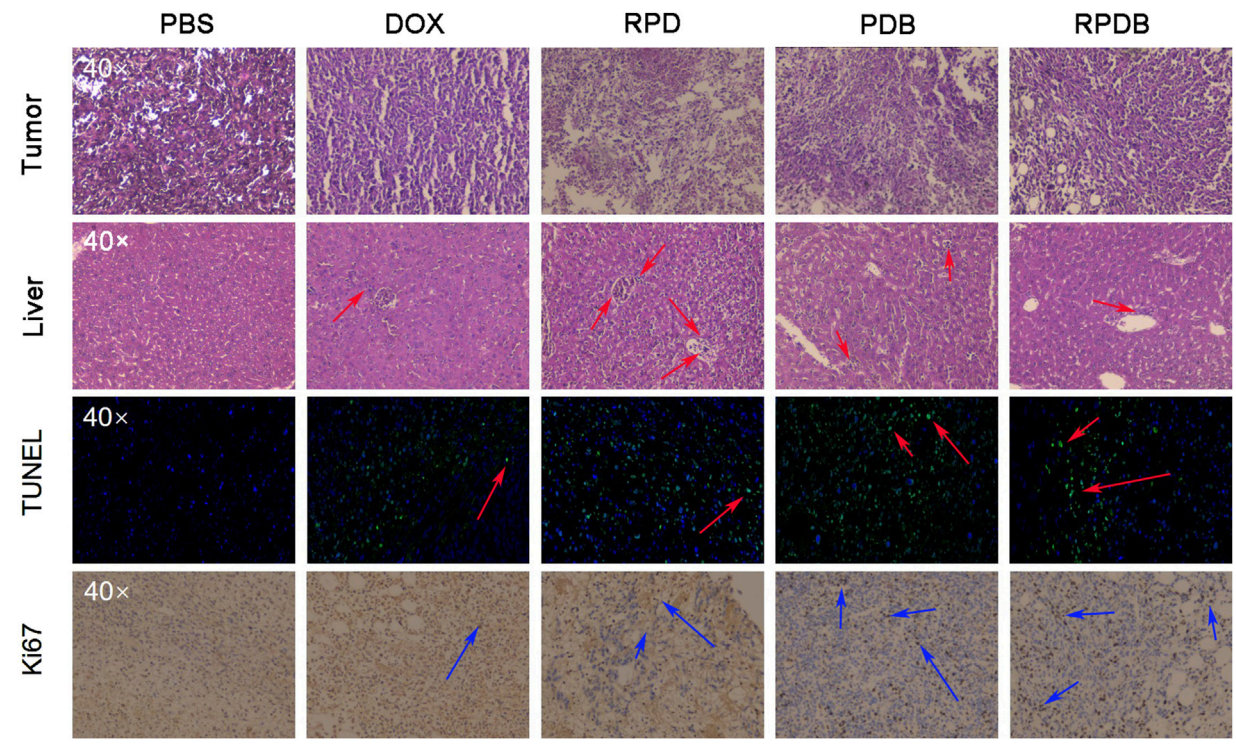

FIGURE 7
Thorough analysis was conducted on the liver and tumor pathological sections of mice injected with nano-micelles (n = 3). In the histopathological section of liver tissue, the red arrows represent Kupffer cells. In TUNEL analysis of tumors, a red arrow indicates DNA fragmentation, which is indicative of cell apoptosis in tumors. Ki67 serves as an indicator of tumor proliferation, with the blue arrow indicating positive areas.

tumors of mice injected with both Cy5.5-modified nanoparticles (RPD NPs and RPDB NPs), as shown in Figure 5A and Supplementary Figure S2. However, RPD NPs exhibited a stronger fluorescence signal in the liver than RPDB NPs did, indicating that reducing energy metabolism of mononuclear phagocyte system-associated organs helped minimize drug accumulation in the liver. Within 24 h of injection, the fluorescence signal of RPDB NPs in the liver was weaker than RPD NPs, as shown in Figures 5B, C. Calculation showed that the tumor fluorescence intensity of the RPDB NPs group was 70% higher compared to that of the RPD NPs group, as depicted in Figure 5D. What's more, the liver fluorescence intensity in the RPDB group was lower, about 40% of that in the RPD group (in Figure 5E). Therefore, the downregulation of macrophage energy metabolism through tailor-made nano-micelle complexes reduces the MPS effect and facilitates drug accumulation in tumors.

3.5 *In vivo* antitumor efficacy

Encouraged by distribution evaluation *in vivo*, these nano-micelles were further administrated intravenously into 4T1-tumor-bearing mice to assess antitumor outcomes. Similar to the assessment of cells toxicity, the experimental grouping and results were shown in Figure 6. After 13 days post-treatment, tumors in mice treated with PBS grew rapidly, while those in the other administration groups were significantly inhibited. These representative images of tumor have been captured and are shown in Figure 6A. The tumor volume was measured and calculated every 2 days over a period of 13 days, as illustrated in Figure 6B. In order to improve therapeutic efficiency, RGD was used to construct delivery systems targeting tumors. Evidently, the control group exhibited a significantly higher average tumor volume compared to the other groups, which is consistent with Figure 6A. Both PDB NPs group and RPDB NPs group exhibited excellent antitumor effects, as evidenced by the mean volume was significantly lower than that of the Dox and RPD groups. The difference in tumor inhibition effect between RPDB NPs and RPD NPs was significant, possibly due to the MPS effect being minimized by the GLUT1 inhibitor. Furthermore, body weight served as the most straightforward indicator for assessing drug toxicity. The absence of significant weight loss in mice during the treatment period, as shown in Figure 6C, indicates that these samples have low toxicity. Additionally, both the PDB NPs and RPDB NPs exhibited significantly higher tumor suppression ratios compared to the Dox and RPD NPs, with rates of 59.1% and 68.3%, respectively, versus 36.2% and 50.1%, as shown in Figure 6D. The inhibitory effects were further validated by the tumor weight presented in Figure 6E, which was consistent with both the tumor volume (Figure 6B) and inhibition rate (Figure 6D). As shown in Supplementary Figure S3, the living cell group (P1) had the most metastases in the lung, followed by the dead cell group and the living cell group (P3), and the dead cell group (P2) had no metastases. These results suggest that factors inhibit metastasis in the P3 group. Subsequently, RPD NPs and RPDB NPs were injected into group P3 respectively, and the results were shown in Figure 6F. RPDB NPs group had a

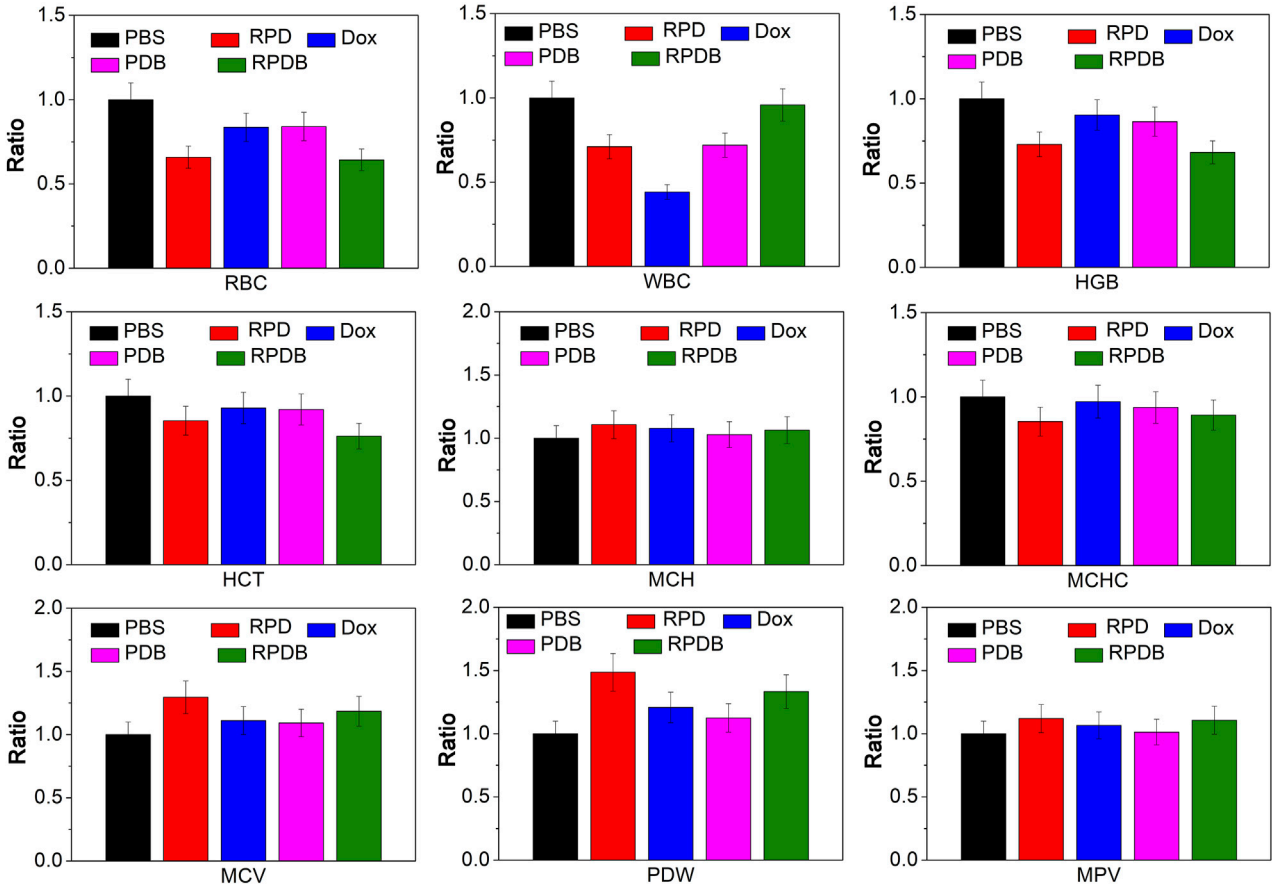

FIGURE 8
The safety of nano-micelles *in vivo* was preliminarily evaluated by analyzing blood routine.

significant lower metastases than RPD group, suggesting that RPDB NPs had an effect on inhibiting tumor metastasis.

3.6 Pathological analysis

Considering the excellent antitumor outcomes of nano-micelles based on macrophage energy metabolism, mice were euthanized to collect liver and tumor samples for pathological analysis. As shown in Figure 7, neither PDB NPs nor RPDB NPs showed a significant increase in Kupffer cells in H&E sections of mouse livers, while RPD NPs exhibited more Kupffer cells in hepatic sinusoids than other groups did, indicating that BAY876 contributed to the ability of nano-micelles to escape the RES effect. Meanwhile, the tumor sections of the PBS group also co-stained with hematoxylin and eosin, but did not present significant necrotic areas. However, in the treatment groups, damage areas were more pronounced, particularly in the PDB NPs and RPDB NPs groups. Based on TUNEL results, the RPDB NP-treated group exhibited a higher number of fluorescent spots indicating DNA breakage within tumors. Such DNA breakage often leads to cell death. Furthermore, the RPDB NPs group exhibited significantly stronger inhibition of cell proliferation compared to the other groups. The Ki-67 staining results revealed that the PBS group displayed a significantly higher proliferation factor compared to the other groups. During the treatment period, both the PDB NPs and RPDB NPs groups showed negligible proliferation of tumor cells. Therefore, pathological analysis suggests that anti-tumor strategies based on energy metabolism could minimize macrophage phagocytosis for tumor inhibition *in vivo*.

3.7 *In vivo* biosafety evaluation

Macrophages in the liver play a crucial role in the immune system. The biosafety of anti-tumor strategies aimed at down-regulating macrophage energy metabolism is further discussed concerning routine inspection and H&E staining. As shown in Figure 8, blood routine results indicate a significant decline in leukocytes for group Dox, consistent with previous reports of acute toxicity. However, nano-micelle complexes RPDB did not induce a drop in leukocytes. Comparing other indicators (HCT, MCH, MCHC, MCV, PDW, and MPV), no significant differences were seen between these groups. RPDB has a weak effect on RBC and HGB, which may be caused by inhibiting GLUT1 of erythrocytes. H&E staining was employed for further *in vivo* safety evaluation of nano-micelles, as shown in Supplementary Figure S4. Negligible inflammation was observed in the heart, lungs, spleen, and kidneys

of both the PDB and RPDB groups compared to the PBS group. The results indicate that both the PDB and RPDB groups demonstrate exceptional biocompatibility, thus holding significant potential for future antitumor applications.

4 Conclusion

Nanoparticles were plagued by various biological obstacles in clinical practice, especially the RES effect of macrophages, which led to a large amount of nanoparticle aggregation in the liver. In this study, nano-micelles complexes were successfully constructed by encapsulating BAY876 and Dox with polymer PEG-SS-PLA. These complexes exhibited excellent inhibitory effects on macrophage energy metabolism to minimize MPS effect. *In vivo*, the fluorescence signal of RPDB NPs was significantly weaker than that of RPD NPs in the liver, indicating that regulating macrophage energy metabolism helped to regulate drug distribution. Similarly, results from pathological sections also showed that there were more macrophages (Kupffer cells) in the groups without inhibitor BAY 867 compared to those with inhibitor. Meanwhile, these nano-platforms have shown significant antitumor outcomes *in vitro* and vivo. Compared with other MPS inhibition strategies, inhibition of energy metabolism did not eliminate macrophages and was beneficial to the recovery of immune function. As expected, nano-micelles based on the energy metabolism of macrophages could reduce the MPS effect for nanoparticles and improve antitumor outcomes, lighting up an alternative strategy in clinical application.

Data availability statement

The original contributions presented in the study are included in the article/Supplementary Material, further inquiries can be directed to the corresponding author.

Ethics statement

The animal study was approved by Institutional Animal Care and Use Committee of Liuzhou People`s Hospital. The study was conducted in accordance with the local legislation and institutional requirements.

Author contributions

LB: Conceptualization, Data curation, Investigation, Methodology, Project administration, Supervision, Writing–original draft, Writing–review and editing. LH: Investigation, Writing–review and editing. AC: Funding acquisition, Methodology, Resources, Writing–review and editing. YY: Data curation, Investigation, Validation, Writing–review and editing. YZ: Investigation, Methodology, Writing–review and editing. HZ: Resources, Writing–review and editing. QZ: Investigation, Methodology, Writing–review and editing. JZ: Validation, Visualization, Writing–review and editing. MQ: Resources, Writing–review and editing. XL: Methodology, Writing–review and editing. YT: Funding acquisition, Project administration, Supervision, Writing–review and editing.

Funding

The author(s) declare that financial support was received for the research and/or publication of this article. This study was supported by Guangxi Science and Technology Bases and Talents (AD21238014); Guangxi Science and Technology Bases and Talents (AD22035017); the Plan of Liuzhou Science and Technology (No. 2022SB033); Doctoral Research Start-up Fund of Guangxi University of Science and Technology (Xiaokebo21Z31); Guangxi medical and health appropriate technology development and application project (S2022144); Basic Ability Improvement Project for Young and Middle-Aged Teachers in Guangxi Province (2022KY0326); Guangxi medical and health appropriate technology development and application project (S2024114).

Acknowledgments

We gratefully acknowledge Wang Jun and the Laboratory Animal Center of Liuzhou People's Hospital for their assistance in the animal experiments of this study.

Conflict of interest

The authors declare that the research was conducted in the absence of any commercial or financial relationships that could be construed as a potential conflict of interest.

Generative AI statement

The authors declare that no Generative AI was used in the creation of this manuscript.

Publisher's note

Supplementary material

The Supplementary Material for this article can be found online at: https://www.frontiersin.org/articles/10.3389/fbioe.2025.1549101/full#supplementary-material

References

Belhadj, Z., He, B., Deng, H., Song, S., Zhang, H., Wang, X., et al. (2020). A combined "eat me/don't eat me" strategy based on extracellular vesicles for anticancer nanomedicine. *J. Extracell. Vesicles* 9, 1806444. doi:10.1080/20013078.2020.1806444

Bonamy, C., Pesnel, S., Ben Haddada, M., Gorgette, O., Schmitt, C., Morel, A.-L., et al. (2023). Impact of green gold nanoparticle coating on internalization, trafficking, and efficiency for photothermal therapy of skin cancer. *ACS Omega* 8, 4092–4105. doi:10.1021/acsomega.2c07054

Chen, Z., Vaeth, M., Eckstein, M., Delgobo, M., Ramos, G., Frantz, S., et al. (2023). Characterization of the effect of the GLUT-1 inhibitor BAY-876 on T Cells and macrophages. *Eur. J. Pharmacol.* 945, 175552. doi:10.1016/j.ejphar.2023.175552

Cheng, L., Zhang, X., Tang, J., Lv, Q., and Liu, J. (2021). Gene-engineered exosomes-thermosensitive liposomes hybrid nanovesicles by the blockade of CD47 signal for combined photothermal therapy and cancer immunotherapy. *Biomaterials* 275, 120964. doi:10.1016/j.biomaterials.2021.120964

Curi, R., de Siqueira Mendes, R., de Campos Crispin, L. A., Norata, G. D., Sampaio, S. C., and Newsholme, P. (2017). A past and present overview of macrophage metabolism and functional outcomes. *Clin. Sci.* 131, 1329–1342. doi:10.1042/cs20170220

Hao, J., Han, T., Wang, M., Zhuang, Q., Wang, X., Liu, J., et al. (2018). Temporary suppression the sequestrated function of host macrophages for better nanoparticles tumor delivery. *Drug Deliv.* 25, 1289–1301. doi:10.1080/10717544.2018.1474965

Jacobs, S. R., Herman, C. E., MacIver, N. J., Wofford, J. A., Wieman, H. L., Hammen, J. J., et al. (2008). Glucose uptake is limiting in T cell activation and requires CD28-mediated akt-dependent and independent pathways. *J. Immunol.* 180, 4476–4486. doi:10.4049/jimmunol.180.7.4476

Li, B., and Lane, L. A. (2019). Probing the biological obstacles of nanomedicine with gold nanoparticles. *WIRs Nanomed. Nanobi.* 11, e1542. doi:10.1002/wnan.1542

Li, Z., Zhu, Y., Zeng, H., Wang, C., Xu, C., Wang, Q., et al. (2023). Mechano-boosting nanomedicine antitumour efficacy by blocking the reticuloendothelial system with stiff nanogels. *Nat. Commun.* 14, 1437. doi:10.1038/s41467-023-37150-3

Liu, Y., Wang, Z., Liu, Y., Zhu, G., Jacobson, O., Fu, X., et al. (2017). Suppressing nanoparticle-mononuclear phagocyte system interactions of two-dimensional gold nanorings for improved tumor accumulation and photothermal ablation of tumors. *ACS Nano* 11, 10539–10548. doi:10.1021/acsnano.7b05908

Mirkasymov, A. B., Zelepukin, I. V., Ivanov, I. N., Belyaev, I. B., Dzhalilova, D. S., Trushina, D. B., et al. (2022). Macrophage blockade using nature-inspired ferrihydrite for enhanced nanoparticle delivery to tumor. *Int. J. Pharm.* 621, 121795. doi:10.1016/j.ijpharm.2022.121795

Mirkasymov, A. B., Zelepukin, I. V., Nikitin, P. I., Nikitin, M. P., and Deyev, S. M. (2021). *In vivo* blockade of mononuclear phagocyte system with solid nanoparticles: efficiency and affecting factors. *J. Control. Release.* 330, 111–118. doi:10.1016/j.jconrel.2020.12.004

Ngo, W., Ahmed, S., Blackadar, C., Bussin, B., Ji, Q., Mladjenovic, S. M., et al. (2022). Why nanoparticles prefer liver macrophage cell uptake *in vivo*. *Adv. Drug Deliv. Rev.* 185, 114238. doi:10.1016/j.addr.2022.114238

Ouyang, B., Poon, W., Zhang, Y.-N., Lin, Z. P., Kingston, B. R., Tavares, A. J., et al. (2020). The dose threshold for nanoparticle tumour delivery. *Nat. Mater.* 19, 1362–1371. doi:10.1038/s41563-020-0755-z

Patel, K. R., Li, M. P., and Baldeschwieler, J. D. (1983). Suppression of liver uptake of liposomes by dextran sulfate 500. *P. Natl. A. Sci.* 80, 6518–6522. doi:10.1073/pnas.80.21.6518

Poon, W., Kingston, B. R., Ouyang, B., Ngo, W., and Chan, W. C. (2020). A framework for designing delivery systems. *Nat. Nanotechnol.* 15, 819–829. doi:10.1038/s41565-020-0759-5

Sakamoto, T., Niiya, D., and Seiki, M. (2011). Targeting the warburg effect that arises in tumor cells expressing membrane type-1 matrix metalloproteinase. *J. Biol. Chem.* 286, 14691–14704. doi:10.1074/jbc.m110.188714

Shi, Q., Shen, Q., Liu, Y., Shi, Y., Huang, W., Wang, X., et al. (2022). Increased glucose metabolism in TAMs fuels O-GlcNAcylation of lysosomal cathepsin B to promote cancer metastasis and chemoresistance. *Cancer Cell* 40, 1207–1222.e10. doi:10.1016/j.ccell.2022.08.012

Tavares, A. J., Poon, W., Zhang, Y.-N., Dai, Q., Besla, R., Ding, D., et al. (2017). Effect of removing kupffer cells on nanoparticle tumor delivery. *P. Natl. A. Sci.* 114, e10871–e10880. doi:10.1073/pnas.1713390114

Venturelli, L., Nappini, S., Bulfoni, M., Gianfranceschi, G., Dal Zilio, S., Coceano, G., et al. (2016). Glucose is a key driver for GLUT1-mediated nanoparticles internalization in breast cancer cells. *Sci. Rep-UK* 6, 21629–21714. doi:10.1038/srep21629

Wan, Z., Zhao, L., Lu, F., Gao, X., Dong, Y., Zhao, Y., et al. (2020). Mononuclear phagocyte system blockade improves therapeutic exosome delivery to the myocardium. *Theranostics* 10, 218–230. doi:10.7150/thno.38198

Wang, C., Cheng, L., and Liu, Z. (2011). Drug delivery with upconversion nanoparticles for multi-functional targeted cancer cell imaging and therapy. *Biomaterials* 32, 1110–1120. doi:10.1016/j.biomaterials.2010.09.069

Wang, Y., Zhang, K., Qin, X., Li, T., Qiu, J., Yin, T., et al. (2019). Biomimetic nanotherapies: red blood cell based core-shell structured nanocomplexes for atherosclerosis management. *Adv. Sci.* 6, 1900172. doi:10.1002/advs.201900172

Xiao, H., Qi, R., Liu, S., Hu, X., Duan, T., Zheng, Y., et al. (2011). Biodegradable polymer– cisplatin (IV) conjugate as a pro-drug of cisplatin (II). *Biomaterials* 32, 7732–7739. doi:10.1016/j.biomaterials.2011.06.072

Yamada, S., Tomiya, T., Yamaguchi, Y., Hiura, M., and Otsuki, M. (2003). Activation of hepatic macrophage contributes to hepatic necrosis after post-ischemic reperfusion in alcoholic fatty liver. *Hepatol. Res.* 26, 209–216. doi:10.1016/s1386-6346(03)00092-5

Yang, B., Han, X., Ji, B., and Lu, R. (2016). Competition between tumor and mononuclear phagocyte system causing the low tumor distribution of nanoparticles and strategies to improve tumor accumulation. *Curr. Drug Deliv.* 13, 1261–1274. doi:10.2174/1567201813666160418105703

Yang, W. S., SriRamaratnam, R., Welsch, M. E., Shimada, K., Skouta, R., Viswanathan, V. S., et al. (2014). Regulation of ferroptotic cancer cell death by GPX4. *Cell* 156, 317–331. doi:10.1016/j.cell.2013.12.010

Yang, Z., Tao, D., Zhong, W., Liu, Z., Feng, L., and Chen, M. (2022). Perfluorocarbon loaded fluorinated covalent organic polymers with effective sonosensitization and tumor hypoxia relief enable synergistic sonodynamic-immunotherapy. *Biomaterials* 280, 121250. doi:10.1016/j.biomaterials.2021.121250

Zhao, F., Zhao, Y., Liu, Y., Chang, X., Chen, C., and Zhao, Y. (2011). Cellular uptake, intracellular trafficking, and cytotoxicity of nanomaterials. *Small* 7, 1322–1337. doi:10.1002/smll.201100001

Frontiers in
Bioengineering and Biotechnology

Accelerates the development of therapies, devices, and technologies to improve our lives

A multidisciplinary journal that accelerates the development of biological therapies, devices, processes and technologies to improve our lives by bridging the gap between discoveries and their application.

Discover the latest Research Topics

See more →

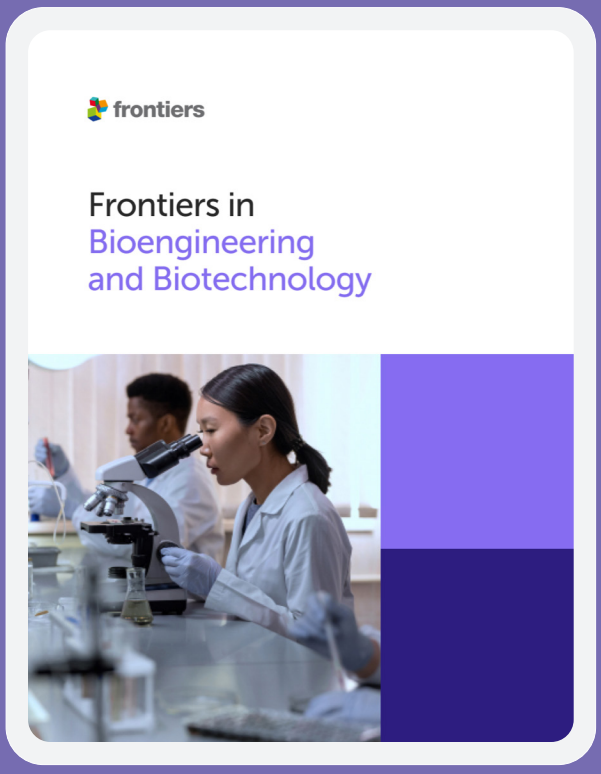

Frontiers

Avenue du Tribunal-Fédéral 34
1005 Lausanne, Switzerland
frontiersin.org

Contact us

+41 (0)21 510 17 00
frontiersin.org/about/contact